



**Development of High Power Fibre Amplifier
Components, Systems and Applications**

Thomas Legg

Department of Electronic and Electrical Engineering

Centre for Microsystems and Photonics

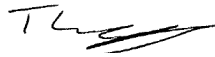
**A thesis submitted to the Department of Electronic and Electrical Engineering of the
University of Strathclyde for the degree of Doctor of Engineering**

February 2012

Declaration of Authenticity and Author's Rights

This thesis is the result of the author's original research. It has been composed by the author and has not been previously submitted for examination which has led to the award of a degree.

The copyright of this thesis belongs to the author under the terms of the United Kingdom Copyright Acts as qualified by University of Strathclyde Regulation 3.50. Due acknowledgement must always be made of the use of any material contained in, or derived from, this thesis.

Signed: 

Date: 30/08/2012

Contribution Statement

I would like to thank the following people for contributions to this thesis:

Kevin Duffin and David Mitchell for the laboratory characterisation of the Raman amplified methane sensor and for conducting field trials. This work is reported in chapter 5 sections 5.4 and 5.5.

Chris Pannell for his contribution to the analysis of thermal effects in an optical isolator, appendices A9.1 and A10.1.

Peter McKay for some magnetic modelling of the Faraday isolator, chapter 10 section 10.3.

Norman Fisher for optical return loss measurements reported in chapter 10 section 10.9.3.

Abstract

This thesis contains two projects – the development of a Raman fibre amplifier system for gas sensing and the development of a fibre-in beam-out isolator for use with fibre lasers.

The first project developed a fibre Raman amplifier which amplified a 10mW narrow linewidth DFB laser at 1651nm to an output power of over 2W. To achieve this high output power from a narrow linewidth Raman amplifier mechanisms to suppress stimulated Brillouin scattering had to be employed. This amplifier system was packaged into a portable 19” rack enclosure and used to demonstrate remote, single-end, tuneable diode laser spectroscopy of methane. The packaged system detected methane concentrations of 100ppm.m at over 100m during challenging field trials. Extrapolation of lab based measurements to longer distances predicts an ultimate sensitivity of the system of 100ppm.m at greater than 200m.

The second project developed a Faraday isolator to be used at the output of industrial fibre lasers. The isolator had an isolation of greater than 30dB, an insertion loss of less than 0.5dB and a return loss of greater than 50dB. The isolator used a dual Faraday rotator design with a half wave plate between the rotators to compensate for thermal stress induced birefringence. Using this approach the isolation was shown to be constant to greater than 60W. The isolator was also compensated for thermal lensing by balancing the positive thermal lens produced in the Faraday rotator with a negative thermal lens in a DKDP crystal. This reduced the thermal lens of the isolator from ~9 Rayleigh length per kW intrinsic to below 2 Rayleigh lengths per kW.

Table of Contents

| | |
|---|-----------|
| Chapter 1 - Introduction and Executive Summary | 1 |
| 1.1 Introduction..... | 1 |
| 1.2 Executive Summary | 2 |
| 1.3 Thesis Structure..... | 3 |
| Chapter 2 - Introduction to the Development of a Long-Range Open-Path Methane Sensor | 5 |
| 2.1 Introduction..... | 5 |
| 2.2 Outline of Proposed System | 6 |
| 2.3 Objectives..... | 8 |
| 2.4 Breakdown of following chapters..... | 8 |
| Chapter 3 - Theory..... | 10 |
| 3.1 Tunable Diode Laser Spectroscopy (TDLS)..... | 10 |
| 3.1.1 Tuneable Diode Laser Spectroscopy with Direct Detection (TDLS-DD)..... | 12 |
| 3.1.2 Tuneable Diode Laser Spectroscopy with Wavelength Modulation Spectroscopy (TDLS-WMS)..... | 14 |
| 3.2 Methane Spectroscopy and State-of-the-Art TDLS Detectors | 18 |
| 3.2.1 Short Range TDLS Methane Sensors | 20 |
| 3.2.2 Long Range TDLS Methane Sensors..... | 21 |
| 3.3 Choice of Laser Source for the Long Range Methane Sensor..... | 23 |
| 3.4 Raman Amplification..... | 25 |
| 3.4.1 Spontaneous Raman Scattering..... | 25 |
| 3.4.2 Stimulated Raman Scattering (SRS) | 28 |
| 3.5 Brillouin Scattering | 33 |
| 3.5.1 Spontaneous Brillouin Scattering..... | 33 |
| 3.5.2 Stimulated Brillouin Scattering (SBS)..... | 34 |
| 3.6 SBS suppression | 37 |
| 3.6.1 SBS Suppression by Broadening Pump Linewidth..... | 37 |
| 3.6.2 SBS Suppression by Broadening the Brillouin Gain Linewidth | 38 |
| 3.7 High Power Narrow Linewidth Raman Amplifiers | 40 |
| 3.8 Summary..... | 41 |
| Chapter 4 - Fibre Amplifier System Development..... | 50 |

| | | |
|---|--|------------|
| 4.1 | <i>Erbium Doped Fibre Amplifier (EDFA)</i> | 50 |
| 4.2 | <i>Modelling CW Double Clad Er:Yb Fibre Amplifier</i> | 53 |
| 4.3 | <i>Raman Amplifier</i> | 58 |
| 4.4 | <i>Modelling of CW Raman Amplifier System</i> | 59 |
| 4.5 | <i>Fibre Amplifier system for the Long Range Methane Sensor</i> | 62 |
| 4.5.1 | Amplified Spontaneous Emission Source | 63 |
| 4.5.2 | High Power Erbium-Ytterbium Fibre Amplifier..... | 65 |
| 4.5.3 | Counter Propagating Raman Fibre Amplifier | 68 |
| 4.5.4 | Co-propagating Raman Amplifier | 71 |
| 4.6 | <i>Suitability for Methane Sensor – Testing of complete system</i> | 73 |
| Chapter 5 - Construction and Testing of Prototype Methane Sensor | | 79 |
| 5.1 | <i>TDLS System</i> | 79 |
| 5.2 | <i>Operating Instructions</i> | 86 |
| 5.3 | <i>Initial demonstration of the TDLS System</i> | 88 |
| 5.4 | <i>Laboratory Trials and Characterisation</i> | 96 |
| 5.5 | <i>Field Trials</i> | 101 |
| Chapter 6 - Conclusion | | 113 |
| 6.1 | <i>Achievements of Raman Amplifier build</i> | 113 |
| 6.2 | <i>Achievements of System Integration</i> | 114 |
| 6.3 | <i>Next Stage Improvements to the Methane Sensor</i> | 115 |
| 6.4 | <i>Further work</i> | 117 |
| Chapter 7 - Development of a Fibre-in Beam-out Isolator for Fibre Amplifiers | | 119 |
| 7.1 | <i>Introduction</i> | 119 |
| 7.2 | <i>Outline of Proposed Isolator</i> | 121 |
| 7.3 | <i>Objectives</i> | 122 |
| 7.4 | <i>Overview of following chapters</i> | 123 |
| Chapter 8 - Faraday Isolator Theory | | 124 |
| 8.1 | <i>Faraday Effect</i> | 124 |
| 8.2 | <i>Derivation of Becquerel's Verdet Constant Expression</i> | 125 |

| | | |
|---|--|------------|
| 8.3 | <i>Faraday Isolators</i> | 127 |
| 8.4 | <i>Thermal Effects in Faraday Isolators</i> | 129 |
| 8.4.1 | Thermal Stress Induced Depolarisation | 130 |
| 8.4.2 | Thermal Lens | 142 |
| 8.4.3 | Thermal dependence of Verdet Constant and Magnetic Field Strength and Compensation | 145 |
| 8.5 | <i>State of the Art</i> | 147 |
| Chapter 9 - Thermal Lens Effect in Faraday Isolator | | 153 |
| 9.1 | <i>Thermal Gradients in Optical Materials</i> | 153 |
| 9.2 | <i>Calculating Thermal Lens Focal Length</i> | 156 |
| 9.3 | <i>Measuring Thermal Lens Power (Geometrical)</i> | 158 |
| 9.4 | <i>Focal Shift in Terms of Rayleigh Length</i> | 160 |
| 9.5 | <i>Our Thermal Lens Measurement Setup – Equipment and procedure</i> | 161 |
| 9.6 | <i>Other Thermal Lens Measurement Techniques</i> | 167 |
| 9.7 | <i>Thermal Lens Compensation</i> | 169 |
| 9.8 | <i>Compensation of thermal lens with DKDP</i> | 171 |
| 9.9 | <i>Temperature variation of the Verdet Constant and magnetic field strength</i> | 173 |
| Chapter 10 - Faraday Isolator Design, Construction and Characterisation..... | | 184 |
| 10.1 | <i>Design of Fibre-in Beam-out Faraday Isolator</i> | 184 |
| 10.2 | <i>Optical Design and Polarisation Changes</i> | 186 |
| 10.3 | <i>Magnet design</i> | 189 |
| 10.4 | <i>TGG</i> | 192 |
| 10.5 | <i>Other Magneto-Optic Materials</i> | 194 |
| 10.6 | <i>Thermal Lens measurement of Isolator</i> | 196 |
| 10.7 | <i>Thermal Lens Compensation using DKDP</i> | 198 |
| 10.8 | <i>Thermal Lens Compensation using Polymer</i> | 203 |
| 10.9 | <i>Low Power Isolator Measurements</i> | 205 |
| 10.9.1 | Isolation Measurements | 205 |
| 10.9.2 | Insertion Loss Measurement | 207 |
| 10.9.3 | Return loss measurement | 207 |

| | | |
|--------------------------------------|--|------------|
| 10.10 | <i>High Power Isolator Measurements</i> | 210 |
| 10.10.1 | Isolation-Power Measurements..... | 210 |
| 10.10.2 | Isolation with Beam Dumps and Temperature Measurements | 211 |
| 10.10.3 | 200hrs 60W Power Handling Test..... | 213 |
| Chapter 11 - Conclusion | | 220 |
| 11.1 | <i>Summary of Isolator Development</i> | 220 |
| 11.2 | <i>Next steps</i> | 221 |
| 11.3 | <i>Fibre-in Fibre-out Isolator</i> | 222 |

Table of Figures

| | |
|---|----|
| Figure 2.1: Simplified schematic of the proposed 1651nm Raman amplifier..... | 7 |
| Figure 2.2: Open path, single end TDLS setup using Raman Amplifier system..... | 8 |
| Figure 3.1: Illustration of the principal of tuneable diode laser spectroscopy with direct detection [3.6]..... | 13 |
| Figure 3.2: System diagram of a typical setup for TDLS-DD..... | 14 |
| Figure 3.3: Illustration of the principal of tuneable diode laser spectroscopy with wavelength modulation spectroscopy. As the wavelength of the laser ω_L is scanned across a gas absorption line the wavelength modulation is converted to an amplitude modulation $\Delta\alpha$ (AM). Over a complete scan of the absorption profile this builds up a trace of the line derivative. [3.7]..... | 16 |
| Figure 3.4 Lorentzian line profile (a) with first (b), second (c) and third (d) derivatives [3.7]...... | 16 |
| Figure 3.5: System diagram of a typical setup for TDLS-WMS..... | 18 |
| Figure 3.6: Methane absorption spectrum from a) 1 μ m to 4 μ m and b) close up of 1651nm..... | 19 |
| Figure 3.7: Oscilloscope traces of detected signal from seed laser (black) and EDFA output (red) at various modulation frequencies [3.23]...... | 22 |
| Figure 3.8: Raman Scattering. An incoming photon of frequency (ν_p) excites a molecule in an initial vibrational state (i) to a virtual state (u). The molecule subsequently emits a Stokes photon with a frequency (ν_s) and returns to a different state (f). If the molecule begins in state (f) then it may return to state (i) forming an anti-stokes photon with frequency (ν_{as})..... | 26 |
| Figure 3.9: Raman gain spectrum of silica optical fibre measured with a 1550nm pump and an orthogonally polarized signal [3.33]. | 28 |
| Figure 3.10: Pump power (green) and signal power (red) evolution in a co-propagating Raman amplifier..... | 30 |
| Figure 3.11: Pump power (green) and signal power (red) evolution in a counter-propagating Raman amplifier..... | 31 |
| Figure 3.12: Pump and signal evolution in a co-propagating Raman amplifier with an input seed power of 1mW (red), 10mW (green), 100mW (Blue) and 1W (black). | 33 |
| Figure 3.13: Stimulated Brillouin Scattering. [3.32]. | 35 |
| Figure 4.1: Cross section of double clad optical fibre showing refractive index profile [4.7]. | 52 |
| Figure 4.2: Energy level diagram of Er:Yb system showing transition paths, pumping rates and decay constants [4.12]. | 54 |
| Figure 4.3: Calculated evolution of pump and signal power in fibre amplifier with 32W 980nm pump and 5mW 1550nm seed. | 57 |
| Figure 4.4: Calculated output signal power Vs pump power in a 10.5m length of ErYb fibre. | 57 |
| Figure 4.5: Evolution of pump (red), signal (blue) and Brillouin (green) powers in a Raman amplifier. | 62 |
| Figure 4.6: ASE seed schematic..... | 64 |

| | |
|--|-----|
| Figure 4.7: Pump-Output characteristics (red) and conversion efficiency (blue) of ASE seed..... | 64 |
| Figure 4.8: ASE seed spectrum at 5mW output power. | 65 |
| Figure 4.9: Schematic of high power EDFA. | 66 |
| Figure 4.10: Pump power Vs output power characteristics of EDFA and optical conversion efficiency..... | 67 |
| Figure 4.11: Spectrum of EDFA at 5W output power..... | 67 |
| Figure 4.12: Counter-propagating Raman Amplifier. | 70 |
| Figure 4.13: Output Power Vs Pump power of Raman amplifier. | 70 |
| Figure 4.14: Backscattered power..... | 71 |
| Figure 4.15: Co-propagating Raman Amplifier. | 72 |
| Figure 4.16: Output power characteristics of co-propagating Raman amplifier. | 72 |
| Figure 4.17: 1650nm backscattered power in Raman amplifier..... | 73 |
| Figure 4.18: Backscatter vs. dither Frequency. Dither 50mA pk-pk..... | 74 |
| Figure 4.19: Backscatter vs. dither depth. | 75 |
| Figure 4.20: Distortion to output waveform due to stimulated Brillouin scattering..... | 76 |
| Figure 5.1: Complete system for TDLS demonstrator. | 80 |
| Figure 5.2: Inside the Optical amplifier system. | 81 |
| Figure 5.3: Schematic of fibre amplifier system and control electronics. [5.1] | 82 |
| Figure 5.4: Inside the amplifier control rack..... | 83 |
| Figure 5.5: Photograph of TDLS electronics rack..... | 84 |
| Figure 5.6: Block Diagram Schematic of TDLS electronics rack..... | 84 |
| Figure 5.7: Inside the transmit/receive head unit. (picture Kevin Duffin) | 85 |
| Figure 5.8: Computer Interface used during trials..... | 86 |
| Figure 5.9: Drive current Vs output power of completed amplifier system. | 88 |
| Figure 5.10: Diagram of setup for laboratory trials of gas sensing system. | 89 |
| Figure 5.11: Gas sensing measurement with 1.2W transmitted power and path length concentration of 10000ppm.m off a concrete backscatter target..... | 90 |
| Figure 5.12: Measurements with different targets at high power – low concentration. | 92 |
| Figure 5.13: Measurements with different targets at low power – low concentration. | 95 |
| Figure 5.14: Measurements of 10,000ppm.m, 1000ppm.m and 100ppm.m concentrations of methane from a concrete block..... | 99 |
| Figure 5.15: Measurement of 100ppm.m (in one tedlar bag) and 200ppm.m (in 2 tedlar bags) samples above background. | 100 |
| Figure 5.16: Output power at 1650nm as a function of pump power..... | 100 |
| Figure 5.17: Photos taken of field trials. | 103 |
| Figure 5.18: Measurements of 10,000ppm.m, 1000ppm.m, 100ppm.m methane samples made using the demonstrator at 105m during field trials. | 104 |
| Figure 5.19: Measurements of different concentrations of methane at 105m. Inset: expanded image of 100ppm.m and background measurement. | 105 |

| | |
|---|-----|
| Figure 7.1: Suppression of back reflection using a) an angled cleave; and b) an end-cap. In each case light in the core of the fibre is lost to the cladding (dotted lines)..... | 120 |
| Figure 8.1: Faraday Isolator basic schematic | 127 |
| Figure 8.2: Polarisation Independent Faraday Isolator using birefringent wedges [8.6]..... | 128 |
| Figure 8.3: Depolarisation distribution of Gaussian beam through a TGG rod a) theoretical and b) experimental..... | 131 |
| Figure 8.4: Thermal birefringence compensated cavity using dual laser rods and a 90 degree quartz rotator..... | 131 |
| Figure 8.5: Laser cavity with 45° Faraday rotator with laser rod broken into retardation plates. This is the polarisation flip cavity analysed by Giuliani and Ristori [8.12]..... | 133 |
| Figure 8.6: Thermal Birefringence compensation using a quarter-wave plate [8.13]. | 133 |
| Figure 8.7: Design of a) traditional Faraday isolator b) isolator with counter-rotating 22.5° Faraday rotators and a half wave ($\lambda/2$) plate and c) isolator with two 22.5° rotators separated by a quartz rotator [8.20]. | 134 |
| Figure 8.8: Dependence of isolation on input power for the three isolator designs. TGG length of 40mm and best orientation angle. | 138 |
| Figure 8.9: Dependence of isolation on length of TGG crystal for the three isolator designs. Best orientation angle..... | 139 |
| Figure 8.10: Dependence of isolation on <001> TGG axis orientation for the three isolator designs. | 139 |
| Figure 8.11: Isolation of half wave plate compensated isolator using <001> TGG in the best and worst orientation and using <111> TGG..... | 140 |
| Figure 9.1: Temperature profile | 155 |
| Figure 9.2: Refractive index in centre of a 6mm radius TGG crystal heated by 1000W Gaussian with spot size 1mm..... | 157 |
| Figure 9.3: Dioptric power of thermal lens against power in 30mm piece of TGG..... | 157 |
| Figure 9.4: Two lens system used to derive argument to compare focal shift in Rz/kW to Dioptres/kW..... | 160 |
| Figure 9.5: Operating Space chart for Nanoscan pyroelectric scanning-slit detector | 162 |
| Figure 9.6: Setup for measurement of thermal lens from an isolator..... | 162 |
| Figure 9.7: Measurement of beam radius with position made by Nanomodscan system..... | 164 |
| Figure 9.8: Example thermal lens measurement. | 165 |
| Figure 9.9: Fibre coupling jig with water (top) and forced air (bottom) cooling. | 166 |
| Figure 9.10: Probe deflection thermal lens measurement [9.22]..... | 168 |
| Figure 9.11: Refractive index profile in 3mm radius DKDP pumped with a 1kW Gaussian laser with a radius of 0.5mm..... | 173 |
| Figure 9.12: Variation of isolation with Temperature caused just by temperature variation of the magnetic field strength and Verdet constant. | 174 |
| Figure 10.1: Mechanical (Top down) schematic of the Faraday isolator..... | 186 |

| | |
|---|-----|
| Figure 10.2: Beam paths through the isolator and polarisation changes for light travelling in the forward and reverse direction. [Mark Gardner]. | 187 |
| Figure 10.3: Birefringent walk-off plate. | 188 |
| Figure 10.4: Diagram of magnetic field produced by the isolator magnet assembly. | 190 |
| Figure 10.5: Magnetic field strength through centre of the TGG rods. | 190 |
| Figure 10.6: Polarisation rotation variation with the separation between magnets at 20°C. | 191 |
| Figure 10.7: Variation of the magnetic field strength radially through the TGG rods. | 191 |
| Figure 10.8: Reflectivity of AR coating on piece of TGG. | 193 |
| Figure 10.9: Image of red alignment laser transmission through isolator, | 194 |
| Figure 10.10: Setup used to measure the thermal lens of a complete isolator. | 197 |
| Figure 10.11: Focus position shift with power of complete isolator. | 197 |
| Figure 10.12: Focal shift of isolator and 15mm DKDP. | 199 |
| Figure 10.13: 99% DKDP sample constructed as isolating component for testing with isolator. | 200 |
| Figure 10.14: Setup used to measure the thermal lens of an isolator and DKDP. | 201 |
| Figure 10.15: Power dependent focal shift of isolator (s/n 01460261) with and without DKDP compensator. | 201 |
| Figure 10.16: Setup used to measure the thermal lens of isolator with DKDP compensation model. | 202 |
| Figure 10.17: Thermal lens measurement of isolator (s/n 01460264) with DKDP module. | 202 |
| Figure 10.18: Propagation of light after exiting the isolator, and inside isolator (ignoring refraction of the crystals). | 203 |
| Figure 10.19: High power testing of Sylgard 184. | 205 |
| Figure 10.20: Isolation measurement beams on a CCD a) isolated beams and b) residual/not isolated beams. | 206 |
| Figure 10.21: Setup for measuring the return loss of an isolator. | 208 |
| Figure 10.22: Measurement of Return Loss of isolator. | 209 |
| Figure 10.23: Setup for measuring isolation at high powers. | 211 |
| Figure 10.24: Isolation against input power. | 211 |
| Figure 10.25: Temperature rise of isolator outer casing and isolation with 28W reverse input power. | 212 |
| Figure 10.26: 200hr test of isolator with greater than 60W input. | 213 |
| Figure 11.1: Path of beams through optical components of single-pass FIFO isolator, side view and top view, and polarisation changes in forward (red) and reverse (blue) propagation. [11.5] | 224 |
| Figure 11.2: Magnetic field around triple magnet design calculated using FEMM. | 225 |
| Figure 11.3: Rotation of TGG in triple magnet design, figure 11.6, with spacers between the magnets. | 225 |

Chapter 1 - Introduction and Executive Summary

In accordance with EngD guidelines this thesis is of a “portfolio” type, covering two distinct but interrelated projects:

1. The development of a high power fibre amplifier system for methane sensing; and
2. The development of a Faraday isolator for high power fibre amplifiers.

This chapter introduces these two projects and explains the connection between them. The chapter also includes an executive summary, highlighting the main outcomes of the two projects, and finishes with a chapter-by-chapter overview of the thesis.

This chapter is structured as follows:

- **Section 1.1 – Introduction**
- **Section 1.2 – Executive Summary**
- **Section 1.3 – Thesis Structure**

1.1 Introduction

The rate of development and adoption of fibre amplifier technology over the past half century has been staggering. Since the initial idea of a fibre based gain medium was proposed by Snitzer in the 1960's [1.1] rare earth doped fibre amplifiers have progressed rapidly from research to application. They are often described as the key enabler of long haul telecommunications, with the development of the erbium doped fibre amplifier in the late 1980's [1.2, 1.3].

In the last couple of decades the power of rare earth doped fibre amplifiers has increased tremendously from a maximum of several watts in the late 1990's to over 1kW today [1.4]. These high powers are now enabling fibre amplifiers to be used in applications like materials processing; where fibre amplifiers, with their “perfect” beam quality and low maintenance, are quickly displacing traditional high power CO₂ and Nd:YAG lasers. The broad gain spectrum of fibre amplifiers is also finding use in applications like optical coherence tomography and long range sensing [1.5].

The development of fibre amplifiers to access new wavelength ranges and higher powers to target new applications is therefore very exciting. As is the development of the fibre optic components required to allow these amplifiers to operate efficiently and robustly. Since most of the key components used in fibre amplifiers, like fused-fibre WDMs and splitters were developed for telecommunication and not

originally intended for use at high powers [1.6]. Therefore, a lot can be done to improve the power handling and reliability of these components.

This dissertation will report on two projects based broadly around the design and development of high power fibre amplifier components and systems. The first project concerns the development of a fibre amplifier system with application to long range methane sensing. The second project examines the development of a Faraday Isolator for use with high power fibre amplifier and laser systems. Faraday isolators are critical components required to protect fibre lasers from back reflected light.

The relationship between these projects is that they both utilise fibre optic technology and advance the state-of-the-art in high power fibre optic amplifier and component design. To improve the robustness of the fibre amplifier system developed in the first project a Faraday isolator, similar to that produced in the second project, could be used at the output. In fact it is believed that back-reflections were responsible for destroying several pump diodes in a high power EDFA during construction of the amplifier system.

1.2 Executive Summary

The first project developed a fibre amplifier which amplified a narrow linewidth 1651nm DFB diode laser from 10mW to over 2W. This was integrated into a prototype module with all of the electronics and software required for remote, single-end, tuneable diode laser spectroscopy of methane. The finished system had a realised sensitivity of 100ppm.m methane above background at 100m, and a predicted final sensitivity of 100ppm.m at 200m.

The fibre amplifier system consisted of a 1651nm Raman fibre amplifier pumped by a 1540nm Er-Yb doped fibre amplifier. The Raman amplifier (frequency shifter) was required because the wavelength range around 1650nm is not accessible with rare earth doped fibre amplifiers. The fibre amplifier needed to have a high output power and a narrow linewidth for high sensitivity spectroscopy. These two properties are incompatible in fibre amplifiers because high power densities induce detrimental nonlinear effects like stimulated Brillouin scattering (SBS) and the threshold power for SBS decreases for narrow linewidths.

Stimulated Brillouin scattering depletes the gain available for Raman scattering and also affects the gain dynamics of the amplifier, distorting any modulation applied to the DFB for methane sensing. Therefore, an important part of this work centred on controlling nonlinearities: suppressing Brillouin scattering and optimising Raman amplification.

The second project developed a fibre-in beam-out Faraday isolator for use at the output end of high power fibre amplifiers. Faraday isolators prevent light from travelling in the reverse direction and re-entering the fibre where it can destabilise the laser output and in some cases damage pump and seed diodes. Isolators are becoming increasingly important as amplifier powers increase and applications become more demanding.

The fibre isolator provided >30dB isolation in the region of 1060nm and maintained this isolation up to at least 60W. The isolator included compensation for thermal stress induced depolarisation and thermal lensing. These effects are caused by absorption heating in the terbium gallium garnet (TGG) Faraday rotator in the isolator.

Thermal lensing is caused predominantly by absorption heating in the TGG which creates temperature and refractive index gradients and cause lensing in much the same way as a graded index lens. To compensate for thermal lensing a piece of DKDP was introduced into the isolator. Around room temperature the refractive index dispersion of DKDP is opposite to TGG. So, by setting up the same temperature profile in the TGG and DKDP we could effectively compensate for path length changes in the TGG with the opposite changes in the DKDP. The thermal lensing of the isolator was effectively reduced from 9 Rayleigh lengths per kW to below 2 Rayleigh lengths per kW.

1.3 Thesis Structure

The remaining 10 chapters of this dissertation are divided equally between the two projects. Chapters 2 to 6 describe the development of the Raman amplifier system for methane gas sensing and chapters 7 to 11 describe the development of the Faraday isolator.

Chapter 2 introduces the Raman amplifier methane sensing project. This chapter describes the reason for undertaking the project and lists the objectives that the development aimed to meet.

Chapter 3 describes the theory behind the operation of the amplifier system and the method of methane sensing using tuneable diode laser spectroscopy and wavelength modulation spectroscopy.

Chapter 4 describes the modelling of Er-Yb and Raman fibre amplifiers. It also shows schematically the layout of our amplifier system and examines the performance of the final amplifier system that was constructed.

Chapter 5 describes the integration of the amplifier system into a stand alone prototype unit capable of remote, single-end detection of methane. The chapter finishes with an analysis of the laboratory characterisation and field trials that the system underwent.

Chapter 6 concludes the project, summarises the main results and discusses improvements which could be made to the system and possible extensions to the project.

Chapter 7 introduces the Faraday isolator project, discussing the need for a Faraday isolator for fibre amplifiers and the specifications that the isolator should meet.

Chapter 8 describes the theory of Faraday isolators and the problems they face going to higher powers. This chapter includes some detailed discussion on thermal stress induced birefringence and thermal lensing.

Chapter 9 describes the theoretical analysis of thermal lensing and examines the literature around thermal lens measurement methods. It also examines thermal lens compensation methods.

Chapter 10 describes the construction of the isolator from both mechanical and optical perspectives. It also reports the results of characterisation of the finished device.

Chapter 11 concludes the isolator project and discusses improvements which could have been made to the system and possible extensions to the project for the future.

References

- [1.1] E. Snitzer, "Proposed fiber cavities for optical masers," J. Appl. Phys., 1961, Vol. 32(1), pp.36-39
- [1.2] R.J. Mears, L. Reekie, I.M. Jauncey and D. N. Payne, "Low-noise Erbium-doped fiber amplifier at 1.54 μ m," Electron. Lett., 1987, Vol. 23, pp.1026–1028
- [1.3] E. Desurvire, J. Simpson, and P.C. Becker, "High-gain erbium-doped traveling-wave fiber amplifier," Optics Letters, 1987, Vol. 12, No. 11, pp. 888–890
- [1.4] Y.Jeong, J.K.Sahu, D.N.Payne, J.Nilsson, "Ytterbium-doped large-core fiber laser with 1kW continuous-wave output power", Electron. Lett., 2004, Vol.40(8), pp.470-472
- [1.5] J. M. Schmitt, "Optical Coherence Tomography (OCT): A Review," IEEE Journal of Selected Topics in Quantum Electronics, 1999, Vol. 5(4),
- [1.6] F. Gonthier, L. Martineau, N. Azami, M. Faucher, F. Seguin, D. Stryckman, A. Villeneuve, "High-power All-Fiber components: the missing link for high-power fiber lasers," Fiber Lasers: Technology, Systems, and Applications, 2004, Vol. 5335, pp. 266-276.

Chapter 2 - Introduction to the Development of a Long-Range Open-Path Methane Sensor

This Chapter introduces the project to develop a long-range open-path methane sensor using fibre optic amplifiers and tuneable diode laser spectroscopy. This project was carried out in collaboration between Gooch and Housego Plc, Evanesco Ltd, Optosci Ltd and Strathclyde University with funding from the Department for Trade and Industry (DTI).

Chapter structure:

- **Section 2.1 – Introduction** – Describes the background to the project and places the need for a long range methane sensor into context.
- **Section 2.2 – Outline of Proposed System** – Describes how we propose to address the problem identified in section 2.1.
- **Section 2.3 – Objectives** – Details the specific objectives of the project.
- **Section 2.4 – Overview of following chapters**

2.1 Introduction

Natural gas is an important and valuable energy resource which is transmitted over vast distances via high pressure pipelines. The main constituent of natural gas is methane (CH_4), which is highly combustible and explosive in the correct mixture with air. It is also a greenhouse gas twenty-five times more potent than carbon dioxide [2.1]. The integrity of natural gas pipelines therefore raises both severe safety and environmental concerns. Consequently, a need exists for simple, fast and effective monitoring of these pipelines.

The traditional tool used to monitor natural gas pipelines has been the pellistor. Pellistors measure the concentration of methane in a gas by oxidising a sample with a catalyst and measuring the amount of heat produced through a resistance change in a conducting platinum wire. Pellistors are highly sensitive devices and are available at low cost, but are vulnerable to catalyst poisoning and signal drift, so they require regular calibration [2.2]. They are also point sensors and need to be *in* the gas of interest to measure it. This makes their use in a mobile application demanding and increases the risk to the operator.

Recently, optical sensors that use tuneable diode laser spectroscopy (TDLS) have become available. These sensors have excellent sensitivity, selectivity and very fast response times, allowing the smallest leaks to be detected without producing false positives. They are also immune to poisoning and, in a well setup system, require very little maintenance or calibration. Most significantly for the

application of pipeline monitoring is that optical sensors can be operated as an open-path, single end system, allowing the possibility of remote detection and vehicle mounting [2.3]. This could increase the efficiency of pipeline inspection and result in better safety and cost savings by reducing man hours and product loss.

The state-of-the-art open-path, single-end TDLS methane sensors have a range limited to around 10m [2.3-2.5]. This is primarily due to the availability and limitations of laser sources, amplifiers and detectors in the correct wavelength ranges.

The aim of this project was to develop a suitable high power laser source to allow the range of these systems to be extended to greater than 100m. This would open up the possibility of a new type of sensor capable of operation from a plane or helicopter. The laser source was to be based on a series of fibre amplifiers and implemented in a stand alone gas sensing system.

2.2 Outline of Proposed System

To extend the range of a TDLS methane sensor to greater than 100m we estimated that a source, targeting one of the strongest near-IR lines at 1650.95nm, would require a power of around 1W. The basis of this assumption is explained in chapter 3. It would also need a narrow linewidth and be continuously tuneable over the gas line.

Distributed feedback lasers are ideal for TDLS because they have narrow linewidths (several MHz) and can be tuned rapidly over a wavelength range of several nanometres by modulating their injection current or temperature. DFB lasers are readily available at 1651nm, however their power is currently limited to around 10mW. The normal solution to increase power would be to use an external optical amplifier. Unfortunately, 1651nm is outside of the gain bandwidth of any of the “conventional” gain materials. The closest optical fibre amplifiers to this wavelength use erbium as the active dopant and can produce gain from 1520nm to 1620nm.

Raman amplifiers use stimulated Raman scattering (SRS), a nonlinear form of Raman scattering, to amplify light. In SRS a low frequency signal photon induces the inelastic scattering of a higher frequency pump photon, producing two signal photons and passing the excess energy to a vibrational state in the medium. In effect the SRS process acts as a frequency shifter, transferring energy from the pump to the signal wavelength. In Silica optical fibre the peak of this frequency shift is around 13.2THz, which corresponds to around 110nm at 1550nm.

In this project we propose to develop a Raman fibre amplifier pumped by the output of an erbium doped fibre amplifier to amplify a 1651nm DFB laser to over 1W. A possible layout for the system is

shown in figure 2.1. The Raman amplifier consists of a long length of optical fibre pumped by the output of an erbium doped fibre amplifier. The Raman amplifier is seeded with a 1651nm DFB laser to be amplified. The optical fibre in a Raman amplifier can in theory be any type of fibre, however a small core diameter and the addition of certain dopants, like Germanium, can increase the Raman gain.

The length of fibre required for efficient Raman amplification in a single pass amplifier ranges from hundreds of meters to several kilometres. This long length of fibre increases the interaction length for nonlinear effects, enhancing both Raman amplification and other competing nonlinear effects like stimulated Brillouin scattering (SBS). In Brillouin scattering a photon inelastically scatters from an acoustic phonon and loses energy. At high power densities scattered photons can induce the scattering of further photons and the effect becomes nonlinear, just like SRS. In optical fibres the frequency shift from SBS is very small compared to the Raman shift, on the order of several MHz. Also in optical fibres, because of momentum conservation, the Brillouin scattered photon travels in the opposite direction to the incident photon. This is very problematic for fibre amplifiers because any light which enters the fibre above the SBS threshold is sent back towards the pump laser and seed diodes.

SBS has a very narrow bandwidth and is especially problematic for narrow linewidth lasers as required for our methane sensor. The threshold power for SBS for a narrow linewidth laser is much lower than the threshold power for SRS. As part of the Raman amplifier development, methods to suppress Brillouin scattering needed investigating.

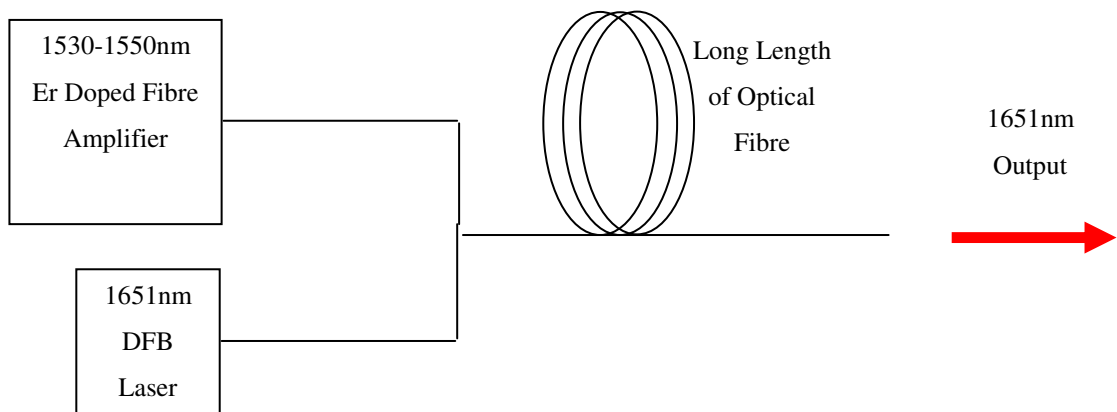


Figure 2.1: Simplified schematic of the proposed 1651nm Raman amplifier.

Following development of the Raman amplifier the intention was to integrate it with all the optics and electronics required for remote, single end tuneable diode laser spectroscopy. Then build it into a demonstration unit for laboratory and field trial testing. A simple plan for the setup is shown in figure 2.2. The output of the fibre amplifier is collimated and transmitted along an open path. It is then reflected off a surface and the backscattered light is collected by the receiving optics. The difference

in received power as the lasers wavelength is scanned across a methane absorption line is then used to determine the concentration of gas in the lasers path.

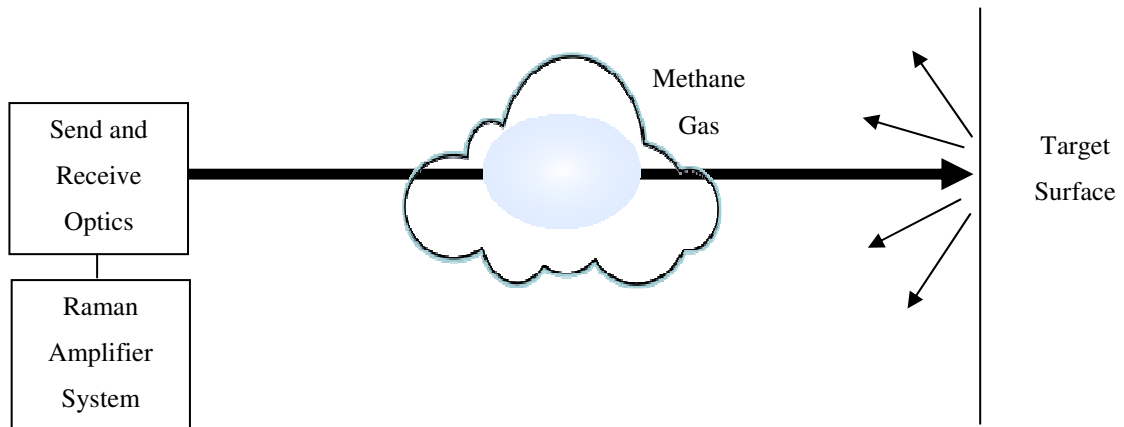


Figure 2.2: Open path, single end TDLS setup using Raman Amplifier system.

2.3 Objectives

The objectives of this project can be broken down into three distinct parts:

- 1) To design and construct a Raman amplifier to amplify a 1651nm DFB laser to greater than 1W.
- 2) To integrate the fibre amplifier system with a complete set of control and detection electronics for tuneable diode laser spectroscopy.
- 3) To demonstrate methane detection in laboratory and field trials with the completed system and benchmark its performance against the lower power TDLS methane sensors currently available.

2.4 Breakdown of following chapters

The rest of this project is discussed in chapters 3 to 6 of this thesis.

Chapter 3 describes the theory of tunable diode laser spectroscopy and will look in detail at two of the most common implementations, direct detection and wavelength modulation spectroscopy. The direct detection is the simplest form of TDLS but suffers from limited sensitivity. Wavelength modulation spectroscopy uses phase sensitive detection to increase the sensitivity, but as a result the setup is more complicated and the returned signals more difficult to analyse.

Chapter 3 will also describe the theory of stimulated Raman amplification and Brillouin scattering and will review the literature and analyse the different methods of suppressing SBS in fibre amplifiers without affecting Raman amplification.

Chapter 4 describes the theory of high power erbium-ytterbium fibre amplifiers and how their performance can be modelled to inform design choice. It also examines an extended model for SRS which aims to include the effects of SBS. The chapter then describes in detail the design of our final fibre amplifier system and the results we obtained – almost 2W at 1651nm.

Chapter 5 describes how the amplifier system was integrated into the final open path methane sensor. It also describes the results of laboratory and field trials made with the system.

Chapter 6 forms a conclusion for the project and discusses any improvements which could be made to the system.

References

[2.1] Intergovernmental Panel on Climate Change, “IPCC Third Assessment Report – Climate Change 2001,” Online: http://www.grida.no/publications/other/ipcc_tar/?src=/climate/ipcc_tar/wg1/248.htm, Retrieved 03/04/2011.

[2.2] A. J. Avenell, “Upgrading from pellistor gas sensors to infrared technology,” Online: <http://www.ngoilgasma.com/article/Upgrading-from-pellistor-gas-sensors-to-infrared-technology/>, Retrieved 03/04/2011.

[2.3] B. van Well, S. Murray, J. Hodgkinson, R. Pride, R. Strzoda, G. Gibson and M. Padgett, “An open-path, hand-held laser system for the detection of methane gas,” *J. Opt. A: Pure Appl. Opt.*, 2005, Vol 7, S420–S424.

[2.4] RMLD Product Literature, Online: http://www.heathus.com/tasks/sites/_hc/assets/File/RMLD_Dual.pdf, Retrieved 20/05/2011.

[2.5] “LaserMethane: Detection at a Distance,” Online: <http://www.crowcon.co.uk/media/Laser%20Methane%20Brochure%20Issue%201.pdf>, Retrieved 20/05/2011.

Chapter 3 - Theory

This chapter describes the theory of tuneable diode laser spectroscopy and Raman amplification required to form a basic understanding of the Raman amplifier methane sensor. It also reviews the literature and analyses any systems which have been reported which closely match this one.

Chapter structure:

- **Section 3.1 - Tuneable Diode Laser Spectroscopy (TDLS)** - Describes the background, theory and implementation of tuneable diode laser spectroscopy.
- **Section 3.2 - Methane Spectroscopy and State-of-the-Art TDLS Detectors** - Describes the spectroscopy of methane and reviews the state-of-the-art methane sensors reported in the literature.
- **Section 3.3 - Choice of Laser Source for the Long Range Methane Sensor** - Analyses the required power and attributes of a laser source for our long range methane sensor.
- **Section 3.4 – Raman Amplification** - Describes the theory of Raman amplification.
- **Section 3.5 – Brillouin Scattering** - Describes stimulated Brillouin scattering.
- **Section 3.6 – SBS Suppression** - Discusses and analyses methods for suppressing SBS.
- **Section 3.7 - High Power Narrow Linewidth Raman Amplifiers** - Discusses the state-of-the-art in narrow linewidth, high power Raman amplifiers.
- **Section 3.8 - Summary.**

3.1 Tuneable Diode Laser Spectroscopy (TDLS)

Tuneable diode laser spectroscopy (TDLS) is a trace gas analysis technique that can be used to measure the concentration, pressure and temperature of a gas. TDLS uses narrow linewidth lasers to interrogate a single molecular absorption in a gas of interest. C. B. Moore [3.1] proposed this idea in 1965 in a paper describing how he used CH₄ to suppress lasing on the fundamental emission line of a Helium Neon laser. In this paper Moore explained how a coincidental overlap between the lasing line at 2947.90 cm⁻¹ (3.3913 μm in air) and a molecular absorption in methane could be used to increase cavity loss at this wavelength and allow lasing on the lower gain line at 2948.79 cm⁻¹ (3.3903 μm in air). Gerritsen (and later Grant) used these lines to demonstrate methane spectroscopy [3.2, 3.3].

The use of fixed wavelength lasers available at that time greatly limited the application of laser spectroscopy, as it limited the molecules and molecular transitions that could be targeted. TDLS only really took off after the development of diode lasers (hence the name). Diode lasers form an ideal source for TDLS because they can be manufactured with a wide range of wavelengths (dependent on the semiconductor structure). They can also have very narrow linewidths and can be tuned

continuously over relatively large wavelength ranges by changing the operating current or temperature.

TDLS uses the transmission of light through a sample to determine the concentration of selected species in the sample. Transmission and concentration are directly related through the Beer-Lambert law, which states that there is a logarithmic dependence between the transmission (T) of light through a sample and the product of the absorption coefficient (α) and the path length (l):

$$T = \frac{I}{I_0} = e^{-\alpha l} = e^{-\sigma N l} \quad (3.1)$$

where I is the transmitted intensity and I_0 is the incident intensity. The absorption coefficient can be broken down further to the product of the absorption cross-section (σ) and the number density of absorbing particles (N). The absorption coefficient is given in units of cm^{-1} ; the absorption cross section cm^2 ; number density cm^{-3} ; and intensity Wm^{-2} .

Dividing the number density of absorbing particles by the number of molecules/atoms in a mole gives the molar concentration (C) in moles/cm^3 . This may be preferable to N for some applications. The number of molecules in a mole is given by Avogadro's number (N_A) and equals 6.022×10^{23} .

In equation 3.1 variables α and σ are functions of wavelength. If they are known for a sample at the measurement wavelength, then the concentration can be calculated simply from a measurement of the transmission of light through the sample and the path length. The absorption cross sections of molecular transitions in common gases at important wavelengths are well documented, and are available from databases like HITRAN [3.4].

In an open path TDLS setup, as described in chapter 2, the path length through the gas sample and the total path length are not fixed. This makes absolute concentration measurements impossible without further topographic information. As such the measurement made is of the path length integrated concentration (Nl in equation 3.1) usually given as ppm-m. It is worth noting that two gas plumes with different concentrations may have the same ppm-m depending on the path length of the laser through the plume; i.e. a 2m path through a 100ppm gas plume is equivalent to a 1m path through a 200ppm gas plume.

The following subsections describe two different methods of conducting tuneable diode laser spectroscopy. The first method (section 3.2.1) tuneable diode laser spectroscopy with direct detection (TDLS-DD) uses the simplest setup. The drawback is limited sensitivity. The second method (section

3.2.2) tuneable diode laser spectroscopy with wavelength modulation spectroscopy (TDLS-WMS) has much improved sensitivity at the expense of a more complex setup and signal processing.

3.1.1 Tuneable Diode Laser Spectroscopy with Direct Detection (TDLS-DD)

Tuneable diode laser spectroscopy with direct detection (TDLS-DD) is the simplest form of TDLS. In TDLS-DD the frequency of a narrow linewidth laser is repeatedly swept over a single molecular absorption line at a low sweep frequency (5-10Hz) as the power transmitted through a gas sample is measured. The result is essentially a trace of the absorption line as shown in figure 3.1. The samples concentration, pressure and temperature are then recovered from the shape and strength of the absorption line profile.

At atmospheric temperatures and pressures where pressure broadening dominates, the absorption line profile can be described by a Lorentzian [3.5]

$$\sigma(\nu - \nu_0) = \frac{\sigma_0}{\left(\left(\frac{\nu - \nu_0}{\gamma} \right)^2 + 1 \right)} = \frac{\sigma_0}{(\Delta^2 + 1)} \quad (3.2)$$

where $\sigma(\nu - \nu_0)$ is the line shape function, ν_0 is the frequency at line centre, σ_0 is the absorption cross section at line centre and γ is the full width at half maximum (FWHM) linewidth. The FWHM linewidth varies with temperature (T) and pressure (P) according to [3.6]:

$$\gamma = \gamma_0 \left(\frac{P}{P_0} \right) \left(\frac{T_0}{T} \right)^{1/2} \quad (3.3)$$

where γ_0 is the FWHM linewidth at standard temperature and pressure $P_0 = 1\text{atm}$ and $T_0 = 300\text{K}$.

Analysis of the line profile and the Beer-Lambert law show that the concentration can be calculated most accurately from the transmission at line centre ($\nu = \nu_0$) [3.10]. It also shows that temperature and pressure measurements can be extracted from measurements of the FWHM linewidth.

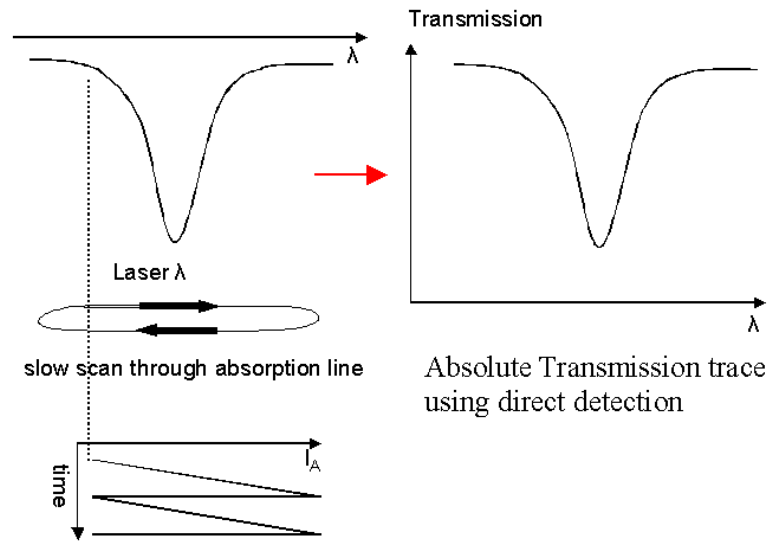


Figure 3.1: Illustration of the principal of tuneable diode laser spectroscopy with direct detection [3.6]

A system diagram for a TDLS-DD setup is shown in figure 3.2. In this setup a signal generator is used to scan the laser wavelength through an absorption line. The laser is then transmitted through a sample to a detector and recorded. In a remote, single end, setup the laser is reflected and scattered from a target to the detector.

Since the intensity of a diode laser also changes with the drive current it is usual to normalise the measurement. To do this a reference beam can be taken off the transmitted beam and sent to a receiver without passing through an absorbing sample. This reference beam will contain the amplitude modulation from the diode laser but not the amplitude modulation from absorption in the gas sample. Dividing the gas signal by the reference signal then effectively removes the intensity variation of the diode laser.

In a remote TDLS setup, losses in the transmission path independent of gas absorption will also change continuously because the path length and target surfaces are not fixed. A ratio of the transmitted and reference beam powers off the absorption line can then be used to calibrate the measurement against changing losses in the transmission path.

In TDLS-DD the sensitivity is limited by the ability to detect a small change in a large signal which is swamped by $1/f$ and random laser noise. If we assume that absorption in the sample is small so that $\sigma Nl \ll 1$ then simplification of the Beer-Lambert law (equation 2.1) shows that the concentration in a TDLS experiment is given by

$$N \approx \frac{\Delta I}{I_o \sigma l} \quad (3.4)$$

where $\Delta I = I - I_0$ is the absorbed power. This has to be greater than the intensity of noise I_{noise} to be measurable and so we have a condition set on the minimum detectable concentration [3.7]

$$N > \frac{I_{\text{noise}}}{I_o \sigma l} \quad (3.5)$$

Thus, to increase the sensitivity we can increase the path length; increase the incident laser intensity; choose an absorption line with a larger absorption cross section or decrease the noise intensity.

In the next section Wavelength Modulation Spectroscopy is explained. This is an extension to the TDLS technique that uses phase sensitive detection to effectively decrease the noise intensity in a measurement and substantially increases sensitivity.

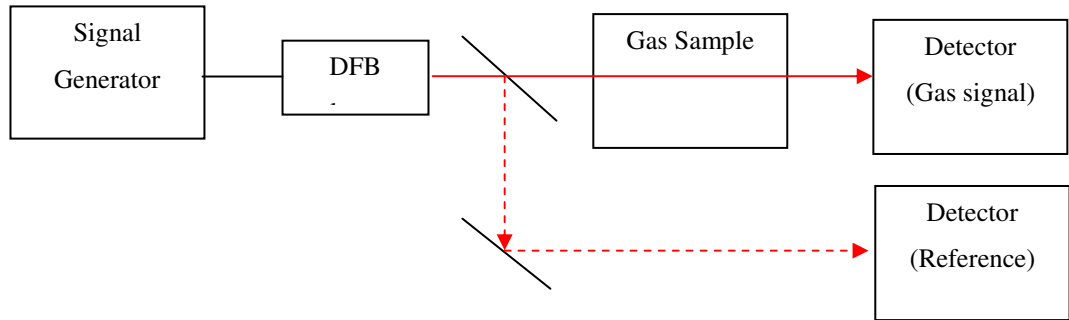


Figure 3.2: System diagram of a typical setup for TDLS-DD.

3.1.2 Tuneable Diode Laser Spectroscopy with Wavelength Modulation Spectroscopy (TDLS-WMS)

Tuneable diode laser spectroscopy with wavelength modulation spectroscopy (TDLS-WMS) is one of a group of techniques that rely on frequency/wavelength modulation of the laser source and narrowband detection to improve the sensitivity of TDLS. TDLS-WMS is reviewed widely in the literature [2.11-2.16].

In TDLS-WMS a small amplitude sinusoidal modulation of frequency ω_m is applied to the laser in addition to the ramp signal. This causes the lasers instantaneous output frequency $\nu(t)$ to vary as

$$\nu(t) = \bar{\nu} + m \cos(\omega_m t) \quad (3.6)$$

where $\bar{\nu}$ is the mean frequency of the laser and m is the modulation index given by

$$m = \frac{\delta\nu}{\gamma} \quad (3.7)$$

where $\delta\nu$ is the maximum frequency deviation about the lasers central wavelength and γ is the FWHM absorption linewidth.

In the gas sample this frequency modulation (FM) is converted into an amplitude modulation (AM) by absorption. This amplitude modulation is detectable with a photodiode and contains components at the modulation frequency and its harmonics $n\omega_m$ ($n=1, 2, 3\dots$). The amplitudes of harmonic components can be measured individually with a lock in amplifier. If $m \ll 1$ then the amplitudes of these harmonic components $A_n(\nu_c)$ are given by (derivation appendix A3.1) [3.8]

$$A_n(\nu_c) \approx \frac{I_0 2^{1-n} NL}{n!} m^n \left. \frac{d^n \sigma}{d\nu^n} \right|_{\nu=\nu_c} \quad (3.8)$$

The amplitudes of these harmonic components are proportional to the concentration of gas N ; the path length through the gas sample L ; the n^{th} power of the modulation index and the n^{th} derivative of the absorption cross-section σ (lineshape). These are recorded as the mean frequency of the laser is swept over the absorption line, producing traces resembling the differentials of the lineshape. As shown in figure 3.3 for first harmonic detection.

A Lorentzian lineshape and the shape of its 1st, 2nd and 3rd derivatives are shown in figure 3.4, with the position of features in the derivatives, relative to the FWHM linewidth. In a gas sensing measurement, detection of the 1st, 2nd and 3rd harmonics are often referred to as 1f, 2f and 3f detection. As you can see in figure 3.4 the 1f and 3f signals have a zero crossing at the absorption line centre, whereas the 2f has a maximum at this point. The gas concentration can be measured from the amplitude of these signals. In low modulation index measurements the maxima and crossing points have a simple relationship to the FWHM linewidth and from these the temperature and pressure of the sample can be calculated.

However, in practice small modulation indices do not maximise the amplitudes of the harmonics and limit the sensitivity of the TDLS-WMS technique. Reid and Labrie [3.9] and Silver [3.10] both show that the optimum modulation index for second harmonic detection of a Lorentzian lineshape is at $m=2.2$. At this modulation index equation 3.8 does not hold closely and the harmonic components

deviate from the derivative. More detailed analysis is then required to theoretically describe the shape of the signals recorded and to accurately retrieve the concentration, temperature and pressure.

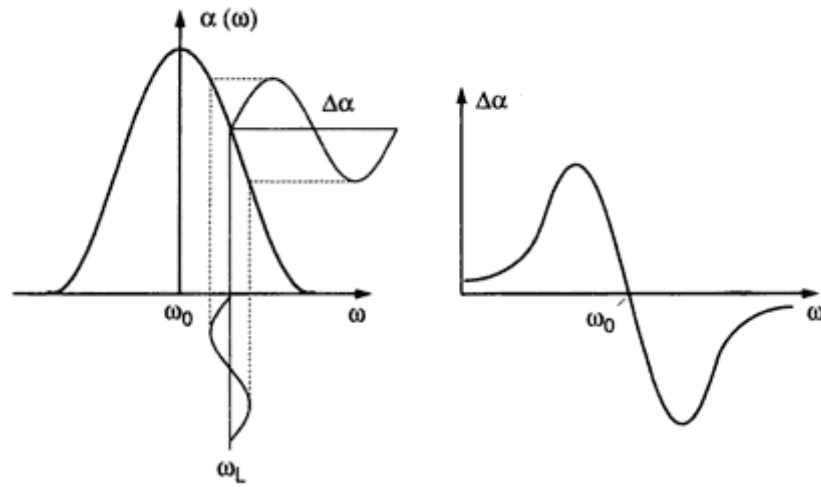


Figure 3.3: Illustration of the principal of tuneable diode laser spectroscopy with wavelength modulation spectroscopy. As the wavelength of the laser ω_L is scanned across a gas absorption line the wavelength modulation is converted to an amplitude modulation $\Delta\alpha$ (AM). Over a complete scan of the absorption profile this builds up a trace of the line derivative. [3.7]

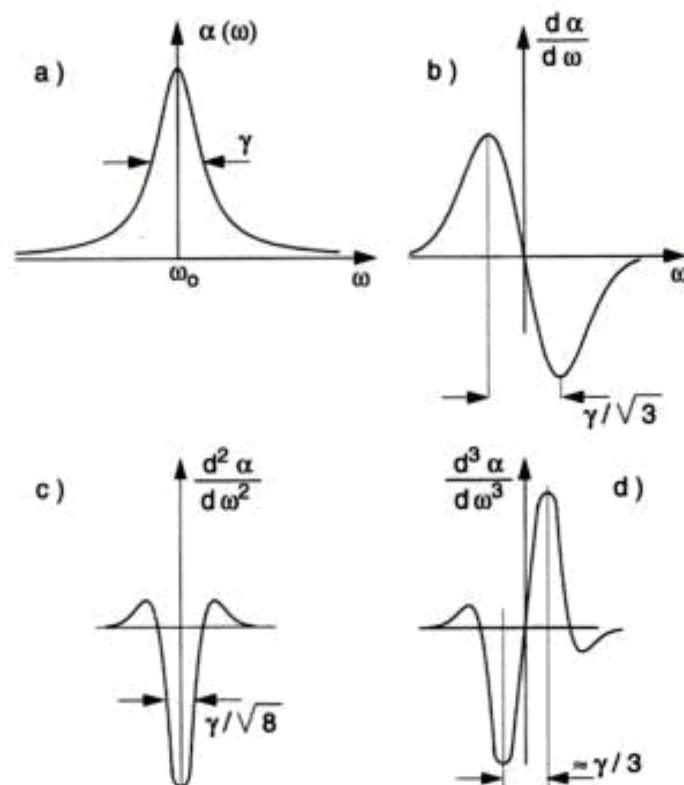


Figure 3.4 Lorentzian line profile (a) with first (b), second (c) and third (d) derivatives [3.7].

The main advantage of using TDLS-WMS over TDLS-DD is that the modulation moves the detection to a higher frequency where sources of noise, such as laser intensity fluctuations and $1/f$ noise, are dramatically reduced. The use of a lock in amplifier (phase sensitive detection) also greatly reduces the detection bandwidth to effectively filter noise.

Noise sources remaining in the TDLS signal are often referred to a residual amplitude modulation (RAM). The largest contributor to RAM is the amplitude modulation (AM) of the laser caused by the frequency dither itself; since the intensity and wavelength of the laser are both dependent on the drive current, just as in TDLS-DD. If the AM response of the laser was entirely linear with current then it would have contributions only at ω_m and would only be detectable in the $1f$ output of the lock-in amplifier, where it is seen as a high background on the first derivative signal. Luckily this is (mostly) the case and explains why $2f$ detection is often preferred over $1f$ as RAM is largely eliminated. In theory higher harmonics have even smaller RAM contributions but also have smaller amplitudes due to dependence on $n!$ as shown in equation 3.8.

As with TDLS-DD, the system losses and RAM in a remote setup are going to change continuously depending on the movement of the system and the position of the scattering target. A method to normalise the measurement is therefore required to compensate for this. This can be achieved in several ways

- 1) By separating off a reference beam, just like in TDLS-DD, and normalising to this.
- 2) By taking the ratio of the $1f$ and $2f$ signals. This requires a much simpler optical setup and works well for optically thin samples where the $1f$ signal is dominated by RAM.
- 3) By normalising each signal against a RAM measurement made at a wavelength away from the gas line.

An intuitive derivation of the signals produced in TDLS-WMS in the low absorption, small modulation index regime that takes account of the intensity modulation (RAM) that is imposed on the diode laser was given by Kevin Duffin et. al. [3.11] (repeated in appendix A3.2). In this analysis, it is shown how a phase difference between the RAM and gas sensing signal can be used to isolate the RAM signal and yield the absolute gas transmission function – just like in TDLS-DD. In the absence of RAM (ideal modulation) the results are equivalent to equation 3.8.

A system diagram for a TDLS-WMS setup can be seen in figure 3.5. In this setup a signal generator applies a low frequency ramp and a higher frequency dither to the diode laser. This varies the output centre wavelength of the laser which is transmitted through a gas sample to the detector. A lock in amplifier then demodulates the detected signal at the dither frequency or an harmonic thereof. The lock in amplifier output is recorded as the laser wavelength is swept through the gas line.

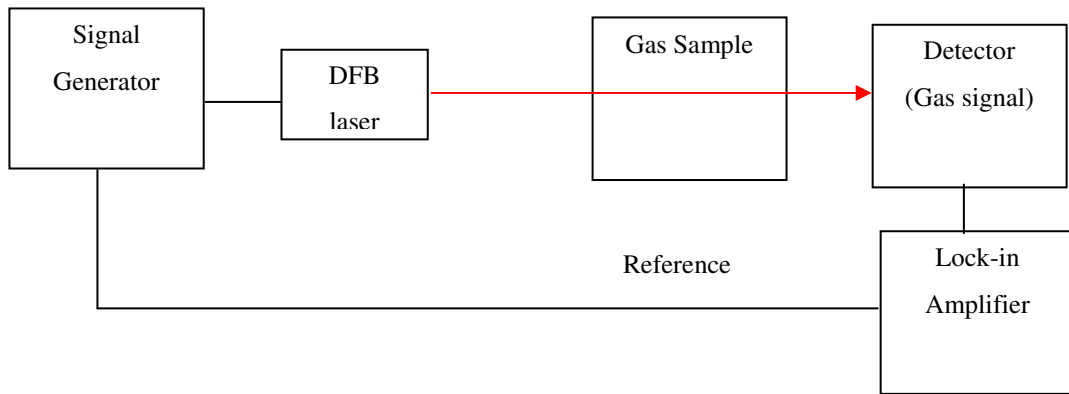


Figure 3.5: System diagram of a typical setup for TDLS-WMS.

3.2 Methane Spectroscopy and State-of-the-Art TDLS Detectors

A methane absorption spectrum taken from $0.1\mu\text{m}$ to $10\mu\text{m}$ is shown in figure 3.6. This shows that methane has its strongest absorption lines (due to fundamental vibrations) in the mid-IR region around $3.3\mu\text{m}$. Hence many optical gas detectors have been developed in this wavelength range [3.12-3.15]. The disadvantage of these mid-IR wavelengths is that they are difficult to access; requiring complex laser sources like cryogenically cooled lead-salt lasers, optical parametric oscillators and quantum cascade lasers. Also, detectors at these wavelengths are expensive and complex, requiring cryogenic cooling before they approach the sensitivity and responsiveness of near infrared detectors [3.16]. Another disadvantage of using a mid-IR system is that fused silica optical fibres are not transparent in the mid-IR region. This greatly reduces the different possible methods for the delivery and collection of the signal light.

Ian Armstrong et. al. [3.14] at Strathclyde University have recently demonstrated methane detection using a mid-IR source obtained by difference frequency generation in periodically poled Lithium Niobate (PPLN). The mixing sources were a 1063.5nm fibre Bragg grating stabilised diode laser and a 1547nm DFB laser, producing a difference frequency around 3403nm . Using a Mercury Cadmium Telluride detector TEC cooled to -50°C they demonstrated direct, $1f$ and $2f$ spectroscopy of methane. Modulation was applied directly to the 1547nm DFB laser.

Lindsay et. al. [3.15] at the University of Twente demonstrated mid-IR wavelength modulation spectroscopy and frequency modulation spectroscopy using a singly resonant OPO. The OPO was pumped by a fibre amplified 1063nm diode laser and produced up to 900mW at the idler wavelength between $3.15\mu\text{m}$ and $3.80\mu\text{m}$. Wavelength modulation was achieved by modulating the pump diode directly. A (HgCd)Te photoconductive detector was used to detect the transmitted signal.

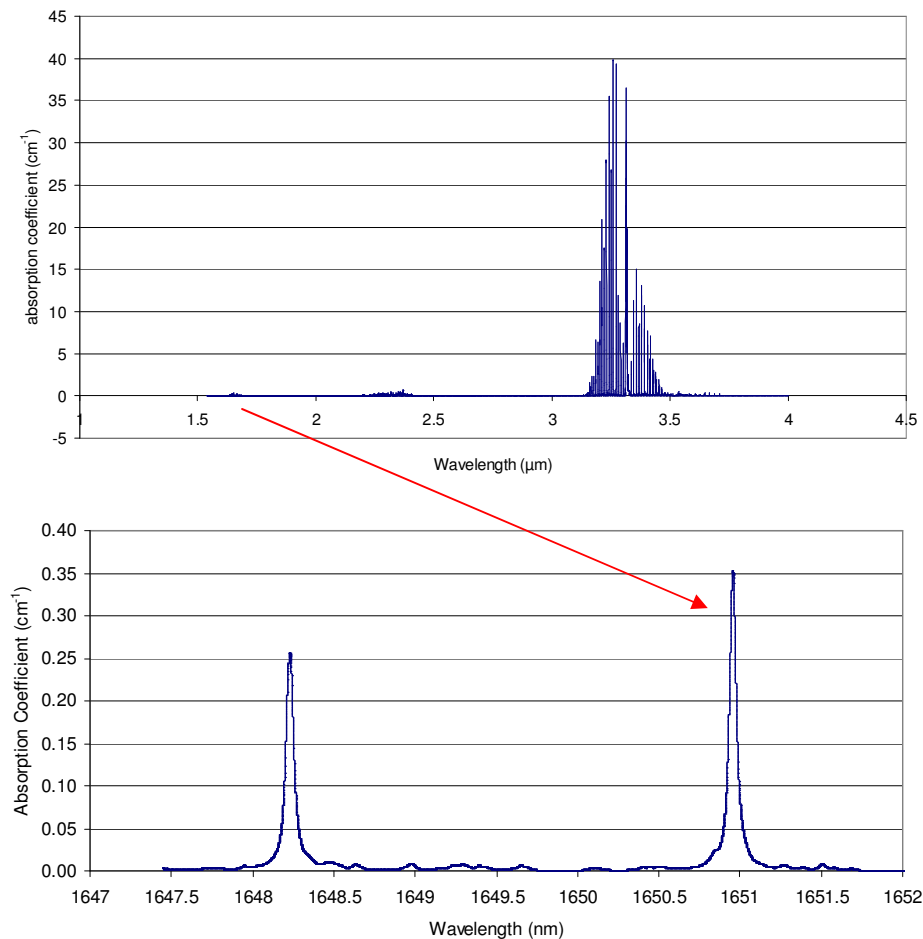


Figure 3.6: Methane absorption spectrum from a) 1 μm to 4.5 μm and b) close up of 1651 nm.

As you can see from the two examples of mid-IR systems above the laser sources and detectors are clearly complex and costly. However, as technology improves these disadvantages should narrow. Recently, several research groups have reported on the production of quantum cascade diode lasers with wavelengths around 3.3 μm [3.54]. These are similar in design and manufacture to regular diode lasers, except with more complex structure, and rely on intra-band transitions to produce light. If these become commercially viable then they could represent a large step forward for mid-IR TDLS sensors.

The first overtone absorption lines of methane are much more conveniently situated in the near-IR around the 1.6 μm spectral region. These overtone lines are 2 to 3 orders of magnitude weaker than the fundamental lines around 3.3 μm. Nevertheless these overtone absorption lines are still attractive for TDLS because the region is easily accessible by high quality laser sources and detectors, including distributed feedback (DFB) lasers and InGaAs detectors, developed widely for their use in telecommunications. This wavelength region is also compatible with transmission by silica optical fibre which opens up many possible design options. For these reasons many more near-IR TDLS systems have been produced than mid-IR systems and they are quickly finding their way into

industrial applications like process control, facility monitoring and pipeline inspection [3.5, 3.17-3.21].

Several of these TDLS systems are of relevance to this project and will be discussed in the following subsections.

- Section 3.3.1 discusses short range (<15m) open-path remote methane sensors. Examining the laser powers that they send and receive; the sensitivity they achieve and the detection methods and configurations they use.
- Section 3.3.2 looks at the literature for long range methane sensors. Examining the amplifier systems and the collection optics that they use and the sensitivities and ranges they have achieved.

3.2.1 Short Range TDLS Methane Sensors

Ben van Well et. al. [3.17] demonstrated a remote, hand-held methane detector in 2004. This used a directly modulated 8mW 1651nm InGaAs laser diode as the source and a 150mm Fresnel lens to collect backscattered light onto an InGaAs photodetector. They found that this arrangement collected backscattered signals of between 10 and 100nW off various common targets at ranges of 4-5m. They used a methane-filled reference cell with feedback circuitry to maintain the laser diode wavelength at the peak of the methane transition. The backscattered light was demodulated at both 1f and 2f and the signals divided to give a measurement of the gas concentration normalised with respect to the varying system losses. Their work culminated in the production and field-testing of several packaged demonstration units. They achieved a detection limit of better than 10ppm.m at 5m.

Takaya Iseki et. al. [3.18] demonstrated a similar hand held methane sensor. This system also used a reference gas cell to lock the lasers central wavelength to the absorption line centre and used the 2f/1f ratio as a normalised gas concentration signal. Their source was an 8.2mW 1651nm DFB laser and they used a 120mm Fresnel lens and a cone concentrator to increase the collection efficiency onto an InGaAs photodiode. The system had a sensitivity of 450ppb.m (with an SNR of 1) at 6m off a magnesium oxide target with a LIA time constant of 100ms. They also looked at the angular reflectance of various “real” targets, like wood, asphalt and tile, and found that even the most specular reflectors produced adequate diffuse reflection to allow detection at large angles. This device was commercialised by Tokyo Gas Co, Ltd with the name Lasermethane. The claimed sensitivity of the commercialised device is 100ppm.m at 30m [3.19].

Mickey Frish et. al. [3.20] also produced a hand held methane sensor using a 10mW 1651nm DFB laser and a 100mm Fresnel collection lens. This was commercialised by Physical Science inc, and

Heath consultants into the Remote Methane Leak Detector (RMLD) [3.21]. The data sheets claim a sensitivity of 5ppm.m at distances up to 15m and 10ppm.m up to 30m. However, these numbers are not consistent with a squared distance scaling law as would be expected for an evenly distributed backscatter. This suggests that they may have used topographic targets with a large specular reflection aligned with the receiver whilst making measurements.

The three systems described above have very different reported detection limits, even though the specification of the detectors and lasers are similar. This could be a result of different lock-in amplifier settings and signal averaging which are not stated in the papers. It could also be the result of the different target surfaces used when making the measurements. The highest sensitivities could be an artefact of optimising the alignment of source and detector with a large specular back reflection. This makes comparison of the systems found in the literature with our system very difficult (and possibly misleading). As we will see in section 3.3 it also makes it very difficult to specify the output power we require of a source prior to building and testing the system.

3.2.2 Long Range TDLS Methane Sensors

According to equation 3.4 after decreasing the noise intensity using WMS, the only other ways to improve the limit of detection (and hence the range) of an open-path methane sensor are to:

1. Increase the power of the source;
2. Decrease non-absorption losses in the beam path;
3. Choose an absorption line with a larger absorption cross section.

In an open-path TDLS setup decreasing non absorption losses is equivalent to improving the efficiency of backscattered light collection. Mickey Frish et al. [3.22] showed this by replacing the standard 10cm Fresnel lens on the handheld RMLD unit with a 25cm modified telescope. By doing this they claim to have increased the detection range to 200m with a sensitivity of 100ppm.m – a sensitivity and range suitable for aerial pipeline inspection. This is interesting for our project as it essentially achieves greater than our target distance and sensitivity using a 10mW DFB laser without using an amplifier.

However, the sensitivity and output powers do not correspond to the powers and detection limits of the other systems identified or with prior experience of methane sensing. Perhaps they use more extensive averaging and a long lock-in amplifier time constant. This will increase the sensitivity of the system at the expense of measurement time, which would be critical in a mobile application. They could also be using topographic targets with large specular back reflection. This was suspected earlier because the claimed sensitivities of the RMLD did not scale according to a square distance law.

In an extension of this work [3.23] they also developed a TDLS system which used an EDFA to amplify a diode laser targeting a methane absorption line at 1618nm. The choice of line was determined by the gain bandwidth of the EDFA. The 1618nm line is over two orders of magnitude weaker than the usually targeted 1651nm line. The DFB was amplified to over 5W using a specially designed long wavelength EDFA from Keyopsis. Using a 25mm diameter Telescope as the collection lens, they estimate a sensitivity of $\sim 5000\text{ppm.m}$ at 2000m. This would be suitable for finding relatively large leaks.

They found that the distance-power relationship for this system did not hold between the unamplified and amplified systems because the temporal gain characteristics of the EDFA interacted with the laser modulation to distort the TDLS wavelength modulation as shown in figure 3.7. This significantly degraded the TDLS signal and limited the system sensitivity.

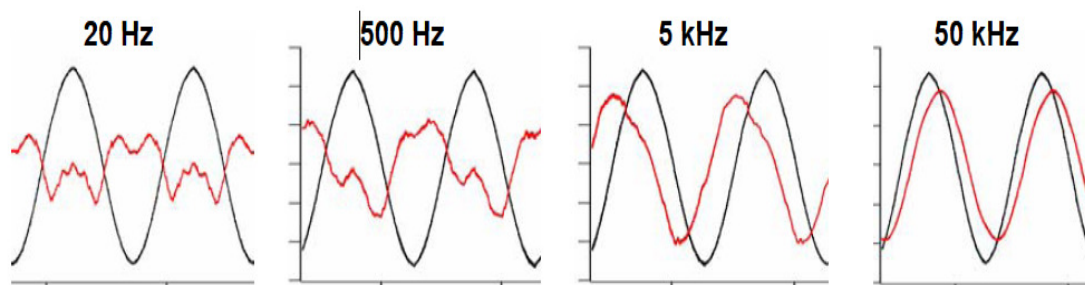


Figure 3.7: Oscilloscope traces of detected signal from seed laser (black) and EDFA output (red) at various modulation frequencies [3.23].

In 2001 P. Vujkovic-Cvijin et. al. [3.24] at SRI International used an EDFA pumped Raman amplifier to increase the power of a 1651nm DFB laser from 5mW to 100mW for use in a TDLS methane sensor, in what appears to be a very similar approach to the one proposed in this project. However, they never released any results on the performance of this source in methane sensing. Their unamplified TDLS sensor had a detection limit of 18ppm.m at a target distance of 12m, so by extrapolation, if the system obeys a square distance rule, the amplified version would provide the same sensitivity over about 50m. If the detection limit is decreased to 100ppm.m (a factor of ~ 5) then the range should be extendable to greater than 100m, assuming that the detection limit scales linearly with received power). Their receiver consisted of a 175mm reflective telescope and a fast InGaAs avalanche photodetector.

The extrapolated performance of these systems suggest that we only require between 10 and 100mW at 1651nm to reach our target range and sensitivity of 100ppm.m at 100m. However, this seems quite low from our experience. In the next section the performance of the systems identified in the last

couple of sections will be analysed to better estimate the output power required from our amplifier to achieve a range of 100m.

3.3 Choice of Laser Source for the Long Range Methane Sensor

Using details from the systems described in section 3.2, it should be possible to gauge the power of a 1651nm source required to produce a methane detector with a range of 100-200m - a suitable distance for aerial pipeline inspection and sensitivity. In an open path methane sensor if the backscatter from the target is distributed evenly over a half hemisphere it is reasonable to assume that the power at the receiver P_{rec} scales as

$$P_{rec} = \left(\frac{A_{col} R_{dif} \eta_{opt}}{R^2} \right) P_{trans} \quad (3.9)$$

where A_{col} is the area of the collection optics, R_{dif} is the differential reflectance of the target, η_{opt} is the optical efficiency, R is the range and P_{trans} is the transmitted power.

It would be desirable for the aerial system to be able to distinguish leaks of 100ppm.m above ambient. This is near the sensitivity achieved by the hand held sensors reported in section 2.3.1 and is sufficient to detect all but the smallest pipeline leaks. The system produced by Ben van Well et. al. [2.23] was reported to have a sensitivity of 10ppm.m at a distance of up to 5m using an 8mW DFB laser and a 150mm diameter Fresnel collection lens. They also reported received powers in the range of 10-100nW from a range of surfaces. Assuming we use the same diameter collection optics with the same optical efficiencies, then for the same sensitivity at 100m we would need a transmit power of 3-8W. They also showed that sensitivity scales linearly with the inverse of received power. Thus, for a detection limit of 100ppm.m we would require 0.3-0.8W.

However, this estimate is probably on the low side for our system because they use a long time constant of between 10ms and 300ms for phase sensitive detection. This would increase their sensitivity considerably but would be unsuitable for a system being flown from an aircraft. The time constant would need to be considerably smaller in order to produce a reasonable number of data points over the gas line. Flying at 50ms^{-1} and sampling the methane concentration above the pipeline at 1m intervals with 10 points sweeping across the pipeline, to build up a topographic picture of methane location, would require a lock in amplifier to produce data points at 500Hz. This would limit the maximum time constant to 2ms; or less with additional processing requirements. This increases the detection bandwidth of the lock in amplifier, increases the noise and lowers the sensitivity of the sensor over the system described above. To compensate for this even more laser power is required.

This analysis suggests that to achieve a sensitivity of 100ppm.m over a range of 100m with a 150mm Fresnel lens targeting the absorption line at 1651nm, we would need a laser source with an output power of between 0.5-1W. This could be reduced by using larger area collection optic. According to equation 3.8 using a 300mm lens would give four times the collection area. So the same received power would be achieved with between 0.125-0.25W.

Using the sensitivities and distances quoted for the RMLD in the datasheet [3.22] then the power would be ~100mW for 10ppm.m detection at 100m using a 150mm lens and a 100ms time constant. However, as was noted in section 2.3.1 these measurements seem optimistic and raise questions about the type of targets and signal averaging used. These measurements are consistent with their long range measurements [2.28], which say that they achieved a detection limit of <200ppm.m at 200m using a 250mm telescope and a 10mW laser. Accordingly, a 10mW laser with a 250mm collector should be able to reach our required sensitivity and range of 100ppm.m at 100m [3.23].

Unfortunately, the analysis in this section has not provided much insight into the power required to reach our target sensitivity. It has simply pointed out the inconsistencies in the literature regarding output powers and TDLS sensitivity. These inconsistencies are probably down to the phase sensitive detection time constants, averaging and topographic targets used to make the measurements and as mentioned earlier are not easily analysable without further information. For the purpose of our system a conservative estimate of 1W should be ample to achieve the range and sensitivity that we require.

Aside from power a laser source for TDLS should also operate on a single longitudinal mode and have a narrow linewidth compared to the width of the absorption line. It should also have a continuously tuneable wavelength over a large enough range to sweep at least one absorption line, more if absolute characterisation and wavelength referencing is required. It should also be easily modulated at a high frequency and, for simplicity, ideally without the need for an external modulator. An ideal laser (not seen in practice) would have no intensity modulation accompanying the wavelength modulation.

Distributed Feedback (DFB) diode lasers fit these ideals very well and so make excellent candidates for TDLS. These are diode lasers formed with periodic structures which form diffraction gratings providing feedback for only a single longitudinal mode. Developed in the near-IR for DWDM telecommunications they generally have linewidths of several MHz (compared to gas linewidths of several GHz in the near-IR), output powers of several milliwatts and operate at near-room temperature. They can be tuned continuously over a large wavelength range by temperature tuning and their output frequency/wavelength can also be modulated directly at high frequency via the drive current. In addition to this, their development for telecoms has led to lasers with long life expectancies and good efficiency. The only downside of DFB lasers is the dependence of output power on drive

current which, as described in section 2.2., produces RAM in the recovered TDLS signal. Werle gave a good review on current diode laser technology [3.25].

To increase the power of the DFB laser it will be necessary to use an amplifier. Unfortunately, 1651nm is outside of the gain bandwidth of erbium Doped Fibre Amplifiers. However, a Raman amplifier pumped at between 1530-1540nm will operate at this point, though several technical challenges need to be overcome to allow the amplifier to reach high powers. The theory of fibre Raman amplification and the challenges of reaching high powers with a narrow linewidth will be discussed in the remainder of this chapter.

3.4 Raman Amplification

3.4.1 Spontaneous Raman Scattering

To increase the range of our TDLS system we plan to amplify the power of a 1651nm laser diode from around 10mW to over 1W. We are targeting the 1651nm methane absorption line because it is one of the strongest in the near-IR. The challenge with this line is that it lies outside of the gain bandwidth of EDFAs which extend from around 1520nm to 1620nm. Fortunately, the tight confinement of light in optical fibres allows us to take advantage of nonlinear effects like stimulated Raman scattering (SRS) to produce amplification at a wide range of wavelengths.

Raman scattering is the inelastic scattering of light by atoms and molecules. Inelastic because the scattered light photons lose (or gain) energy from the interaction. The atoms also change energy by moving to a different vibrational state. In the interaction between a photon and a molecule the molecule is excited to a virtual state. From this state three things can occur:

- 1) The molecule may return to the state in which it began by releasing a photon with the same energy (wavelength) as the incident photon. Albeit, with a random direction. This is an elastic scattering event known as Rayleigh scattering.
- 2) The molecule may drop down to a higher energy vibrational state than it began by releasing a photon with less energy than the incident photon. This less energetic photon has a longer wavelength than the incident photon and is often referred to as a Stokes photon. This process is often referred to as Stokes Raman scattering.
- 3) The molecule may drop down to a lower energy vibrational state than it began by releasing a photon with more energy than the incident photon. This energetic photon has a shorter wavelength than the incident photon and is often referred to as an anti-Stokes photon.

These processes are shown diagrammatically in figure 3.8. In the atmosphere Rayleigh scattering is the most common form of scattering, only about 1 in 10^6 photons undergo Raman scattering compared to Rayleigh scattering. Raman scattering was discovered by C. V. Raman in 1928 for which he won the Nobel Prize in 1930. It is unique from Fluorescence because it relies on a *virtual* intermediate state with a very short lifetime and is thus present at all wavelengths.

The wavelength shift (Stokes shift) due to the Raman Effect is determined by the spacing between vibrational states and the ground state, and is typically in the THz region. Stokes Raman scattering is much more likely than anti-Stokes Raman scattering because of the initial population N of each state which follows a Boltzmann distribution

$$N \sim \exp\left(-\frac{E}{K_B T}\right) \quad (3.10)$$

where E is the energy of the state, K_B is the Boltzmann constant and T is the temperature. This shows that the population of a vibrational state in equilibrium decreases exponentially with the energy of the state. So a photon is much more likely to begin in the ground state and fall to a higher energy state than begin in an excited state and fall to a lower state.

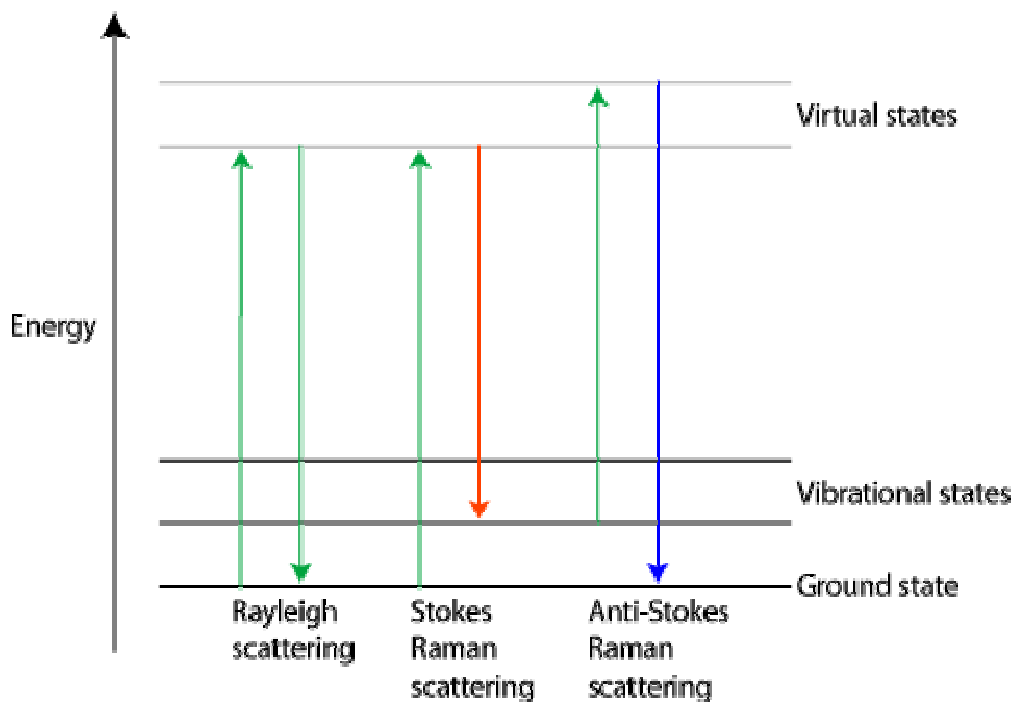


Figure 3.8: Diagram showing the energy (state) transitions involved in the processes of Rayleigh scattering, Stokes Raman scattering and anti-Stokes Raman scattering..

The semi classical explanation of Raman scattering developed by Placzek, is based on the polarisability of electric dipoles [3.26]. The explanation is as follows [3.27]:

The electric field strength of an electromagnetic wave oscillates with time t at an amplitude E_0 and angular frequency ω_p

$$E = E_0 \sin(\omega_p t) \quad (3.11)$$

When the electric field interacts with a molecule it induces an electric dipole moment P

$$P = \alpha E = \alpha E_0 \sin(\omega_p t) \quad (3.12)$$

where α is the polarisability of the molecule. If the molecule rotates with a frequency ω_{vib} around an equilibrium position then its instantaneous displacement q is

$$q = q_0 \cos(\omega_{vib} t). \quad (3.13)$$

If the polarisability of a molecule is assumed to be a weak function of q then we can expand it in a Taylor series to first order.

$$\alpha = \alpha_0 + \frac{\partial \alpha}{\partial q} q + \dots \quad (3.14)$$

Inserting (3.13) and (3.14) into (3.12) the induced dipole moment becomes

$$P = \alpha_0 E_0 \sin(\omega_p t) + \left(\frac{\partial \alpha}{\partial q} \right) \frac{E_0 q_0}{2} (\cos((\omega_p - \omega_{vib})t) + \cos((\omega_p + \omega_{vib})t)) \quad (3.15)$$

The first term is vibrating at the frequency of the incident light. This term relates to the dominant Rayleigh scattered light. The second and third terms are vibrating at $(\nu_p - \nu_{vib})$ and $(\nu_p + \nu_{vib})$ these scatter frequency downshifted (Stokes) and frequency upshifted (anti-Stokes) photons respectively. These are the origin Raman scattering.

3.4.2 Stimulated Raman Scattering (SRS)

If the intensity of Raman scattered light increases enough then the process can enter a nonlinear “stimulated” regime where Raman scattered photons stimulate the emission of more photons. When this occurs the power in the Stokes wave grows rapidly. This process is known as stimulated Raman scattering (SRS) and is used as the method of light amplification in Raman lasers and amplifiers.

This effect is often exploited in optical fibres because the tight confinement of light can produce very high intensities for moderate input powers, and the long interaction length can produce efficient gain without the need for a cavity. The amorphous structure of silica leads to a broadening of the molecular absorption levels into bands producing the Raman gain spectrum shown in figure 3.9. This gain spectrum stretches over 20THz with a peak at around 13.2THz (~105nm at 1550nm). To convert between a frequency bandwidth and a wavelength bandwidth use

$$\Delta \nu = \frac{c}{\lambda^2} \Delta \lambda \quad (3.16)$$

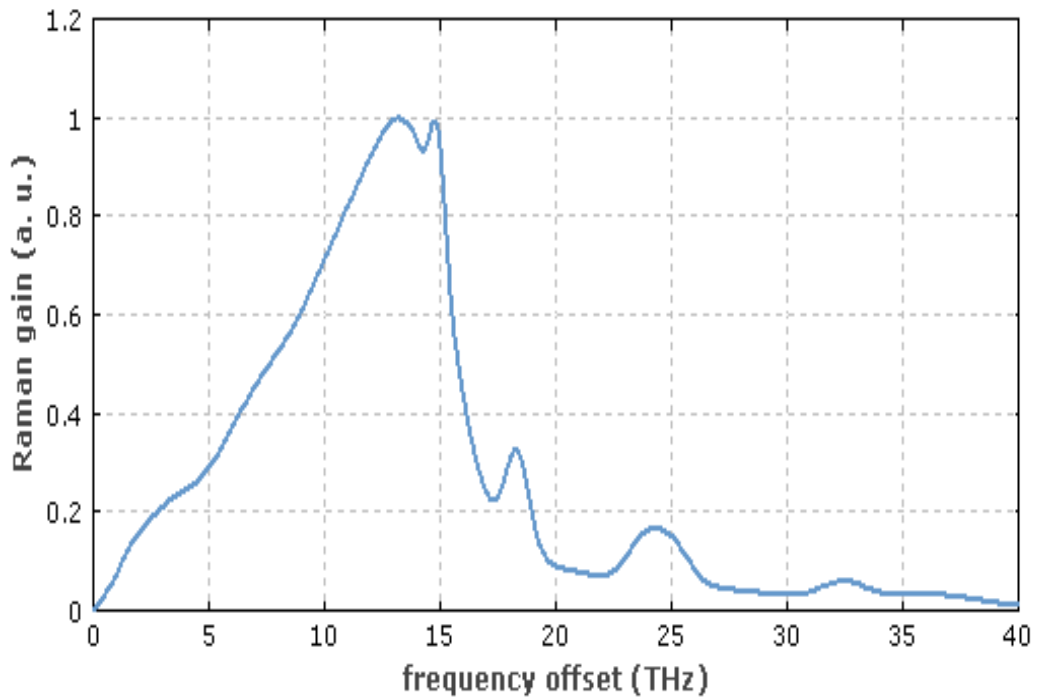


Figure 3.9: Raman gain spectrum of silica optical fibre measured with a 1550nm pump and an orthogonally polarized signal [3.33].

The evolution of the pump power P_p and signal power P_s in a continuous wave Raman fibre amplifier are governed by the equations:

$$\begin{aligned}\frac{dP_s}{dz} &= g_r P_p P_s - \alpha_s P_s \\ \frac{dP_p}{dz} &= \mp \frac{\omega_p}{\omega_s} g_r P_p P_s \mp \alpha_p P_p\end{aligned}\quad (3.17)$$

where ω_p and ω_s are the angular frequencies of the pump and Stokes wave, α_p and α_s are the fibre attenuation coefficients at the pump and Stokes wavelengths, z is the propagation distance and g_r is the Raman gain coefficient of the fibre [3.28]. The - signs are used for a co-propagating Raman amplifiers and the + signs for counter-propagating amplifiers.

The Raman equations 3.17 show that the overall number of photons in Raman amplification remains constant – this allows for very high optical efficiencies. The intrinsic quantum efficiency for the SRS process is 100%. The limit on actual optical efficiency is determined by the absorption of the fibre/material. The solution to equations 3.17 for a co-propagating amplifier is shown in figure 3.10. These were solved using a numerical Runge-Kutta technique, with the boundary conditions

$$\begin{aligned}P_p(0) &= 10W \\ P_s(0) &= 10mW\end{aligned}\quad (3.18)$$

And parameters,

$$\begin{aligned}g_r &= 0.5 \times 10^{-13} mW^{-1} \\ \alpha_p &= 0.0002 dBm^{-1} \\ \alpha_s &= 0.0005 dBm^{-1} \\ \lambda_p &= 1540nm \\ \lambda_s &= 1651nm \\ A &= 7.3 \times 10^{-11} m^2\end{aligned}\quad (3.19)$$

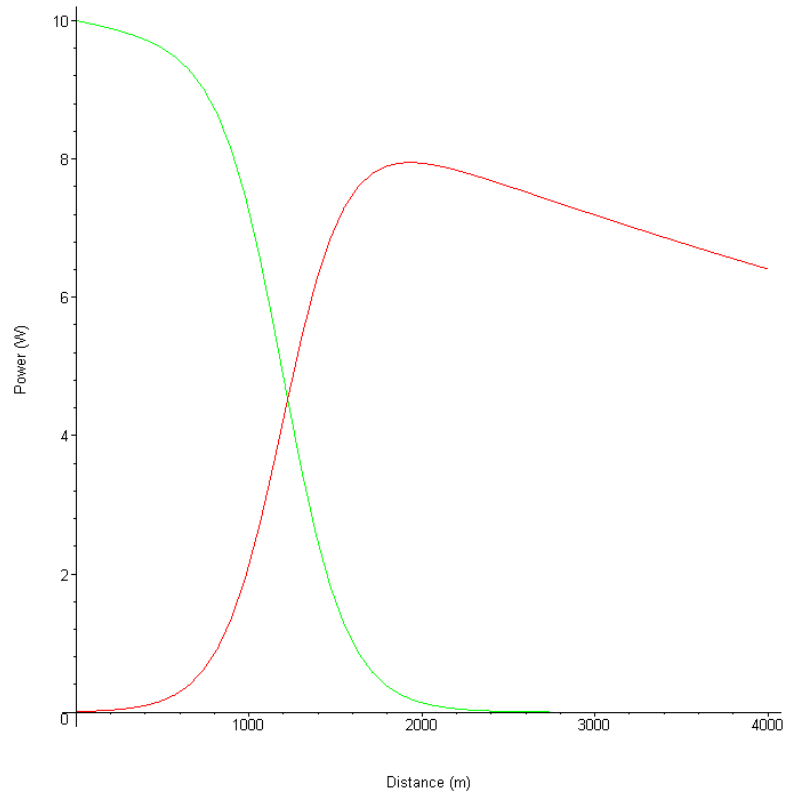


Figure 3.10: Pump power (green) and signal power (red) evolution in a co-propagating Raman amplifier.

For comparison the evolution of the pump and signal powers in a Raman amplifier pumped in a counter-propagating configuration, where the pump and signal enter from opposite ends of the fibre, are shown in figure 3.11. The boundary conditions are

$$\begin{aligned} P_p(2400) &= 10W \\ P_s(0) &= 10mW \end{aligned} \tag{3.20}$$

The equations were solved using a shooting method for boundary value problems. The length of the fibre is chosen to maximise the output signal at the fibre end for a given pump power.

The gain per unit length is clearly smaller in the counter-propagating amplifier, leading to a smaller overall transfer of power between the pump and signal. In a counter-pumped Raman amplifier it is not possible to fully transfer the pump power to the signal. This limits the maximum amplification for a 10W pump to just over 5W compared to around 8W in a co-propagating amplifier. However, counter-propagating designs have other benefits, including a higher threshold for stimulated Brillouin scattering and a lower transfer of noise from the pump to the signal.

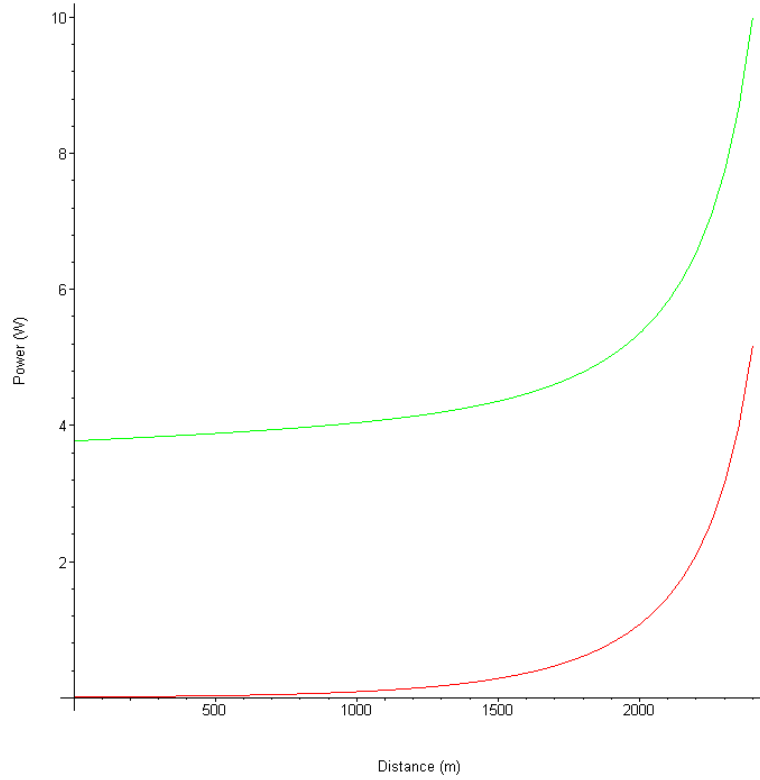


Figure 3.11: Pump power (green) and signal power (red) evolution in a counter-propagating Raman amplifier.

If pump depletion (the first term in the second equation) is ignored then equations 3.17 can be solved analytically. This is a valid approximation if we want to estimate the Raman threshold power for a length of fibre L with an effective core area A_{eff} . The result of this analysis shows that [3.34]

$$P_s(L) = P_s(0)e^{\left(\frac{g_R P_0 L_{eff}}{A_{eff}} - \alpha_s L\right)} \quad (3.21)$$

Where P_0 is the incident pump power and

$$L_{eff} = \frac{1 - e^{-\alpha_p L}}{\alpha_p} \quad (3.22)$$

L_{eff} represents an effective interaction length which accounts for pump absorption. Equation 3.21 shows that the gain can be increased by decreasing the area of the fibre core or by choosing a fibre with a larger Raman gain coefficient. There is also clearly a trade-off between the length and absorption in the fibre which determines the maximum gain and the optimum length. The threshold condition (Where $P_s(L)=P_s(0)$) is

$$\frac{g_R P_0 L_{eff}}{A_{eff}} \geq \alpha_s L \quad (3.23)$$

Following the analysis of RG Smith [3.29] and Agrawal [3.28], where they define Raman threshold as the input power at which the Stokes power becomes equal to the pump power at the fibre output, an approximate condition for the critical input power at threshold gain is

$$P_0^{Critical} \approx \frac{16 A_{eff}}{L_{eff} g_R} \quad (3.24)$$

Assuming that (to a good approximation) $\alpha_s = \alpha_p$; that the Raman gain spectrum (figure 3.8) resembles a Lorentzian function and that the pump and signal maintain a parallel polarization through the fibre. This analysis holds for co-propagating pump and Raman light. For counter-propagating light the factor of 16 becomes a 20. If the polarization state of the pump and signal vary then the Raman threshold is increased by a factor of between 1 (parallel polarization) and 2 (scrambled polarization). In a conventional (non polarization maintaining) optical fibre the polarization state of transmitted light is scrambled upon propagation. The scrambling is random and so over long distances pump and signal can be considered unpolarised.

The threshold pump power can be considerably reduced if light at the Stokes wavelength is injected into the fiber with the strong pump. This process is known as seeding and the input signal is known as the seed. This can be used to lower the threshold at frequencies away from the peak of the Raman gain spectrum, so that they can experience gain before SRS starts depleting the available pump power at the peak shift of 13.2THz. Seeding becomes very efficient at high powers, indeed with a pump of several watts it is predicted that most of the pump energy can be coupled into the signal. The effect of seed power is shown in figure 3.12.

From figure 3.12 we can see that the optimum length of fibre for a Raman amplifier is dependent on the power of the seed laser. The higher the power the shorter the minimum length with a 1mW seed and a 10W pump the optimum fibre length occurs at around 2400m. If the seed power is increased to 10mW the optimum length reduces to 1800m. The output power and overall gain of the amplifier does not vary very much with the input seed power except when the seed power gets very high.

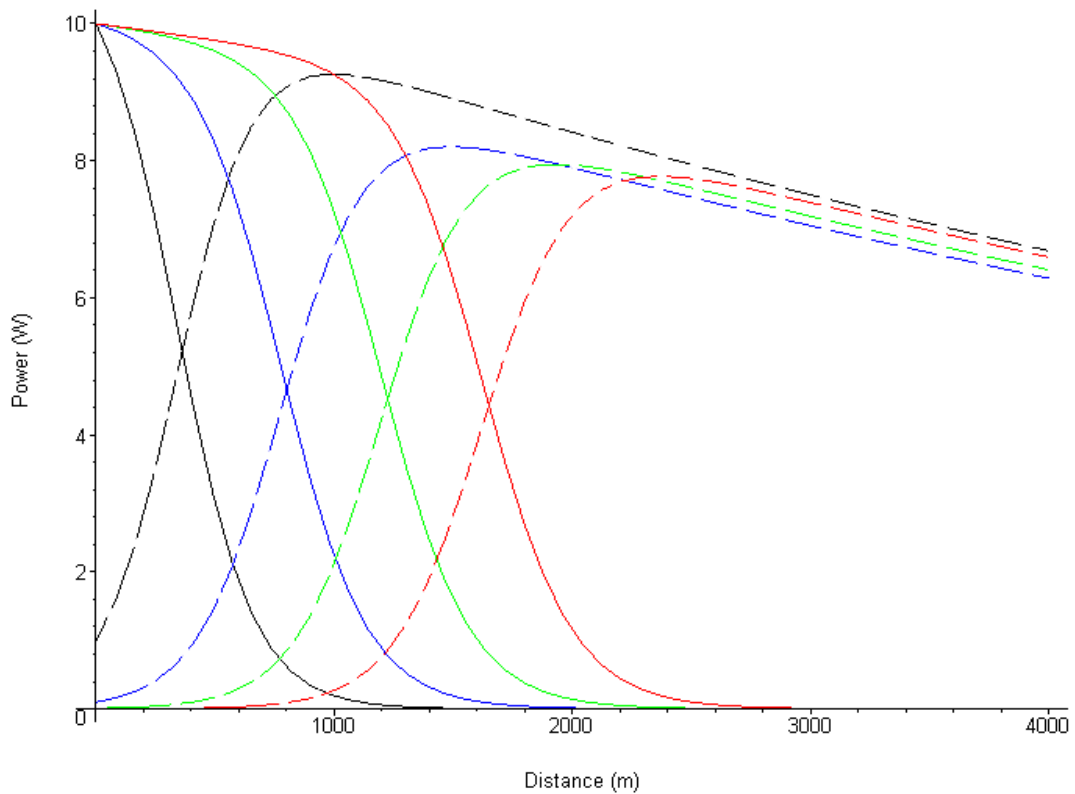


Figure 3.12: Pump (solid) and signal (dashed) power evolution in a co-propagating Raman amplifier with an input seed power of 1mW (red), 10mW (green), 100mW (Blue) and 1W (black).

The proposed pump in this work will be an EDFA producing light around 1540nm, which given the 13.2THz peak Stokes shift in fused silica, will provide a Raman gain peak at around 1651nm. To lower the required pump power for threshold the Stokes signal at 1651nm will be seeded using a DFB laser. The addition of a DFB seed laser will also be beneficial for the production of the gas sensor as its wavelength can be ramped and modulated in the manner required for TDLS with WMS.

In theory the modulation in the Raman Amplifier should match the modulation in the DFB laser almost exactly since the Raman amplifier acts like a fully inverted amplifier with a short lived upper state. This should avoid the amplifier distortion effects seen in the EDFA based TDLS system produced by Frish et. al. described earlier [3.22].

3.5 Brillouin Scattering

3.5.1 Spontaneous Brillouin Scattering

Brillouin scattering describes another type of inelastic scattering; this time of photons scattered from acoustic waves (phonons) within a material. These have much lower frequency than the optical phonons involved in Raman scattering and so produce much smaller shifts in the Stokes and anti-

Stokes waves ($\sim 10\text{GHz}$ ($\sim 0.08\text{nm}$)). The process of Brillouin scattering can be considered as a parametric interaction between three waves: the pump wave, Stokes wave and acoustic wave. Since energy and momentum must be conserved we get the usual phase matching conditions

$$\begin{aligned}\omega_A &= \omega_P - \omega_S \\ \overline{K}_A &= \overline{K}_P - \overline{K}_S\end{aligned}\tag{3.25}$$

Where ω and K are the frequencies and wave vectors of the acoustic, pump and Stokes waves. Since $|\overline{K}_P| \approx |\overline{K}_S|$ then using the law of cosines [3.31]

$$\omega_A = |\overline{K}_A|V_A = 2V_A|\overline{K}_P|\sin\left(\frac{\theta}{2}\right)\tag{3.26}$$

Where θ is the angle between the pump and stokes wave and V_A is the velocity of the acoustic wave. This shows that the frequency shift of the Stokes wave depends on the scattering angle and is a maximum for backward scattering ($\theta=180^\circ$) and vanishes for forward scattering ($\theta=0^\circ$). In the case of backward scattered light the frequency shift is given by

$$\nu_B = \frac{\omega_A}{2\pi} = \frac{2nV_A}{\lambda_P}\tag{3.27}$$

At high enough optical intensities Brillouin scattering may also become nonlinear, when this happens the Stokes wave and acoustic wave grow rapidly. This process is known as Stimulated Brillouin scattering (SBS) and can be thought of simply using a classical model as will be described in the next section.

3.5.2 Stimulated Brillouin Scattering (SBS)

At high optical powers the pump wave itself can induce an acoustic (pressure) wave through the process of electrostriction. Electrostriction occurs when an electric field is applied to a dielectric. The electric field causes dipoles in the dielectric to become oppositely charged so that they attract each other, reducing the material thickness in the direction of the applied field. This changes the density

and refractive index of the material. If the electric field is periodic like an EM-wave then the refractive index (pressure) will vary periodically. This creates a refractive index (pressure or acoustic) wave which travels through the material with a velocity dependent on the material properties. From the parametric model described above it is apparent that the velocity is related to the velocity of the wave envelope of the beat signal between the pump and Brillouin shifted waves.

The acoustic wave acts as a travelling Bragg grating, reflecting the pump light with a Stokes frequency shift produced by the Doppler effect of the travelling acoustic wave. This process is self reinforcing as the reflected signal light reinforces the beat signal which increases the depth of electrostriction and produces a stronger acoustic wave. The process is illustrated in figure 3.13 [3.32].

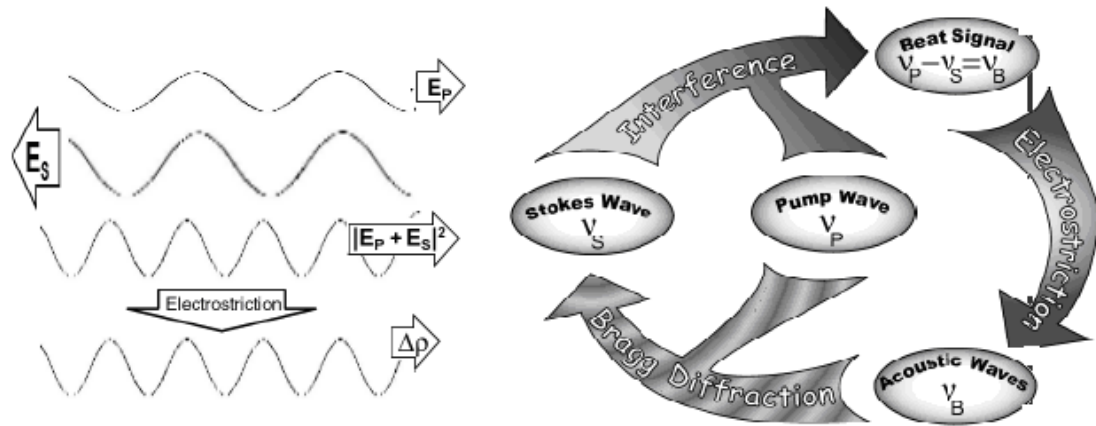


Figure 3.13: Stimulated Brillouin Scattering. [3.32].

Stimulated Brillouin scattering can be modelled using a pair of coupled differential equations

$$\begin{aligned} \frac{dP_s}{dz} &= -g_B P_p P_s + \alpha_s P_s \\ \frac{dP_p}{dz} &= -\frac{\omega_p}{\omega_s} g_B P_p P_s - \alpha_p P_p \end{aligned} \quad (3.28)$$

Where ω_p and ω_s are the angular frequencies of the pump and Stokes wave; α_p and α_s are the fiber attenuation coefficients at the pump and Stokes wavelengths; z is the propagation distance and g_B is the Brillouin gain coefficient of the fibre [3.28]. These equations are almost identical to the rate equations used to model Raman scattering (equations 16) except the sign of dP_s/dz has been changed to account for the fact that the Brillouin signal always travels in the opposite direction to the pump which produced it. Since the Stokes shift is small it is common to simplify the equations with $\alpha_s = \alpha_p = \alpha$ and $\omega_s = \omega_p = \omega$.

If the acoustic waves in a sample are assumed to decay as $\exp(-t/T_B)$ with a characteristic time constant T_B then the Brillouin gain spectrum can accurately be described by a Lorentzian profile

$$g_B(\nu) = g_B(\nu_B) \frac{(\Delta\nu_B/2)^2}{(\nu - \nu_B)^2 + (\Delta\nu_B/2)^2} \quad (3.29)$$

Where $\Delta\nu_B$ is the linewidth of the Brillouin gain spectrum; ν is the frequency shift from the pump frequency and $g_B(\nu_B)$ is the peak value of the Brillouin gain coefficient. The peak value of the Brillouin gain coefficient is dependent upon the material properties of the medium and is given by [3.28]

$$g_B(\nu_B) = \frac{2\pi n^7 p_{12}^2}{c \lambda_p^2 \rho_0 V_A \Delta\nu_B} \quad (3.30)$$

Where p_{12} is the longitudinal elasto-optic coefficient; V_A is the acoustic wave velocity; ρ is the materials density; n is the refractive index of the medium; c is the speed of light in a vacuum and λ_p is the pump wavelength.

If the pump linewidth $\Delta\nu_p$ is larger than the Brillouin linewidth $\Delta\nu_B$ then the peak value of the Brillouin gain $g_B(\nu_B)$ is reduced to

$$g_B(\nu_B) = \left(\frac{2\pi n^7 p_{12}^2}{c \lambda_p^2 \rho_0 V_A \Delta\nu_B} \right) \left(\frac{\Delta\nu_B}{\Delta\nu_B \otimes \Delta\nu_p} \right) \quad (3.31)$$

The Brillouin gain coefficient is still given by equation 3.30 but with the reduced peak value. This shows that increasing the spectral width of the pump is an efficient way to suppress SBS. Smith [3.29] empirically found that the threshold power for SBS is given by

$$P_0^{Critical} \approx \frac{21A_{eff}}{L_{eff} g_B} \quad (3.32)$$

In optical fibres stimulated Brillouin scattering normally dominates over Stimulated Raman scattering because the intrinsic Brillouin gain coefficient is much larger than the Raman gain coefficient. To decrease the effective Brillouin gain coefficient (equation 3.29) in an optical fibre we can increase the linewidth of the pump and Brillouin waves.

3.6 SBS suppression

Comparing the critical threshold powers for SRS and SBS (equations 3.24 and 3.32) it is clear that the only way to suppress SBS, without reducing SRS, is to reduce the effective Brillouin gain coefficient. As indicated by equation 3.29 this can be achieved in several ways:

- 1) By increasing the linewidth of the pump laser $\Delta\nu_p$.
- 2) By increasing the fibres Brillouin gain spectrum linewidth $\Delta\nu_B$.
- 3) By using fibres with different material properties e.g. higher density, lower elastic strain coefficient p_{12} , lower refractive index or higher acoustic wave velocity.

If the fibre is used just for transmission, and not Raman amplification, then SBS may also be reduced by increasing the effective area of the fibre core, or by decreasing the length. However, these both also affect Raman gain. Since SBS and SRS are parametric processes the gain of both can also be affected by the relative dispersion of the interacting waves in the fibre.

In the following subsections we will review SBS suppression techniques. Section 3.6.1 will consider SBS suppression by broadening the line width of the pump laser; and section 3.6.2 will consider SBS suppression by broadening the Brillouin gain line width. Some of these techniques will be applied to the Raman amplifier that we produce.

3.6.1 SBS Suppression by Broadening Pump Linewidth

Increasing the laser linewidth entering a fibre suppresses SBS but not SRS because of the difference in the gain bandwidths. The gain bandwidth for Raman is around 10THz as opposed to about 50MHz for Brillouin. Thus, a broad linewidth source (100's GHz) will effectively all contribute to a single Raman Stokes signal but will amplify multiple Brillouin Stokes signals. These will individually remain below the critical threshold power for SBS even though the overall power may be very large.

Ohki et. al. [3.34] examined this effect by studying the SBS reflection of several diode lasers supporting different numbers of longitudinal modes. Reasoning that the longitudinal modes of a laser will each produce their own SBS signal as the spacing between longitudinal modes is usually much larger than the Brillouin gain bandwidth. Therefore by increasing the number of modes propagating in a fibre you can increase the total power transmitted before SBS begins. However, increasing the number of modes produced by a diode laser increases the line width which is obviously unacceptable for TDLS. It also increases the relative intensity noise of the diode laser.

When the characteristics of a single longitudinal mode laser (like a DFB) are needed then it is possible to increase the effective line width (as seen by the fibre) by dithering the output wavelength. This is well known in the literature [3.35-3.39] and was developed to allow long haul optical fibre transmission with greater distance between repeaters and amplifiers. The principal is simple. When a DFB lasers drive current is modulated its wavelength changes. This causes the wavelength of light entering the fibre to change with time. If the transmission time through the fibre is long compared to the rate of wavelength change then many wavelengths may be present in the fibre at once (varying with distance). Along the length of the fibre these wavelengths will undergo Brillouin scattering, however, if the wavelength sweep is much larger than the Brillouin gain linewidth then scattering at different points in the fibre will not all contribute to the same Stokes reflection. The individual Stokes waves generated can then be kept below threshold even though the overall power is large. Effectively, this reduces phase matching between scattering events at different positions in the fibre.

The advantage of the dither approach is that it keeps the instantaneous linewidth of the laser small (several kHz for a DFB laser). This is especially advantageous for our application of TDLS since the linewidth must be kept narrow for sensitivity. Also, since the wavelength has to be dithered for TDLS-WMS anyway it should be possible to use this modulation to also suppress SBS in the Raman amplifier.

Hence, the intention is to suppress SBS at the pump wavelength (1540nm) by broadening the seed for the EDFA. Suppression at the signal wavelength (1650nm) will be achieved through broadening by modulation.

3.6.2 SBS Suppression by Broadening the Brillouin Gain Linewidth

Stimulated Brillouin scattering can also be suppressed by broadening the Brillouin gain linewidth of a fibre. This can be achieved by

- Applying temperature and strain distributions along an existing fibre.
- Designing and manufacturing optical fibres with properties that change along its length.
- Concatenating different types of fibre with different Brillouin shifts
- Introducing extra elements like fibre Bragg gratings into the fibre.

The first of these methods – applying a temperature distribution to the fibre broadens the Brillouin gain line width by altering the refractive index in different parts of the fibre through the thermo-optic effect. This causes the peak Brillouin shift (equation 3.27) to change along the length of the fibre. If

the peak shift in different portions of the fibre is greater than the Brillouin bandwidth then scattering in one section cannot stimulate scattering in another section.

The temperature distribution is usually cited as a reason for unexpectedly high SBS thresholds in high power end pumped fibre amplifiers [3.40, 3.41]. From equation 3.27 the change in Brillouin frequency with refractive index is given by

$$\frac{d\nu_B}{dn} = \frac{2\nu_A}{\lambda_p} \quad (3.29)$$

If the acoustic velocity in an optical fibre is $V_A = 5960\text{ms}^{-1}$ [3.42] and the refractive index variation with temperature is $dn/dT = 1 \times 10^{-5}\text{K}^{-1}$ [3.43] then the change in Brillouin frequency with temperature is found to be

$$\frac{d\nu_B}{dT} = \frac{d\nu_B}{dn} \frac{dn}{dT} = \frac{2\nu_A}{\lambda_p} \frac{dn}{dT} = 0.77\text{MHzK}^{-1} \quad (3.30)$$

Assuming a typical value of $\Delta\nu_B = 40\text{MHz}$ then we would require a temperature gradient of $\sim 50\text{K}$ along the fibre to introduce one bandwidth shift in the Brillouin (Stokes) shift frequency.

Applying a strain distribution to the fibre works in a similar way. The strain induces a change in the refractive index of the fibre through the photoelastic effect. This is used in distributed Brillouin strain sensors [3.44, 3.45].

If the Brillouin shift increases with strain at a rate of $0.05\text{MHz}/\mu\epsilon$ [3.46] then it will take a strain of $800\mu\epsilon$ to shift the Brillouin gain peak by the Brillouin gain linewidth (40MHz). If the Young's modulus of a fibre optic is $E=72\text{GPa}$ then this requires a force of

$$F = EA_0\epsilon = 72 \times 10^9 \times 1.23 \times 10^{-8} \times 800 \times 10^{-6} = 0.7\text{N} \quad (3.31)$$

$$\epsilon = \frac{\Delta L}{L}$$

assuming standard SMF with a diameter of $125\mu\text{m}$. This could be achieved through winding of the fibre onto different diameter reels or simply by adjusting tension during the fibre winding process, or by winding onto a non-cylindrical reel.

Stimulated Brillouin Scattering can also be suppressed by altering fibre parameters along the length of the fibre. The parameters which can be varied need to alter the Brillouin shift frequency (according to equation 3.27) these are the refractive index of the fibre and the acoustic wave velocity. The refractive index can be varied either through non-uniform doping of the core or cladding glass prior to fibre pulling [3.47] or by concatenating multiple different fibres [3.48]. The acoustic wave velocity in the fibre can be changed by doping or by altering the geometric dimensions of the fibre by varying the fibre pull speed as the fibre is produced [3.49].

Taiji Sakamoto et. al. [3.50] developed a hole-assisted fibre with a low overlap between the acoustic and optical modes in the fibre. This fibre has the same mode field diameter as SMF 28 but increases the SBS threshold by 13.5dB.

Agrawal et. al. [3.51] also show that SBS can be suppressed by introducing fibre Bragg gratings along the fibre length. The idea is that these are transparent to the pump wavelength but not at the Stokes wavelength. Any SBS produced in that section of fibre is then reflected so that it co-propagates with the pump that produced it. The Stokes wave is now travelling in the forward direction so it does not stimulate further Brillouin scattering and since the backward travelling wave never reaches high powers it cannot take advantage of the exponential gain of SBS. This can be repeated at multiple points along the fibre.

3.7 High Power Narrow Linewidth Raman Amplifiers

The aim of this section is to review some of the high power Raman amplifier systems found in the literature, concentrating on narrow linewidth and high power amplifiers which could be suitable for TDLS. After searching the literature only one use of Raman amplification for high power and narrow linewidth amplification in the wavelength range of interest to this project, around 1650nm, could be found [3.24]. However it only had an output power of 100mW and the specifics of the system or its performance were not discussed. Several fibre Raman amplifiers in the 1150-1300nm wavelength range pumped by ytterbium fibre lasers have been identified.

One of the most interesting to this project is the Raman fibre amplifier that was constructed at the European Southern Observatory by Yan Feng et. al. [3.52]. Their aim was to amplify a narrow linewidth laser at 1178nm to high powers for efficient frequency conversion to 589nm for use as a laser guide star. Using a simple amplifier design, as shown in figure 3.17, they amplified a 9mW 1178nm DFB laser with a linewidth of <10MHz to 4.8W. The pump laser was at 1120nm provided by a 45W single mode Yb-fibre laser and the Raman amplifier fibre was 150m Nufern 1060XP.

They suggest that the power distribution in a high power Raman amplifier decreases the effective length of the fibre (as used in the threshold equations) and increases the maximum gain of the fibre before the onset of SBS. As shown in figure 3.11 the signal only reaches high intensities in the end section of the amplifying fibre. This suggests that the effective length in the threshold equations should be adjusted to account for the non-uniform pump distribution.

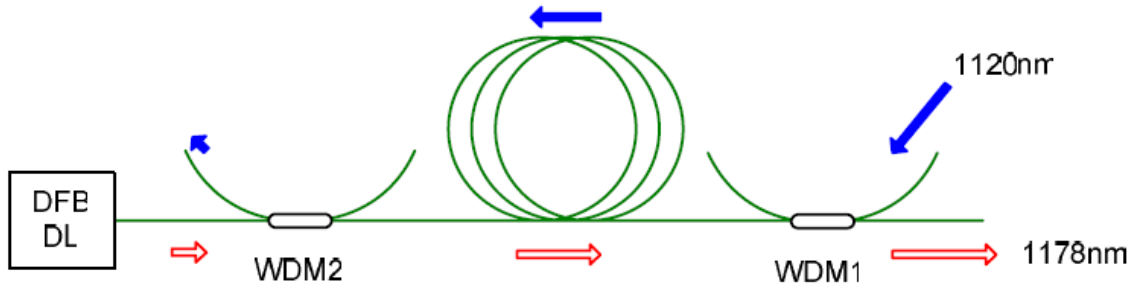


Figure 3.17: Schematic of Raman system at European southern observatory.

As a figure of merit for a fibre to be chosen for narrow linewidth SRS Feng et. al. [2.53 - patent] suggest using the ratio of the SRS critical power (equation 3.24) to the SBS critical power (equation 3.32). This yields

$$\frac{P_0^{Critical,SRS}}{P_0^{Critical,SBS}} \approx \frac{16g_R}{21g_B} \quad (3.32)$$

However, the Brillouin and Raman gain coefficients are wavelength dependent and not well characterised for regular single mode fibres.

In a recent publication Nagel et. al. [3.49] used two Raman fibre amplifiers to amplify two seed lasers, one at 1271.7074nm and one at 1271.817nm. The wavelengths were chosen to correspond to an online and offline measurement for ratiometric sensing of Oxygen. Their amplifier used a specially produced phosphosilicate fibre with a modulating core to suppress SBS. Pump light was provided by a 1087nm Yb fibre laser. Using this system they produced outputs of 2.4W at 1271.7074nm and 0.5W at 1271.817nm without the onset of SBS. They also dithered the seed inputs, as necessary for TDLS, and found no distortion in the dithered output due to the gain dynamics of the amplifiers.

3.8 Summary

In summary, this chapter has introduced the project to develop a long distance, remote methane sensor for gas pipeline health monitoring. It has covered the theory of tuneable diode laser spectroscopy;

Raman amplification in fibre and stimulated Brillouin scattering. It has also developed the framework for where this system sits within the wider fields of Raman amplification and TDLS methane sensing.

After reading this chapter, the reader should be aware of how a Raman amplifier works and the possible techniques and challenges associated with creating a high power fibre Raman amplifier with a narrow linewidth. The next three chapters will discuss the system created in this project much more specifically.

Chapter 4 will describe the Raman amplifier system developed during this project and expand on the theory of the different sections – including modelling of Er-Yb amplifiers and Raman amplifiers. It will look at the efficiencies of the completed 1650nm Raman amplifier and assess its suitability as a source for TDLS.

Chapter 5 will then explain how the Raman amplifier system was integrated into a complete TDLS system for the remote detection of methane. It will also discuss the results of laboratory and field gas sensing trials conducted at Strathclyde University.

Chapter 6 concludes the project with an executive summary and proposals for refinements to the Raman amplifier and TDLS system. It also looks at wider improvements which could form the basis for future work.

References

- [3.1] C. B. Moore, "Gas-Laser Frequency Selection by Molecular Absorption," *Applied Optics*, 1965, Vol. 4 Issue 2, pp.252-253
- [3.2] W. B. Grant, "He-Ne and CW Co₂-Laser Long-Path Systems for Gas-Detection," *Applied Optics*, 1986, Vol. 25 Issue 5, pp.709-719
- [3.3] H. J. Gerritsen, M. E. Heller, "High-Resolution Tuned-Laser Spectroscopy," *Applied Optics*, 1965, Vol. 4 Issue 1, pp.73-77
- [3.4] L.S. Rothman, I.E. Gordon, A. Barbe, D. C. Benner, P.F. Bernath, M. Birk, et al. "The HITRAN 2008 molecular spectroscopic database [J]," *Quantitative Spectroscopy and Radiative Transfer*, 2009, Vol. 110, pp.533-572.
- [3.5] G. Stewart, C. Tandy, D. Moodie, M.A. Morante, F. Dong, "Design of a fibre optic multi-point sensor for gas detection," *Sensors and Actuators B: Chemical*, 1998, Vol. 51, Number 1, pp. 227-232(6)
- [3.6] K. Duffin, "Wavelength Modulation Spectroscopy with Tuneable Diode Lasers: a Calibration-Free Approach to the Recovery of Absolute Gas Absorption Line-Shapes," PhD thesis, EEE University of Strathclyde, 2007
- [3.7] W. Demtröder, "Laser spectroscopy: Experimental techniques," Springer; 4th ed. 2008

- [3.8] P. Werle, "A review of recent advances in semiconductor laser based gas monitors," *Spectrochimica Acta Part A*, 1998, Vol 54, pp.197–236.
- [3.9] J. Reid and D. Labrie, "Second-Harmonic Detection with Tunable Diode Lasers - Comparison of Experiment and Theory," *Appl. Phys. B*, 1981, Vol. 26, pp. 203-210
- [3.10] J. A. Silver "Frequency-modulation spectroscopy for trace species detection: theory and comparison among experimental methods," *Applied Optics*, 1992, Vol. 31, No. 6
- [3.11] K. Duffin, A. J. McGettrick, W. Johnstone, G. Stewart, and D. G. Moodie, "Tunable Diode-Laser Spectroscopy with Wavelength Modulation: A Calibration-Free Approach to the Recovery of Absolute Gas Absorption Line Shapes," *Journal of Lightwave Technology*, 2007, Vol. 25
- [3.12] D. J. M. Stothard, M. H. Dunn and C. F. Rae, "Hyperspectral imaging of gases with a continuous-wave pump-enhanced optical parametric oscillator," *Opt. Express*, 2004, Vol. 12 pp. 947-55
- [3.13] G. M. Gibson, M. Ebrahimzadeh, M. Padgett and M. Dunn, "Continuous-wave optical parametric oscillator based on periodically poled KTiOPO_4 and its application to spectroscopy," *Opt. Lett.*, 1999, Vol. 24, pp. 397-9
- [3.14] I. Armstrong, W. Johnstone, K. Duffin, M. Lengden, A. L. Chakraborty and K. Ruxton, "Detection of CH_4 in the Mid-IR using Difference Frequency Generation with Tunable Diode Laser Spectroscopy," *IEEE Journal of Lightwave Technology*, 2010, Vol. 28, No. 10, pp. 1435-1442
- [3.15] I. D. Lindsay, P. Groß, C. J. Lee, B. Adhimoolam and K.-J. Boller, "Mid-infrared wavelength- and frequency modulation spectroscopy with a pump-modulated singly-resonant optical parametric oscillator," *Optics Express*, 2006, Vol. 14, No. 25
- [3.16] P. Werle, F. Slemr, K. Maurer, R. Kormann, R. Mucke, B. Janker, "Near- and mid-infrared laser-optical sensors for gas analysis," *Optics and Lasers in Engineering*, 2002, Vol.32, pp. 101-114
- [3.17] B. van Well, S. Murray, J. Hodgkinson, R. Pride, R. Strzoda, G. Gibson and M. Padgett, "An open-path, hand-held laser system for the detection of methane gas," *J. Opt. A: Pure Appl. Opt.*, 2005, Vol. 7, S420–S424
- [3.18] T. Iseki, H. Tai, and K. Kimura, "A portable remote methane sensor using a tunable diode laser," *Meas. Sci. Technol.*, 2000, Vol. 7, pp. 594–602.
- [3.19] "LaserMethane: Detection at a Distance," online:
<http://www.crowcon.co.uk/media/Laser%20Methane%20Brochure%20Issue%201.pdf>, Retrieved: 20/05/2011
- [3.20] M. B. Frish, R. T. Wainner, J. Stafford-Evans, B. D. Green, M. G. Allen, S. Chancey, J. Rutherford, G. Midgley, and P. Wehnert, " Standoff Sensing of Natural Gas Leaks: Evolution of the Remote Methane Leak Detector (RMLD)," in *Conference on Lasers and Electro-Optics/Quantum Electronics and Laser Science and Photonic Applications, Systems and Technologies, Technical Digest (CD) (Optical Society of America, 2005)*, paper JThF3.
- [3.21] RMLD Product Literature, online:
http://www.heathus.com/tasks/sites/_hc/assets/File/RMLD_Dual.pdf, Retrieved: 20/05/2011

- [3.22] R. T. Wainner, M. B. Frish, B. D. Green, M. C. Laderer, M. G. Allen "Tuneable Diode Laser Wavelength Modulation Spectroscopy (TDL-WMS) Using a Fibre Amplified Source," CLEO/QELS, May 2007
- [3.23] R. T. Wainner, M. B. Frish, B. D. Green, M. C. Laderer, M. G. Allen, and J. R. Morency. "High Altitude Aerial Natural Gas Leak Detection System," April 2007, Department of Energy final report Contract No. DE-FC26-04NT42268
- [3.24] P. Vujkovic-Cvijin, E. Lavelle, J. E. van der Laan, R. E. Warren, D. E. Cooper and K. Krist "Mobile Remote Sensor for Leak Detection in Natural Gas Pipelines," Online: www.kgu.or.kr/download.php?tb=bbs_017&fn=Do02.pdf, Retrieved: 20/05/2011
- [3.25] P. Werle, F. Slemr, K. Maurer, R. Kormann, R. Mucke, B. Janker, "Near- and mid-infrared laser-optical sensors for gas analysis," *Optics and Lasers in Engineering*, 2002, Vol. 37, pp. 101-114
- [3.26] G.Placzek, *Hand buchder Radiologie VI Leipzig: Akademische Verlagsgellschaft, Teil II* 205,1934.
- [3.27] J. R. Ferraro, K. Nakamoto, C. W. Brown, "Introductory Raman Spectroscopy," Academic Press, 2003
- [3.28] G. P. Agrawal, "Nonlinear Fiber Optics," 4th edition, Academic Press, Boston, 2007
- [3.29] R. G. Smith, "Optical Power Handling Capacity of Low Loss Optical Fibers as Determined by Stimulated Raman and Brillouin Scattering," *Applied Optics*, 1972, Vol. 11, No. 11, pp. 2489- 2494
- [3.30] R. Billington, "Measuerment methods for stimulated Raman and Brillouin scattering in optical fibers," NPL Report, COEM 31, 1999.
- [3.31] P. E. Powers, "Fundamentals of Nonlinear Optics," CRC Press, New York, NY, 2011
- [3.32] Brillouin scattering picture, http://lhcp.web.cern.ch/LHCP/PLO/LHC_Seminars/fellay2003.pdf, Retrieved: 20/05/2011
- [3.33] RP Photonics, Raman gain spectrum picture Online: http://www.rp-photonics.com/raman_gain.html, Retrieved: 20/05/2011
- [3.34] Y. Ohki, N. Hayamizu, S. Irino, H. Shimizu, J. Yoshida and N. Tsukij, "Pump Laser Module for Co-propagating Raman Amplifier," *Furukawa Review*, No. 24 2003
- [3.35] D. A.Fishman, J. A Nagel, Y.Park, "Reduction of stimulated brillouin scattering in a fiber optic transmission system," United States Patent: 5329396. Publication date 12/07/1994.
- [3.36] L. E. Adams, C. G. Bethea, L. E. Eskildsen, G. R. Nykolak, T. Tanbun-Ek, "Optical system for reduced SBS," US patent number: 6331908. Published 18/12/2001
- [3.37] D. A Fishman, and J. A. Nagel, "Degradation due to stimulated Brillouin scattering in multigigabit intensity-modulated fiberoptic systems," *J. Lightwave Tech.*, 1993, Vol. 11, pp. 1721-1728
- [3.38] K. Korotky et al., "Efficient Phase Modulation Scheme for Suppressing Stimulated Brillouin Scattering," IOOC'95, WD2-1, Hong Kong, 1995.
- [3.39] P. B. Hansen, L. Eskildsen, U. Koren, B. Miller, "SBS suppression using a temperature Wavelength-modulated laser diode with low residual AM," *Optical Fiber Communications*, 1996,

- [3.40] Y. Jeong, J. K. Sahu, D. B. S. Soh, C. A. Codemard, and J. Nilsson, "High-power tunable single-frequency single-mode erbium:ytterbium codoped large-core fiber master-oscillator power amplifier source," *Opt. Lett.*, 2005, Vol.30(22), pp. 2997–2999
- [3.41] B. Morasse, S. Agger, C. Hovington, S. Chatigny, E. Gagnon, J. de Sandro, and C. Poulsen, "10W ASE-free single-mode high-power double-cladding Er³⁺-Yb³⁺ amplifier," *Proc. SPIE*, 2007, pp. 654324
- [3.42] M. Yoshikawa, "Analysis and simulation of Fibre optic temperature sensor using mode-division multiplex," *IEICE Transactions on Electronics*, 1999, No 3, pp 562-564
- [3.43] J. Hansryd, F. Dross, M. Westlund, P. A. Andrekson, and S. N. Knudsen "Increase of the SBS Threshold in a Short Highly Nonlinear Fiber by Applying a Temperature Distribution," *Journal of Lightwave Technology*, 2001, Vol. 19, No. 11, pp1691-1697
- [3.44] A. Liu "Suppressing stimulated Brillouin scattering in fiber amplifiers using nonuniform fiber and temperature gradient," *Optics Express*, 2007, Vol. 15, Issue 3, pp. 977-984
- [3.45] J. M. Chavez Boggio, J. D. Marconi, and H. L. Fragnito "Experimental and Numerical Investigation of the SBS-Threshold Increase in an Optical Fiber by Applying Strain Distributions," *Journal of Lightwave Technology*, 2005 Vol. 23, Issue 11, pp. 3808
- [3.46] N Yoshizawa, T Imai, "Stimulated Brillouin Scattering Suppression by means of applying strain distribution to fiber with cabling," *J. Lightwave Tech.*, 1993 Vol. 11, pp.1518-1522
- [3.47] C. A. Galindez, A. Ullan, F. J. Madruga, J. M. López-Higuera, "Brillouin gain spectrum tailoring technique by using fiber concatenation and strain for fiber devices," *Microwave and Optical Technology Letters*, 2010, Vol. 52, Issue 4, pp. 787–790
- [3.48] M. Ohashi, M. Tateda, "Design of Strain-Free-Fiber with Nonuniform Dopant Concentration for Stimulated Brillouin Scattering Suppression," *Journal of Lightwave Technology*, 1993, Vol. 11, No. 12
- [3.49] J. A. Nagel, V. Temyanko, J. Dobler, E. M. Dianov, A. S. Biriukov, A. A. Sysoliatin, R. A. Norwood, and N. Peyghambarian, "High-Power Narrow-Linewidth Continuous-Wave Raman Amplifier at 1.27 μ m," *IEEE Photonics Technology Letters*, 2011, Vol. 23, No. 9
- [3.50] T. Sakamoto, T. Matsui, K. Shiraki, and T. Kurashima, "SBS Suppressed Fiber With Hole-Assisted Structure," *Journal of Lightwave Technology*, 2009, Vol. 27, No. 20, pp. 1941-1945
- [3.51] H. L. Govind, P. Agrawal, "Suppression of stimulated Brillouin scattering in optical fibers using fiber Bragg gratings," *Optics Express*, 2003, Vol. 11, No. 25, pp. 3467-3472
- [2.52] Y. Feng, L. Taylor, and D. B. Calia, "Multiwatts narrow linewidth fiber Raman amplifiers," *Opt. Express*, 2008, pp. 10927-10932
- [3.53] Taylor, Luke R., Feng, Yan, Hackenberg, Wolfgang, Holzlöhner, Ronald Calia, Domenico Bonaccini, "Narrow Band Raman Optical Amplifier", United States Patent Application 20110038035 02/17/2011
- [3.54] J. Faist, F. Capasso, D. L. Sivco, A. L. Hutchinson, S. Sung-Nee, G. Chu, and A. Y. Cho, "Short wavelength 3.4 μ m. quantum cascade laser based on strained compensated nGaAs/AlInAs," *Applied Physics Letters*, 1998, Vol. 72, No. 6, pp. 680-682

Appendix A3.1: Derivation of Equation 3.8 (Werle [3.8])

To arrive at equation 3.7 for the harmonic coefficients of a TDLS-WMS signal we begin with the Beer-Lambert law

$$I(\nu) = I_0(\nu)e^{-\sigma(\nu)NL} \quad (\text{A1.1})$$

If the instantaneous frequency is modulated as

$$\nu = \bar{\nu} + m \cos(\omega_m t) \quad (\text{A1.2})$$

Then the intensity can be expanded as a Fourier cosine series

$$I(\nu, t) = \sum_{n=0}^{\infty} A_n \cos(n\omega_m t) \quad (\text{A1.3})$$

Using the properties of Fourier transforms the individual harmonic coefficients can be found. For a function $f(x)$

$$A_n = \frac{1}{\pi} \int_{-\pi}^{\pi} f(x) \cos(nx) dx \quad (\text{A1.4})$$

Since our cosine Fourier series is symmetric

$$A_n = \frac{2}{\pi} \int_0^{\pi} I_0(\bar{\nu} + m \cos \theta) e^{-\sigma(\bar{\nu} + m \cos \theta)LN} \cos(n\theta) d\theta \quad (\text{A1.5})$$

Where $\theta = \omega_m t$. In the ideal case the laser can be scanned across the absorption line with no change in I_0 and the equation becomes

$$A_n = \frac{2I_0}{\pi} \int_0^{\pi} e^{-\sigma(\bar{\nu} + m \cos \theta)LN} \cos(n\theta) d\theta \quad (\text{A1.6})$$

In trace gas analysis the absorption is low ($\sigma LN \ll 1$), thus

$$A_n = \frac{2I_0LN}{\pi} \int_0^\pi -\sigma(\bar{\nu} + m \cos \theta) \cos(n\theta) d\theta \quad (\text{A1.7})$$

This is the general case solution for the harmonic coefficient (in the ideal case of no RAM). If the modulation index m is small then this equation can be simplified by Taylor expansion of the absorption cross section σ about the mean frequency.

$$\sigma(\nu) = \sigma(\bar{\nu}) + \left. \frac{d\sigma(\nu)}{d\nu} \right|_{\nu=\bar{\nu}} m(\nu - \bar{\nu}) + \left. \frac{1}{2!} \frac{d^2\sigma(\nu)}{d\nu^2} \right|_{\nu=\bar{\nu}} m^2(\nu - \bar{\nu})^2 + \dots + \left. \frac{1}{n!} \frac{d^n\sigma(\nu)}{d\nu^n} \right|_{\nu=\bar{\nu}} m^n(\nu - \bar{\nu})^n \quad (\text{A1.8})$$

Putting equation A1.2 into A1.8 and expressing as a series yields

$$\sigma(\nu) = \sigma(\bar{\nu}) + \sum_{n=1}^{\infty} \left. \frac{1}{n!} \frac{d^n\sigma(\nu)}{d\nu^n} \right|_{\nu=\bar{\nu}} m^n \cos^n \theta \quad (\text{A1.9})$$

Putting this into equation A1.7 produces

$$A_n = \frac{2I_0LN}{\pi} \int_0^\pi - \left(\sigma(\bar{\nu}) + \sum_{n=1}^{\infty} \left. \frac{1}{n!} \frac{d^n\sigma(\nu)}{d\nu^n} \right|_{\nu=\bar{\nu}} m^n \cos^n \theta \right) \cos(n\theta) d\theta \quad (\text{A1.10})$$

Evaluating the integral using

$$\int_0^\pi \cos^n(\theta) \cos(n\theta) = \frac{\pi}{2^n} \quad (\text{A1.11})$$

Gives us our final result

$$A_n = \frac{2^{1-n} I_0LN}{n!} m^n \left. \frac{d^n\sigma(\nu)}{d\nu^n} \right|_{\nu=\bar{\nu}} \quad (\text{A1.12})$$

Appendix A3.2: Intuitive derivation of TDLS-WMS signals which account for RAM contributions

An intuitive derivation of the signals produced in TDLS-WMS in the low absorption, small modulation index regime was given by Duffin et. al. [3.11]. This is useful because it takes account of the residual amplitude modulation (RAM) that is imposed on the diode laser

On the assumption of small absorption ($\sigma LN \ll 1$) the Beer-Lambert Law can be approximated to

$$I(\nu) \approx I_0 (1 - \sigma(\nu) LN) \quad (\text{A2.1})$$

If a dither is applied to the drive current of the laser then the central frequency varies as

$$\nu = \bar{\nu} + m \cos(\omega_m t) \quad (\text{A2.2})$$

This dither also causes the transmitted intensity to modulate

$$I_0 = I(\bar{\nu}) + \Delta I \cos(\omega_m t) \quad (\text{A2.3})$$

Where $\bar{\nu}$ is the mean frequency of the laser and ΔI is the magnitude of the intensity dither. Putting equation A2.3 into A2.1 yields

$$I(\nu) \approx \left(I(\bar{\nu}) + \Delta I \cos(\omega_m t) \right) (1 - \sigma(\nu) LN) \quad (\text{A2.4})$$

If the modulation index is small ($m \ll 1$) then we can Taylor expand the cross section around the mean frequency

$$\sigma(\nu) = \sigma(\bar{\nu}) + \left. \frac{d\sigma(\nu)}{d\nu} \right|_{\nu=\bar{\nu}} m(\nu - \bar{\nu}) + \frac{1}{2!} \left. \frac{d^2\sigma(\nu)}{d\nu^2} \right|_{\nu=\bar{\nu}} m^2(\nu - \bar{\nu})^2 + \dots + \frac{1}{n!} \left. \frac{d^n\sigma(\nu)}{d\nu^n} \right|_{\nu=\bar{\nu}} m^n(\nu - \bar{\nu})^n \quad (\text{A2.5})$$

Truncating equation A2.5 at the third term and substituting into equations A2.2 and A2.5 results in

$$I(\nu) \approx \left(I(\bar{\nu}) + \Delta I \cos(\omega_m t) \right) \left(1 - \sigma(\bar{\nu}) LN - \left. \frac{d\sigma(\nu)}{d\nu} \right|_{\nu=\bar{\nu}} m \cos(\omega_m t - \phi) LN - \frac{1}{2!} \left. \frac{d^2\sigma(\nu)}{d\nu^2} \right|_{\nu=\bar{\nu}} m^2 \cos^2(\omega_m t - \phi) LN \right) \quad (\text{A2.6})$$

Where ϕ accounts for the phase difference between the lasers frequency/wavelength modulation (FM) and the lasers intensity/amplitude modulation (AM). Then using the trigonometric identity

$$\cos^2(x) = \frac{1}{2}(1 + \cos(2x)) \quad (\text{A2.7})$$

It is easy to separate out the coefficients of the DC, 1f and 2f components (as measured by the lock in detector).

$$A_{DC} = I(\bar{\nu})(1 - \sigma(\bar{\nu})LN) \quad (\text{A2.8})$$

$$A_{1f} = \Delta I \cos(\omega_m t) - \Delta I \cos(\omega_m t) \sigma(\bar{\nu})LN - I(\bar{\nu}) \left. \frac{d\sigma(\nu)}{d\nu} \right|_{\nu=\bar{\nu}} m \cos(\omega_m t - \phi)LN \quad (\text{A2.9})$$

$$A_{2f} = -\frac{1}{2} \Delta I \left. \frac{d\sigma(\nu)}{d\nu} \right|_{\nu=\bar{\nu}} m \cos(2\omega_m t - \phi)LN - \frac{1}{4} I(\bar{\nu}) \left. \frac{d^2\sigma(\nu)}{d\nu^2} \right|_{\nu=\bar{\nu}} m^2 \cos 2(\omega_m t - \phi)LN \quad (\text{A2.10})$$

Note that the small DC contribution from the 2nd harmonic term has been neglected. As have all contributions from higher harmonic terms. The interesting thing about this derivation is that it does not neglect the residual amplitude modulation (RAM) from the sinusoidal current applied to modulate the laser. The RAM contribution is captured in the terms containing ΔI .

The 1f and 2f gas signals are given by the last terms in equation A2.9 and A2.10 respectively. As expected these are proportional to the first and second derivatives of the absorption cross section, the path length and the gas concentration. In fact they are almost identical to the result obtained in equation 3.8 (derived in appendix A3.1) except they are skewed by the relative phase to the RAM signal ϕ .

Chapter 4 - Fibre Amplifier System Development

This chapter describes the development of the fibre amplifier system, beginning with an overview of the theory and modelling of an Er-Yb amplifier; before recapping the theory of Raman amplifiers and extending the model introduced in chapter 3 to include the effect of SBS. The second half of the chapter then looks at the specific design of the different parts of our amplifier (as constructed) and discusses the results obtained. This chapter is structured as follows:

- **Sections 4.1 - Erbium Doped Fibre Amplifier (EDFA)** - Describe the background, theory and modelling of erbium-ytterbium doped fibre amplifiers.
- **Sections 4.2 - Modelling CW Double Clad Er:Yb Fibre Amplifiers**
- **Sections 4.3 – Raman Amplifiers** - Describe narrow linewidth Raman fibre amplifiers including an extended model to include the effects of SBS.
- **Section 4.4 - Modelling of CW Raman Fibre Amplifiers**
- **Section 4.5 - Fibre Amplifier system for the Long Range Methane Sensor** - Describes the 1650.95nm fibre amplifier system designed and built for the TDLS methane sensor. This section is split up into three parts one for each different section of the amplifier. The performance of the amplifier is looked at in this section and compared to the models of sections 4.2 to 4.4.
- **Section 4.6 - Suitability for Methane Sensor** - Analyses the results and measurements made on the completed fibre amplifier system confirming its suitability as a source for TDLS methane sensing.
- **Section 4.7 - Summary**

4.1 Erbium Doped Fibre Amplifier (EDFA)

Erbium doped fibre amplifiers (EDFAs) were developed in the mid 1980's at Southampton University and Bell Labs [4.1, 4.2]. They were designed to produce optical gain at around 1550nm, the region of lowest attenuation in optical fibres, to enable long distance telecommunication spans without the need for electronic repeaters. Previously, neodymium doped fibres had been shown to produce gain around 1000nm. Due to their prevalence in telecommunications the theory behind EDFAs is very well understood and widely available [4.3, 4.4]. This section limits itself to a brief and qualitative overview of the theory focussing particularly on recent advances which have allowed the extension of EDFAs to high powers.

Erbium doped fibre amplifiers (EDFAs) use silica optical fibre doped with erbium as a gain medium to amplify light. The erbium ions in the fibre form a three-level lasing system that can be efficiently

pumped with a 980nm laser, producing gain in the 1550nm region. The gain bandwidth of EDFAs is large from around 1480nm to over 1600nm.

The gain efficiency of EDFAs can be very high because of the small mode area of the fibre and the long length of the amplifier. This can produce very high gains (over 40dB) in a single stage for moderate pump powers. The gain of EDFAs is usually limited not by the available pump power but by other parasitic processes, especially amplified spontaneous emission (ASE).

In an EDFA, as in any gain medium, stimulated emission is accompanied by a small amount of spontaneous emission. This spontaneous emission is not coherent with the stimulated emission and can have any wavelength under the gain spectrum of the EDFA. If it is emitted in a direction that falls within the NA of the fibre then it is guided and can go on to induce stimulated emission. This produces light with low temporal coherence (because of the broad range of wavelengths) but strong spatial coherence (because of the confinement to the fibre core). This process (and the light produced) is known as amplified spontaneous emission (ASE). ASE limits the gain which is achievable at the signal wavelength, since, at these unwanted wavelengths, it quickly depletes the population inversion available for gain at the signal wavelength.

If higher gain is required then multiple stage amplifiers are usually required. These have additional components like filters, isolators or modulators between stages to suppress ASE.

In recent years the powers of EDFAs have increased dramatically, the result of several significant technological advances, the introduction of double clad fibres and co-doping with ytterbium [4.5, 4.6]. Double clad fibres have a small (often single mode) doped inner core which guides the signal light to be amplified and a large, lower refractive index, inner cladding to guide high power multimode pump lasers, as shown in figure 4.1. This allows the use of pump sources with high power but poor beam quality which aren't compatible with standard single mode fibres.

In a double clad fibre the pump absorption is reduced, to a first approximation, by the overlap between the mode field area of the core and inner cladding. Consequently, to achieve the same pump absorption longer lengths of fibre are required for the amplifier. To counteract this effect the erbium doping concentration in the core has to be increased. The mode field diameter of the core is also made as large as possible, while still maintaining single mode propagation.

Unfortunately, the doping concentration of erbium fibres cannot be taken much beyond 1% because of concentration quenching (clustering). When the concentration of erbium ions gets too high, non-radiative losses increase substantially because the ions in close proximity interact with each other. This low doping level would make double clad amplifiers impractically long. The longer length

decreases the threshold for nonlinear effects like stimulated Raman scattering and stimulated Brillouin scattering, which ultimately limit the power achievable with a fibre amplifier.

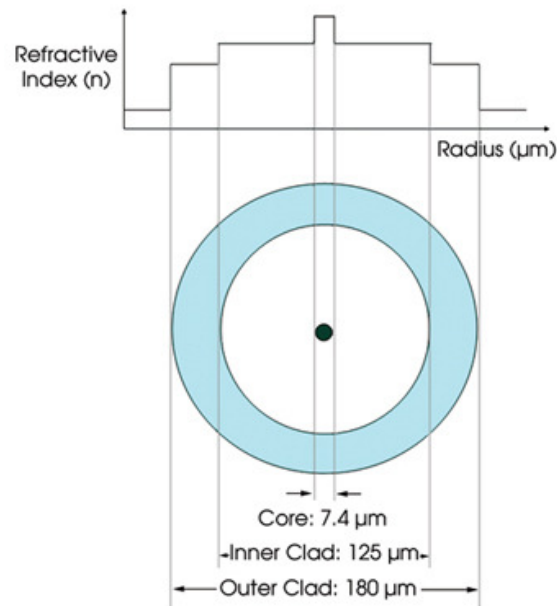


Figure 4.1: Cross section of double clad optical fibre showing refractive index profile [4.7].

Fortunately, the pump absorption can be increased substantially by co-doping the fibre with ytterbium. ytterbium has a larger absorption cross section than erbium and can be incorporated into silica fibre in much higher concentrations without clustering. Through a cross relaxation process an ytterbium ion will efficiently transfer energy to a nearby erbium ion. The excited erbium ion can then decay via stimulated emission and contribute to gain at the signal wavelength. This effectively increases the pump absorption while avoiding the problem of clustering. Co-doping also opens up a broader absorption band from around 900nm-1000nm, compared to erbium alone which can only be efficiently pumped at 980nm. This relaxes the tolerances required of pump laser source.

Using double clad Er:Yb doped fibres several groups have realised fibre amplifiers with powers greater than 100W. Jeong et. al. [4.8] developed a two stage Er:Yb amplifier with an output power of 150W. The signal was a 10mW tuneable laser (1530-1610nm) with a linewidth of 1MHz. The first stage was a commercial fibre amplifier which increased the signal power to ~1.8W. The final stage was a double clad Er:Yb amplifier with a 30μm diameter core and a 650μm diameter inner cladding. The amplifier was pumped with a 450W diode stack and amplified the signal to over 150W with negligible nonlinear effects or linewidth broadening. The 30μm core was not single mode, but still produced an almost diffraction limited output.

Bertrand Morasse et. al. [4.9] produced a 10W Er:Yb amplifier at 1550nm using a monolithic fibre design (they used all fibre or fibre coupled components). They used an Er:Yb double clad fibre with a 10 μ m core and a 130 μ m inner cladding. Their main aim was to understand how temperature affected the absorption cross section of the dopants in the fibre at different wavelengths. They reasoned that this knowledge is important for accurate modelling as the large quantum defect creates substantial temperature gradients in the fibre. They confirmed this by comparing an adapted model to the performance of the EDFA they constructed.

Carter et. al. [4.10] produced an 18W polarisation maintaining Er:Yb amplifier. Their fibre has a slightly unusual double clad structure, in that it has a section around the core with a raised refractive index which they call a pedestal. This decreases the number of modes supported by the fibre core while allowing a larger mode field diameter for the propagating single mode. This increases the threshold for nonlinear effects and ultimately the maximum power of the amplifier.

To create a Raman amplifier with an output power of greater than 1W we estimate that we will need an Er:Yb amplifier with a broad linewidth and an output power of greater than 5W (section 4.4). Er:Yb amplifiers with up to 5W output are readily available commercially [4.11, 4.12]. However, due to the ready availability parts at Gooch and Housego, Torquay, it was decided that we should design and build our own. The obvious place to start is with a model to help inform the design.

4.2 Modelling CW Double Clad Er:Yb Fibre Amplifier

The modelling of CW Er:Yb double clad fibre amplifiers and lasers is usually done using rate equations derived from the energy level transitions involved in the lasing process. A typical energy level diagram for an Er³⁺:Yb³⁺ amplifier is shown in figure 4.2 [4.12]. In this diagram level ²F_{7/2} is the ground state Yb³⁺ level and ²F_{5/2} is an excited Yb³⁺ state. K_{cr} is the cross relaxation coefficient which describes the transfer of energy from the ²F_{5/2} Yb³⁺ level to the ⁴I_{11/2} Er³⁺ level. Level ⁴I_{13/2} is the upper laser level of the system and ⁴I_{15/2} is the Er³⁺ ground state. In this model we will ignore the effects of the upconversion process in Er³⁺. We will also assume that the fast non-radiative decay between the ⁴I_{11/2} and ⁴I_{13/2} levels prevents population build up in the ⁴I_{11/2} level and back conversion to the ²F_{5/2} level.

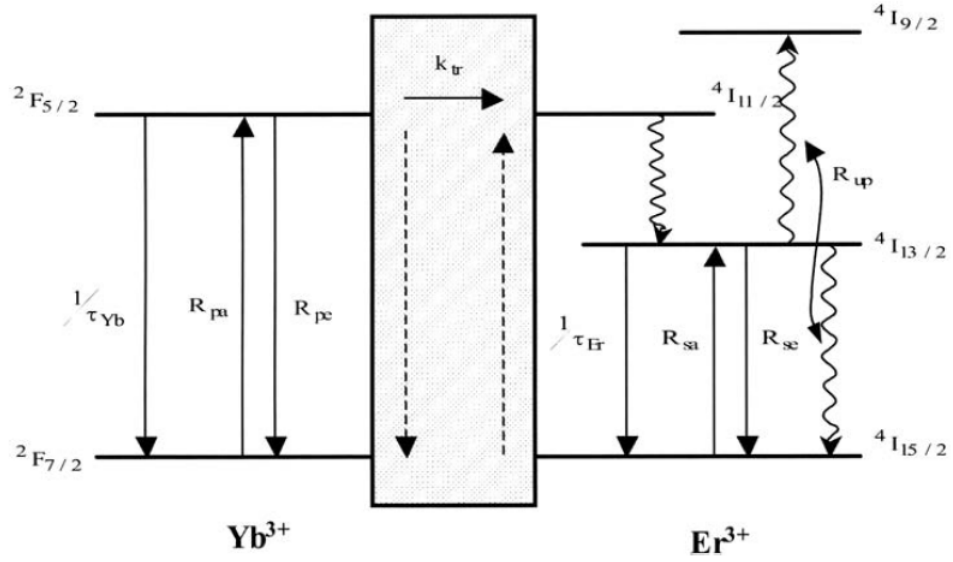


Figure 4.2: Energy level diagram of Er:Yb system showing transition paths, pumping rates and decay constants [4.12].

The rate equations for the population changes of the Yb³⁺ levels and the Er³⁺ levels are

$$\begin{aligned}
 \frac{dN_2^{Yb}}{dt} &= -\frac{dN_1^{Yb}}{dt} = R_{pa}N_1^{Yb} - R_{pe}N_2^{Yb} - \frac{N_2^{Yb}}{\tau_{Yb}} - k_{tr}N_2^{Yb}N_1^{Er} \\
 N_1^{Yb} + N_2^{Yb} &= N_{Yb} \\
 \frac{dN_2^{Er}}{dt} &= -\frac{dN_1^{Er}}{dt} = R_{sa}N_1^{Er} - R_{se}N_2^{Er} - \frac{N_2^{Er}}{\tau_{Er}} + k_{tr}N_2^{Yb}N_1^{Er} \\
 N_1^{Er} + N_2^{Er} &= N_{Er}
 \end{aligned} \tag{4.1}$$

where N_1^{Yb} and N_2^{Yb} are the populations of the $^2F_{7/2}$ and $^2F_{5/2}$ ytterbium energy levels respectively and N_1^{Er} and N_2^{Er} are the populations of the $^4I_{15/2}$ and $^4I_{13/2}$ erbium energy levels. N_{Yb} and N_{Er} are the total number of Yb³⁺ and Er³⁺ ions. The rate of transitions between levels due to pumping, stimulated emission and spontaneous emission are given by the R_{xx} values. τ_{Yb} and τ_{Er} are the radiative lifetimes of the ytterbium and erbium ion upper states.

In terms of directly measurable quantities the rate equations can be expressed as [4.13]

$$\begin{aligned}\frac{dN_2^{Yb}}{dt} &= \left(\frac{\lambda_p \Gamma_p}{hcA} \right) (\sigma_{pa} N_1^{Yb} - \sigma_{pe} N_2^{Yb}) P_p - \frac{N_2^{Yb}}{\tau_{Yb}} - k_{tr} N_2^{Yb} N_1^{Er} \\ N_1^{Yb} + N_2^{Yb} &= N_{Yb}\end{aligned}\tag{4.2}$$

$$\begin{aligned}\frac{dN_2^{Er}}{dt} &= \left(\frac{\lambda_s \Gamma_s}{hcA} \right) (\sigma_{sa} N_1^{Er} - \sigma_{se} N_2^{Er}) P_s - \frac{N_2^{Er}}{\tau_{Er}} + k_{tr} N_2^{Yb} N_1^{Er} \\ N_1^{Er} + N_2^{Er} &= N_{Er}\end{aligned}$$

Where P_p and P_s are the pump and signal powers; λ_p and λ_s are the pump and signal wavelengths; σ_{pa} and σ_{pe} are the stimulated absorption and stimulated emission cross sections at the pump wavelength and σ_{sa} and σ_{se} are the corresponding cross sections at the signal wavelength. Planck's constant is h and c is the speed of light in a vacuum. Γ_p and Γ_s is an "overlap" factor which accounts for the spatial overlap of the fibre mode in the core/cladding and the dopants in the core.

Using these equations the populations of the Er and Yb states can be calculated in the steady state CW regime. The pump and signal evolution along the fibre are given by the differential equations

$$\begin{aligned}\frac{dP_p^\pm}{dz} &= \pm \Gamma_p (\sigma_{pe} N_2^{Yb} - \sigma_{pa} N_1^{Yb}) P_p^\pm - \alpha_p P_p^\pm \\ \frac{dP_s}{dz} &= \Gamma_s (\sigma_{se} N_2^{Er} - \sigma_{sa} N_1^{Er}) P_s - \alpha_s P_s\end{aligned}\tag{4.3}$$

Where α_p is the background loss of the cladding at the pump wavelength and α_s is the background loss of the core at the signal wavelength. The \pm sign corresponds to co-propagation and counter-propagation of pump with the signal respectively.

The absorption coefficient of the fibre (which is usually given on the data sheet) for cladding absorption at the pump wavelength α_{clad} and core absorption at the signal wavelength α_{core} are approximately given by (assuming small background loss)

$$\begin{aligned}\alpha_p &\approx \Gamma_p \sigma_{pa} N_{Yb} \\ \alpha_s &\approx \Gamma_s \sigma_{sa} N_{Er}\end{aligned}\tag{4.4}$$

Model Results/Predictions

The set of equations in 4.3 and 4.4 were solved numerically for a co-propagating amplifier, using Euler's method with the boundary conditions

$$\begin{aligned} P_p(0) &= P_{pump} \\ P_s(0) &= P_{seed} \end{aligned} \quad (4.5)$$

The parameter values used are given in table 4.1. These are believed to be appropriate for the fibre that we used for the amplifier (Nufern, MM-EYDF-12/130-HE). Exact values for some of the parameters were unobtainable and so their values were chosen to be of the same magnitude as found from other sources.

| Parameter | Value | Unit |
|---------------|-----------------------|----------------------|
| λ_p | 915 | nm |
| λ_s | 1550 | nm |
| Γ_p | 5×10^{-4} | |
| Γ_s | 0.8 | |
| τ_{Yb} | 1.5×10^{-3} | s |
| τ_{Er} | 11×10^{-3} | s |
| σ_{pa} | 2×10^{-25} | m^2 |
| σ_{pe} | 5×10^{-25} | m^2 |
| σ_{sa} | 2×10^{-25} | m^2 |
| σ_{se} | 6.6×10^{-25} | m^2 |
| N_{Er} | 5×10^{19} | Ions/cm ³ |
| N_{Yb} | 5×10^{20} | Ions/cm ³ |
| A | 4.5×10^{-10} | m^2 |

Table 4.1: Parameter values used in Er-Yb amplifier model.

Figure 4.3 shows the evolution of the pump and signal in a co-propagating configuration with a pump power of 32W and a seed power of 5mW. This corresponds to our maximum available pump and seed powers.

Figure 4.4 shows the calculated signal output power versus pump power for a 10.5m length of fibre..

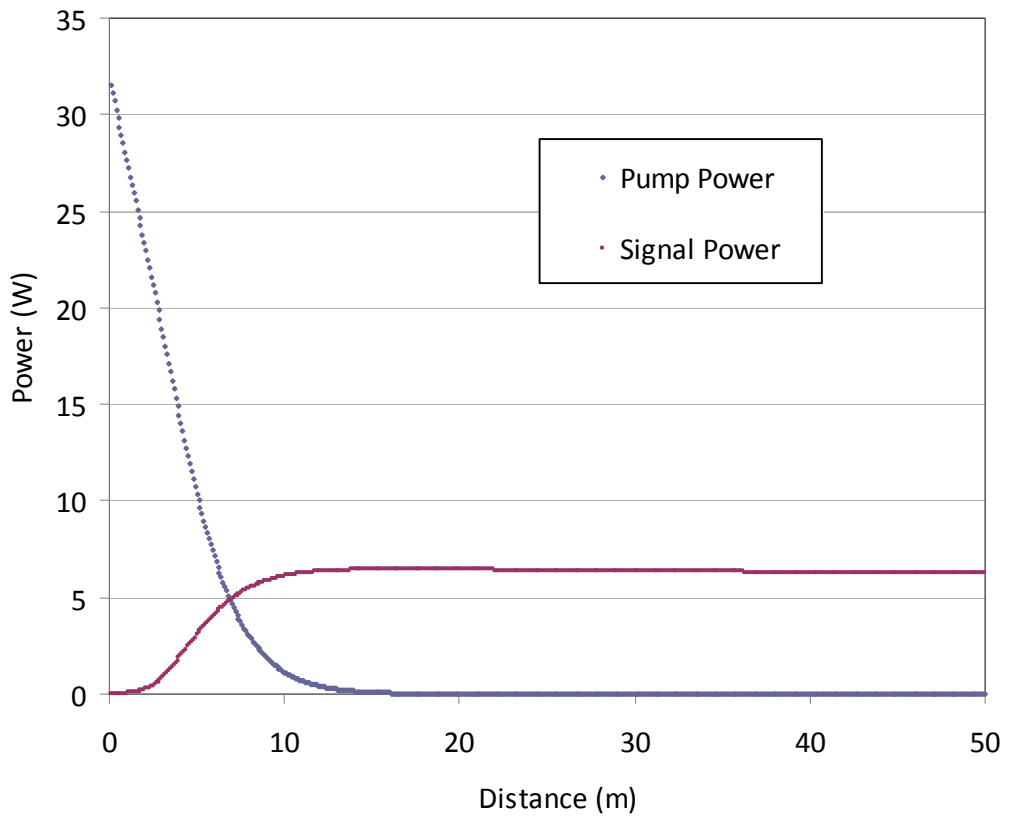


Figure 4.3: Calculated evolution of pump and signal power in fibre amplifier with 32W 980nm pump and 5mW 1550nm seed.

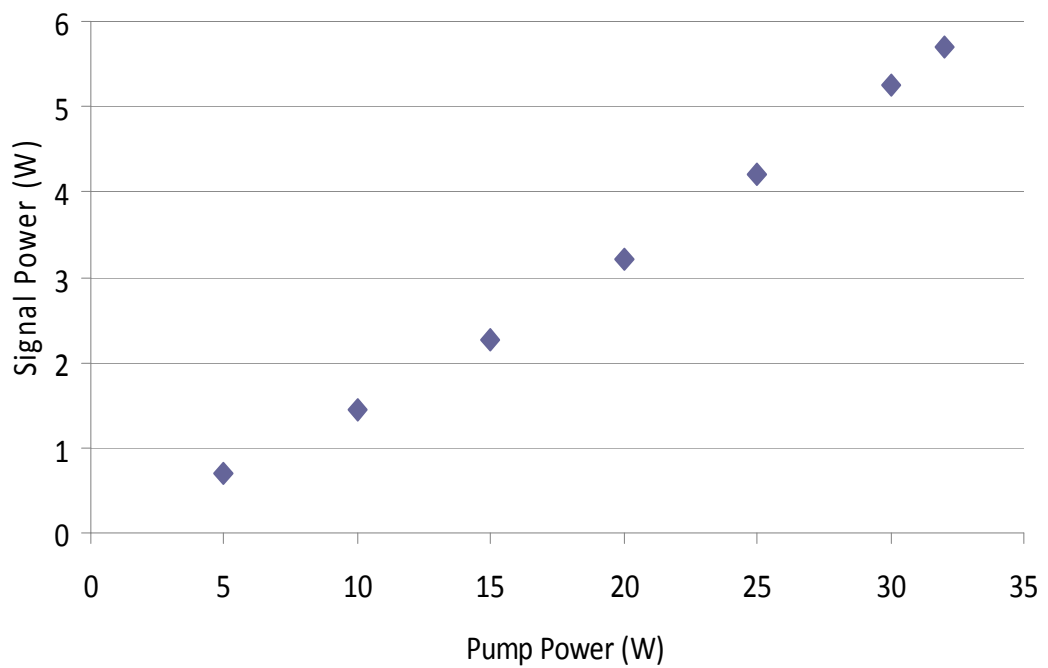


Figure 4.4: Calculated output signal power Vs pump power in a 10.5m length of ErYb fibre.

The maximum conversion efficiency from a co-propagating Er-Yb amplifier occurs near the same point where the pump power falls to zero, around 15m in figure 4.3. After this point the power in the signal only falls slowly, governed by the residual absorption of the fibre core. Thus to create an efficient Er-Yb amplifier it is sufficient to choose the fibre length just on the level of pump absorption. For fibres this is usually stated in decibels, so a fibre length with in excess of around 10dB of pump absorption should be sufficient. Making the fibre excessively long should be avoided if you would like to reach very high powers because nonlinearities increase with fibre length.

In our Raman amplifier system the Er-Yb amplifier will be used as a pump. The next section will recap the operation of a Raman amplifier and explain a more complete model applicable to our amplifier.

4.3 Raman Amplifier

To recap chapter 3, Raman amplification uses Stimulated Raman Scattering (also known as the Raman Effect) to amplify light. Raman scattering is an inelastic scattering of an incident photon by a molecule to a lower frequency photon with excess energy resonantly transferred to the molecule as a change in state. Above a certain threshold this effect becomes “stimulated” and enters a nonlinear regime where most of the incident pump photons are rapidly scattered into signal photons. This efficiently amplifies the signal light.

As long as a suitably powerful pump source with the correct wavelength is available then Raman amplification can be used to provide gain at wavelengths outside of the gain bandwidth of the usual laser dopants. The effect can also be cascaded to produce amplification at multiples of the shifted frequency. The effect is exploited in telecommunication systems to provide amplification to multiple wavelength division multiplexed channels, with the gain spectrum tailored by the choice of pump wavelengths and power. Amplification occurs for both co-propagating and counter-propagating signals.

In chapter 3 the basic model which is often used to analyse Raman amplifiers was described. This model is sufficient to describe the action of Raman amplifiers with moderate gain or large bandwidths where stimulated Brillouin scattering is not a problem. When amplifying a narrow linewidth laser to high power then it would be useful to be able to predict the amount of backscattered light due to SBS and the effect that this has on the power of the signal and pump waves. The next section will describe an extended model for a Raman amplifier which includes SBS and the Raman amplification of backscattered light.

4.4 Modelling of CW Raman Amplifier System

To model the performance of a Raman amplifier with a narrow linewidth it is necessary to consider both stimulated Raman scattering and stimulated Brillouin scattering. Another effect which seems to be overlooked in most models and discussions of Raman amplifiers is Raman amplification of the Brillouin scattered light. This effect was incorporated into a model by combining the Raman amplification and Brillouin amplification rate equations described in Chapter 3. Arriving at this final set of coupled equations

$$\begin{aligned}
 \frac{dP_S}{dz} &= \frac{g_R P_P P_S}{A} - \frac{g_B P_S P_{SBS}}{A} - \alpha_S P_S \\
 \frac{dP_P}{dz} &= \pm \frac{\lambda_S}{\lambda_P} \frac{g_R P_P P_S}{A} \pm \frac{\lambda_S}{\lambda_P} \frac{g_R P_P P_{SBS}}{A} \pm \alpha_P P_P \\
 \frac{dP_{SBS}}{dz} &= -\frac{g_B P_P P_S}{A} + \frac{g_R P_P P_{SBS}}{A} - \alpha_S P_{SBS}
 \end{aligned} \tag{4.6}$$

Equation 4.6a describes the power evolution of the Raman signal wave. The first and second terms on the right hand side of the equation correspond to the Raman gain from the pump and the loss of power which goes to pumping the Brillouin wave; the third term is the intrinsic loss of the fibre at the signal wavelength. Equation 4.6b describes the power evolution of the Pump. The first two terms of this equation correspond to the Raman gain of the Signal and Brillouin wave respectively. If the pump and signal are counter-propagating then use the upper signs in the equation; if co-propagating use the lower. Equation 4.6c describes the power evolution of the Brillouin wave. This has terms which correspond to Brillouin gain from the signal and Raman gain from the pump.

These can be solved numerically with appropriate boundary conditions. The Boundary conditions which need to be specified are the input signal power $P_S(0)$, input pump power at $P_P(0)$ or $P_P(L)$ (co-propagating and counter propagating respectively) and the input Brillouin wave power $P_{SBS}(L)$. Note that the Brillouin wave and the signal wave always propagate in different directions, since in an optical fibre Brillouin scattered light always travels in the opposite direction to the incident light. This 2-point boundary value problem is much more difficult to solve than the initial value problems usually considered for Raman amplifiers (Chapter 3). A numerical solver in Maple based around a relaxation method was used to solve these equations.

In an actual amplifier SBS builds up from noise along the length of the fibre so there is no “defined” input power for SBS to use as the boundary condition. Smith et. al [4.14] reproduced by Agrawal [4.15] in their analysis of SBS using the traditional rate equations use the power equivalent of

injecting one photon per mode into the input of the fibre. The power associated with one photon in the Raman gain bandwidth is given by [from noise figure assumptions]

$$P_{SBS} (L) \approx h \nu_{SBS} \Delta \nu_g \quad (4.7)$$

Where $\Delta \nu_g$ is the Raman gain Bandwidth of the fibre; ν_{SBS} is the frequency of the Brillouin Wave and h is Planck's constant. This is equivalent to injecting a power of approximately $1\mu\text{W}$ into the fibre to seed the SBS process.

In equations 4.6 it is assumed that the Raman gain coefficient and absorption coefficient are the same for the signal and Brillouin waves. This is valid because of the small shift between the signal and its Brillouin component. It also assumes that the Raman gain coefficient is the same regardless of direction between the pump and Raman amplified waves.

These equations ignore the effect of other losses, such as splice losses and component insertion losses in a real Raman amplifier. However, these can be accounted for ad hoc by increasing the absorption coefficient. This is only legitimate if the discrete losses are small at any one point, so that there are no large discontinuities in the power propagating in the fibre which would significantly affect gain. The model also ignores the effect of spontaneous Raman scattering and Raman ASE which could become a problem if SBS is sufficiently suppressed. These effects are difficult to model using a rate equation approach because they would need to be added in as extra equations (one for each wave) with boundary conditions which are poorly defined, like $P_{SBS}(L)$.

This model can be used to model unidirectional pumping Raman amplifiers only. If bidirectional pumping was used then separate equations for the pump propagation in the forward $P_p^+(z)$ and backward $P_p^-(z)$ directions would be required. This was recently analysed in [4.16] using the equations

$$\begin{aligned} \frac{dP_S}{dz} &= \frac{g_R P_P P_S}{A} - \alpha_S P_S - \frac{g_B P_S P_{SBS}}{A} \\ \frac{dP_P^+}{dz} &= -\frac{\lambda_S}{\lambda_p} \frac{g_R P_P^+ P_S}{A} - \alpha_S P_P^+ - \frac{\lambda_S}{\lambda_p} \frac{g_R P_P^+ P_{SBS}}{A} \\ \frac{dP_P^-}{dz} &= \frac{\lambda_S}{\lambda_p} \frac{g_R P_P^- P_S}{A} + \alpha_S P_P^- + \frac{\lambda_S}{\lambda_p} \frac{g_R P_P^- P_{SBS}}{A} \\ \frac{dP_{SBS}}{dz} &= -\frac{g_B P_P P_S}{A} - \alpha_S P_{SBS} + \frac{g_R P_P P_{SBS}}{A} \\ P_P &= P_P^- + P_P^+ \end{aligned} \quad (4.8)$$

Model Results/Predictions

The Raman model described above was solved using the parameters in table 4.2. These parameters should be approximately correct for dispersion shifted fibre (DSF). The Brillouin gain coefficient is given by Agrawal [4.15] and is appropriate to smf 28.

| Parameter | Value |
|--------------------------------------|-------------------------|
| Attenuation @ 1550nm | 0.22dB/km |
| Mode field diameter @1550nm | 8.1 μ m |
| Raman gain coefficient | 4×10^{-14} m/W |
| Effective Brillouin gain coefficient | 4×10^{-13} m/W |
| Pump wavelength | 1550nm |
| Signal Wavelength | 1651nm |

Table 4.2: Raman model parameters for SMF28

If we use a 4W Er-Yb amplifier as a pump source for the Raman amplifier and a 10mW 1651nm seed in a counter-propagating (counter-pumped) configuration then the boundary conditions for the model become

$$\begin{aligned}
 P_p(L) &= 4W \\
 P_s(0) &= 10mW \\
 P_{SBS}(L) &= 1\mu W
 \end{aligned}
 \tag{4.9}$$

where L is the length of fibre.

The evolution of the pump, signal and idler powers in a 4.5km fibre are shown in figure 4.5. As you can see the signal and pump powers develop similarly to the predictions of the earlier models. The interesting part is the backscattered power, this is not just amplified by SBS but also by SRS from the pump, in fact the contribution of Raman amplification is much larger than the contribution of Brillouin. The depletion of the pump wave by the SBS wave can be seen in figure 4.5 between 0 and 1500m where there is a small change in gradient in the pump power (red line) and an increase in the SBS power (green line). This is due to Raman amplification of the backscattered wave. In this model SBS interactions occur only between the pump and the signal wave, because the pump is assumed to have a large linewidth.

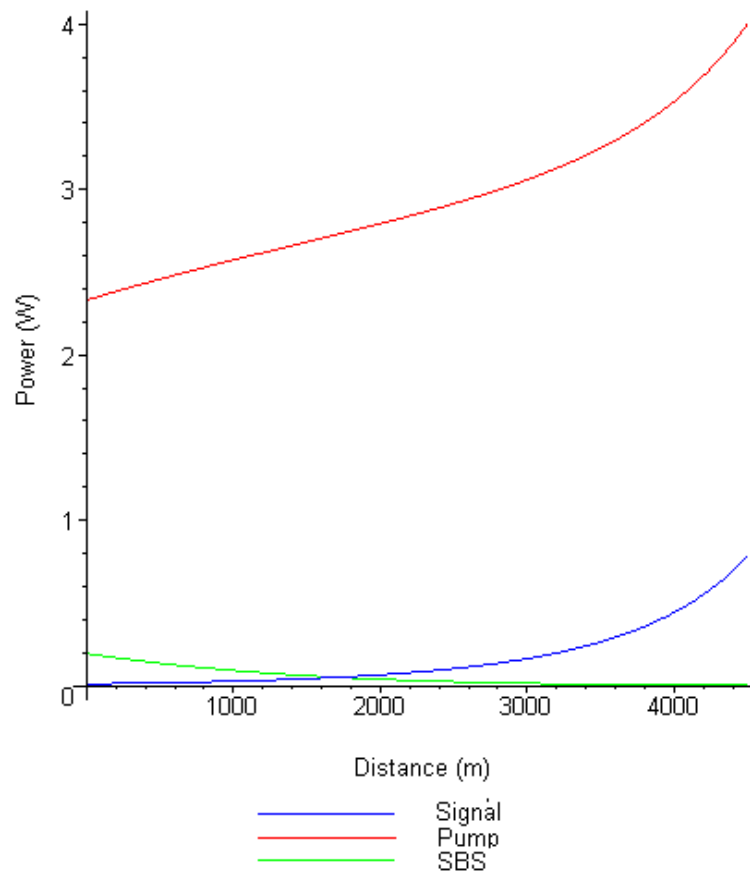


Figure 4.5: Evolution of pump (red), signal (blue) and Brillouin (green) powers in a Raman amplifier.

4.5 Fibre Amplifier system for the Long Range Methane Sensor

In this section the construction of the fibre amplifier system is described. Evaluating the results of the build to the theory and modelling presented earlier.

To ease understanding the laser source has been broken down into three parts, an amplified spontaneous emission (ASE) source; a high power EDFA and the Raman amplifier. A full schematic of the laser broken into these three parts can be seen in appendix A4.1.

The following subsections will cover each of these parts individually explaining their operation and how they link to the other sections.

- Section 4.5.1 ASE source
- Section 4.5.2 EDFA
- Section 4.5.3 Raman Amplifier

4.5.1 Amplified Spontaneous Emission Source

As explained in section 4.1 amplified spontaneous emission (ASE) is spontaneous emission which has been amplified by stimulated emission. ASE is problematic in fibre amplifiers because any spontaneous emission which is emitted within the numerical aperture of the fibre is guided through the gain medium and is amplified along with the signal light. This reduces the gain available for the signal and raises the level of background light which contributes to noise at a detector. However, applications requiring broadband optical radiation like Optical Coherence Tomography, wavelength multiplexed sensing applications and component testing can make use of ASE. ASE offers a source of broadband light with excellent spatial coherence, but poor temporal coherence. ASE sources (sometimes called superluminescent) designed for specific applications are available commercially [4.17, 4.18].

In our amplifier system an ASE source is used to produce a broadband (~20nm) input seed for the high power double clad Er-Yb amplifier (EDFA). After amplification this broadband source is used to pump the Raman amplifier. The large bandwidth is needed to prevent stimulated Brillouin scattering from becoming a problem in the Raman amplifier at the pump wavelength.

A schematic of our ASE source can be seen in figure 4.6. It consists of a 5m length of single mode erbium doped fibre (Nufern, EDFC-980-HC) which is pumped by a 20mW single mode 980nm diode laser through a 980/1550nm fused fibre wavelength division multiplexer WDM (Gooch and Housego (Torquay)). The erbium fibre emits a broad spectrum of light across its gain spectrum via spontaneous emission. This is then amplified by stimulated emission to produce ASE. The 980/1550nm WDM between the pump laser and erbium fibre prevents the ASE travelling back toward the pump diode (where it may cause problems). The 1550nm arm of the WDM has a straight cleave so that ~4% of the ASE travelling in this direction was reflected back through the erbium fibre where it can cause further stimulated emission in the forward direction and contribute to the output. A coarse wavelength division multiplexing (CWDM) filter with a centre wavelength around 1550nm and a pass band of almost 20nm was used to shape the spectrum for input into the EDFA so that it is ideally suited for Raman amplification later.

A 1% 1550nm tap was used to monitor the output power of the ASE source. During testing (before connecting the ASE source to the EDFA) the output arm of the 1% tap was angle cleaved to prevent back reflections. Back reflections from this end would have formed a cavity which could have resulted in spurious lasing at much lower output powers. In-line fibre isolators were incorporated into the design later to prevent feedback from the high power EDFA. It should be noted that except for the erbium fibre all other fibre was Corning SMF 28e.

The output power of the ASE source with pump power and the optical-to-optical conversion efficiency is shown in figure 4.7. The maximum output power is just over 5mW and is limited by the available pump power. Figure 4.8 shows the spectrum of the ASE seed at full output power.

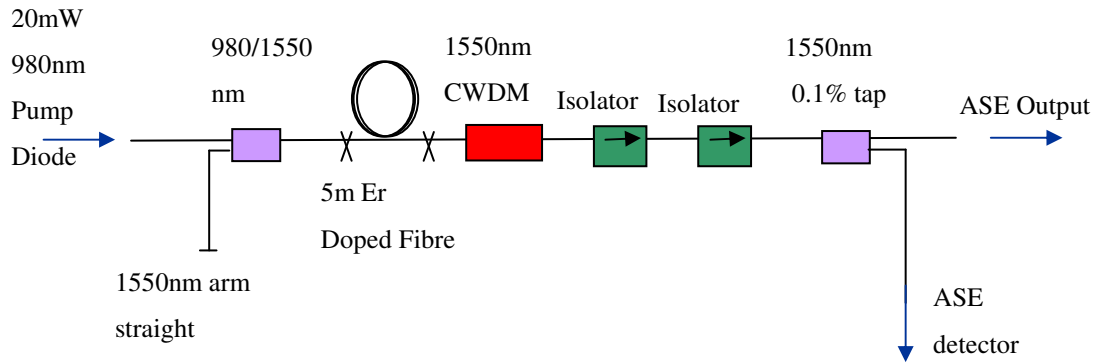


Figure 4.6: ASE seed schematic.

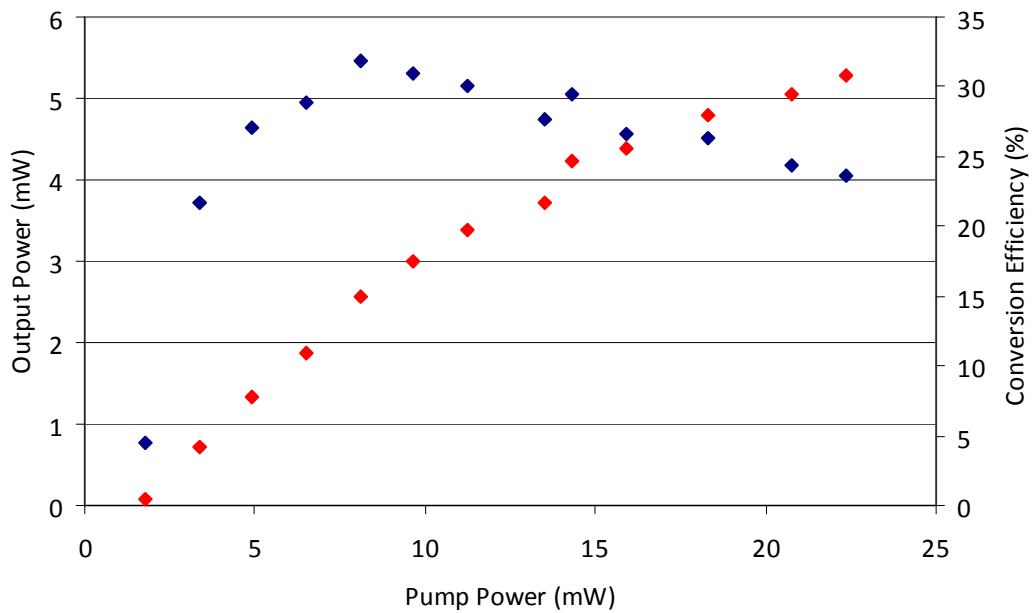


Figure 4.7: Pump-Output characteristics (red) and conversion efficiency (blue) of ASE seed.

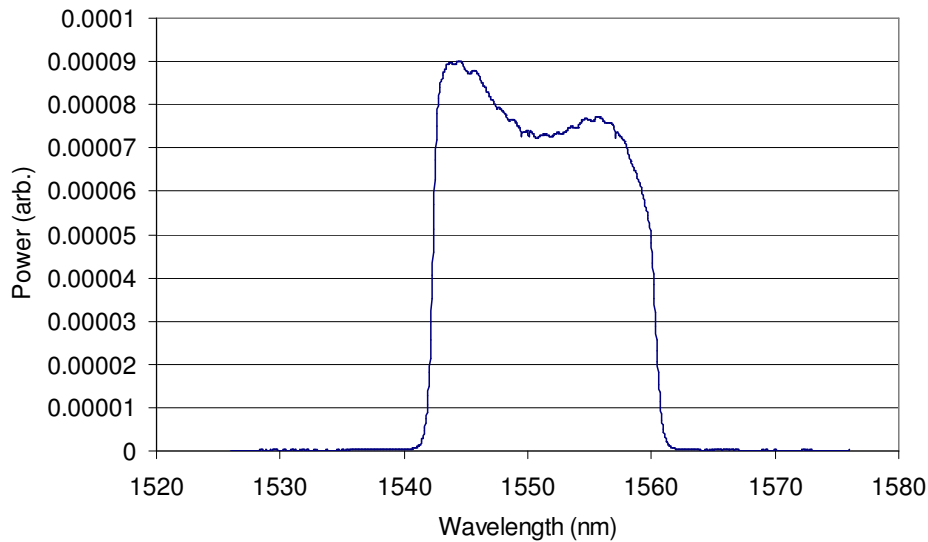


Figure 4.8: ASE seed spectrum at 5mW output power.

4.5.2 High Power Erbium-Ytterbium Fibre Amplifier

The next section of our amplifier system is the erbium-ytterbium double clad fibre amplifier. This takes the broadband seed signal from the ASE source and amplifies it to a high power. This is used as the pump for the final stage 1651nm Raman amplifier.

A schematic of the erbium-ytterbium amplifier can be seen in figure 4.9. The ASE output is spliced into a 6+1x1 pump combiner with signal feed through (Gooch and Housego (Torquay)). This combiner has 7 input fibres, 6 multimode inputs with 105/125 μm 0.22NA fibre and one single-mode signal fibre (SMF28e). The output fibre of the combiner is a single-mode double clad fibre (DCF). This combiner allows the ASE seed signal to pass through into the single-mode core of the DCF and couples the pump diode light from the six multimode inputs into the inner cladding of the DCF. Pump light for our Er-Yb amplifier is provided by four 8.5W 915nm diodes (JDSU, L3 series) with 105/125 μm 0.22NA fibre.

The DCF output of the combiner is then spliced to a 10.5m length of double clad ErYb doped fibre (Nufern, MM-EYDF-12/130-HE). This fibre has a 12 μm core which is few-moded at 1550nm and a 130 μm cladding to guide the pump light. The larger core of this fibre increases the overlap between the dopants in the core and the pump light in the cladding, this increases the absorption efficiency of the fibre so that a shorter length of fibre can be used in the amplifier. The downside is that the loss at the splice between the ErYb DCF and the single-mode SMF28e afterwards is increased because higher order modes are stripped out.

A 5W inline fibre isolator (OFR, IO-K-1064) after the ErYb DCF stops back reflected light from entering the gain fibre. In a fibre system back reflected light can arise from many sources including Fresnel reflection from the silica-air interface at the output of a cleaved fibre; reflection from a refractive index variation at a splice between fibres; Rayleigh backscatter, spontaneous emission and ASE in a doped fibre, Brillouin scattering and Raman scattering. Back reflected light interferes with the operation of an amplifier in several ways,

If the frequency of light is within the gain bandwidth of the amplifier then it will be amplified. This creates ASE and increases the noise in the system. If the intensity of backscattered light is high enough then it will deplete the population inversion in the amplifier available for signal gain. It can also cause instability in the seed laser which operates at a much lower power than the amplifier and is sensitive to back reflected light. In the extreme case amplified light can reach a level where it causes damage to the pump and seed sources.

A 1550nm 0.1% tap is spliced onto the output of the ErYb amplifier for power monitoring. The pump power characteristics of the erbium ytterbium amplifier can be seen in figure 4.10. The maximum output power of the amplifier was around 6W and this was limited by the available pump power. The optical-to-optical conversion efficiency at full output was around 18%.

The spectrum of the EDFA at 5W output is shown in figure 4.11. The spectrum of the EDFA operating at full power matches the ASE seed spectra (figure 4.8) quite well. The increase in the peak height at 1545nm is thought to be the result of a combination of things including the spectral gain variation of the Er-Yb doped fibre or an artefact of the wavelength variation of the monitoring 0.1% tap.

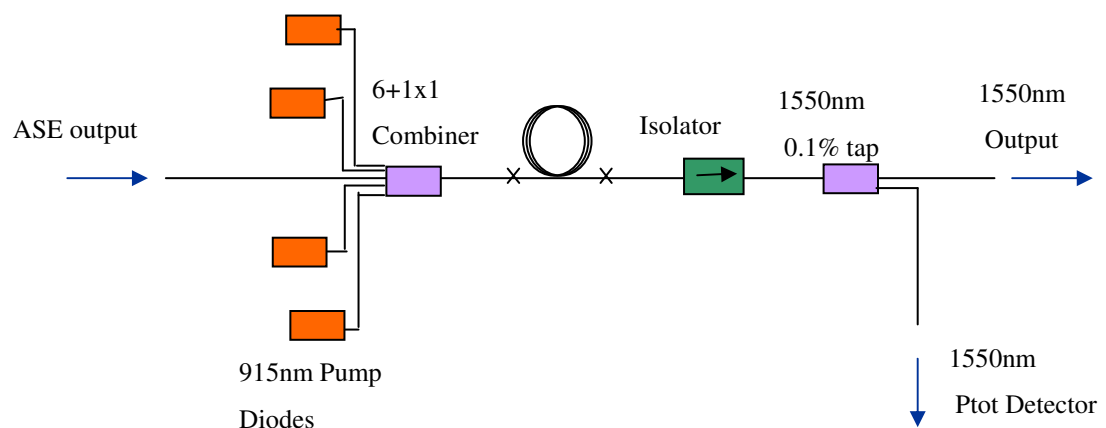


Figure 4.9: Schematic of high power EDFA.

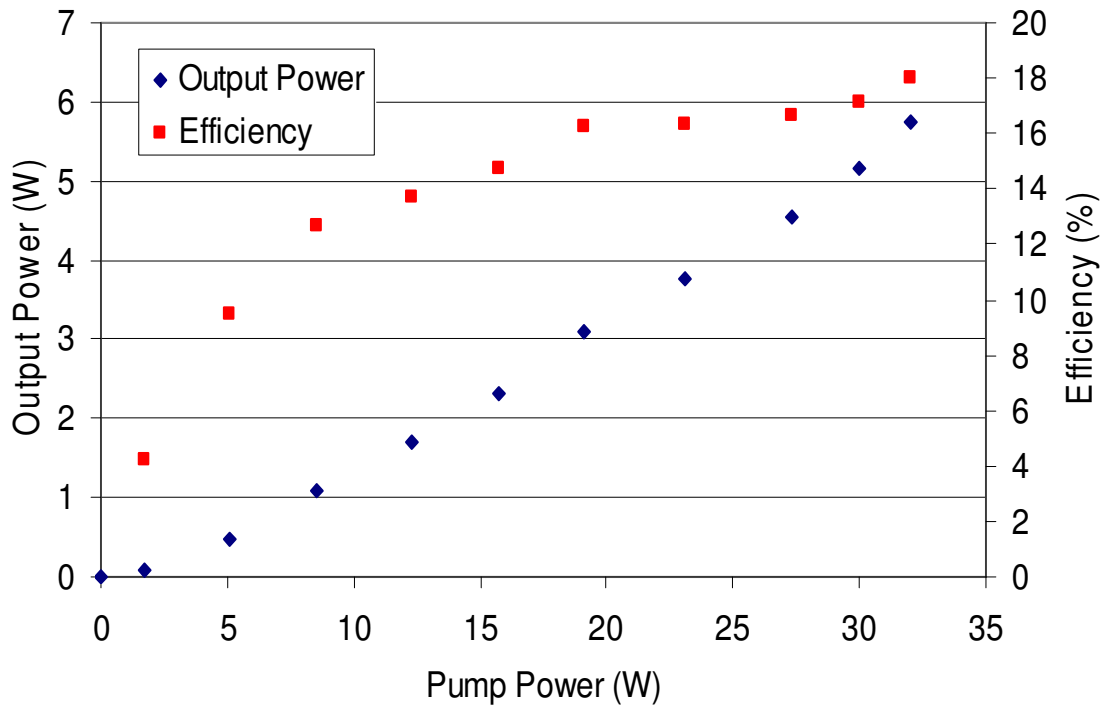


Figure 4.10: Pump power Vs output power characteristics of EDFA and optical conversion efficiency.

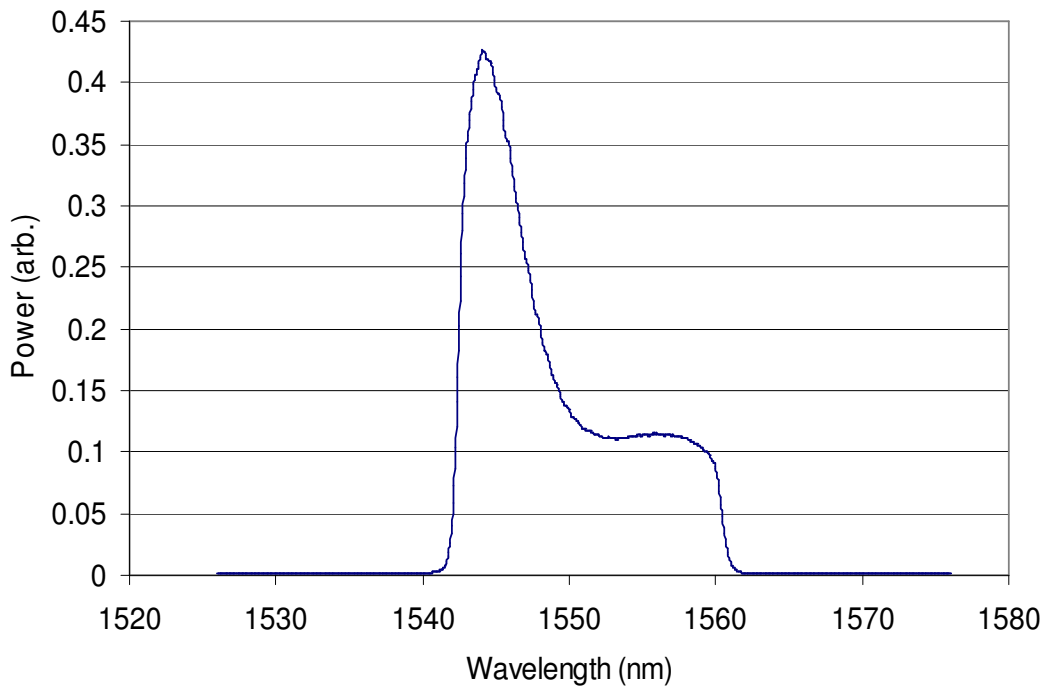


Figure 4.11: Spectrum of EDFA at 5W output power.

4.5.3 Counter Propagating Raman Fibre Amplifier

The final section of the system is a counter-propagating Raman fibre amplifier. This amplifies the output of our narrow linewidth 1651nm DFB laser to be used for gas sensing. In a counter-propagating amplifier the signal light travels in the opposite direction to the pump light. This decreases the efficiency of amplification, compared to the co-propagating configuration, but increases the noise performance because transfer of relative intensity noise (RIN) from the pump laser to the signal is smaller. It is also believed that a counter-propagating amplifier can have a higher ultimate output power than a co-propagating amplifier because the effect of Raman amplification between the pump and backscattered wave is smaller. Results of the amplifier in a co-propagating configuration are shown in section 4.5.4.

Figure 4.12 shows the layout of the counter-propagating Raman amplifier. The 1550nm pump from the EDFA is spliced into the 1550nm carrying arm of a 1550/1650nm WDM. The 1550/1650nm common output of the WDM is then spliced onto a 4.5km length of dispersion shifted fibre (DSF) (Sumitomo). The DSF is where the Raman amplification takes place. Dispersion shifted fibre has a higher Raman gain coefficient at 1650nm than smf28e. This is because the fibre is doped with Germanium to shift the zero dispersion wavelength. It also has a smaller core size and mode field diameter which also enhances Raman gain. The length of dispersion shifted fibre was chosen to optimise Raman conversion for our pump and input signal powers as shown in sections 3.8 and 4.4. This length was calculated initially from modelling and then optimised empirically through measurements made by David Mitchell at Strathclyde University.

The residual pump then passes through another 1550/1650nm WDM and exits through the 1550nm arm. A 0.1% tap monitors the power of the residual pump; the rest is absorbed in a beam dump. The measurement of residual pump is a useful indicator that the Raman amplifier is operating correctly. In a counterpropagating Raman amplifier the absorption of pump and signal are both very small and complete conversion from the pump to the signal is not possible.

The 1651nm signal enters the Raman amplifier through the 1650nm arm of the second WDM. Along this arm is an inline isolator to stop back reflected light from entering the seed diode and a 0.1% tap. The 0.1% tap is orientated to detect light travelling towards the 1650nm seed diode. The purpose of this tap is to detect stimulated Brillouin scattering. After the WDM the signal travels through the 4.5km DSF fibre in the opposite direction to the pump and is amplified. The second WDM demultiplexes the signal and pump. The amplified signal passes through a 0.1% tap to monitor the power and exits the amplifier as a free space beam ready to be used for remote methane sensing.

The 1651nm seed signal is from a 10mW distributed feedback (DFB) diode laser. As mentioned earlier DFB lasers are ideal for tuneable diode laser absorption spectroscopy because they have

narrow linewidths (~10-100MHz), compared to absorption linewidths (several GHz), and their wavelength can be rapidly dithered and tuned via their injection current over a range of about $\pm 2\text{nm}$ from their central wavelength.

The DFB is connected via a bias-T to a function generator which can apply a dither of between 0 and 100mA pk-pk from 1kHz to 1MHz. The dither is necessary to suppress SBS at the 1650nm wavelength because of the narrow line width of the DFB laser. The dither suppresses SBS by introducing a range of frequencies into the fibre. This artificially broadens the linewidth of the laser by the range of frequencies propagating within the fibre at any instantaneous time. For optimum SBS suppression the dither frequency should be chosen so that a full modulation cycle (and hence all spectral components) fit within the optical fibre at the same time. This will depend upon the effective length of the fibre and the speed of light in the material (c/n). The minimum dither frequency f is given by [4.19]

$$f = \frac{c}{2nL_{eff}} \quad (4.10)$$

To optimally suppress SBS the dither depth should be as large as possible and the limit is set by the frequency response of the DFB. However, for TDLS the dither depth is chosen to maximise the second harmonic signal produced during absorption.

The output power characteristics of the Raman amplifier can be seen in figure 4.13. The maximum output power is just under 2W at full pump power. The efficiency of the Raman process increases rapidly at higher pump powers reaching over 30% at full power. The output power fits well with the predictions of the model presented in section 4.4 with the parameters in table 4.2 for the DSF fibre. The Brillouin gain coefficient was reduced to reflect the fact that the effective bandwidth seen in the fibre is much larger than the instantaneous bandwidth (equation 3.31).

The backscattered power versus pump power can be seen in figure 4.13. The backscattered power increases rapidly with increasing power, at 2W output power the SBS power is almost 20mW (1% of the Raman amplifier power).

| Parameter | Value |
|--------------------------------------|--------------------------|
| Raman gain coefficient (g_R) | $1.8e^{-14} \text{ m/W}$ |
| Effective Brillouin gain coefficient | $1E^{-13} \text{ m/W}$ |
| Absorption at 1650nm | 0.3dB/km |
| Absorption at 1550nm | 0.2dB/km |

Table 4.2: Parameters of DSF fibre.

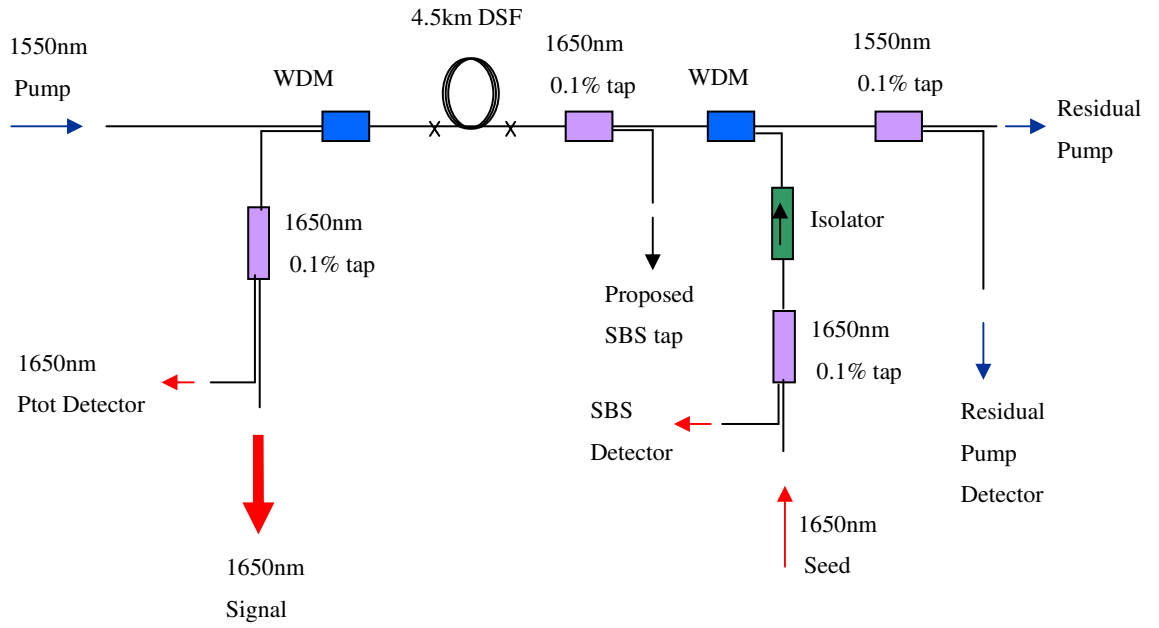


Figure 4.12: Counter-propagating Raman Amplifier.

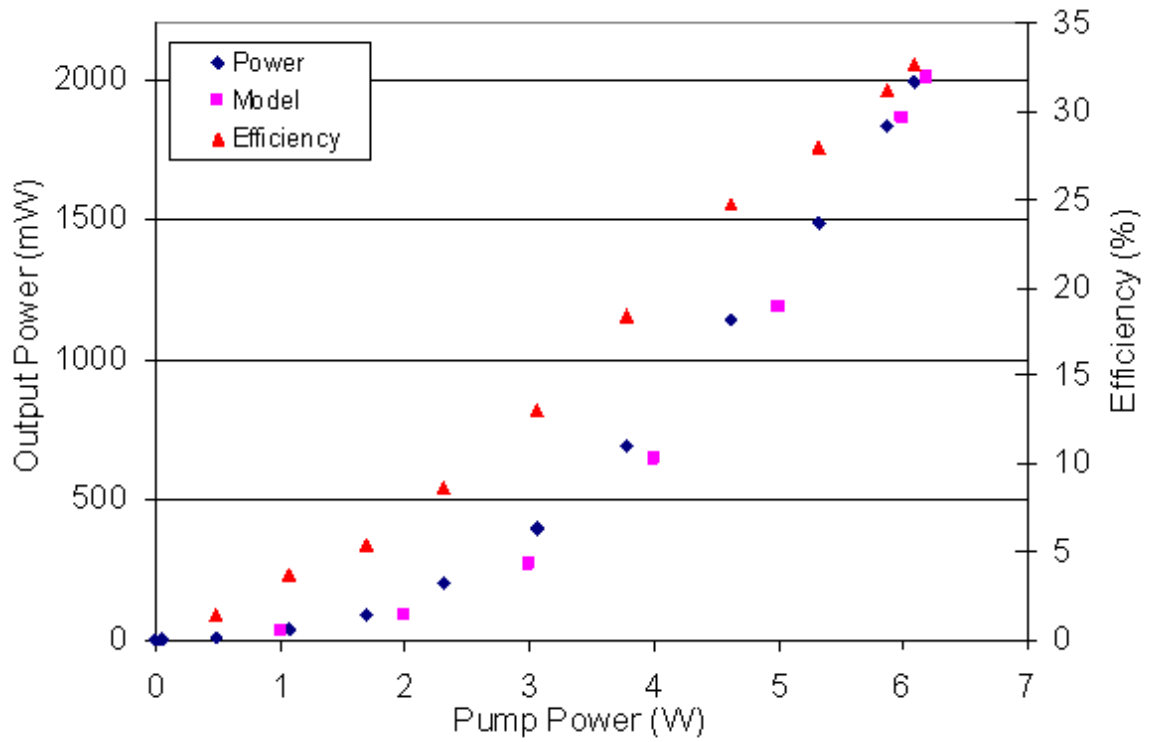


Figure 4.13: Output Power Vs Pump power of Raman amplifier.

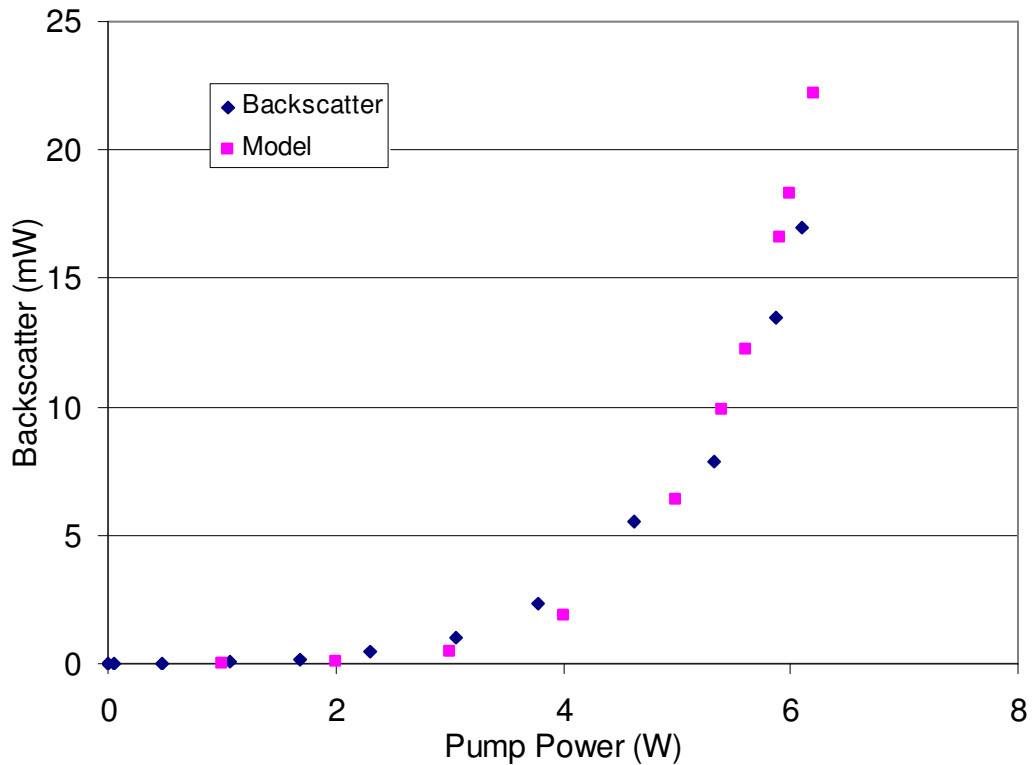


Figure 4.14: Backscattered power

4.5.4 Co-propagating Raman Amplifier

The Raman amplifier was also tested in a co-propagating configuration with the pump and seed injected from the same side of the DSF fibre. To achieve this, the system layout was modified as shown in figure 4.15.

The output power characteristics of the co-propagating Raman amplifier are shown in figure 4.16. These results show that Raman conversion is much more efficient in a co-propagating amplifier, with output powers reaching 2.5W for our 6W pump (c. f. ~2W for counter-propagation). The reduction in the rate of signal growth and efficiency seen after around 1.8W output power is because of the increase in backscatter power shown in figure 4.17.

In a co-propagating amplifier the Raman amplification of Brillouin backscattered light is much stronger than in a counter-propagating amplifier. This is because the backscattered light and pump light are both highest at the input end of the fibre through where the SBS exits. At 2W output the backscattered power in the co-propagating amplifier is around 40mW compared to 20mW for the counter-propagating Raman amplifier at the same output power. This shows that the threshold power

for SBS is lower in a co-propagating amplifier than a counter-propagating amplifier. Potentially this could affect the ability of the fibre amplifier to track wavelength changes in the input signal.

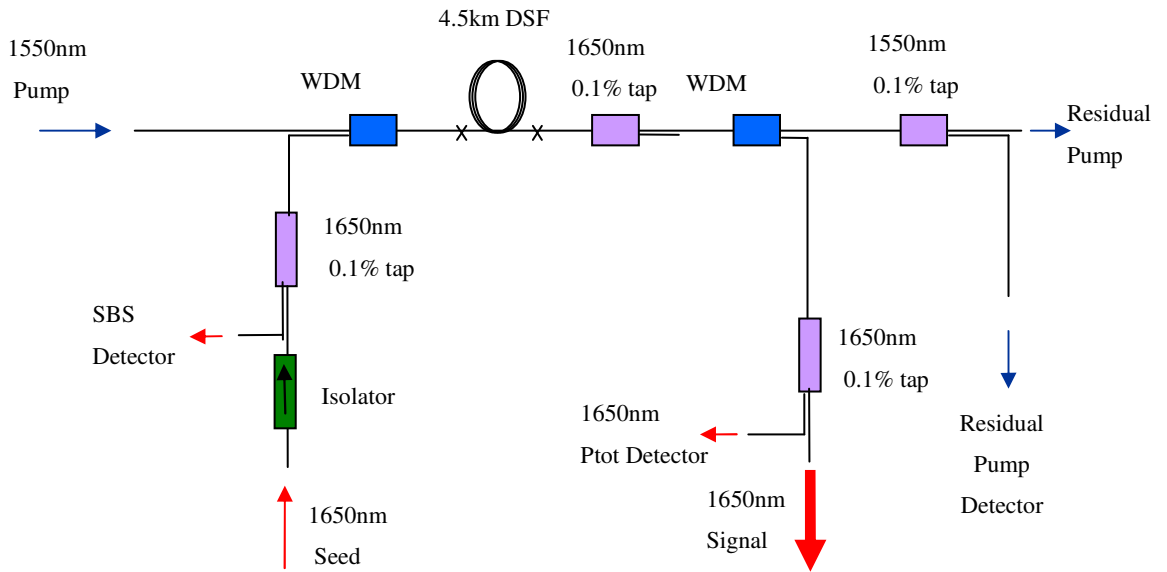


Figure 4.15: Co-propagating Raman Amplifier.

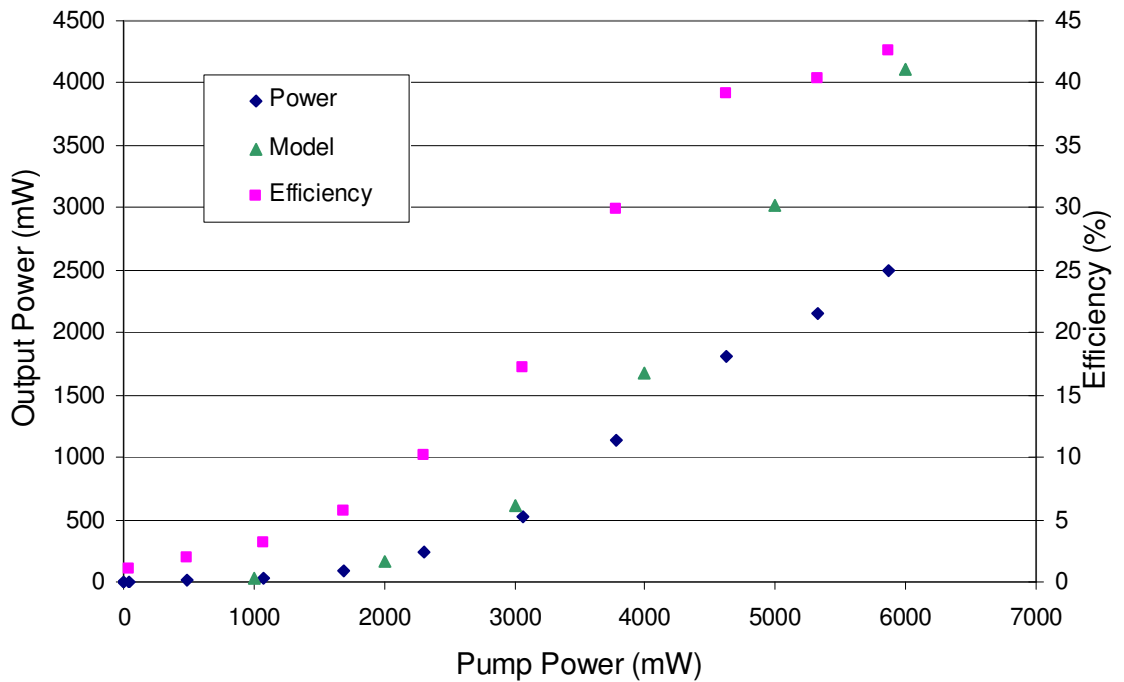


Figure 4.16: Output power characteristics of co-propagating Raman amplifier.

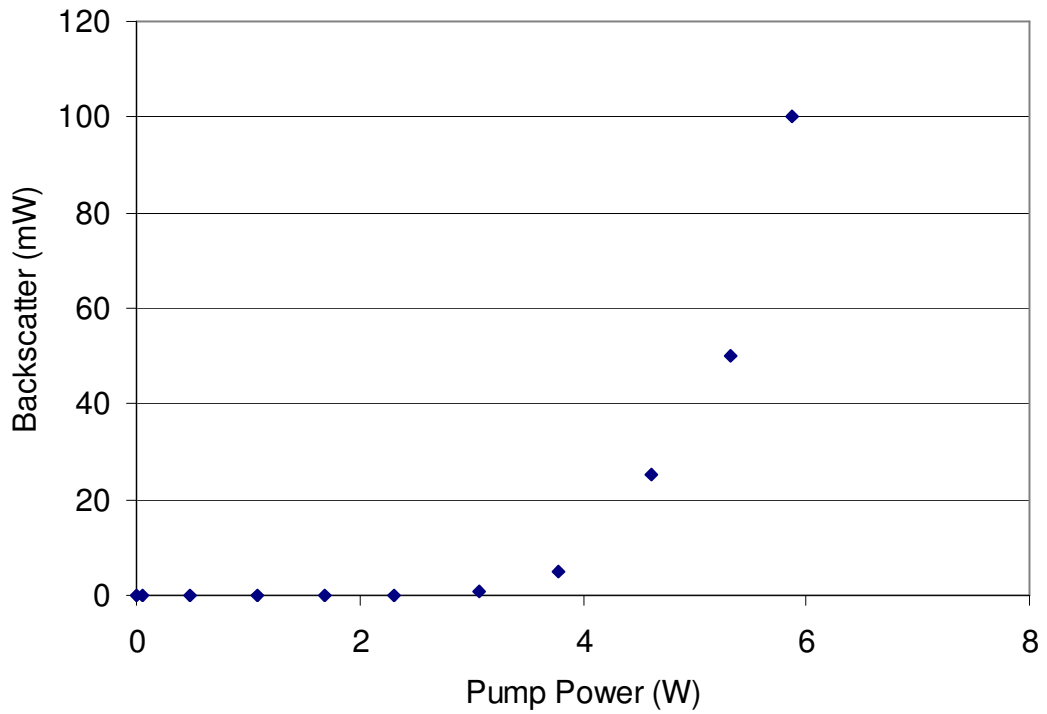


Figure 4.17: 1650nm backscattered power in Raman amplifier.

4.6 Suitability for Methane Sensor – Testing of complete system

The modulation frequency and modulation depth of the DFB laser being amplified has a massive effect on the onset of SBS in the Raman amplifier, because they affect the effective linewidth of the laser source as seen by the amplifier fibre. They also have an effect on the sensitivity of TDLS. As mentioned in section 3.1.2 the optimum modulation depth for the traditional TDLS method is around $m=2.2$.

If the modulation frequency or modulation depth is decreased sufficiently then the suppression of SBS is ineffective. At this point SBS kicks in and distorts the amplitude modulation of the output power. The effect of changing the dither frequency and dither depth of the DFB laser can be seen in figures 4.18 and 4.19. From the work of Fishman [4.19], the optimum frequency for SBS suppression is given by

$$f = \frac{c}{2nL_{eff}} \quad (4.11)$$

Where

$$L_{eff} = \frac{1 - e^{-\alpha_s L}}{\alpha_s} \quad (4.12)$$

If α_s is 0.002m^{-1} and the length of our fibre is 4500m then the optimum dither frequency for SBS suppression should be around 33kHz . This point is clearly visible in figure 4.18 and proves the efficacy of this method of SBS suppression.

Altering the depth of the modulation dither changes the effective linewidth of the source. To a good approximation the linewidth increases linearly with dither depth in the linear region of laser power-wavelength-current response. At higher modulation frequencies and depths this generality breaks down as the laser cannot respond to changes in its operating current quickly enough. As shown in figure 4.19 the backscattered SBS power decreases significantly with dither depth/laser linewidth as predicted by the theory, equation 3.31.

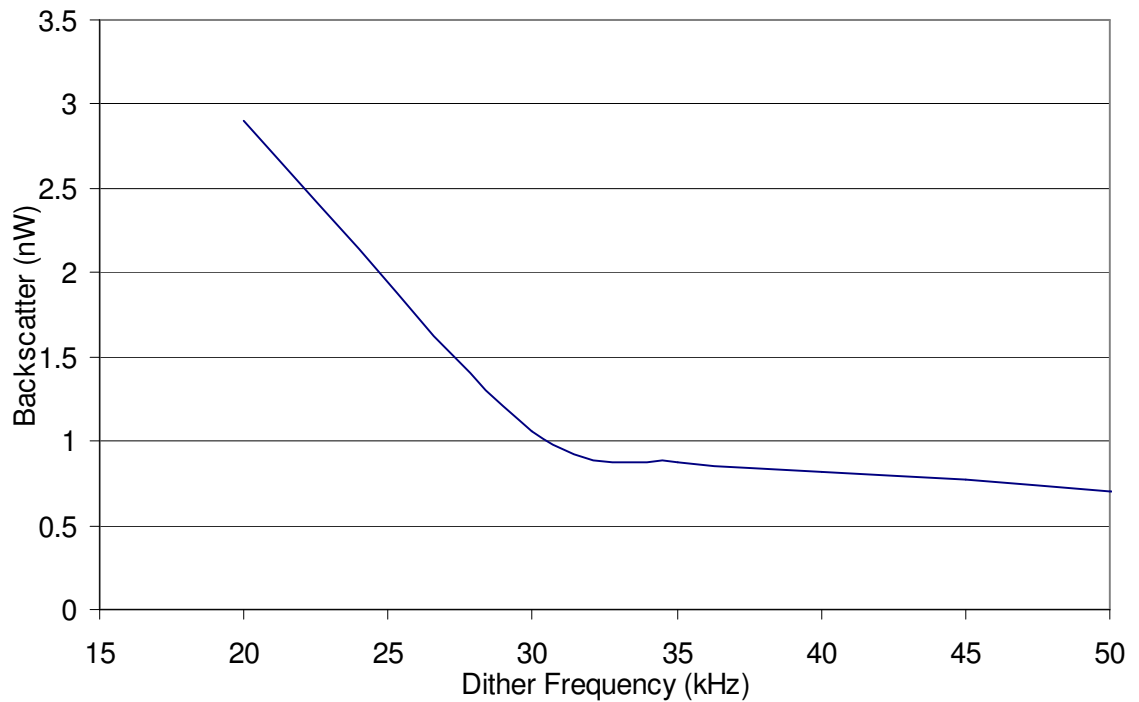


Figure 4.18: Backscatter vs. dither Frequency. Dither 50mA pk-pk.

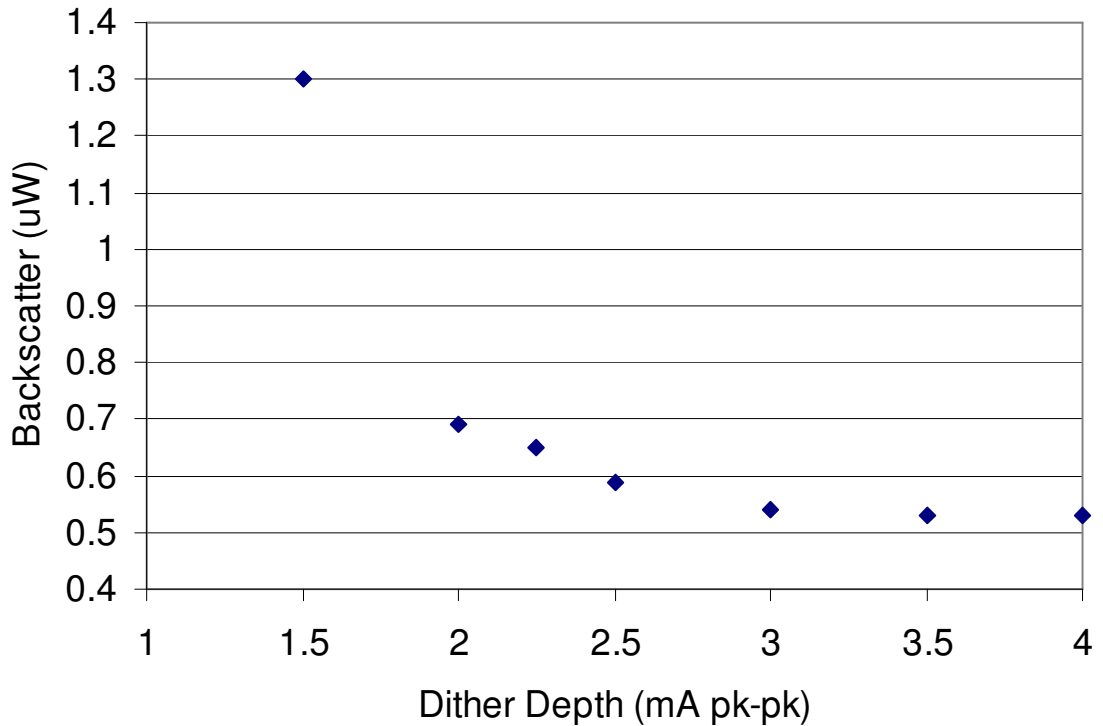


Figure 4.19: Backscatter vs. dither depth.

To be useful for tuneable diode laser spectroscopy it is also important that the laser source can be swept without distortion from the fibre amplifier. In section 3.2.2 a system was described that used an EDFA to amplify a DFB laser for methane sensing [4.19]. They found that the temporal dynamics of the gain in the EDFA distorted the modulation applied to the laser for wavelength modulation spectroscopy.

The power of the amplified laser beam from our Raman amplifier was measured in the time domain and as expected, from the almost instantaneous emission of Raman amplifiers, showed no distortion at low powers. At high powers, greater than 1.2W, a slight distortion was seen in the output modulation of the amplifier, shown in figure 4.20. This was measured by David Mitchell and Kevin Duffin at Strathclyde University and was found to be attributable to multipath interference in the Raman amplifier.

By tightly controlling splice loss and other possible sources of reflection within the fibre amplifier it was found that the threshold power for this effect could be increased. At the extremes the onset power of this effect is probably limited by Rayleigh backscatter from impurities in the fibre, a process known as double Rayleigh scattering (DRS). It was found during investigation by David Mitchell and Kevin Duffin that the effect could be reduced by increasing the dither depth (or modulation amplitude). This

is believed to be because it changes the temporal coherence between the forward propagating and the backscattered beams which take a different path through the amplifier system.

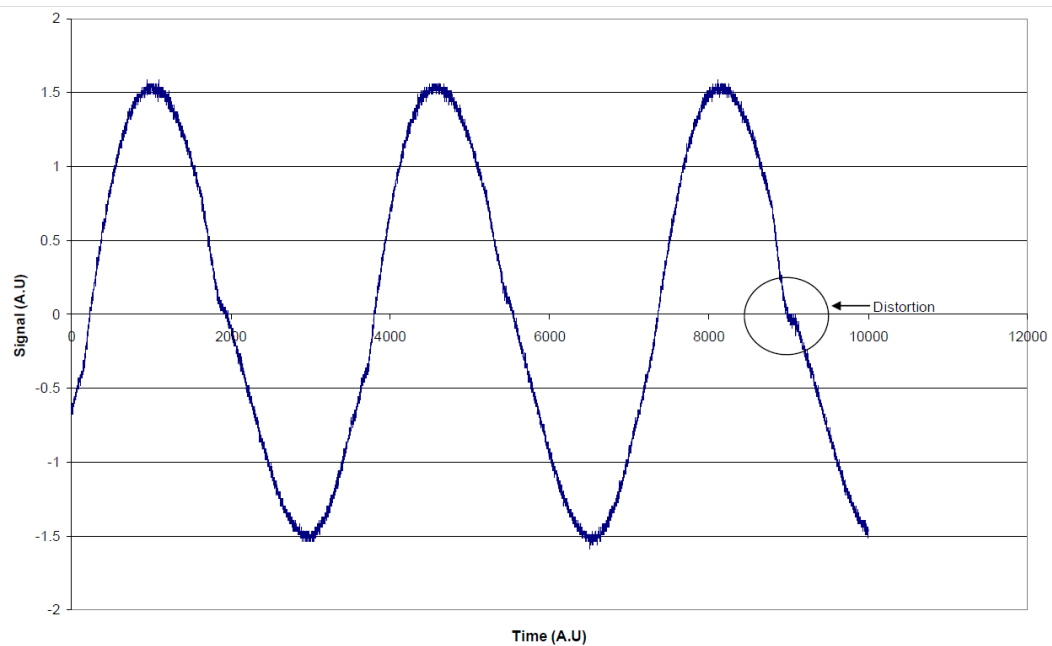


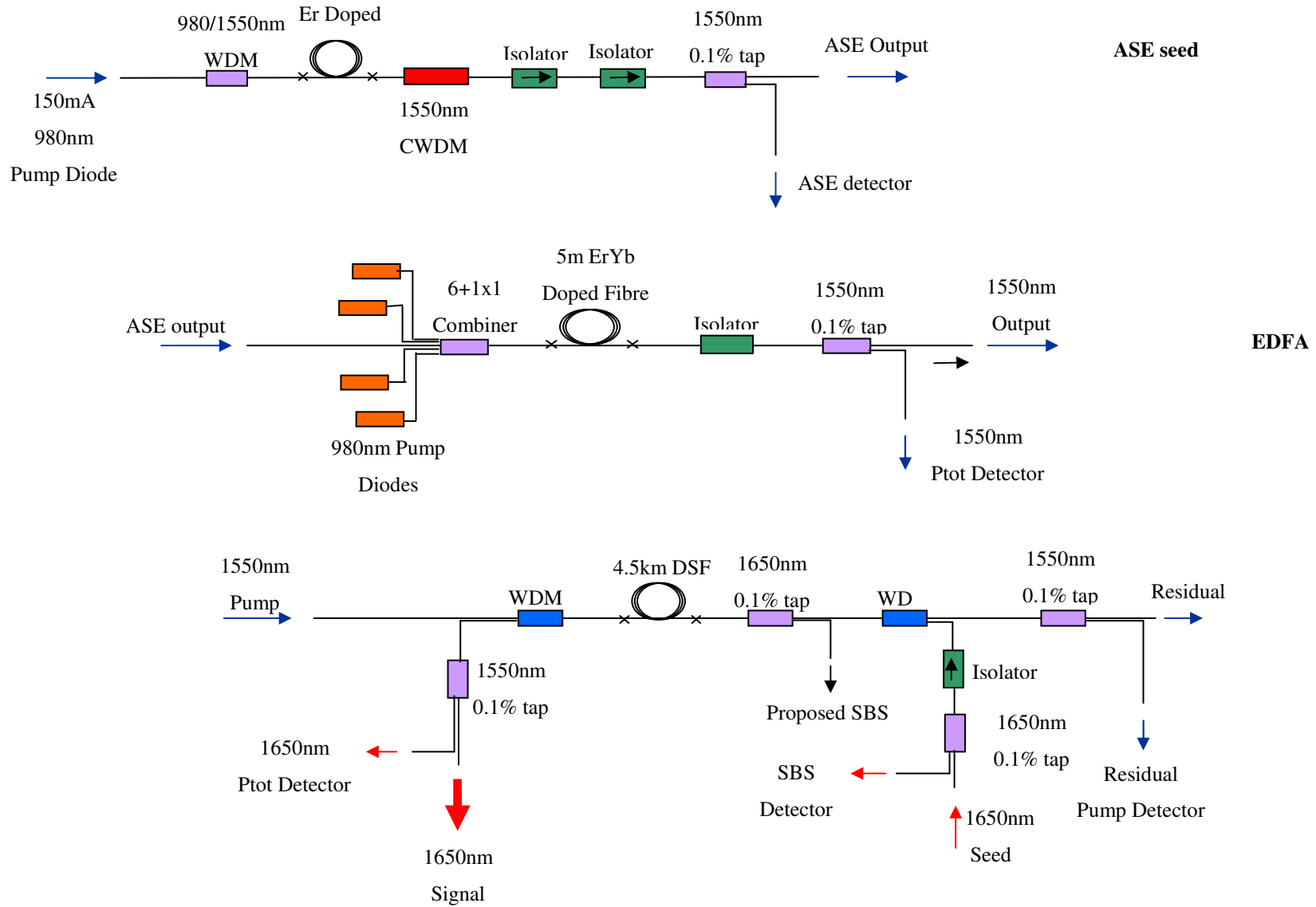
Figure 4.20: Distortion to output waveform due to stimulated Brillouin scattering.

References

- [4.1] R.J. Mears, L. Reekie, I.M. Jauncey and D. N. Payne, "Low-noise Erbium-doped fiber amplifier at 1.54 μm ," *Electron. Lett.*, 1987, Vol. 23, pp.1026–1028
- [4.2] E. Desurvire, J. Simpson, and P.C. Becker, "High-gain erbium-doped traveling-wave fiber amplifier," *Optics Letters*, 1987, Vol. 12, No. 11, pp. 888–890
- [4.3] Emmanuel Desurvire, "Erbium-doped fiber amplifiers: principles and applications," Wiley-Interscience, 2002
- [4.4] M. Digonnet, "Rare-Earth-Doped Fiber Lasers and Amplifiers," CRC Press, 2001
- [4.5] E.Snitzer, H.Po, F.Hakimi, R.Tumminelli and B.C.McCollum, "Double-clad offset core Nd fiber laser," *Proc. Of Optical Fiber Sensors*, 1988, New Orleans
- [4.6] M. E. Fermann *et al.*, "Efficient operation of an Yb-sensitised Er fiber laser at 1.56 μm ", *Electron. Lett.*, 1988, M. E. Fermann *et al.*, "Efficient operation of an Yb-sensitised Er fiber laser at 1.56 μm ," *Electron. Lett.* 24, 1988, Vol. 24, pp. 1135
- [4.7] Hank Hogan, "A single optical probe does double duty," <http://www.photonics.com/Article.aspx?AID=32723>, Retrieved 03/06/2011

- [4.8] Y. Jeong, J. K. Sahu, D. B. S. Soh, C. A. Codemard, and J. Nilsson "Tunable single-frequency ytterbium-sensitized erbium-doped fiber MOPA source with 150 W (51.8 dBm) of output power at 1563 nm," OFCNFOEC Technical Digest Optical Fiber Communication Conference, 2005
- [4.9] B. Morasse, S. Agger, C. Hovington, S. Chatigny, E. Gagnon, J. de Sandro, and C. Poulsen, "10W ASE-free single-mode high-power double-cladding Er³⁺-Yb³⁺ amplifier," Proc. SPIE, 2007
- [4.10] A. Carter, J. Farroni, K. Tankala, B. Samson, D. Machewirth, N. Jacobson, W. Torruellas, Y. Chen, M. Cheng, A. Galvanauskas, and A. Sanchez, "Robustly Single-Mode Polarization Maintaining Er/Yb Co-Doped LMA Fiber for High Power Applications," in Conference on Lasers and Electro-Optics/Quantum Electronics and Laser Science Conference and Photonic Applications Systems Technologies, OSA Technical Digest Series (CD) (Optical Society of America, 2007), paper CTuS6.
- [4.11] IPG "EAR SF Series: 1-100W C & L Band Single Frequency Erbium Fiber Amplifier Laser" Online: EDFA http://www.ipgphotonics.com/products_15_micron_amplifiers_single_ear_sf_series.htm, Retrieved 04/06/2011
- [4.12] Yves JAOUEN, Sylvain BORDAIS, Elena OLMEDO, Gabor KULCSAR, Jean-Yves ALLAIN, "High power cladding-pumped Er³⁺/Yb³⁺ fiber amplifiers: technologies, performances and impact of nonlinear effects," Ann. Telecomm., 2003, 58, n° 11-12
- [4.13] Dong Shufu, Yang Lingzhen, Cheng Guanghua, Chen Guofu, "Highly Efficient Er³⁺-Yb³⁺ Co-doped Double-cladding Fiber Amplifiers with Fiber Bragg Gratings and Shorter Fibers," 2004, Acta Photonica Sinica, Vol. 33(3), pp. 257-260
- [4.14] R. G. Smith, "Optical Power Handling Capacity of Low Loss Optical Fibers as Determined by Stimulated Raman and Brillouin Scattering," Applied Optics, 1972, Vol. 11, No. 11
- [4.15] G. P. Agrawal, "Nonlinear Fiber Optics," 4th edition, Academic Press, Boston, 2007
- [4.16] Jinyong Leng, Shengping Chen, Wuming Wu, Jing Hou, Xiaojun Xu J, "Analysis and simulation of single-frequency Raman fiber amplifiers," Opt. Commun., 2011, Vol. 284, Iss. 12, pp. 2997-3003
- [4.17] Nuphoton Technologies, NP2000ASE Broadband Source, Online: <http://www.nuphoton.com/NP2000ASE.html> Retrieved: 05/06/2011
- [4.18] NP Photonics, C & L Band ASE Source, Online: <http://www.npphotonics.com/>, Retrieved: 05/06/2011
- [4.19] Fishman, Daniel A. Nagel, Jonathan A. Park, Yong-Kwan "Reduction of stimulated brillouin scattering in a fiber optic transmission system," United States Patent: 5329396. Publication date 12/07/1994.
- [4.20] Richard T. Wainner, Mickey B. Frish, B. David Green, Matthew C. Laderer, Mark G. Allen "Tuneable Diode Laser Wavelength Modulation Spectroscopy (TDL-WMS) Using a Fibre Amplified Source," CLEO/QELS, 2007

Appendix A4.1: Final Design of Raman Amplifier System



Chapter 5 - Construction and Testing of Prototype Methane Sensor

This chapter describes how the fibre amplifier system was constructed into a stand alone unit with all the necessary electronics and controls for remote, single-end methane sensing. It also describes the results of laboratory and field trials conducted at Strathclyde University. This chapter is structured as follows:

- **Section 5.1 – TDLS System** - Describes how the amplifier system was built into a 19” rack with control and detection electronics.
- **Section 5.2 – Operating Instruction**
- **Section 5.3 - Initial Demonstration of the TDLS System** – Preliminary measurements made at Gooch and Housego (Torquay).
- **Section 5.4 - Laboratory Trials and Characterisation** - Describes the results of laboratory trials conducted at Strathclyde University.
- **Section 5.5 - Field Trials** - Describes the results of field trials conducted by Strathclyde University.
- **Section 5.6 – Summary**

5.1 TDLS System

The final goal of this project was to produce a prototype system to demonstrate long-range methane sensing using a Raman fibre amplified source in laboratory and field trials. The footprint of the prototype was a 12U 19” rack cabinet with a separate unit for transmit and receive optics. The prototype would be a “stand alone” unit containing all the electronics required to control the fibre amplifier and to transmit, detect, and analyse the TDLS signal. Figure 5.1 shows the completed prototype.

The prototype was constructed from several discrete modules units which were individually constructed by the different project partners using their expertise. These were then integrated onsite at Gooch and Housego (Torquay). This is partly the reason why a standardised 19” rack unit was chosen, for ease of integration. It is also cheaper to build something using standard parts than to design and construct a package “in house”.

The prototype, as shown in figure 5.1 can be deconstructed, on the basis of function, into four different modules –

- 1) The optical amplifier system.
- 2) The amplifier control electronics

- 3) The TDLS electronics.
- 4) The transmit and receive optics head

Module 1) the optical amplifier system contains the ASE source, Er-Yb amplifier and Raman amplifier described in chapter 4. It also contains the four 8W pump diodes (JDSU, L3) for the Er-Yb amplifier mounted on a heat sink with suitable forced air cooling. The 980nm single mode pump diode for the ASE source is mounted on a control board with thermoelectric cooler in the TDLS electronics module. The temperature of the TEC and the drive current set point are stored in memory on the board so that the ASE source powers up immediately when the power is turned on. This prevents the Er-Yb amplifier from being run with no seed, which could potentially result in parasitic lasing and cause damage to the system. As an extra precaution a detector in the amplifier control electronics module also stops this from occurring, providing an extra level of redundancy and safety.

A picture of the inside of the optical amplifier system is shown in figure 5.2 the 4.5km reel of DSF fibre is prominent at the front. The components of the amplifier system are mounted to the three metal base plates and the fibres are held in position with a low stress silicone epoxy. The routing of fibre is especially important for the Raman amplifier, which because of the longer wavelength (1651nm) experiences greater bend sensitivity. The loops of fibre in the Raman amplifier were kept as large as practical.

The output of the Raman amplifier (2W 1651nm) leaves the rack via an armoured cable at the rear of the optical amplifier system. This connects to the transmit optics in the transmit/receive head by an FC/APC connector. The tap outputs which were used for power monitoring during the lab build and characterisation of the amplifier leave the rear of the optical amplifier module. These are connected to the amplifier control electronics module which monitors and controls the amplifier.

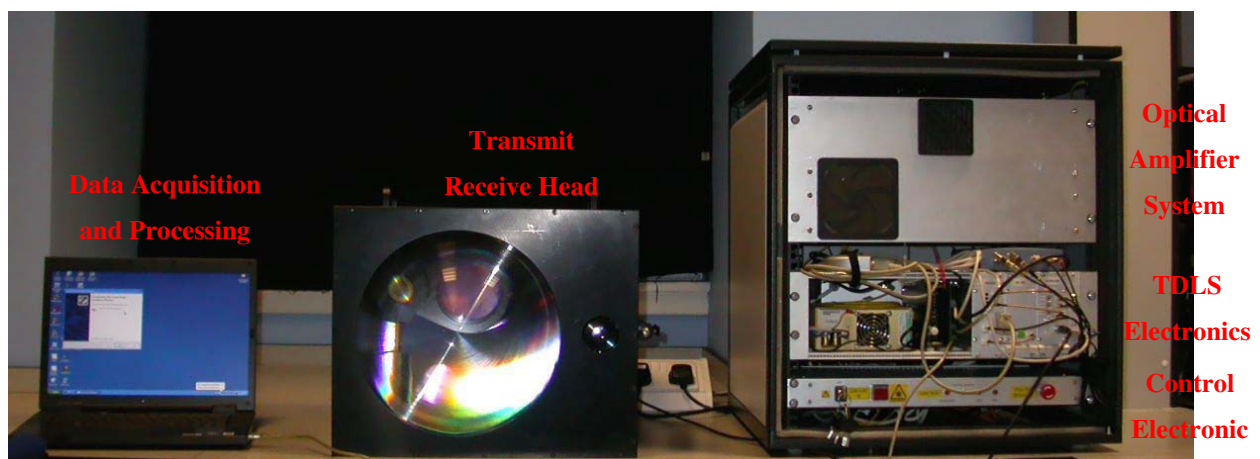


Figure 5.1: Complete system for TDLS demonstrator.

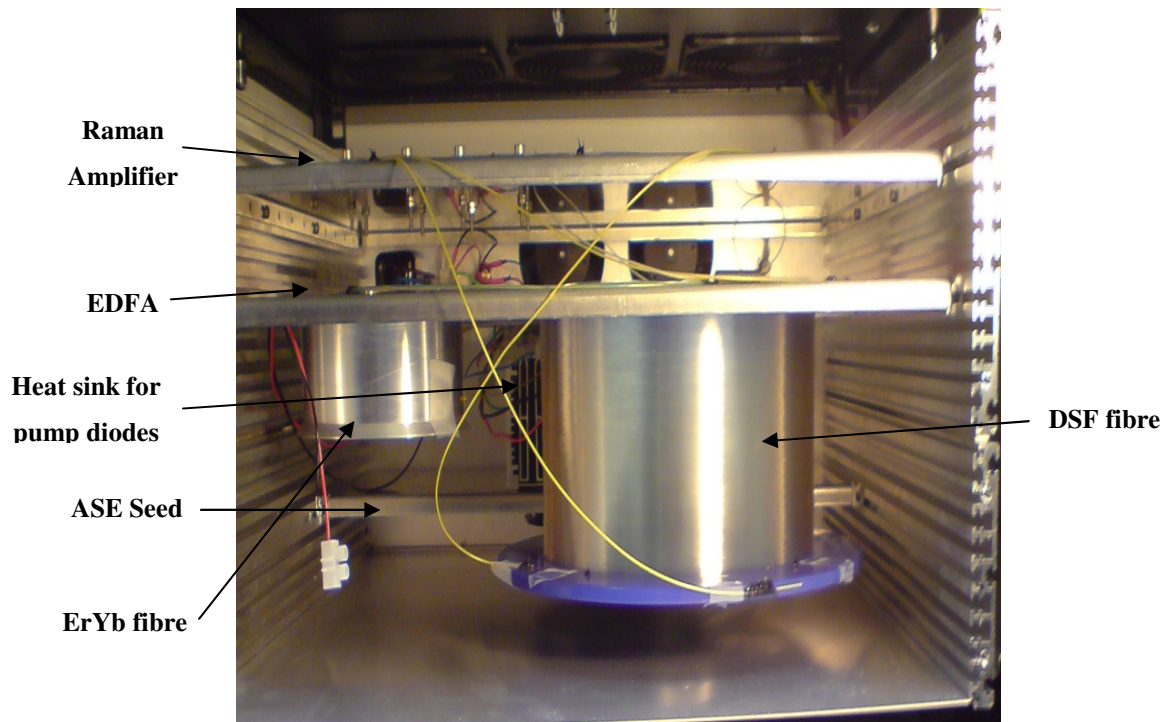


Figure 5.2: Inside the Optical amplifier system.

Module 2) the amplifier control electronics contains photodetectors and electronics which provide closed loop control for the amplifier system output power. The control shelf also produces a soft start/stop for the amplifier to protect the pump diodes, and incorporates a number of system alarms and safety features, like a key and switch ignition and an emergency stop button. The amplifier control electronics were designed and constructed by Ross Elliot and Jeffrey Marshall at Evanesco Ltd.

Figure 5.3 shows a schematic of the fibre amplifier system with the control electronics detector positions and interconnections. There are five detectors in total

- 1) PASE detector – This detects the ASE seed output power. If this is not above a set threshold then it will trigger an alarm and stop the Er-Yb amplifier pump lasers from powering up. This ensures that the EDFA cannot be switched on without a seed laser being present and protects the entire system from parasitic lasing (as mentioned earlier).
- 2) 1650nm Ptot detector – This measures the amplifier output power.
- 3) 1545nm Ptot detector – This measures the residual pump power left after the Raman amplifier.
- 4) SBS detector - Detects the power of backscattered light from the Raman amplifier. If this rises above a threshold level then it will trigger an alarm which cuts power to the Er-Yb amplifier pump lasers.
- 5) Ptot detector – This detects the output power of the Er-Yb amplifier. This is used as the feedback signal to maintain the amplifier at a set output power. If this output drops then the

control electronics increase the drive current to the pump lasers. If the drive current increases too much, indicating a problem with the amplifier, then the system shuts down.

The control shelf also detects the temperature of the heat sink that the pump diodes are mounted to. If this gets too hot then the system shuts down and triggers an alarm. Alarms are indicated by LEDs on the front panel of the control shelf.

An image of the inside of the control shelf can be seen in figure 5.4. The “key and button” ignition are on the left of the front panel. On the right of the front panel is an emergency shut off switch. This links up with another emergency shut down on the side of the transmit/receive head. The LEDs on the front panel light if an alarm condition is breached. The alarm thresholds are set by the variable resistors visible on the circuit board.

The fibre coupled photodetectors are connected to FC/APC bulkheads on the rear of the rack. A 15-pin D-sub connects to the driver (Lumina, LD150-10-15) for the Er-Yb amplifier pump diodes. Another 15-pin D-sub carries the output photodiode signals so they can be monitored remotely.

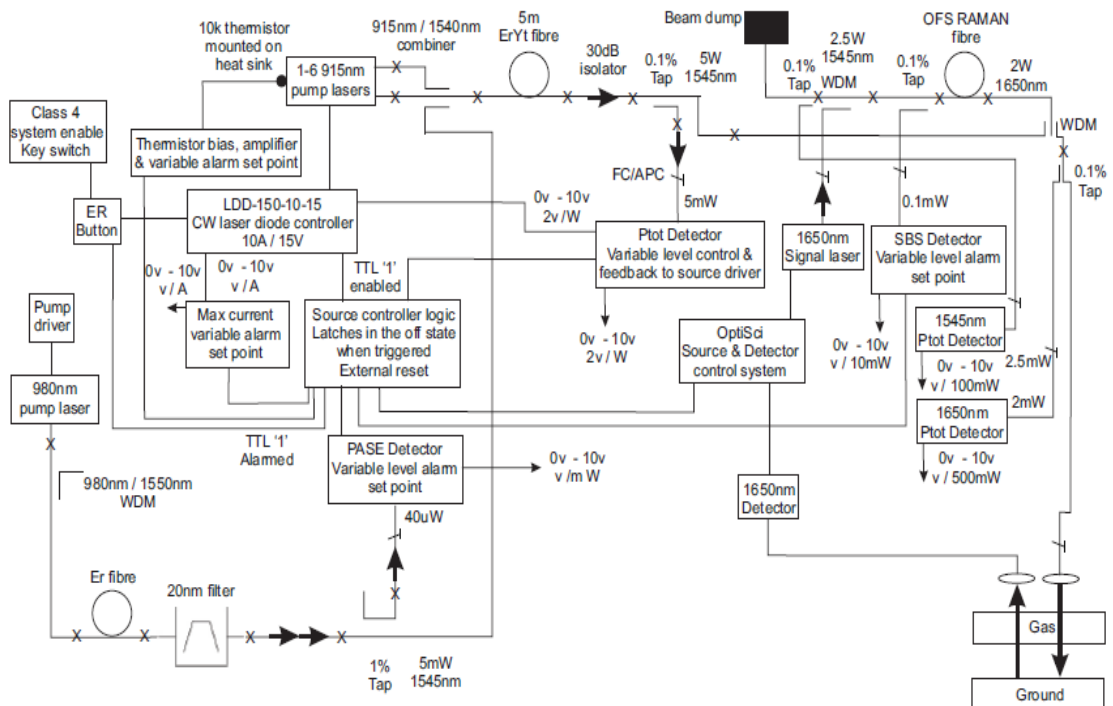


Figure 5.3: Schematic of fibre amplifier system and control electronics. [5.1]

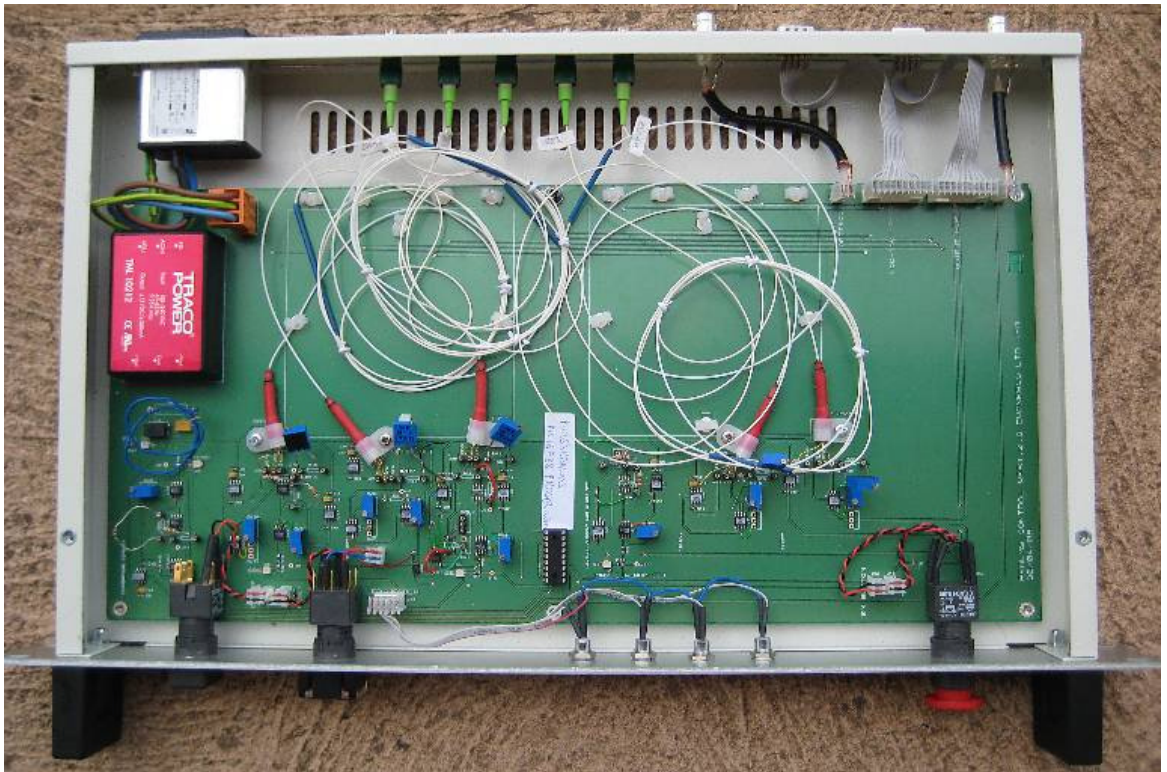


Figure 5.4: Inside the amplifier control rack.

Module 3) the TDLS electronics rack was developed by Optosci Ltd. and could be viewed as a complete TDLS system. It contains a 1651nm DFB laser, signal generator and lock-in amplifier. These occupy separate modules in the rack and can be clearly seen in the photo (figure 5.5) and on the schematic (figure 5.6).

The module on the left contains the 10mW 1651nm DFB laser with current driver and temperature controller. This is connected into the Raman amplifier to be amplified to 2W for the long range TDLS system.

The module next to this contains a signal generator which produces the low frequency ramp and high frequency dither that are applied to the DFB for TDLS-WMS. The function generator also has two outputs which output a signal at 1x and 2x the dither frequency. The phase of these outputs can be controlled and they act as reference signals for the lock-in amplifier.

The last module in the TDLS electronics rack is the lock in amplifier that is used to recover the 1f and 2f TDLS signal. This has two inputs for the 1f and 2f reference signals and 3 outputs for the raw photodiode output and 1f demodulated and 2f demodulated signals. These are fed into an electronic oscilloscope (Picoscope) shown in the top right of figure 5.5 for analysis by software.

The modules of the rack connect to a PC through a common USB interface (on the right) for control by software.

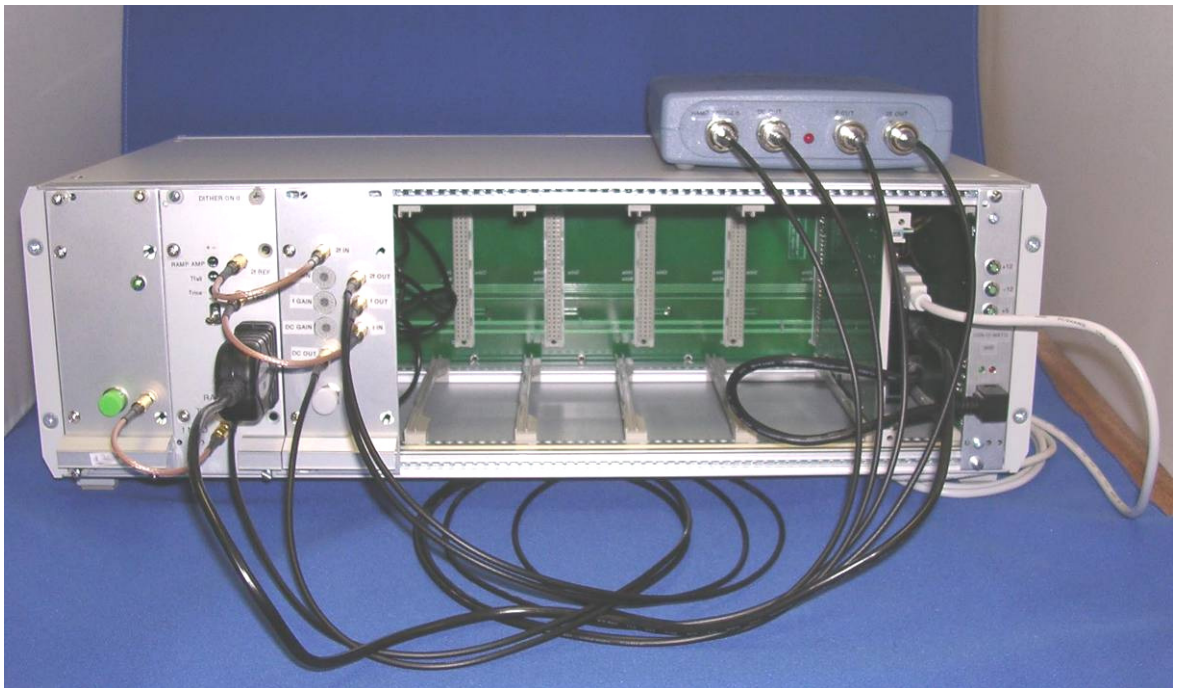


Figure 5.5: Photograph of TDLS electronics rack.

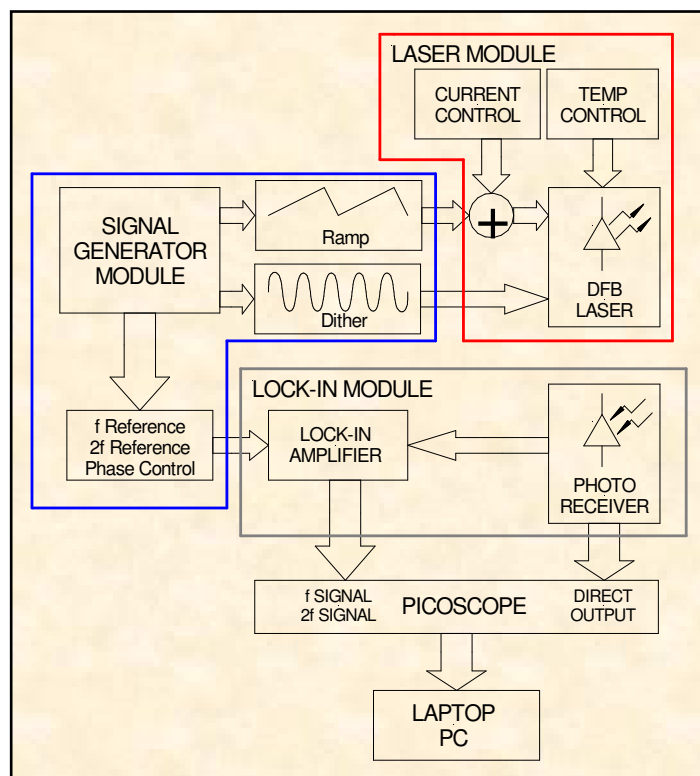


Figure 5.6: Block Diagram Schematic of TDLS electronics rack.

Module 4) the transmit and receive optics module contains a Kepler type telescope to expand and collimate the output of the Raman amplifier. Producing a 3cm beam at 10m from the optical head. It also contains a 12" Fresnel lens (Edmund Optics) to collect the backscattered light from topographic targets and an InGaAs photoreceiver with pre-amplifier (PDA-10CS, Thorlabs). Figure 5.7 shows the inside of the transmit and receive optics module.

The output of the photoreceiver is transmitted to the lock in amplifier to be demodulated. The raw and demodulated signals are recorded by an oscilloscope onto the computer/laptop to be analysed. Figure 5.8 shows the analysis and system control software interface. The program REALMS PDRV (on the right in figure 5.8) sets the operating point, modulation frequency and modulation depth of the 1650nm DFB laser. It was also used to set the phase delay of the reference signal for 1f and 2f demodulation at the lock in amplifier (LIA).

The Picoscope program (on the left in figure 5.8) displays raw and normalised linear traces of the signals returned by the photodetector and lock-in amplifier. It calculates the path-length concentration product from these traces as discussed in chapter 2. These traces can also be saved.

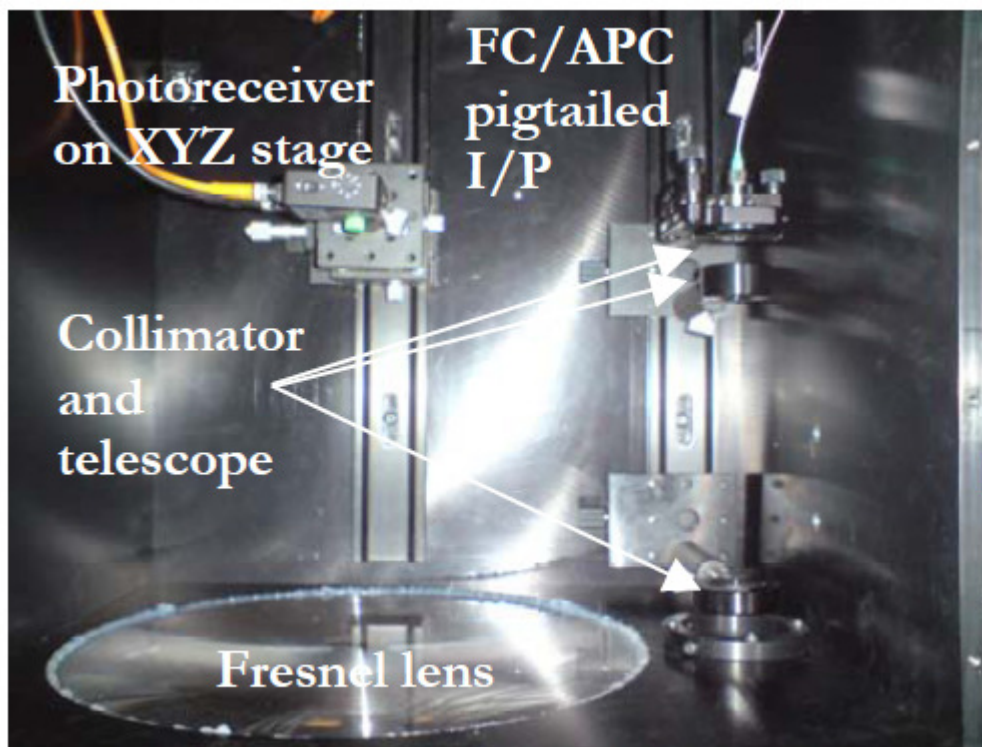


Figure 5.7: Inside the transmit/receive head unit. (picture Kevin Duffin)

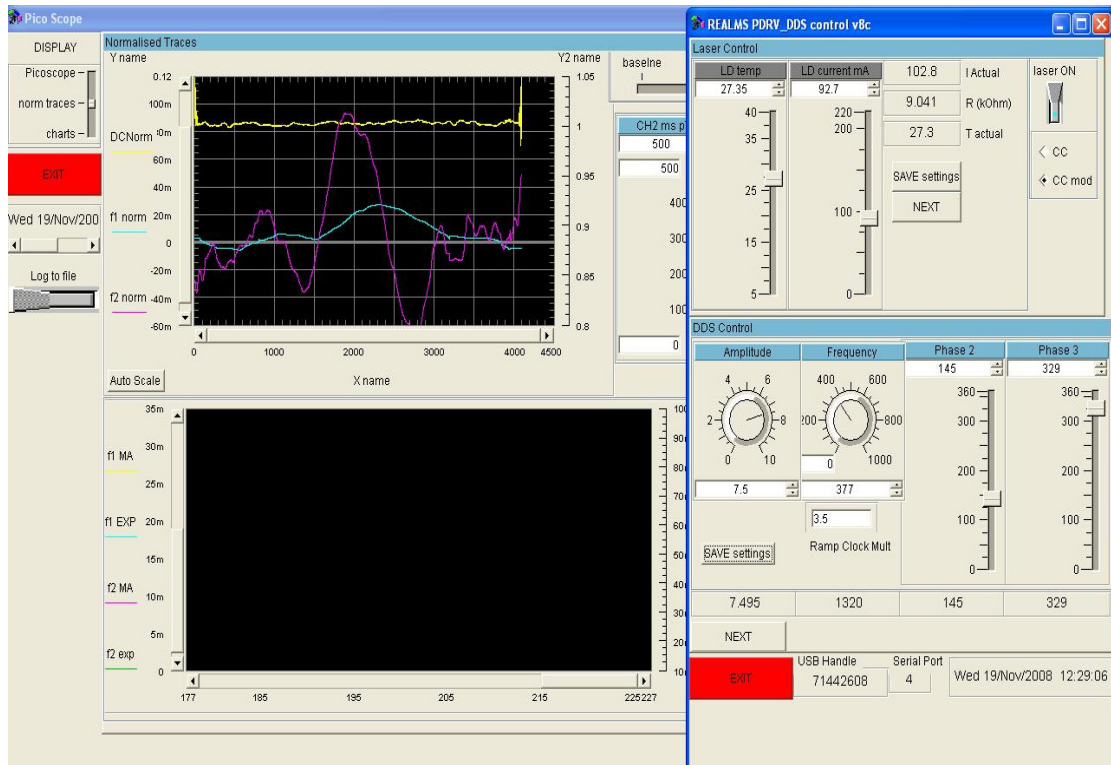


Figure 5.8: Computer Interface for the long range methane sensor.

5.2 Operating Instructions

In this section the operating procedure of the system is described, as it has to be switched on in a certain order to operate. It also runs through the procedure for changing the output power of the system.

Switching On

- 1) Plug in the rack system and head.
- 2) Connect to the PC and run the laser operating software.
- 3) Turn the 1550nm ASE lasers drive current up to 150mA using software.
- 4) Turn on the 1650nm laser at required drive current, dither frequency and depth using the REALMS PDRV software.
- 5) Turn the key on the lower shelf and push the red button.
- 6) The system will now ramp up until the required optical feedback is received and maintain this optical feedback by adjusting the EDFA pump power accordingly as the system settles.
- 7) If an alarm triggers then the system will ramp down automatically.

If an alarm triggers a red LED indicator lights up on the front panel of the lower rack. There are four alarms **ASE**, **SBS**, **Current** and **Temperature**.

- **ASE** triggers if the power of the ASE seed for the EDFA is insufficient.
- **SBS** triggers if the backscattered power rises significantly.
- **Current** triggers if the drive current of the EDFA pump diodes required to maintain the optical output of the EDFA at the right level, exceeds a preset maximum.
- **Temperature** triggers if the temperature of the pump diodes heat sink block rises to high.

The set points for the alarms are set at appropriate levels to protect the system. These may require changing if the output power of the system is altered.

Changing Output Power

To increase/decrease the power of the amplifier system it is necessary to change the feedback level which the closed loop electronics maintain. If increasing the power it may also be necessary to increase the maximum current alarm set point. These actions require potentiometer levels to be changed on the circuit board inside the control shelf.

The maximum current alarm set point is changed by the potentiometer nearest to the part of the circuit labelled current. Whilst tweaking the potentiometer the control voltage can be measured between ground and pin 2 of the output D-sub. The voltage measured here corresponds to the maximum diode drive current. It is set so that $1V = 2A$, $2V = 4A$, etc... Do not set current to exceed around 10.5A (5.25V). This is the maximum operating current of the L3 diodes

The output power of the amplifier is changed using the potentiometer in the top left corner of the raised board. Care needs to be taken as this will require changing with the system laser/amplifier switched on. The output power of the amplifier can be monitored during this process and set to the required new position.

If you cannot measure the output directly from the patchcord then you can measure the current leaving the Lumina diode driver. The graph in figure 5.9 shows the relationship between drive current and output power for the amplifier.

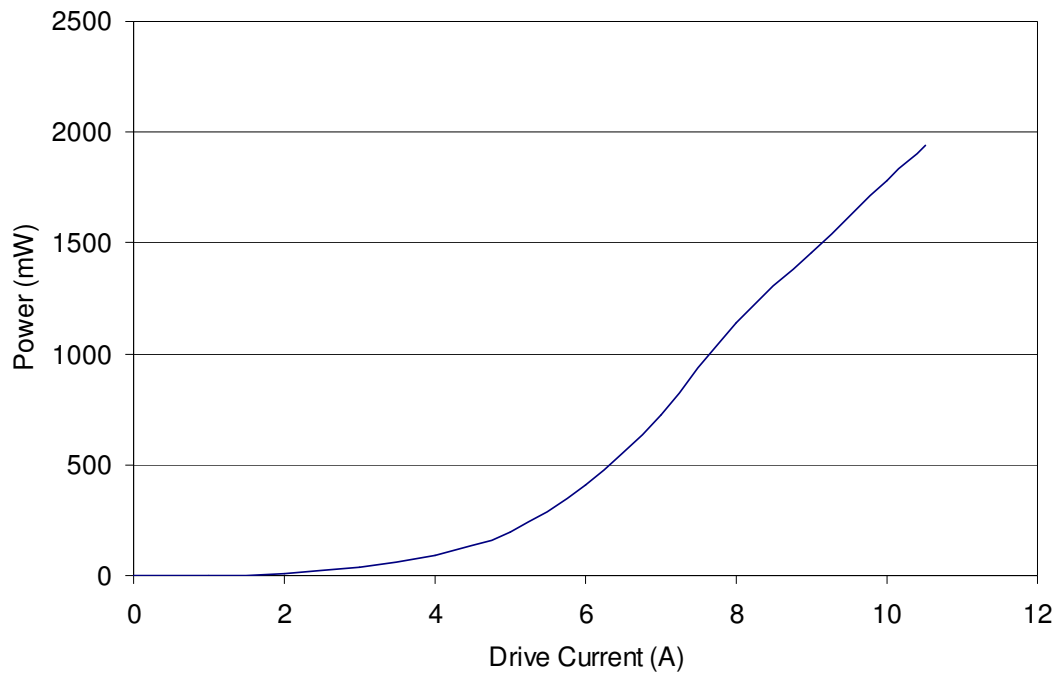


Figure 5.9: Drive current Vs output power of completed amplifier system.

Switching Off

To turn off the system:

- 1) Turn the key on the lower rack and the amplifier will wind down.
- 2) ASE and 1650nm lasers can be shut down using the software controls (if necessary). If they are left on when the power is switched off then they should power up to the previous set values automatically when power is next supplied.
- 3) Unplug.

5.3 Initial demonstration of the TDLS System

After construction and an initial demonstration of the completed methane sensor at Gooch and Housego (Torquay) the system was taken to Strathclyde University for laboratory testing and characterisation. At this time I went to Strathclyde to setup the system and make some initial measurements. This section will show the results of these measurements. It will also discuss some changes which were made to the system at this time. Kevin Duffin and David Mitchell at Strathclyde University helped with these measurements and later conducted more thorough laboratory trials and fully characterised the system (section 5.4). They also took the system out for field trials (section 5.5).

To make our initial measurements the system was set up in a lab with a range of 10.5m from the optical head to a target backscatter surface. Target surfaces were a concrete block, white cardboard, wood and a rusty metal plate. These all have different reflectance and were chosen to be representative of targets which may be present during real operation. Methane samples of different concentrations were placed into the beam path in front of the Fresnel collection lens - so that the light makes only one pass through the sample. This was important because the methane samples were held inside a Perspex cell with an attenuation of 67%. A diagram of the setup can be seen in figure 5.10.

The settings of the dither depth and dither frequency of the 1651nm laser and the phase of the reference signals for the lock in amplifier were optimised to maximise the magnitude of the 2f TDLS signal. This was done with a high concentration of methane in the beam path. These were then set for the duration of the trials with dither frequency 377kHz and dither depth of 7.5mA pk-pk (modulation index $m \sim 2.2$). The low frequency sweep applied to the laser was at 5Hz.

An ideal example of a gas trace taken at high concentration and high power can be seen in figure 5.11. The raw photodetector output (in blue) shows the applied modulations in the backscattered signal received at the photodetector. The 377kHz modulation and 5Hz sweep applied to the DFB are clear. The raw 1f and 2f signals (pink and red) show the demodulated outputs of the LIA with the characteristic derivative shapes of the gas line.

The system was then run through a series of tests to see how well it performed. The first test, described in section 5.3.1, showed detection of low concentration methane (100ppm.m above background) at a target distance of 10m with a moderately high output power of 620mW. The second test, section 5.3.2, used a low power output of 35mW to simulate detection over a longer range and showed the ability to detect low concentration methane (100ppm.m above background) at 10m.

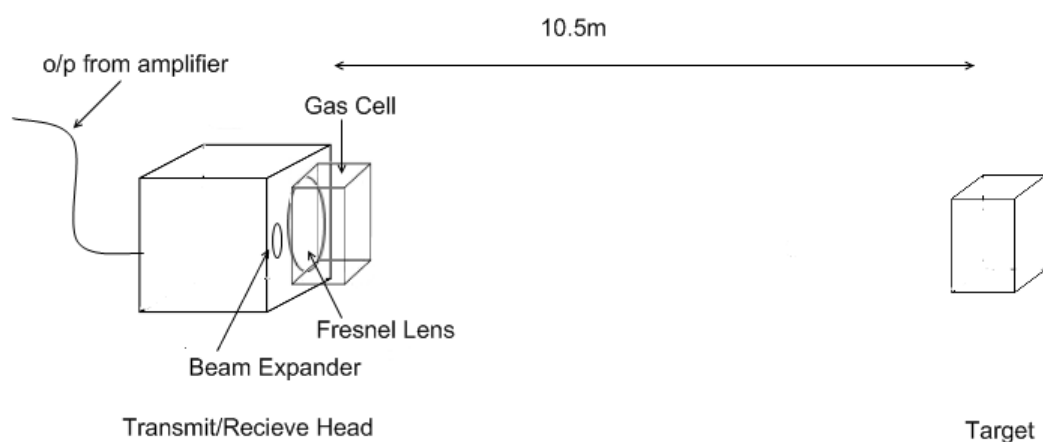


Figure 5.10: Diagram of setup for laboratory trials of gas sensing system.

10.13% CH₄:N₂ at atmospheric pressure and room temp, path length 10cm, target distance 10.5m, target = concrete block, armoured patch O/P ~ 1.2W

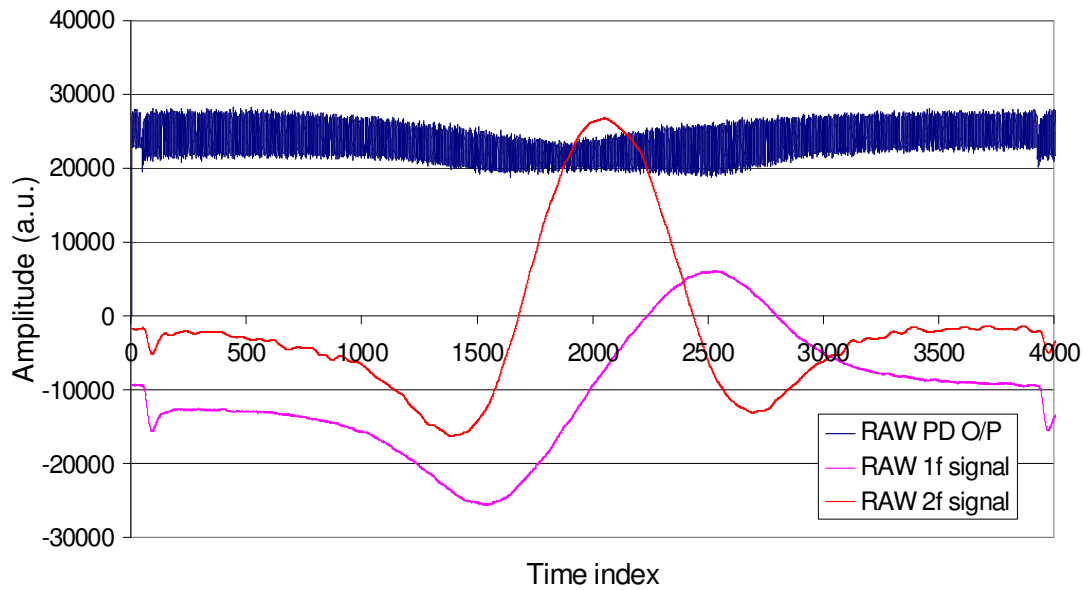


Figure 5.11: Gas sensing measurement with 1.2W transmitted power and path length concentration of 10000ppm.m off a concrete backscatter target.

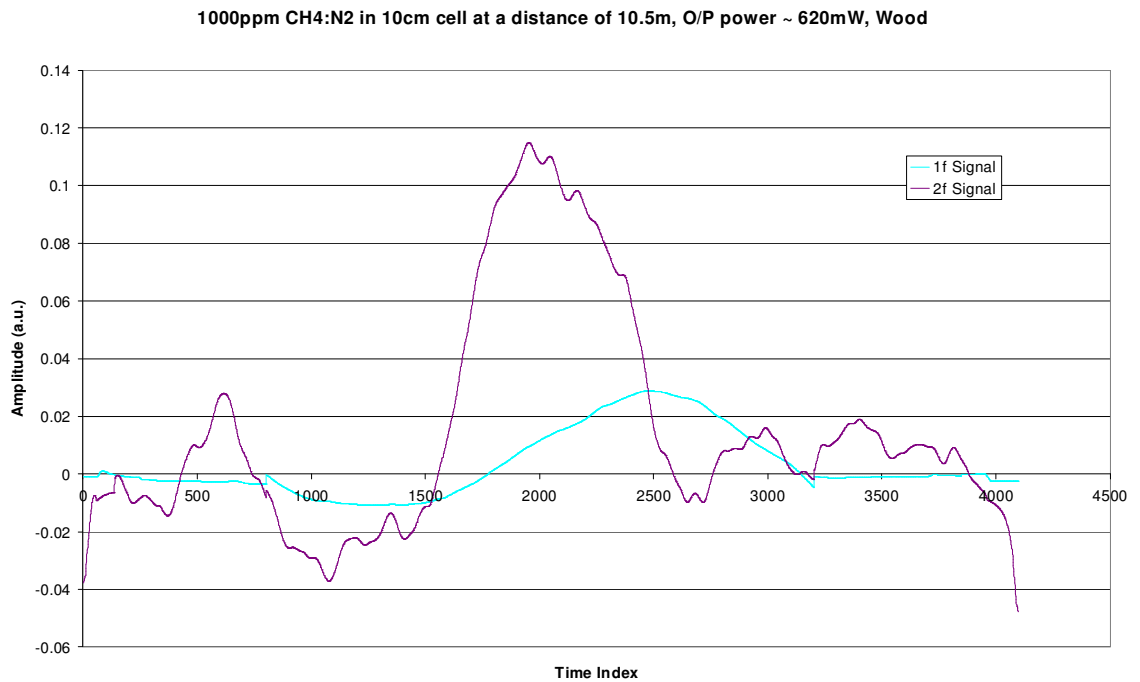
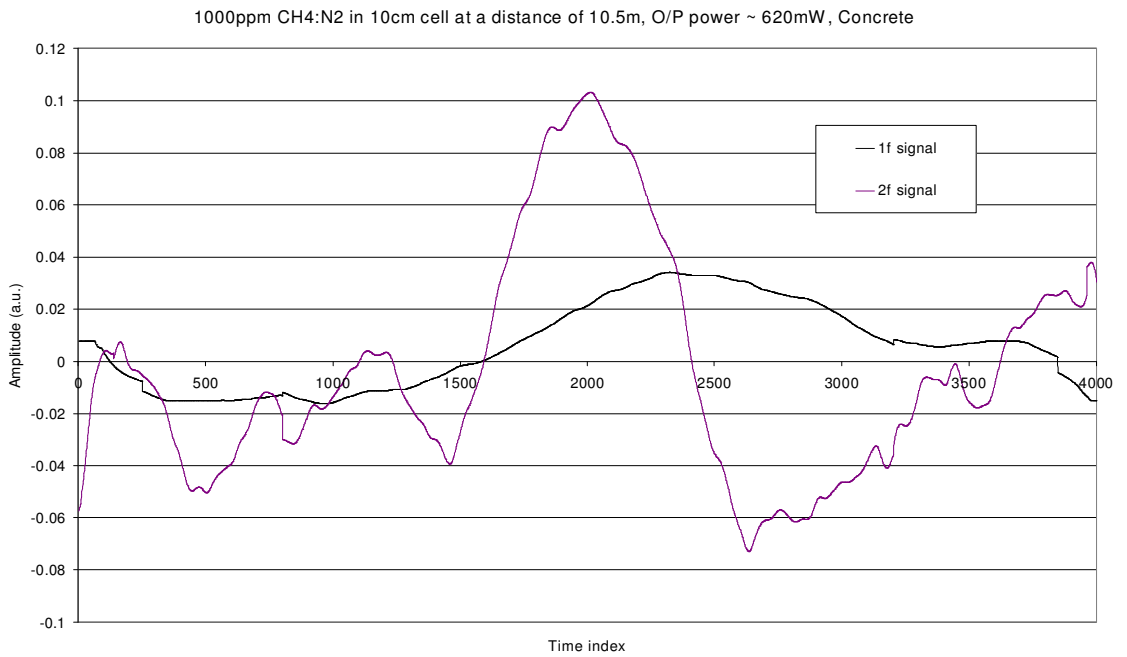
5.3.1. High Power – Low Concentration Measurements

The first test that we conducted with the methane sensor was to see if it could measure a 100ppm.m sample of methane above background using a moderately high output power. The purpose of this experiment was simply to demonstrate the principle of gas sensing and to test that the system was operating as expected.

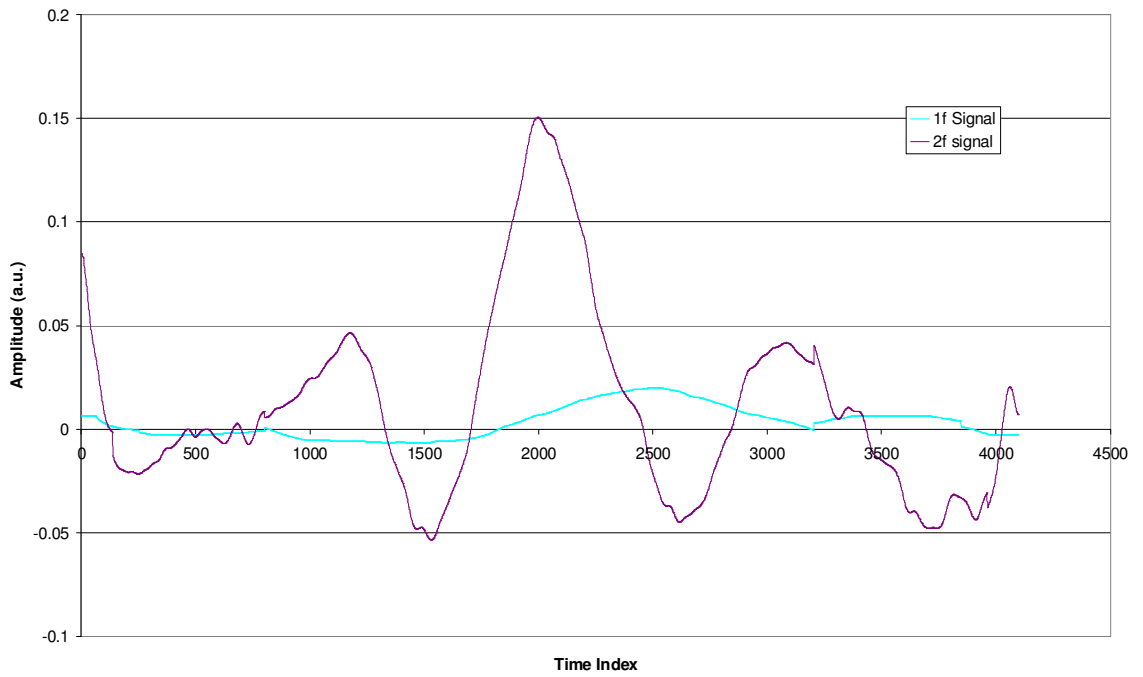
During these measurements the output power from the amplifier was set at a power of 620mW as measured directly from the transmit/receive head. A gas sample of 1000ppm CH₄:N₂ inside a 10cm deep Perspex cell, giving a path integrated concentration of 100 ppm.m, was placed in front of the 30cm Fresnel lens. The received signal power at the photodetector with the Perspex box in place using the concrete target at a distance of 10m was 488nW (~1478nW without the perspex box).

The various targets were then tested in turn to see if they each returned enough signal light to allow the methane sample to be detected. The received 1f and 2f signals from each target can be seen in figures 5.12. In all cases the 1f and 2f signals can be clearly identified, signifying the presence of methane in the optical path. The presence of the gas cell was easily distinguishable from background in these measurements. This shows that we are far above the noise floor of the sensor.

After this demonstration it was decided that the same measurement at lower output power would be useful for comparison. Assuming that the returned backscattered power scales proportionally to the output power, as discussed in section 3.3, then it should be possible to estimate the effective range of the sensor simply by finding the minimum output power required to detect a known gas sample at a shorter distance and extrapolating. The assumptions behind this will be discussed in more detail in section 5.4.



1000ppm CH₄:N₂ in 10cm cell at a distance of 10.5m, O/P power ~ 620mW, Rusty Plate



1000ppm CH₄:N₂ in 10cm cell at a distance of 10.5m, O/P power ~ 620mW, White Card

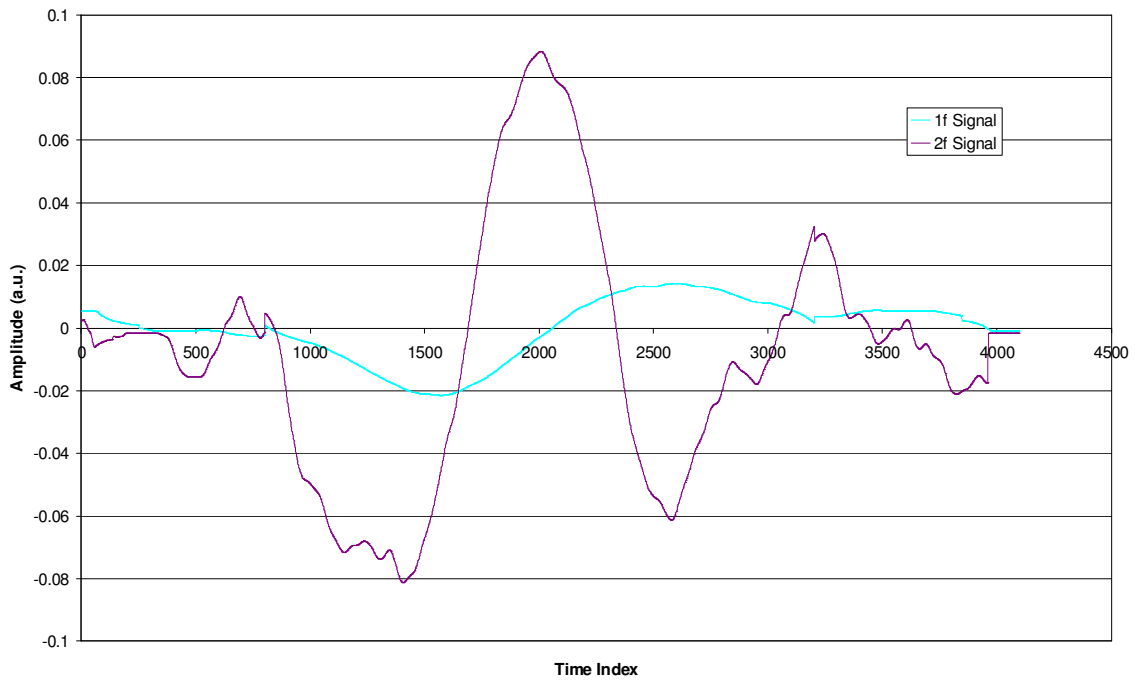


Figure 5.12: Measurements with different targets at high power – low concentration.

5.3.2 Low Power – Low Concentration Measurements

To test the methane sensor nearer its limit of detection the output power from the transmit/receive head was reduced from 620mW to 35mW. This would simulate a longer range to the target by reducing the amount of received power at the detector. In theory the received power should scale linearly with output power and according to an inverse square law with target distance (section 3.3). Therefore, this reduction in power is equivalent to increasing the distance by a factor of 4.2.

To ensure that the amplifier gain had no effect on the output signal modulation between the two trials, the output power of the amplifier was kept the same. The power was attenuated by inserting a 5% tap coupler between the Raman amplifier and the transmit/receive head. The tap arm was then connected to the collimator-telescope and the excess power dumped. The Perspex cell containing the 100ppm.m sample of methane was placed in front of the Fresnel lens as before.

The received signal power from the concrete target was 151nW (457nW without the Perspex cell). It was noted that the received power did not scale linearly with launch power– the reason for this is thought to be due to the angular alignment of the transmitting telescope and Fresnel lens. Later during full characterisation the telescope was changed to allow more alignment flexibility and the relationship between output power, received power and distance were confirmed.

This received power was too low to produce a measurement, so the Perspex box was changed for a Tedlar bag with the same path length but with a higher transmission of 78%. This increased the power of the backscattered signal to 356nW. This was found to be adequate for detection and figure 5.13 shows the results of measurements off the different reflective targets.

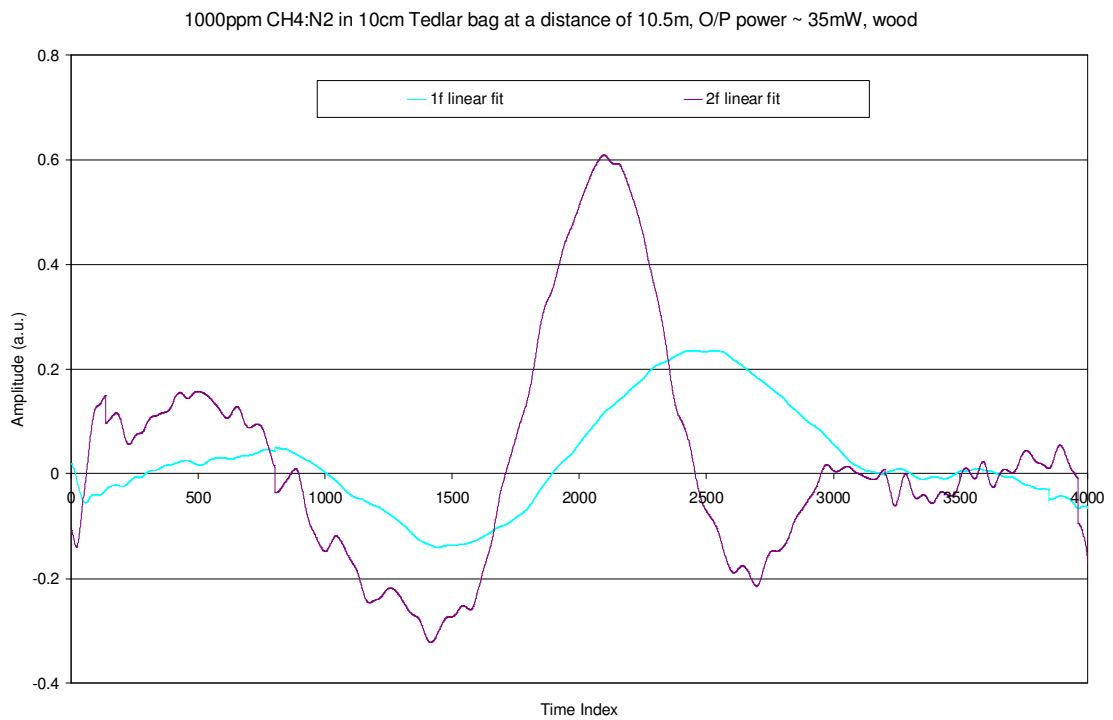
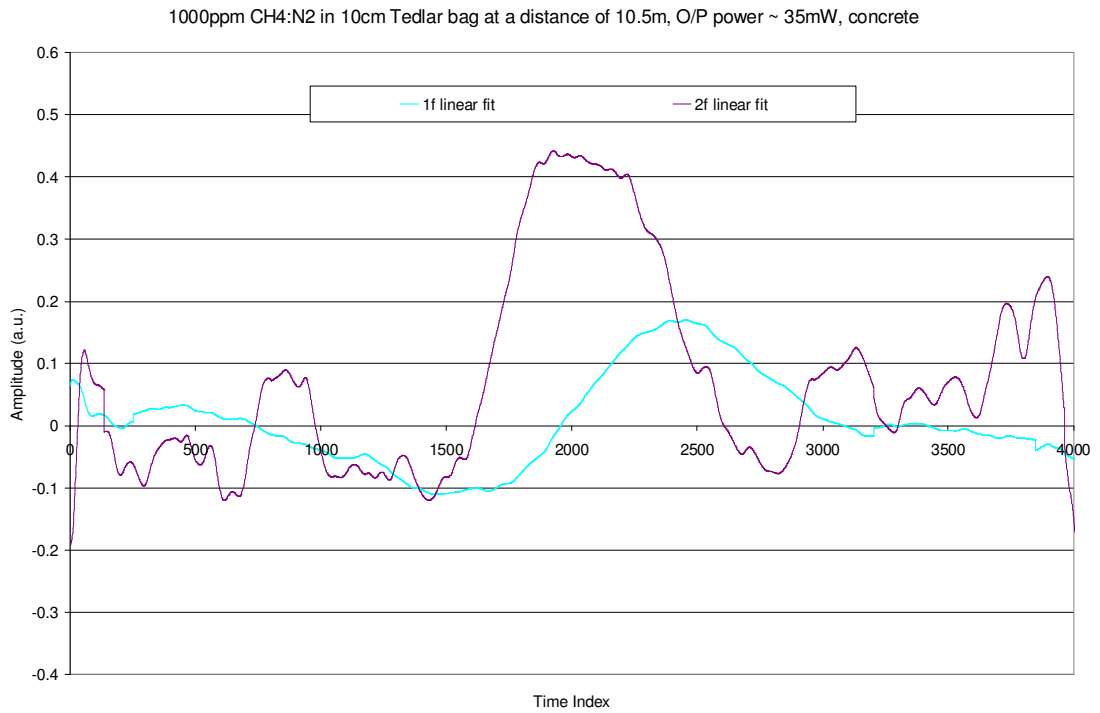
From these measurements we can see that the transmit power needed for a detection limit of 100ppm.m above threshold for this setup lies somewhere between a received power of 151nW (with Perspex cell) and 356nW (with Tedlar bag). If we ignore absorption in the Tedlar bag and assume that the threshold is reached at around 30mW output power then this suggests a range of less than 100m at 2W output power.

The detection limit output power P_{short} at short range R_{short} is related to the detection limit output power P_{long} at long range R_{long} by

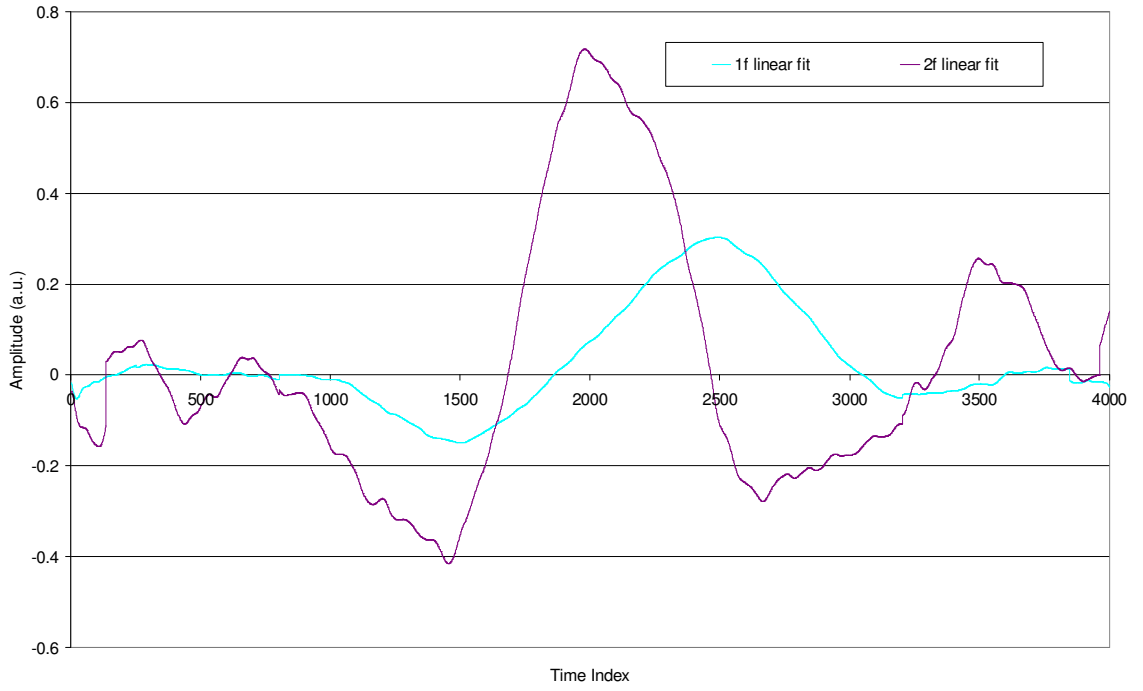
$$\frac{P_{long}}{P_{short}} = \left(\frac{R_{long}}{R_{short}} \right)^2 \quad (5.1)$$

Under the conditions that the backscattered power varies linearly with output power and to the inverse square of distance.

Previous experience at Strathclyde University suggested that our received powers were much lower than expected. As mentioned earlier we suspect that this was because of the alignment of the Fresnel lens and detector with the transmit telescope. After these trials the design of the optics in the transmit/receive head were changed to allow more precise alignment and optimisation. Full characterisation of the system was then undertaken at Strathclyde.



1000ppm CH4:N2 in 10cm Tedlar bag at a distance of 10.5m, O/P power ~ 35mW, white card



1000ppm CH4:N2 in 10cm Tedlar bag at a distance of 10.5m, O/P power ~ 35mW, rusty plate

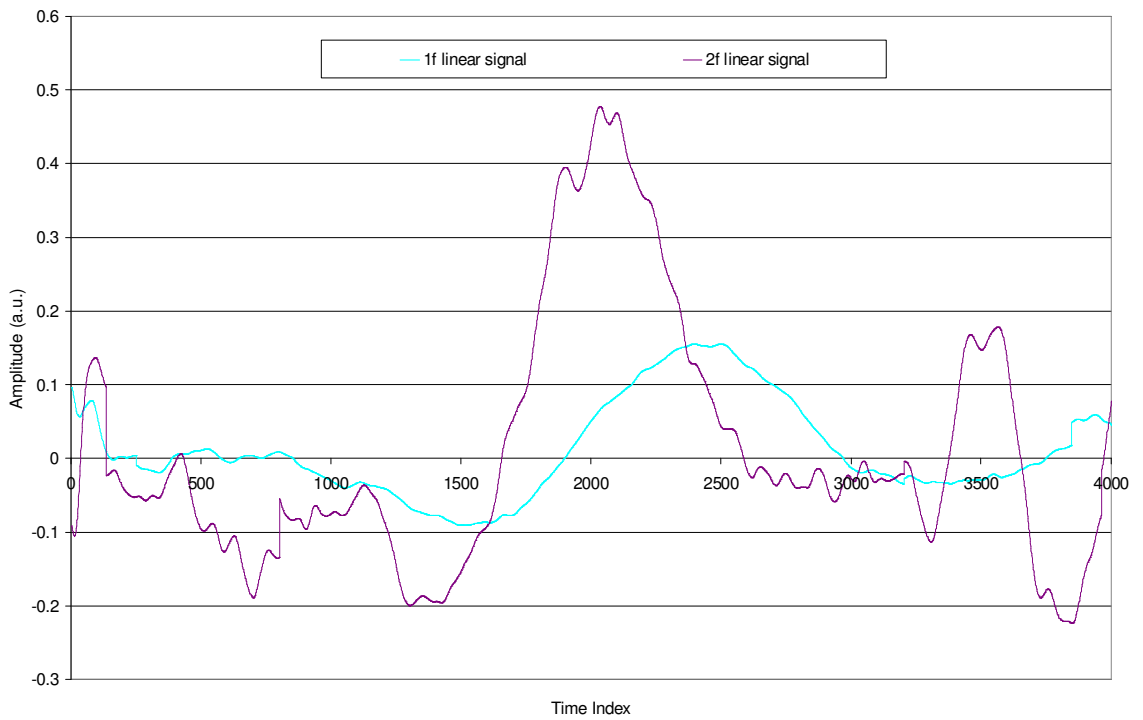


Figure 5.13: Measurements with different targets at low power – low concentration.

5.4 Laboratory Trials and Characterisation

At Strathclyde University a full characterisation of the system was undertaken. The aim was to find the minimum transmit power required to be able to measure 10000ppm.m, 1000ppm.m and 100ppm.m methane above background at a known range. The setup was very similar to the setup used in the initial low power demonstration (figure 5.10) except the high power output of the amplifier was attenuated with a 5% tap before being transmitted. A variable neutral density filter in the beam path allowed the transmit power to be attenuated further and varied.

The transmit beam was attenuated until the signal to noise ratio of the first harmonic was reduced to 3:1. The 3:1 ratio was chosen for measurement consistency and represents what is deemed to be the smallest resolvable signal. This was then recorded as the minimum transmit power required to detect the methane sample. The power was then adjusted to account for the insertion loss of the Perspex sample cell. Table 5.1 records the minimum transmitted power needed to measure 10000ppm.m, 1000ppm.m and 100ppm.m concentrations of methane using white card, concrete and a rusty metal plate as backscatter targets.

You can see from this table that the minimum detectable transmit power required to detect a 100ppm.m increase in methane concentration above ambient is 3.3mW. This is much less than the 30mW measured in the preliminary trials (section 5.3). This shows the importance of being able to optimise the alignment of the transmit telescope position and photodetector in the transmit/receive head.

The table also shows that the minimum detectable transmit power is similar (usually the same) for all three surfaces. This suggests that the component of backscatter that falls within the acceptance angle of our collection lens from each target is comparable. I would guess that if we look at the angular dependence of reflectance for these samples we would find that each has a large specular component. This would also explain why the alignment of the transmitted beam and the Fresnel collection lens are so important.

If we assume that 3.3mW is the lowest transmit power that we need to detect a 100ppm.m increase in methane above background at 10m distance then to increase the distance to 100m (a factor of 10) we would need a transmit power of around 350mW (from equation 5.1 – inverse square law). To increase the distance to 200m then we would need a transmit power of 1.4W. This is comfortably within the capabilities of the Raman amplifier system, which has a maximum output power of 2W. With 2W power (and under lab conditions) we could potentially reach a range greater than 250m.

| Target Surface | Gas Conc. | ReALMS prototype | Lab based system |
|----------------|------------|------------------------------|------------------------------|
| | | Min Detectable Tx Power (mW) | Min Detectable Tx Power (mW) |
| White Paper | 10000ppm.m | 0.330 | 0.269292 |
| Rusty Plate | | 0.330 | 0.269292 |
| Concrete | | 0.330 | 0.269292 |
| White Paper | 1000ppm.m | 0.495 | 1.256696 |
| Rusty Plate | | 0.495 | 1.436224 |
| Concrete | | 0.66 | 1.436224 |
| White Paper | 100ppm.m | 3.3 | 3.536583 |
| Rusty Plate | | 3.3 | 1.718683 |
| Concrete | | 3.3 | 3.770088 |

Table 5.1: Summary of minimum detectable transmit powers for various gas concentrations and target surfaces. [5.3]

The 2f signals obtained from the concrete block target for methane concentrations of 10,000ppm.m, 1000ppm.m and 100ppm.m are shown in figure 5.14. The same measurements using a rusty metal target and a white card target are given in appendix A5.1.

Figure 5.15 shows a comparison of a 100ppm.m and 200ppm.m measurement. The difference between the two measurements is clearly resolvable. This confirms that the system is capable of resolving a 100ppm.m increase in methane concentration even when operating at near the noise floor. To make this measurement two tedlar bags with path lengths of 10cm filled with 1000ppm CH₄:N₂ were placed in front of the Fresnel lens. The 200ppm.m measurement includes an additional 22% loss, due to the second tedlar bag, which is not accounted for in the signal. So in a “real” application the difference would be even larger.

The next step in the project was to take the completed system out for field trials. Unfortunately, before this happened the amplifier system developed a fault and a fibre fuse initiated at a splice between the double clad passive output fibre of the 6+1x1 pump combiner and the Er-Yb double clad fibre in the erbium-ytterbium amplifier. At this point the inner cladding of the fibre is carrying more than 30W of 915nm pump light. At the splice any loss is coupled into the outer cladding where it is guided at the fibre-air interface. Debris on the fibre can then couple out the light, where it may initiate damage. To prevent this the splice was enclosed in a metal tube with an elastomer seal. It is thought that perhaps condensation from the actively cooled heat sink on which the splice sat may have caused the failure. Fortunately, the alarm system shutdown the pump diodes fast enough to prevent significant damage to the rest of the system.

To allow field trials to take place the Er-Yb amplifier was replaced by a high power OEM amplifier (Keyopsis) which was available at the University. This had a lower output power than the original Er-Yb amplifier. To compensate for this the wavelength of the ASE seed was changed by replacing the

1550nm CWDM filter with a 1531nm CWDM filter. This channelled more of the power into a spectral region with higher Raman gain. Figure 5.16 shows the output power against pump power of the Raman amplifier with the new seed and EDFA compared to the original system. You can see straight away that the efficiency of the Raman amplifier has been improved greatly. With 5W of pump power it achieves 2.2W 1651nm output compared to 1.2W from the original system. The maximum output using the 5W EDFA and the 1530nm CWDM filtered seed is 2.4W. The maximum output of the original system was 2W for 7.5W pump. If the 1531nm CWDM filter was used with the 7.5W Er-Yb amplifier then we would expect even greater output power – probably pushing the ultimate limit set by SBS.

The gas sensing performance of the modified system was then retested and the sensitivity was found to be the same for a given output power as the original system. The system was now ready for field trials.

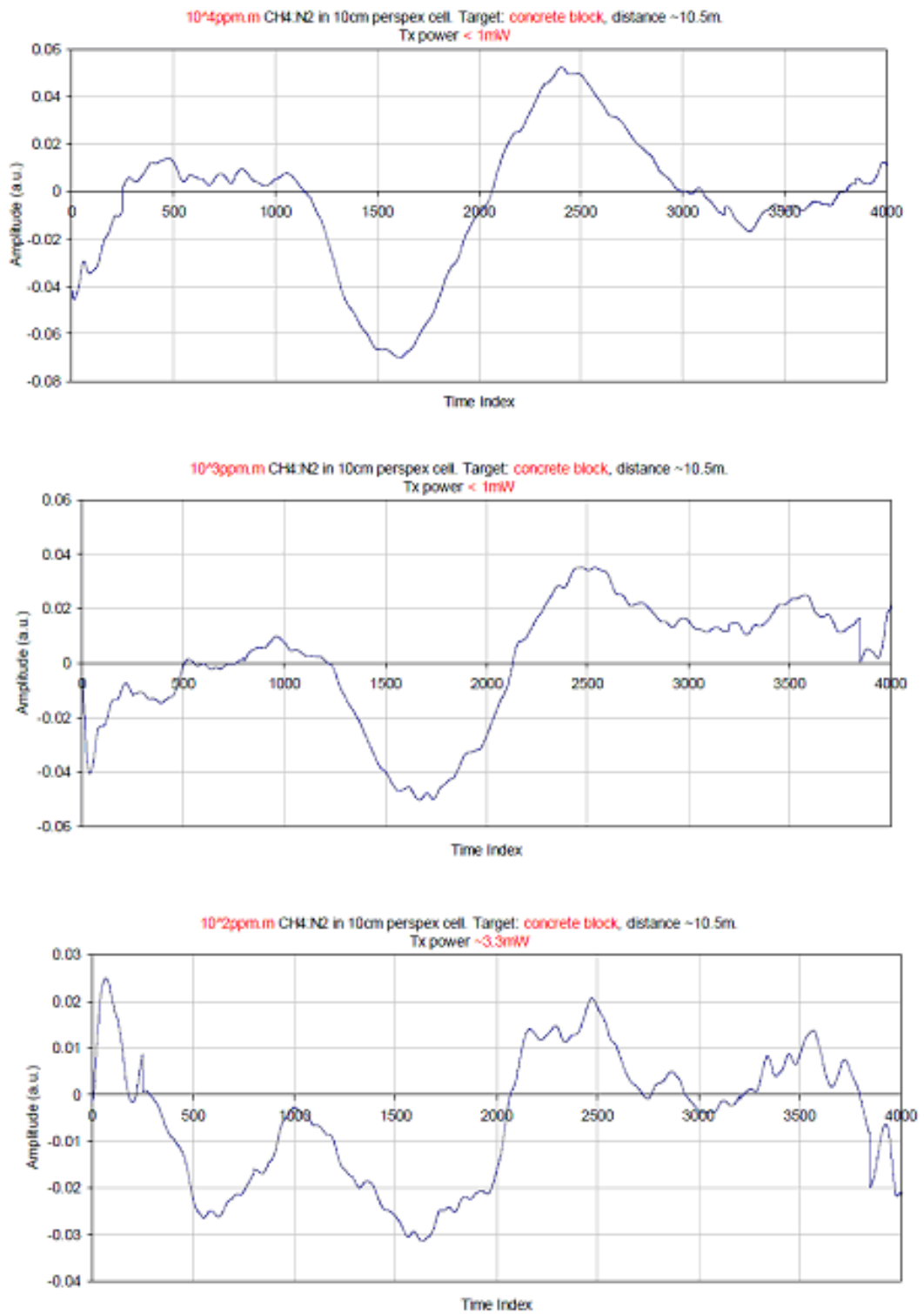


Figure 5.14: Measurements of 10,000ppm.m, 1000ppm.m and 100ppm.m concentrations of methane from a concrete block.

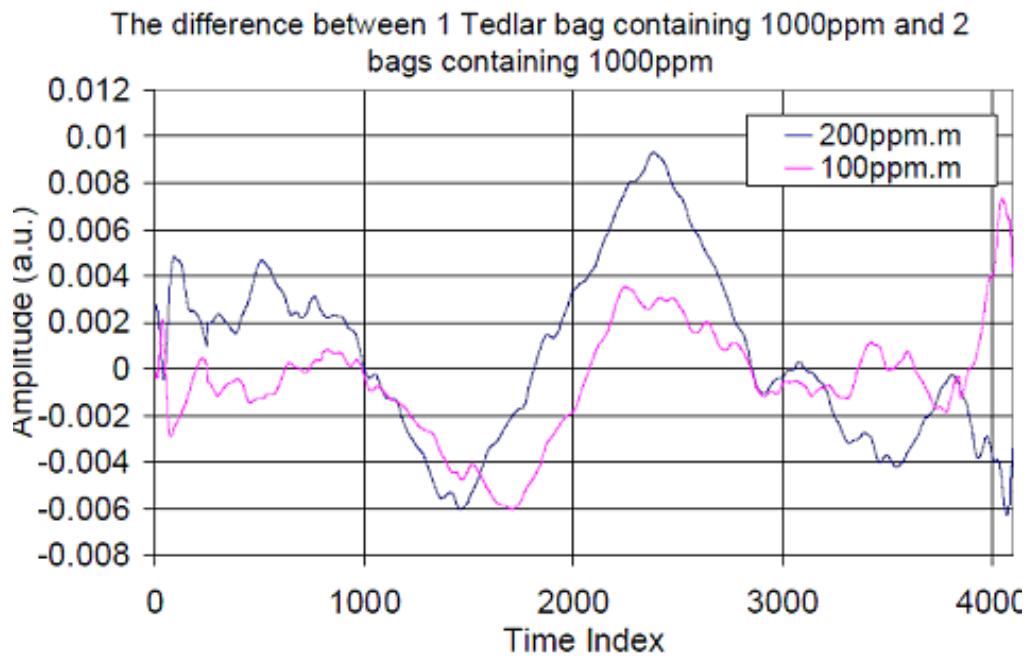


Figure 5.15: Measurement of 100ppm.m (in one tedlar bag) and 200ppm.m (in 2 tedlar bags) samples above background.

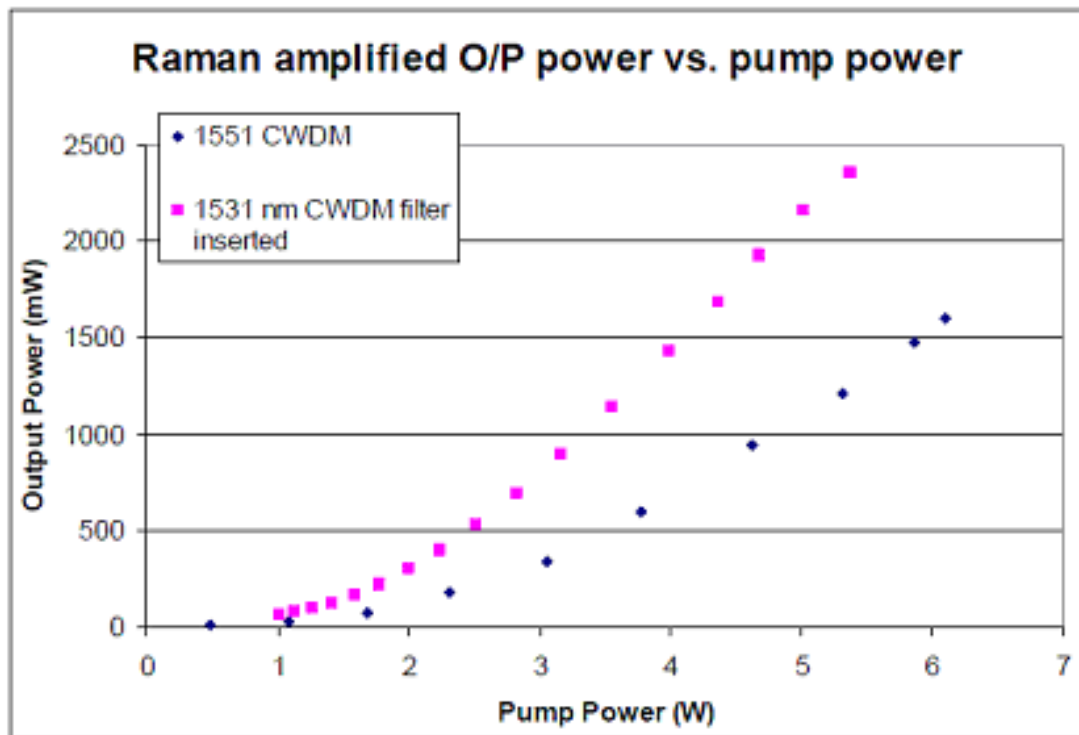


Figure 5.16: Output power at 1650nm as a function of pump power.

5.5 Field Trials

To demonstrate the operation of the methane sensor in a “real” environment it was taken out for field trials in February 2009. The field trial location was a 5-hectare field near Falkirk chosen for its remoteness, away from people and traffic that may be at risk from the high power laser. The intentions of field trials were:

1. To increase the operating distance, beyond the length of the laboratory, to greater than 100m to meet our original specification.
2. To compare the performance of the methane sensor against predictions from the laboratory trials.
3. To see how the sensor performs under realistic conditions.

During field trials the system was set up in the back of a van with power provided by a petrol generator. The target surfaces were placed on a stand and aligned with the output beam. To align the reflective target the system was switched on with a 10,000ppm.m sample placed in the beam path. The target surface was then moved into the beam path, when in the beam path a gas signal would be measured. The target surface orientation was then manipulated to maximise the backscattered light. The 10,000ppm.m sample was then swapped for a 100ppm.m sample to ensure that this could be adequately detected.

CH₄:N₂ samples were taken from Strathclyde University in Tedlar bags, the same type used during laboratory trials. These were seen as more practical than using the Perspex cell as they have a lower attenuation (22%) and are less permeable. The output power of the Raman amplifier was set to 1.9W for the duration of the trials giving an effective transmit power of 1.5W when corrected for the 22% attenuation by the Tedlar bag.

Photographs of the system in the rear of the van and the placement of a concrete target surface can be seen in figure 5.17 (note the less than ideal weather conditions).

The target distance was increased until the 1f receiver signal had a signal-to-noise ratio of ~3:1. Using a 100ppm.m CH₄:N₂ sample and a concrete target this was determined to be at 105m. This is longer than our original target distance of 100m, but shorter than the distance predicted from the laboratory trials. Laboratory trials predict that with a 1.5W effective output power that our detection range should be around 200m. There are potentially many reasons for this discrepancy:

1. It was noticed that the generator noise created a high DC background signal at the detector, which reduced the SNR.

2. Natural daylight conditions introduced a substantial and changing background signal at the detector. A bandpass filter (Thorlabs) had previously been employed but this introduced around a further 20% attenuation at 1650nm.
3. Natural daylight saturated the IR card making optimal alignment of the laser and target difficult.
4. A laser pointer that had been aligned with the beam at a distance of 76m in a long corridor at the University failed to operate in the cold weather outside.
5. The Tedlar bags deflated over the course of the day and so lost concentration. They would also have been diluted by air.
6. Rain created wet optics, targets and Tedlar sample bags. This would have altered the reflection from the surfaces and caused scattering.

The graphs in figure 5.19 show the 1f traces from a concrete target with sample concentrations of 10,000ppm.m, 1000ppm.m and 100ppm.m. There is also a 1f trace of the background methane signal – at this distance the background concentration is approximately 360ppm.m (1.7ppm over a 210m path length). 1f traces from plywood and white card targets are in appendix A5.2.

The graph in figure 5.19 shows a comparison between the different concentration measurements made using a plywood target to show the correlation between signal amplitude and concentration. Inset in figure 5.19 is a comparison between the signal of a 100ppm.m measurement and the background methane measurement. These look almost indistinguishable, however we have to take into account the 22% attenuation of the Tedlar bag which was present in the 100ppm.m measurement and not in the background measurement.

Given the difficulties noted earlier we are confident that at 105m we should easily be able to resolve an increase in methane of 100ppm.m. By removing sources of noise, better generator/power supply, better 1651nm bandpass filter to reduce ambient light on the detector and operating in better conditions (less wind and rain) then we are confident that the system should more closely match the laboratory performance of the sensor and detect a 100ppm.m increases in methane at around 200m.

Other improvements to the system have the potential to increase the range and usability of the system even further. These will be discussed in chapter 6.

As pointed out earlier I would like to thank David Mitchell and Kevin Duffin for their efforts in making laboratory measurements and characterisation of the system and for conducting field trials in the wind and rain.

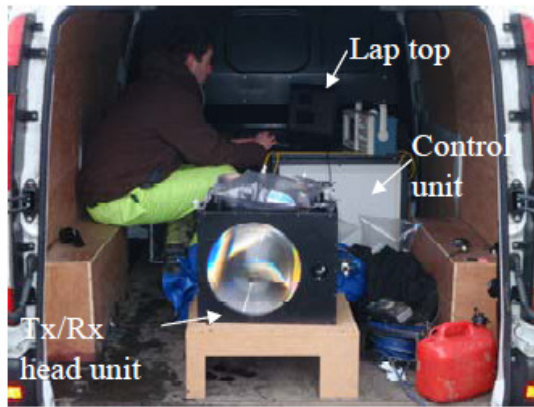
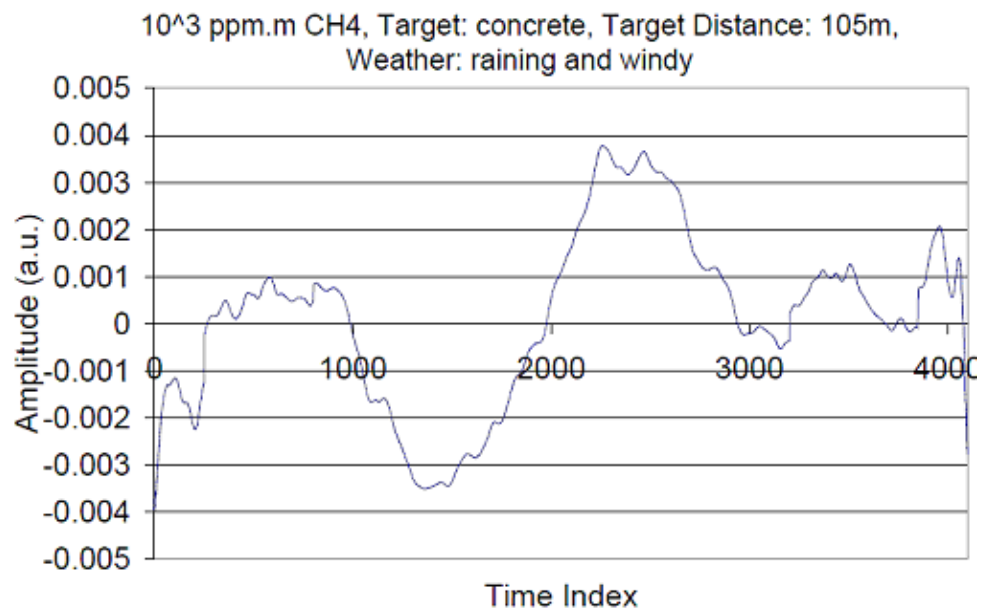
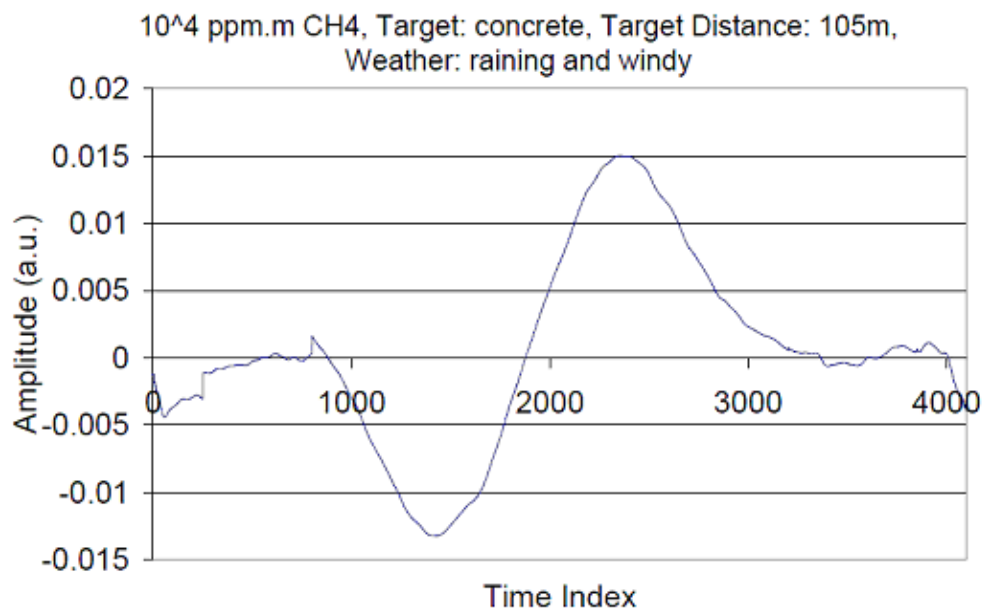


Figure 5.17: Photos taken of field trials.



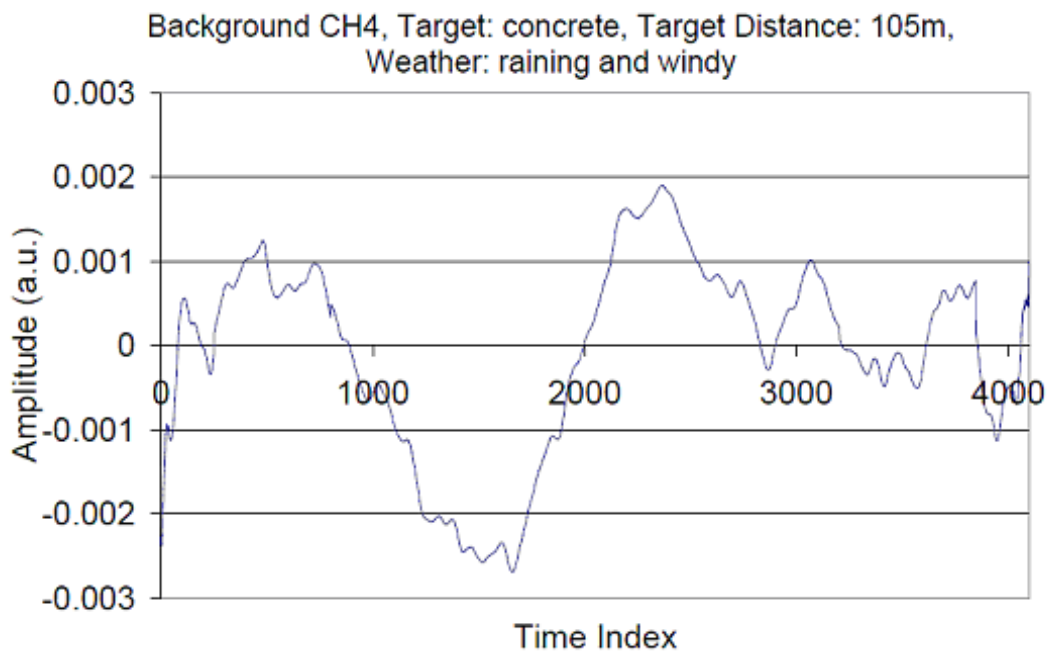
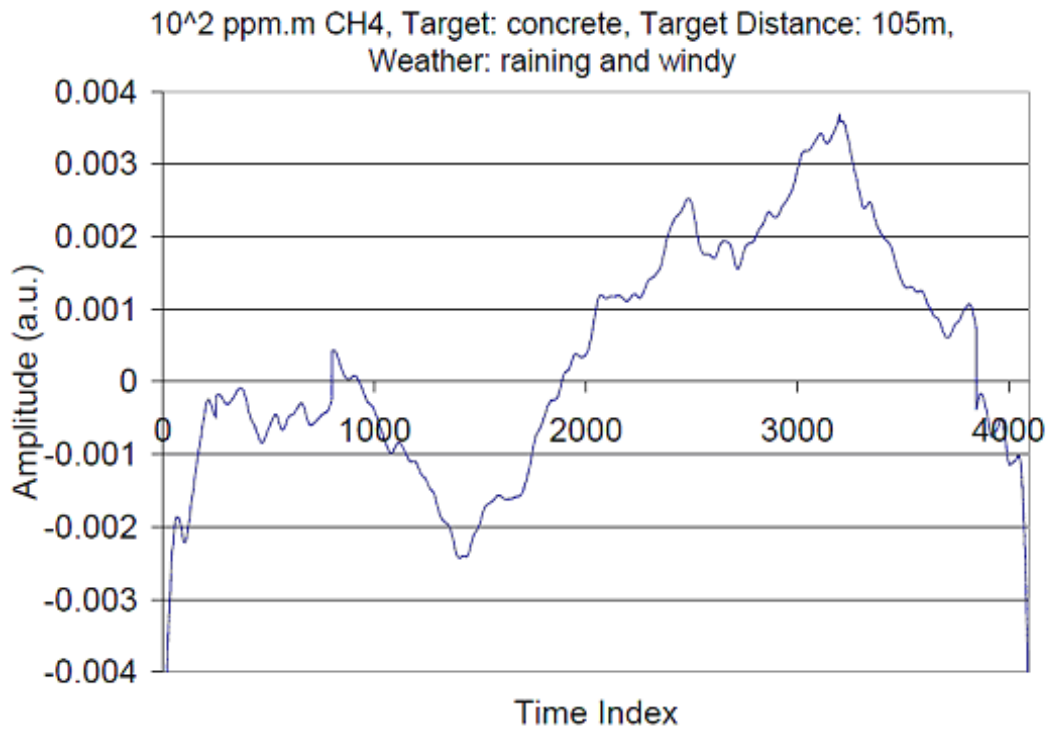


Figure 5.18: Measurements of 10,000ppm.m, 1000ppm.m, 100ppm.m methane samples made using the demonstrator at 105m during field trials.

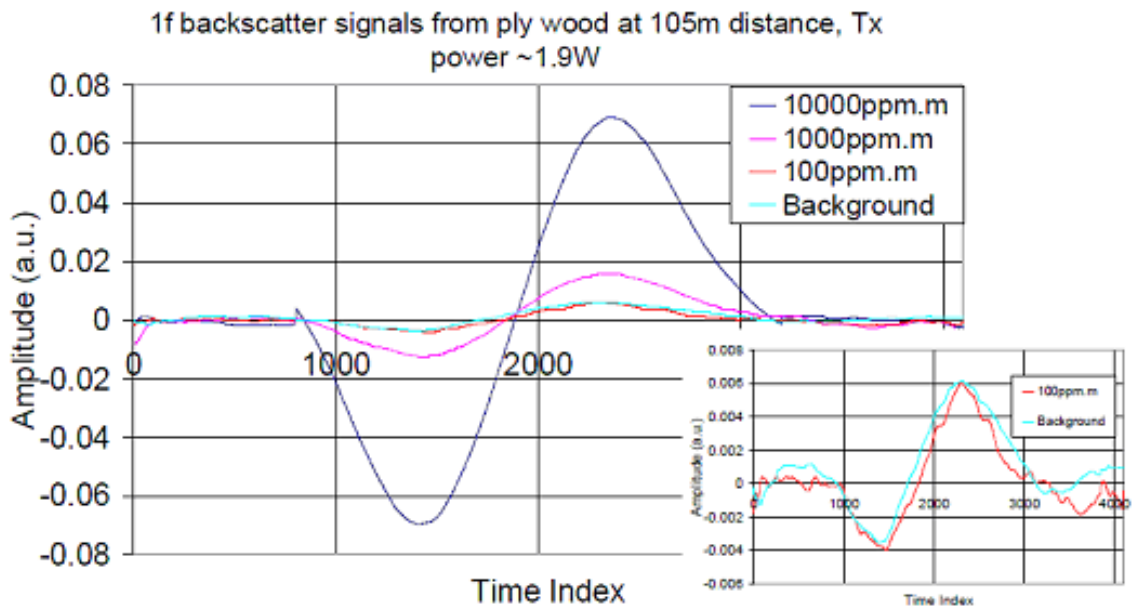


Figure 5.19: Measurements of different concentrations of methane at 105m. Inset: expanded image of 100ppm.m and background measurement.

References

- [5.1] Ross Elliot, Evanesco Ltd. Internal correspondence
- [5.2] David Moodie, Optosci. Internal correspondence
- [5.3] Kevin Duffin and David Mitchell, University of Strathclyde, Internal correspondence

Appendix A5.1: Laboratory methane concentration measurement off a rusty metal plate and white card.

Rusty Metal...

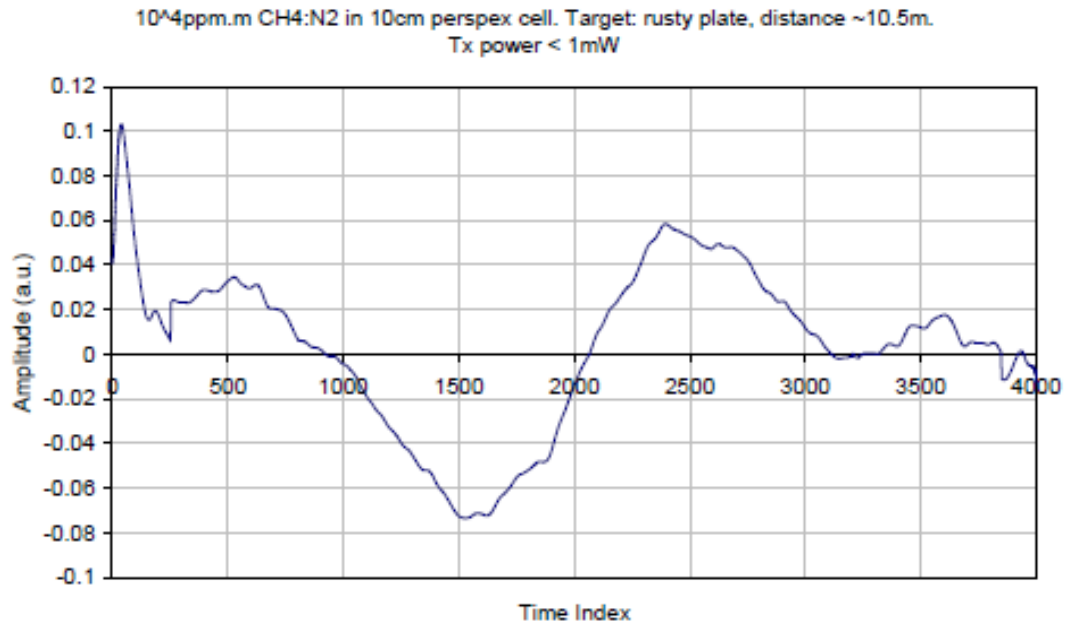


Figure A1: 10,000ppm.m CH₄, rusty metal

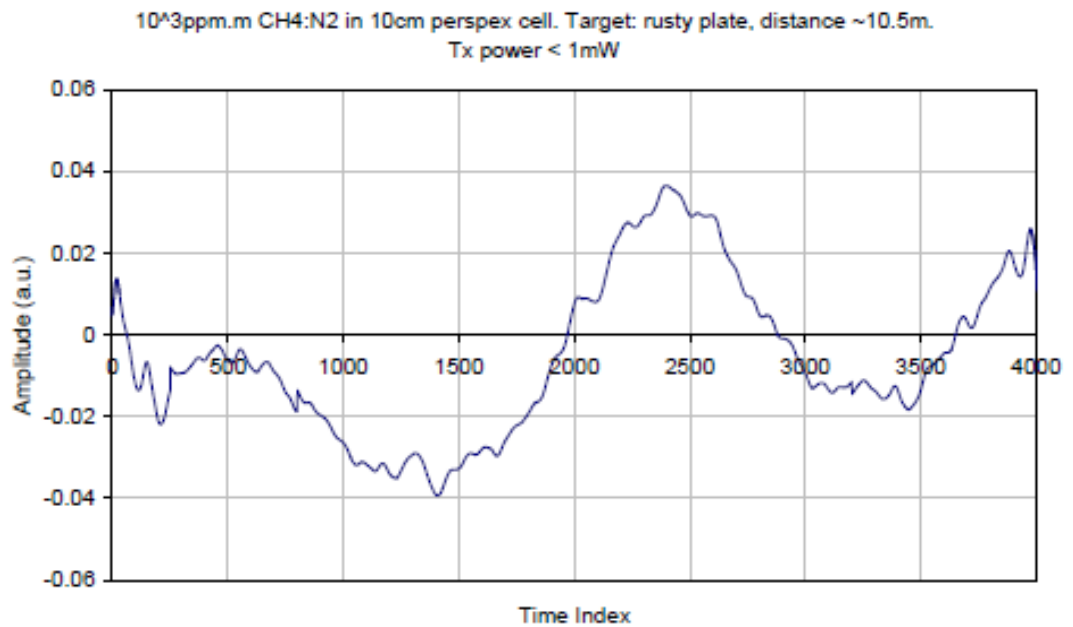


Figure A2: 1,000ppm.m CH₄, rusty metal

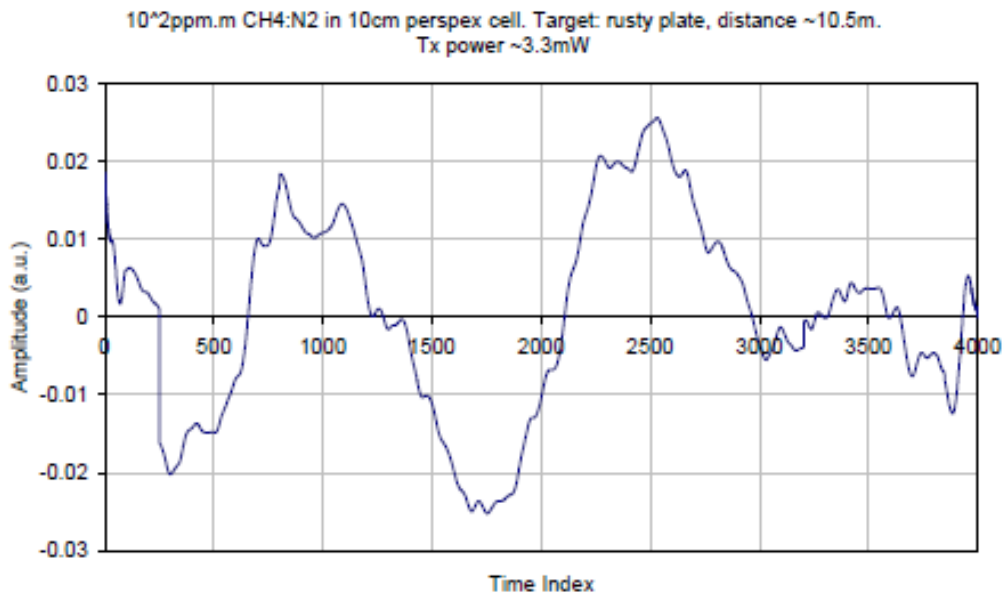


Figure A3: 100ppm.m CH₄, rusty plate

White Card...

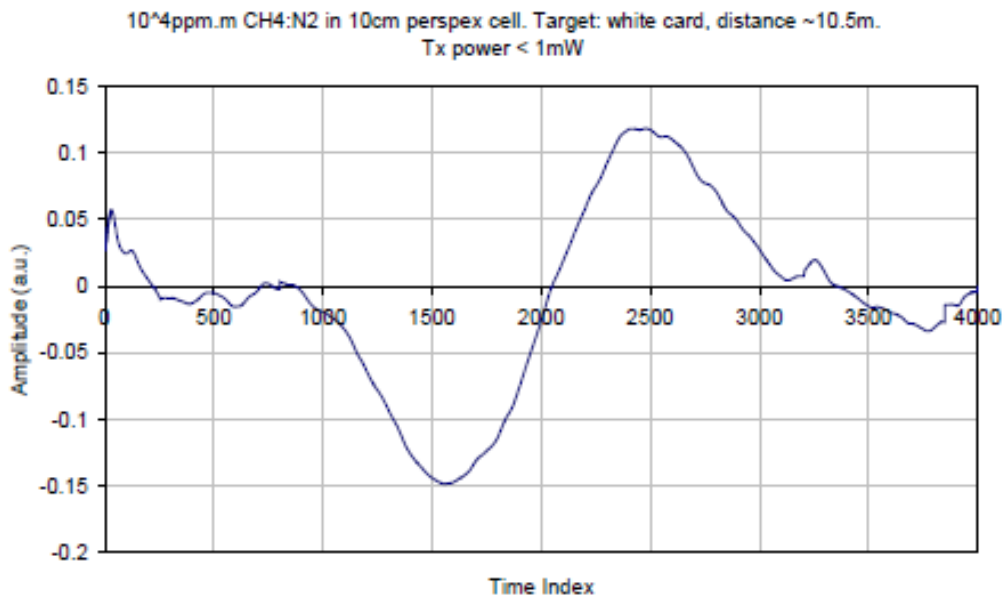


Figure A4: 10,000ppm.m CH₄, white card

10^3 ppm.m CH₄:N₂ in 10cm perspex cell. Target: white card, distance ~10.5m.
Tx power < 1mW

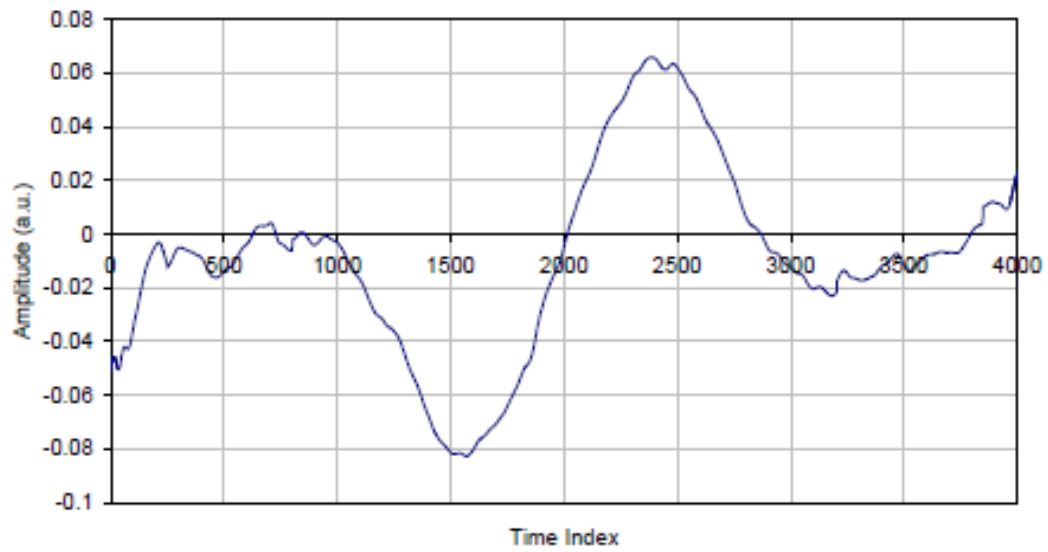


Figure A5: 1,000ppm.m CH₄, white card

10^2 ppm.m CH₄:N₂ in 10cm perspex cell. Target: white card, distance ~10.5m.
Tx power ~3.3mW

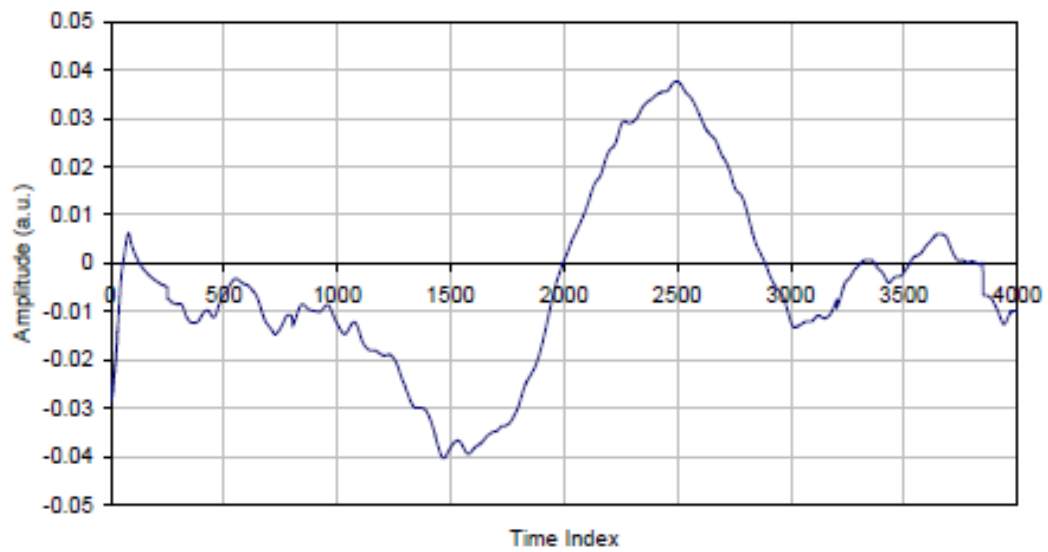


Figure A6: 100ppm.m CH₄, white card

Appendix A5.2: Field trial measurements at 105m range from plywood and white card.

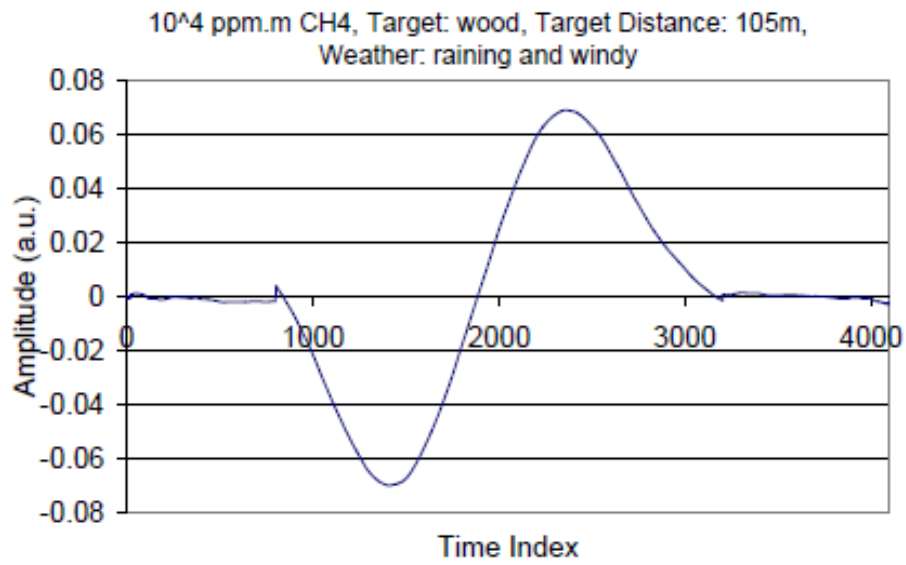


Figure B1: 10,000ppm.m CH₄ plywood

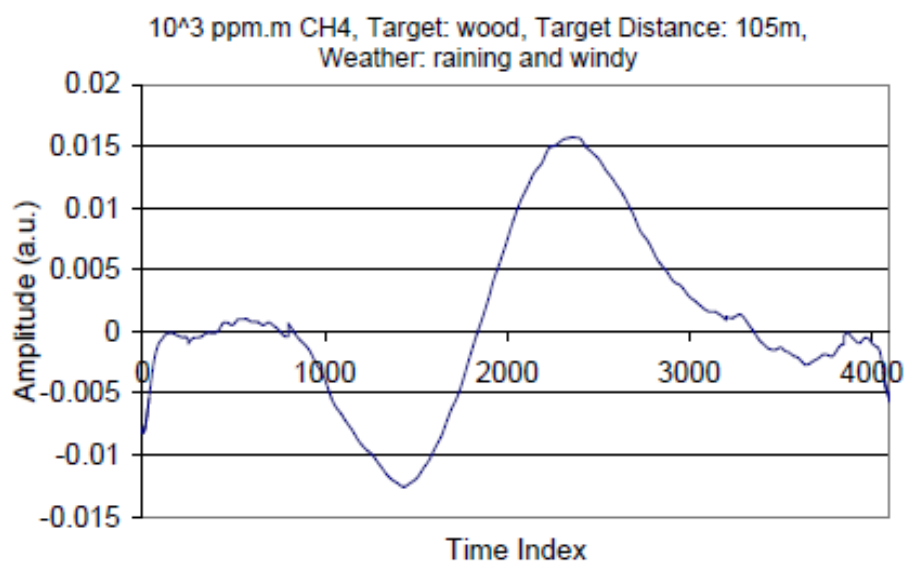


Figure B2: 1,000ppm.m CH₄ plywood

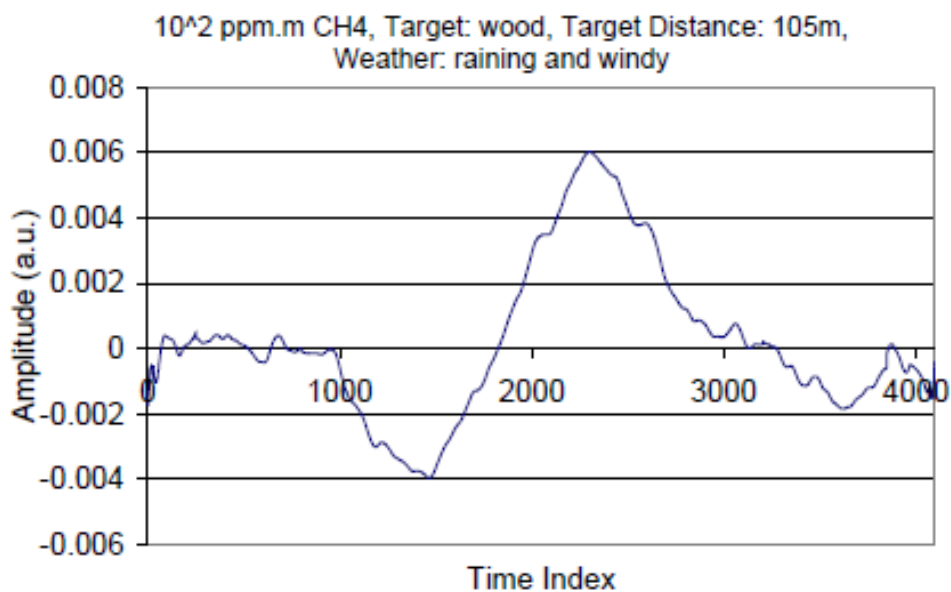


Figure B3: 100ppm.m CH₄, ply wood

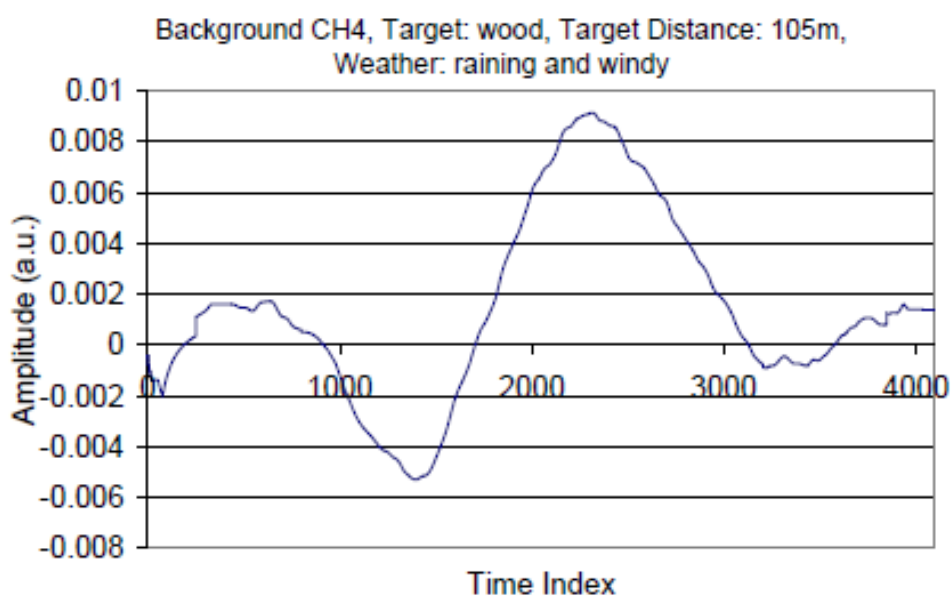


Figure B4: Background CH₄, ply wood

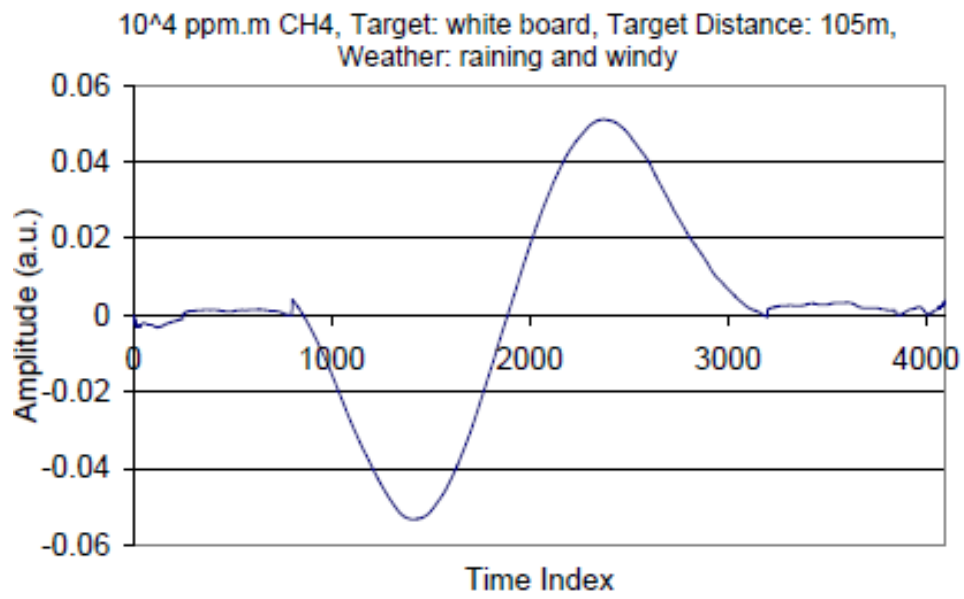


Figure B5: 10,000ppm.m CH₄ white board

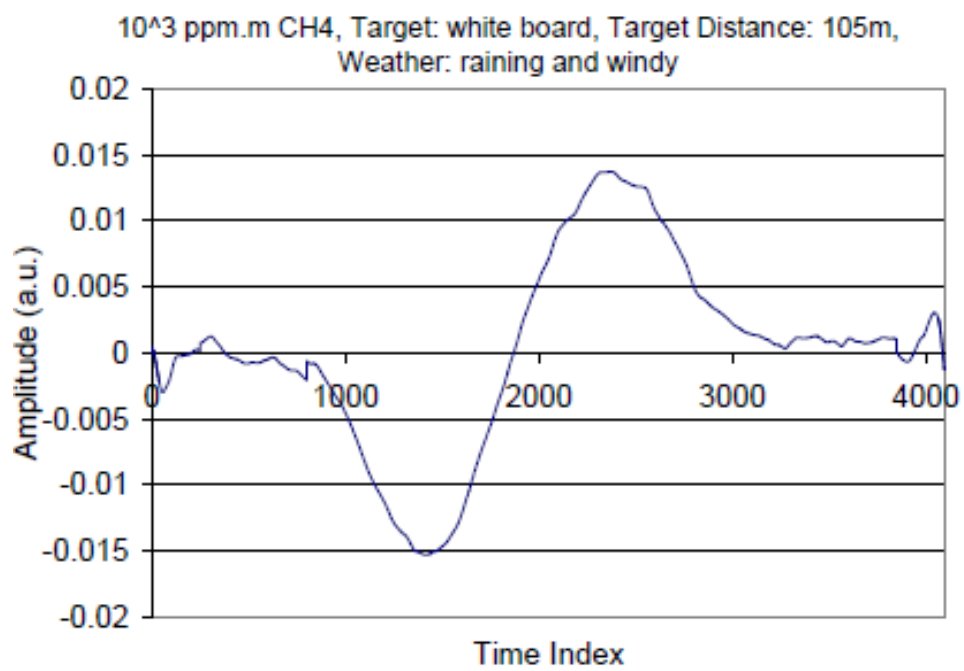


Figure B6: 1,000ppm.m CH₄ white board

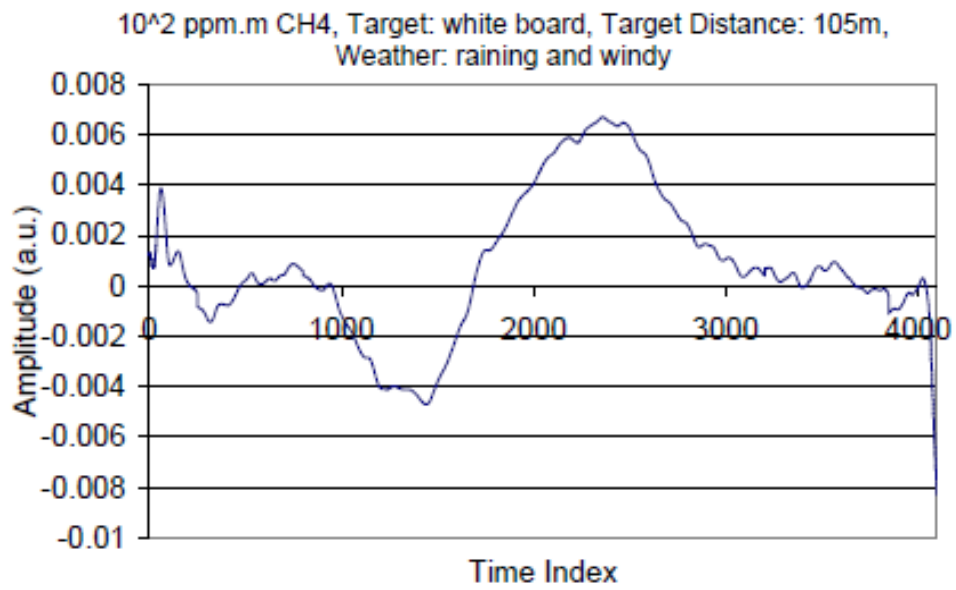


Figure B7: 100ppm.m CH₄, white board

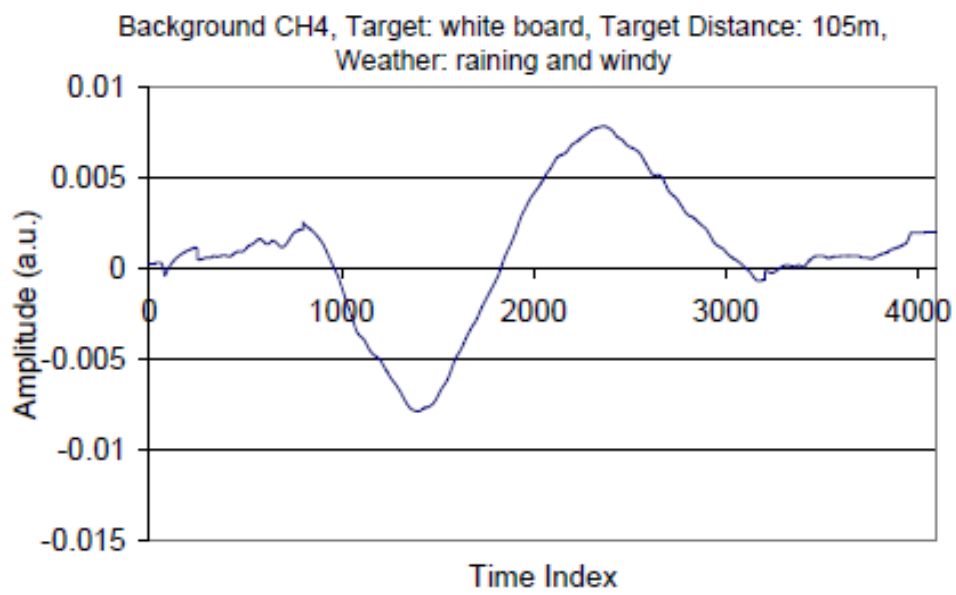


Figure B8: Background CH₄, white board

Chapter 6 - Conclusion

This chapter summarises the results and conclusions that can be drawn from the Raman fibre amplifier build and prototype methane sensor development. It also includes suggestions for improvements to the system and further development work that could be done to advance the system.

This chapter is structured as follows:

- **Section 6.1 - Achievements of Raman Amplifier build** - Summarises the achievements of the Raman amplifier build.
- **Section 6.2 - Achievements of System Integration** - Summarises the achievements of the integration of the system.
- **Section 6.3 - Next Stage Improvements to the Methane Sensor** - Puts forward suggestions for improvements which could be made to the methane sensor.
- **Section 6.4 - Would be interesting / Further work** - Suggests possible next steps in the development of the methane sensor including things which would be necessary for commercialisation and additional features which could be useful to investigate and demonstrate.

6.1 Achievements of Raman Amplifier build

The long range TDLS methane sensor that formed the principle output of this project required the development of an advanced fibre amplifier system, with a high output power and a narrow linewidth at 1651nm. It also needed to amplify the signal as the wavelength was dithered for TDLS without distorting the output waveform. The completed amplifier utilised a combination of an Er-Yb amplifier and a Raman amplifier (frequency shifter) to amplify a 10mW DFB laser to beyond 2W without significantly degrading the narrow linewidth inherent to the DFB laser.

The amplifier system was constructed from commercial off the shelf fibres and parts and constitutes a significant development in the use of Raman amplifiers for high power, narrow linewidth laser amplification. Narrow linewidth Raman amplifiers are usually limited to much lower output powers because of the onset of stimulated Brillouin scattering (SBS). To achieve amplification to these power levels methods to suppress SBS were required.

The use of Raman amplifiers for narrow line width amplification has recently been reported at around 1178nm by Fang et. al. at the European Southern Observatory [6.1]. They also use dithering to broaden the effective linewidth of the laser. They require a narrow linewidth for efficient second harmonic generation in an external bulk optic cavity. Their end application is for use as a guide star

targeting a Sodium absorption line at 589nm. They have so far achieved greater than 20W at 1178nm (10W at 589nm) and have also (more recently) shown coherent beam combination of the Raman fibre lasers [6.2, 6.3]

Our 2W 1651nm output significantly exceeded the 1W requirement which we estimated would be needed to match at 100m the sensitivity of the short range 10m TDLS methane sensors already commercially available (section 3.2).

The output power of the Raman amplifier in the original configuration (chapter 2) was limited only by the available pump power from the 7W Er-Yb amplifier. When this malfunctioned it was replaced with a commercial EDFA (Keyopsis) with an output power limited to around 5W. To compensate for the lower pump power the 1550nm CWDM filter in the ASE seed was replaced with a 1530nm CWDM filter. This channelled more power into the optimal Raman gain wavelength around 1540nm and increased the efficiency of the Raman amplifier considerably resulting in a maximum output of 2.36W. If this seed was used with the more powerful Er-Yb amplifier then 3W output would not seem unreasonable – especially if additional SBS suppression techniques like fibre strain and temperature distributions were used.

In the co-propagating configuration an output of 2.5W was reached before SBS threshold (assuming threshold at 1% backscatter power). The threshold for SBS is lower in co-propagating amplifiers than counter-propagating amplifiers because the interaction length in the fibre where both the Stokes and Signal intensities are high is longer. This is illustrated in the results of the model (section 4.2).

A model of Raman amplification which incorporates stimulated Brillouin Scattering was developed (section 4.4). This describes the processes within the amplifier well and predicts adequately the power evolution of the pump, Raman and Brillouin waves in the Raman amplifier.

6.2 Achievements of System Integration

The amplifier system was integrated into a stand alone long range methane detector. This system included electronics to monitor and control the fibre amplifier system providing closed loop power control and safety shut-down and interlock features. It also included all the hardware required to control the DFB laser for tuneable diode laser spectroscopy and a lock in amplifier and oscilloscope to demodulate and output the 1f and 2f TDLS signals. A 12” Fresnel lens and InGaAs photodetector with preamplifier were used to collect the backscattered light from topographic targets to make remote measurements.

The prototype system was characterised in a laboratory and it was found that 3.3mW was the minimum transmit power required to detect a 100ppm.m increase in methane concentration above background at a distance of 10.5m. From this we extrapolated that the system at 2W should be able to achieve the same sensitivity at greater than 200m, assuming that the backscattered power follows a square law relationship with distance. This is more than twice the original target distance of 100m that was considered to be a reasonable height for a helicopter in flight.

The prototype system was taken out for field trials to demonstrate operation at full range. These demonstrated detection of 100ppm.m methane from a range of surfaces including concrete, plywood and a white card at a range of 105m. They also demonstrated detection of background methane at ~360ppm.m from all surfaces. The demonstration of the system at longer distances was hampered by several unexpected problems which illustrate the difficulties in moving a system from the laboratory to a real environment.

If a second prototype and set of field trials were to be attempted then several of these problems could be rectified. The first problem was generator noise at the detector this was put down to poor running efficiency on a rarely used generator, as the power rating of the generator far exceeded the load. A new generator with better voltage/power regulation should solve this. The second problem was changing ambient light conditions from daylight and moving clouds. This substantially raised the background light level increasing noise. The solution to this is to use a band-pass filter centred on the 1651nm signal in front of the detector. Unfortunately, the band-pass filter that was chosen introduced substantial loss (~20%) at 1651nm and so was not used. The other problems associated with the field trials were logistical, like transporting methane samples to the test site, protecting the optics from rain and aligning the output with the target. These could be overcome with extra resources and preparation.

Given these improvements it is believed that the system should be more than capable of detection of 100ppm.m methane above background at 200m.

6.3 Next Stage Improvements to the Methane Sensor

If the methane sensor was going to be taken through to a second prototype stage then a couple of other improvements could/should be made to the design. Firstly the Er-Yb amplifier should be rebuilt with a more robust splice between the Er-Yb fibre and the passive double clad fibre of the pump combiner. The best way to achieve this is probably to perform the splice on a fusion rig and package the splice in the same way as a high power pump combiner. It may even be possible to produce a pump combiner with the Er-Yb fibre as the output fibre.

The CWDM filter in the ASE seed should also be changed from the 1550nm channel to the 1530nm channel. This would improve the efficiency of Raman amplification and allow the amplifier to reach an even greater output power. Hopefully limited not by available pump power but by the onset of nonlinear effects. It would then be possible to investigate other suppression techniques to push the power even higher. Following these simple improvements the output power could be increased to 3W or above. This would increase the range of the system, based on previous assumptions, to greater than 300m.

The next improvements to make would be to the send and receive optics. The first change would be to replace the 12" Fresnel lens used to collect the backscattered light with a telescope or off-axis parabolic mirror of the same size. The Fresnel lens that we used is made of Perspex and has an attenuation of approximately 20% at 1650nm an off axis parabolic could potentially have a much smaller attenuation. The other option would be to find a Fresnel lens from a material with lower attenuation at 1650nm. This would increase the range and sensitivity of the methane sensor by increasing collection efficiency at the detector.

In theory the received power should vary linearly with the transmitted power and to the inverse square of distance. Therefore if the collection efficiency of the receive optics is increased by $T\%$ then the distance can be increased by $1 - (1/\sqrt{1-T})\%$.

Along a similar route the size of the Fresnel lens could be increased to capture light over a larger area. Following the analysis in section 3.5 the power at the receiver is proportional to the area of the collection lens. So, doubling the lens diameter improves collection by a factor of 4. This only works to a point as generally the larger the lens the longer the focal length and the larger the focal spot (which would overfill the detector).

Another improvement could be to use a cone concentrator at the detector. This would recover some of the light which falls outside of the detector area. Takaya Iseki et. al. [6.4] use this approach for their short range detector because it allows for efficient collection of reflections at both long and short range without needing to alter the position of the photodetector to account for the change in focal position.

The final improvement would be to bring the send and receive optics onto a single optical axis. This would simplify the alignment of the system. With the send and receive optics on separate optical axis the photodetector position has to be optimised every time the range to the target is changed. Placing the send and receive optics on the same optical axis would help to eliminate this problem. However, if the backscatter targets reflection has a large specular component then the angle to the surface will always make a big difference to the received power.

6.4 Further work

To extend the work even further it would be interesting to team the system up with a scanning system. This could be used to visualise gas leaks from a distance as shown in the work of Miles Padgett et al [6.5]. They used a rotating polygonal mirror to scan the beam over a grid and synchronized this with a CCD camera. They overlaid the gas concentration measurements onto the CCD image to produce a real time (several Hz) video of the gas leak.

If the system was to be used on an aircraft or fast moving vehicle then it would probably be necessary to link the system with a GPS position. So that leak detections could be followed up easily by ground based inspection and maintenance.

A very similar system to ours using an ytterbium amplifier to Raman amplify a DFB laser at $1.27\mu\text{m}$ for sensing of Oxygen has recently been reported [6.6]. This used two Raman amplifiers and two DFB lasers, one online and one offline to produce a ratiometric gas measurement. We should in theory be able to readily adapt our amplifier to this wavelength and demonstrate the powerful TDLS-WMS technique. In theory we could target any gas with an absorption line at a wavelength within a Stokes frequency shift of a rare earth fibre amplifier.

To lead us into the second project it is worth mentioning that a Faraday isolator on the output of the amplifier would help prevent reflected light from re-entering the fibre and travelling the wrong way through the amplifier. Light travelling in this direction depletes gain and changes the dynamics of the amplifier and can destabilise the output. This would affect the sensitivity of the TDLS technique. In extreme cases the reflected light can be amplified to such an extent that it can cause damage to the pump and seed laser diodes in the amplifier.

During the first construction of the 7W EDFA we experienced multiple diode failures at the same time. It is believed that this occurred because of back-reflected light from a fibre end which was not angle cleaved. The rest of this thesis describes the development of a Faraday isolator for ytterbium fibre amplifiers operating around 1060nm, but the basics of the design could be carried forward, with a different choice of materials, to other wavelength ranges.

References

- [6.1] Yan Feng, Luke Taylor, and Domenico Bonaccini Calia, "Multiwatts narrow linewidth fiber Raman amplifiers," *Opt. Express*, 2008, Vol. 16, pp. 10927-10932
- [6.2] Yan Feng, Luke R. Taylor, and Domenico Bonaccini Calia, "25 W Raman-fiber-amplifier-based 589 nm laser for laser guide star," *Opt. Express*, 2009, Vol. 17, pp. 19021-19026
- [6.3] Luke Taylor, Yan Feng, and Domenico Bonaccini Calia, "50W CW visible laser source at 589nm obtained via frequency doubling of three coherently combined narrow-band Raman fibre amplifiers," *Opt. Express*, 2010, Vol. 18, pp. 8540-8555
- [6.4] Takaya Iseki, Hideo Tai and Kiyoshi Kimura, "A portable remote methane sensor using a tunable diode laser," *Meas. Sci. Technol.*, 2000, Vol. 11, pp. 594–602.
- [6.5] Graham Gibson, Ben van Well, Jane Hodgkinson, Russ Pride, Rainer Strzoda, Stuart Murray, Steve Bishton and Miles Padget "Imaging of methane gas using a scanning, open-path laser system," *New J. Phys.*, 2006, Vol. 8
- [6.6] J. A. Nagel, V. Temyanko, J. Dobler, E. M. Dianov, A. S. Biriukov, A. A. Sysoliatin, R. A. Norwood, and N. Peyghambarian "High-Power Narrow-Linewidth Continuous-Wave Raman Amplifier at 1.27 μm ," *IEEE Photonics Technology Letters*, 2011, Vol. 23, No. 9

Chapter 7 - Development of a Fibre-in Beam-out Isolator for Fibre Amplifiers

This chapter introduces the second project in this dissertation, to develop a Faraday isolator for use at the output of high power fibre amplifiers and lasers. This was an internal project with the aim of producing a completely new product and capability within Gooch and Housego. The project used expertise from multiple sites across the Gooch and Housego Group.

This chapter introduces the background, motivation and aims of this project and is structured as follows:

- **Section 7.1 – Introduction** – Describes the background to the project explaining the need for a Faraday isolator.
- **Section 7.2 – Outline of Isolator** – Describes how we propose to address the problems associated with making a high power isolator.
- **Section 7.3 – Objectives** – Lists the specific objectives of the project.
- **Section 7.4 – Overview of following chapters**

7.1 Introduction

Fibre lasers and amplifiers due to their high gain and wave-guiding nature are highly susceptible to optical back-reflections. These can cause the laser output to destabilise and are often cited as a damage mechanism, causing failure of the seed and pump diodes.

In a fibre amplifier system back-reflections generally arise at two points:

- 1) From the silica-air interface at the output end of the fibre; and
- 2) From external reflections off focussing optics and the work piece.

The first source of back reflections from the silica-air interface can easily be reduced by cleaving the fibre at an angle, splicing a coreless section of fibre (an end-cap) onto the end of the fibre or by depositing an anti-reflection (AR) coating onto the fibre/end-cap surface.

If we think about the structure of a single mode fibre then angle cleaving prevents back reflections by altering the angular divergence of the reflected light with respect to the core, as demonstrated in figure 7.1a. The reflected light then falls outside of the numerical aperture of the core and is lost to the cladding. Light in the cladding is quickly attenuated or can be stripped out with a high index coating.

End-caps suppress back reflections by allowing the light to diverge away from the fibre core before reflecting off the silica-air interface. The light travelling back towards the fibre then diverges further so that most of the returned light does not couple into the core of the fibre, as shown in figure 7.1b. The reflected light is lost as cladding modes which are quickly attenuated as before.

Anti-reflection (AR) coatings use interference to reduce the Fresnel reflection from the silica-air boundary and can be applied to a perpendicularly cleaved fibre; an angle cleaved fibre or an end-cap.



Figure 7.1: Suppression of back reflection using a) an angled cleave; and b) an end-cap. In each case light in the core of the fibre is lost to the cladding (dotted lines)

The ratio of the output power from a fibre to the amount of back reflected light captured by the core of the fibre is known as the return loss (or optical return loss) measured in decibels (dB) This is an important measurement which is used to characterise fibre optic devices. Angled cleaves and end caps have been shown to reduce optical return loss from around -14dB for a perpendicular cleave to below -60dB [7.1].

The second source of back reflections from external optics and work pieces are more difficult to eliminate. This is a consequence of optical reversibility and the fact that the optics designed to create an image of the fibre core at the work piece will also image the work piece onto the fibre core. The outcome of this is that any reflected light falling within the numerical aperture of the focussing lens will automatically be refocused onto the fibre core.

The obvious way to minimise this is to angle the work piece and reduce specular reflection from the optical system. However, this is not always desirable from a process point of view, especially when working with highly reflective materials like copper. A more robust solution to the problem is to place a non-reciprocal optical element in the beam path between the fibre and the work piece. This non-reciprocal element would be transparent to light travelling in one direction but opaque/reflective to light travelling in the other direction. This non-reciprocal element is a Faraday isolator.

The aim of this project is to develop a fibre-in beam-out Faraday isolator to be used with fibre amplifier systems for material processing. It would also be useful for fibre amplifier systems such as

that described in chapters 1-6 of this thesis. The fibre isolator will target continuous wave and pulsed fibre amplifiers with output powers of greater than 50W. These lasers require Faraday isolators for robust operation and are currently underserved by device manufacturers. Though, since the project began the number of manufacturers targeting this market has increased quickly [7.2-7.4].

The challenge of creating a Faraday isolator for high power operation comes down to the management of thermal effects. Thermal effects disrupt the operation of a Faraday isolator by inducing unwanted polarisation changes. These affect the isolation and insertion loss of the isolator. They also cause thermal lensing which affects the application by changing the waist position and spot size of the focussed beam.

In non-commercial (cost insensitive) applications these effects can be overcome by increasing the beam size through the device. This decreases the light intensity and temperature gradients in the device. However, this requires scaling of the Faraday isolator materials and considerably increases the cost of the Faraday isolator. The alternative approach is to include compensation schemes which counteract the unwanted effects, whilst keeping the isolator dimensions small. This approach, although much more complex, should allow a Faraday isolator to be produced at an acceptable cost.

7.2 Outline of Proposed Isolator

To build an isolator which operates at 50W or more we assume that we will have to overcome thermal effects caused by the small residual absorption in the optical components. The three most important effects have been identified as thermal stress induced depolarisation, thermal lensing and the thermal dispersion of the Verdet constant.

Thermal stress induced birefringence, as the name suggests, is birefringence which is created by stresses induced by temperature rises and thermal gradients. These stresses are temperature dependent and generally get worse with increasing temperature. The birefringence that they create changes the polarisation of light as it passes through the material. In the case of an isolator this can have a disastrous effect on the isolation, and a slight effect on the insertion loss.

Thermal stress induced birefringence also affects high power solid state lasers and consequently has been well researched. Methods to compensate for thermal stress induced depolarisation include splitting the gain medium into two identical pieces, with the same temperature profiles, separated by a 90° polarisation rotator; or rotating the beam through 90° and double passing the same element. If we consider the birefringent crystal to be a phase plate with an arbitrary phase profile then double passing after swapping the radial and tangential polarisation components effectively cancels any phase change with an equal and opposite phase change on the second pass [7.5]. The same principals can be applied

to Faraday isolators [7.6]. In the course of this work isolator designs which compensate for thermal stress induced depolarisation will be discussed and analysed.

Thermal lensing is caused by the change in the refractive index of materials with temperature. If the temperature gradients in a material are symmetric around the beam centre and parabolic, as is the case with Gaussian pumping, then the refractive index of the material has a parabolic profile. This acts like a lens duct and focuses the beam. The focal length of this lens is power dependent as more power gives larger gradients. A method to compensate for thermal lensing by introducing an element with a negative thermal lens and balancing positive and negative thermal lenses in the isolator will be tested as part of the isolator development.

The thermal dispersion of the Verdet constant introduces non uniform rotation across the beam. This causes a shift in the polarisation between different parts of the beam. At the polarisers this “depolarisation” causes an increase in loss in the forward direction and transmission in the reverse direction. A method to compensate for this loss will be discussed.

The isolator will be of a “traditional” polarisation-independent, bulk optic design coupled to a fibre collimator. The aim is to have a power independent isolation of greater than 30dB up to 50W output power and an insertion loss of less than 0.5dB to match up with the specification of commercially available lower power isolators [7.2-7.4].

When this project was started the highest power commercially available fibre coupled isolators had maximum average power handling of between 10W and 20W. However, in the last year several companies have introduced higher power isolators with average power handling of 30W to 50W [7.2, 7.4]. The state of the art in non-commercial Faraday isolator development is being conducted for the laser interferometers used in the gravitational wave observatories, especially LIGO, which are moving to higher powers to increase sensitivity. These are described in more detail in section 8.5.

7.3 Objectives

The specific objectives of the project are:

1. To design and construct a polarisation independent faraday isolator with a fibre input.
2. To investigate Faraday isolator designs that compensate for thermal effects.
3. To implement thermal lens compensation on the isolator.
4. To characterise the isolators performance up to (or greater than) 50W.

7.4 Overview of following chapters

The rest of this project is discussed in chapters 8 to 11 of this thesis.

Chapter 8 describes the theory of the Faraday Effect and how it can be used to produce optical isolators. It also discusses the thermal effects which affect the performance of Faraday isolators at high powers.

Chapter 9 continues the discussion of thermal effects concentrating mostly on thermal lensing. It describes how thermal lensing can be modelled, predicted, measured and compensated.

Chapter 10 Describes the design of the isolators that we built and examines the measurements made to characterise them.

Chapter 11 concludes the project and looks at how the Faraday isolator could be advanced and how it is being advanced in the future.

References

- [7.1] Alexandre Wetter, Mathieu Faucher, Benoit Sévigny, Nelson Vachon, "High core & cladding isolation termination for high power lasers and amplifiers," Fiber Lasers VI: Technology, Systems, and Applications, Proceedings of the SPIE, 2009, Vol. 7195
- [7.2] EOT Isolators, online: <http://www.eotech.com/>, Retrieved: 20/07/2011
- [7.3] OFR Isolators, online: http://www.ofr.com/io_intro.htm, Retrieved: 20/07/2011
- [7.4] Agiltron Isolator, online:
<http://www.agiltron.com/pdfs/high%20power%20fiber%20collimator%20with%20isolator.pdf>
Retrieved: 20/12/2011
- [7.5] W. Koechner, "Solid-State Laser Engineering," 6 ed., Berlin: Springer, 2006.
- [7.6] Efim A. Khazanov, Oleg V. Kulagin, Sanichiro Yoshida, David B. Tanner, and David H. Reitze, "Investigation of Self-Induced Depolarization of Laser Radiation in Terbium Gallium Garnet," IEEE Journal of Quantum Electronics, 1999, Vol. 35, No. 8

Chapter 8 - Faraday Isolator Theory

This chapter explains the theory needed to understand the operation of a Faraday Isolator and introduces the thermal effects which limit the operation of isolators at high power. The chapter finishes with a brief overview of the state-of-the-art in Faraday isolator development.

This chapter is structured as follows:

- **Sections 8.1 – Faraday Effect** –Describes the Faraday Effect introducing key concepts like the Verdet constant.
- **Section 8.2 - Derivation of Becquerel’s Verdet Constant Expression** – Description of the origin of the Verdet constant.
- **Section 8.3 – Faraday Isolators** - Describes some basic theory required for an understanding of the operation of an isolator.
- **Section 8.4 - Thermal Effects in Faraday Isolators** – Describes thermal effects in Faraday isolators.
- **Section 8.5 – State of the Art** - Describes the state of the art in the field of isolator development.

8.1 Faraday Effect

In 1845 Michael Faraday discovered that the plane of polarisation of light rotated as it passed through a lead glass in the presence of a magnetic field, the “Faraday Effect” [8.1]. He attributed this to circular birefringence, a difference in phase velocity between right and left circularly polarised light, induced by the magnetic field. Empirically he found that the magnitude of rotation θ was given by

$$\theta = VB.l \quad (8.1)$$

Where B is the magnitude of the magnetic field parallel to the light propagation direction, l is the distance travelled in the material and V is a material proportionality constant known as the Verdet constant. The Verdet constant is usually expressed in Radians $T^{-1}m^{-1}$, and by convention is positive if the rotation is clockwise when the light travels in the direction of the magnetic field. [8.2]

The Faraday Effect is unique from most other optical effects because the rotation it causes is non reciprocal, i.e. it does not “undo” itself if the light travels through the material in the opposite direction. Instead, the rotations add to give twice the rotation of a single pass. This can seem counterintuitive from the dot product term in equation 8.1, since reversing the direction changes the

sign of the vector and the sense of rotation of the light. This is resolved by looking at the effect from two different reference frames, the lab frame and one which travels with the light.

If you were to “ride along” with the light through a Faraday material then you would see that the sense of rotation changes with the direction of the magnetic field. The light would rotate clockwise when travelling in the direction of the magnetic field vector and anti-clockwise when travelling in the opposite direction. However, when viewed from a single direction (the “lab frame”) the sense of rotation would appear to be independent of the direction in which the light was travelling.

A theoretical explanation for the origin of the Faraday Effect was not recognised until 1887 by Becquerel. Becquerel used a classical model of electrons as a collection of harmonic oscillators and realised that the difference in refractive index for left and right circularly polarised light was the result of Larmor precession of electrons in the presence of a magnetic field. Arriving at an expression for the Verdet constant [8.3, 8.4]

$$V = -\frac{e\lambda}{2mc} \frac{dn}{d\lambda} \quad (8.2)$$

Where e and m are the charge and mass of an electron, λ is the wavelength, c the speed of light, n the refractive index and $dn/d\lambda$ is the wavelength dispersion of the refractive index.

8.2 Derivation of Becquerel’s Verdet Constant Expression

The electric field $E(z,t)$ of an EM wave travelling in the z direction can be decomposed into 2 orthogonal components [8.5]

$$\begin{aligned} E(z,t) &= \hat{x}E_x(z,t) + \hat{y}E_y(z,t) \\ E_x(z,t) &= E_{0x} e^{i(kz - \omega t)} \\ E_y(z,t) &= E_{0y} e^{i(kz - \omega t + \phi)} \end{aligned} \quad (8.3)$$

Where E_{0x} and E_{0y} are the magnitudes of the x and y components respectively and ϕ is the phase difference between E_x and E_y .

If there is no phase difference ($\phi=0$) between the x and y components then the electric field vector travelling in the z-direction traces out a straight line in the x/y plane with both position and time with a relative slope given by E_{0x}/E_{0y} . Such a wave is said to be plane polarised.

If the phase difference between the x and y components is $\pm\pi/2$ ($\pm 90^\circ$) and $E_{0x} = E_{0y}$ then the electric field vector traces out a circle in the x-y plane, like a corkscrew around the z-direction. Such a wave is circularly polarised. By convention, a wave with an electric field which rotates in the clockwise direction ($\phi=+\pi/2$) is right circularly polarised; a left-handed wave rotates anti-clockwise.

All other combinations of the electric field vector are described as elliptical polarisations.

It can readily be shown from equation 8.3 that a linearly polarised EM wave is produced by the addition of equal magnitude left circularly and right circularly polarised waves, with a slope determined by the phase difference between the two circularly polarised waves.

In a medium with circular birefringence left and right circularly polarised waves experience a different refractive index. This creates a phase difference between the two circularly polarised waves which manifests itself as a rotation of the plane of polarisation. The rotation angle θ is given by (see appendix A8.1)

$$\theta = (n_R - n_L) \frac{\pi d}{\lambda} \quad (8.4)$$

Where n_R is the refractive index of the right circularly polarised wave and n_L is the refractive index of the left circularly polarised wave, d is the distance travelled through the medium and λ is the wavelength of light.

When a magnetic field is applied to a material the charged electrons (dipoles) preferentially align with the magnetic field and precess at the Larmor frequency ν_L

$$\nu_L = \frac{eB}{4\pi m} \quad (8.5)$$

where e and m are the electrons charge and mass and B is the magnitude of the magnetic field. Right and left circularly polarised light travelling through the material will have effective frequencies shifted up or down by the Larmor frequency respectively [8.3]. Since refractive index is frequency dependent then

$$\begin{aligned}
n_R - n_L &= n(v + v_L) - n(v - v_L) \\
n_R - n_L &= \left(n(v) + \frac{dn}{dv} v_L \right) - \left(n(v) - \frac{dn}{dv} v_L \right) \\
n_R - n_L &= 2v_L \frac{dn}{dv}
\end{aligned} \tag{8.6}$$

Putting equations 8.5 and 8.6 into 8.4 and using the chain rule yields

$$\theta = \frac{e}{2mc} \lambda \frac{dn}{d\lambda} Bd \tag{8.7}$$

Comparing to equation 8.1 gives Becquerels expression for the Verdet constant.

8.3 Faraday Isolators

The non-reciprocal rotation caused by the Faraday Effect can be used to make optical isolators. These act like diodes for light and allow light to pass in just one direction, while blocking or redirecting light from the other direction. The simplest design of a Faraday isolator can be seen in figure 8.1. In this design, light travelling in the forward direction (from left to right) is vertically polarised by polariser 1, then rotated clockwise 45° by a Faraday rotator before passing through polariser 2 with its axis at 45° relative to polariser 1. Light travelling in the reverse direction (from right to left) is polarised at 45° by polariser 2 then rotated anticlockwise 45° by the Faraday rotator so that it is horizontally polarised and thus rejected/absorbed by polariser 1.

The downside of this simple isolator design is that it only works with a low insertion loss for an input beam with a plane polarisation which can be aligned with the transmission axis of polariser 1, for this reason it is known as a polarisation-sensitive isolator. This type of isolator would be suitable for use with fibre lasers and amplifiers made from polarisation maintaining (PM) fibre. These have linearly polarised outputs with high polarisation extinction ratio.

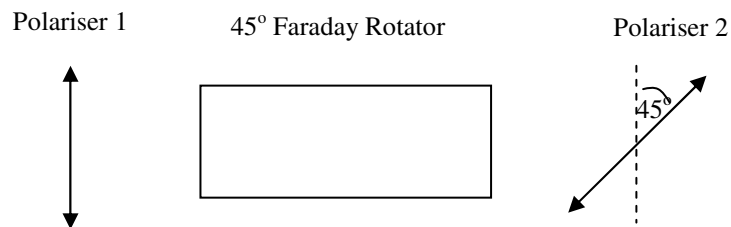


Figure 8.1: Faraday Isolator basic schematic

However, most fibre lasers are not made from PM fibre and as a result will not work with the design of isolator in figure 8.1. In general fibre lasers and amplifiers have a “random” time-varying polarisation output. This means that the isolator design has to be made polarisation-insensitive. To make a polarisation insensitive isolator we need to change the method of polarisation. The first polariser needs to separate the input light into its two orthogonal polarisation states, so they can be rotated separately by the Faraday rotator before being recombined by the second polariser. An example of a polarisation insensitive isolator can be seen in figure 8.2.

The design in figure 8.2 uses birefringent wedges with different refractive index for the e- and o-polarisation states to spatially separate (and recombine) the orthogonal polarisation states of the light either side of a 45° Faraday rotator. The polarisation changes in the forward direction cause the beams to recombine at the second birefringent wedge. In the reverse direction the beams do not recombine and leave with an offset from the input.

Polarisation insensitive isolators are ideal for lasers with random or unpolarised outputs because they will effectively transmit all polarisations of light. They may be unsuitable for polarised sources because the different paths taken by the two orthogonal polarisation states can result in a phase change between them which will change with temperature and wavelength. Thus the recombined output beam may not have a well defined polarisation state. In polarisation insensitive isolators used in telecommunications the optical path lengths through the device are often matched to prevent polarisation mode dispersion. [8.6]

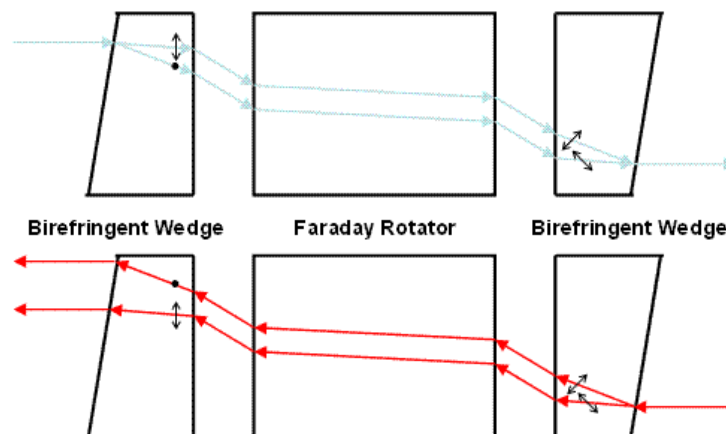


Figure 8.2: Polarisation Independent Faraday Isolator using birefringent wedges [8.6].

The material chosen for the Faraday rotator in an isolator should have a high Verdet constant V and low absorption α at the isolation wavelength. A figure-of-merit often used to compare materials is [8.7, 8.8]

$$FOM = \frac{V}{\alpha} \quad (8.8)$$

For high power applications it is also important that the Faraday material has a high laser induced damage threshold, a low nonlinear refractive index n_2 , a low refractive index temperature dispersion and a high thermal conductivity. In the $1\mu\text{m}$ region (of interest to this project) terbium gallium garnet $\text{Tb}_3\text{Ga}_5\text{O}_{12}$ (TGG) is the most commonly used material. TGG has a Verdet constant of around $-40 \text{ RadT}^{-1}\text{m}^{-1}$ and in a well prepared sample can have an absorption of below 0.0015cm^{-1} giving a FOM of around 27. For comparison, terbium doped borosilicate glass which is often used for low power applications has an FOM of around 7 [8.8].

The magnetic field around the Faraday rotator is generated with an assembly of permanent magnets, most usually neodymium-iron-boron magnets. The magnet configuration is designed to maximise the magnetic field strength through the Faraday rotator while maintaining good field uniformity across the Faraday rotator. According to equation 8.1 the higher the field strength B the greater the rotation per length. This allows the shortest Faraday rotators to be used and reduces the effects of parasitic absorption and nonlinearities. The spatial uniformity of the magnetic field across the rotator is important so that all parts of the beam rotate the same amount. This ensures optimum isolation and insertion loss.

Additional components are often added to isolators to provide extra benefits. A rotatable waveplate can be added, this allows the user to tune the isolator for maximum isolation over a range of wavelengths and temperatures by compensating for non 45° rotations. This trades off some isolation in the reverse direction for insertion loss in the forward direction. An optically active material with a coefficient of rotation which varies with wavelength or temperature inversely to the Faraday rotator can be used passively for this same purpose. The downside is that the isolator can only be optimised for isolation or insertion loss (transmission) but not both and if insertion loss is optimised then the isolation will vary with wavelength and temperature, and vice versa.

As fibre amplifier powers increase it becomes more and more difficult to find suitable materials from which to construct a Faraday isolator. The main problem arises from self-heating of the Faraday rotator by absorption. This creates thermal gradients and stresses in the Faraday rotator that induce birefringence and form power dependent thermal lenses.

8.4 Thermal Effects in Faraday Isolators

At mid to high powers thermal issues become important to the efficient operation of a Faraday isolator. These effects are caused by self-heating from optical absorption. The three most dominant

effects are thermal stress induced birefringence, thermal lensing and the temperature coefficient of the Verdet constant. This section introduces these effects – the theory behind why they occur and methods which have (or could) be employed to mitigate them. The section is divided as follows:

- Section 8.4.1 describes thermal stress induced birefringence in detail.
- Section 8.4.2 describes thermal lensing.
- Section 8.4.3 describes the effect of the temperature coefficient of the Verdet Constant.

Chapter 9 will expand on the theory of thermal lensing with a more theoretical treatment and provide specifics about how it can be measured and compensated.

8.4.1 Thermal Stress Induced Depolarisation

The first thermal effect to become apparent as power increases is thermal stress induced birefringence. In a Faraday isolator as power increases the temperature of materials increase because of absorption. This causes thermal expansion and induces stress in the optical materials because different parts expand more, or less, than others due to temperature gradients. This stress introduces unwanted linear birefringence within the crystals which alters the polarisation state of the light as it travels through the isolator and causes depolarisation. In the forward direction depolarised light (in the orthogonal polarisation state) is lost at the polariser and increases the insertion loss. In the reverse direction depolarised light passes through the polariser and reduces the isolation.

The distribution of stress birefringence in the crystal is dependent on the temperature distribution within the crystal and on the orientation of the crystal axis (stress field) with regard to the input polarisation. Mapping the depolarisation across the physical aperture of a TGG rod at the output end of the rod there is a ‘cross pattern’ showing the worst regions of leakage at 90 degree intervals. In the regions in between there is better performance (lower levels of spurious polarised light) because the polarisation of the light in these regions has not been well aligned to the stress field. This depolarisation pattern was shown theoretically and experimentally by Khazanov et. al., figure 8.3 [8.10].

The following parts of this section will discuss compensation of thermal stress induced birefringence as applied to a) laser cavities and b) the Faraday isolator.



Figure 8.3: Depolarisation distribution of Gaussian beam through a TGG rod a) theoretical and b) experimental [8.10].

a) Thermal Stress Induced Birefringence Compensation in Laser Cavities

Stress induced birefringence is a common problem in single polarisation lasers; and as such several compensation schemes have been developed. The simplest uses a rotating element, like a quartz rotator, to swap the radial and tangential polarisation components between two identical laser rods [8.11]. As shown in figure 8.4. The objective is to achieve an equal optical path length (phase retardation) for both the tangential and radial polarisations through the two crystals. When this occurs the birefringence in the first crystal is “cancelled” by birefringence with an equal and opposite effect in the second. The efficacy of this method depends crucially on the stress distribution in both rods having the same form and amplitude and also the modes of the laser in each rod matching spatially.

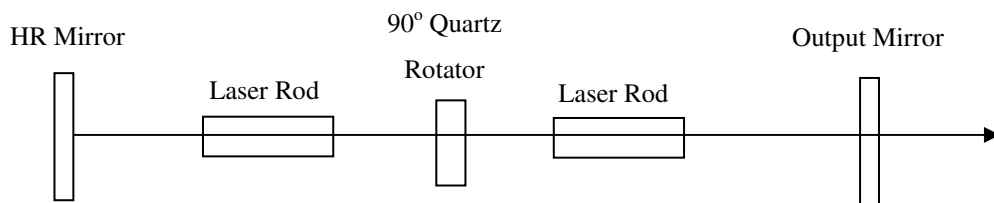


Figure 8.4: Thermal birefringence compensated cavity using dual laser rods and a 90 degree quartz rotator.

The same compensation method can be achieved in a single rod design by placing a 45° Faraday rotator between the laser rod and HR mirror, as shown in figure 8.5. Unfolding the cavity reveals that this is essentially the same as placing a 90° rotator between two laser rods with the added advantage of simplicity in the cavity design. This is demonstrated in the work of Giuliani and Ristori [8.12] into polarisation flip cavities. They use simple Jones matrix calculations to show that a wave A travelling through a series of retardation plates and a 45° Faraday rotator exits as wave A' with no phase retardation, just a 90° rotation in the polarisation axis due to the Faraday rotator. In working through

the derivation from the paper there are several typographic errors. The correct Jones Matrix for a retardation plate [R.P.] should be

$$[R.P.] = \begin{bmatrix} \cos\left(\frac{\phi}{2}\right) + i \sin\left(\frac{\phi}{2}\right) \cos(2\alpha) & i \sin\left(\frac{\phi}{2}\right) \cos(2\alpha) \\ -i \sin\left(\frac{\phi}{2}\right) \cos(2\alpha) & \cos\left(\frac{\phi}{2}\right) - i \sin\left(\frac{\phi}{2}\right) \cos(2\alpha) \end{bmatrix} \quad (8.9)$$

The Jones matrix for a Faraday rotator [F.R.] is

$$[F.R.] = \begin{bmatrix} \cos \theta & \sin \theta \\ -\sin \theta & \cos \theta \end{bmatrix} \quad (8.10)$$

Using these two matrices it follows that a light wave \vec{A} with an undetermined polarisation defined by the vector

$$\vec{A} = \begin{pmatrix} a_x \\ a_y \end{pmatrix} e^{i(\omega t - kz)} \quad (8.11)$$

that travels through the system in figure 8.5 (Where the laser rod has been broken into a series of retardation plates) is transformed to \vec{A}' by the Matrix operation

$$\vec{A}' = [R.P.]_{\phi_n, \alpha_n} [R.P.]_{\phi_1, \alpha_1} [F.R.]_{\theta=45^\circ}^2 [R.P.]_{\phi_1, \alpha_1} [R.P.]_{\phi_n, \alpha_n} \vec{A} \quad (8.12)$$

$$\vec{A}' = \begin{bmatrix} 0 & 1 \\ -1 & 0 \end{bmatrix} \vec{A}$$

The final matrix for the system has no dependence on the phase retardation plates because their effect cancels on the second pass. The polarisation of the output light will simply have its radial and tangential components swapped (rotated by 90°). Thus the action of double passing removes any birefringence from the beam. Unfolding the cavity in figure 8.5 reveals that it is equivalent to the double rod, 90° rotator design of figure 8.4.

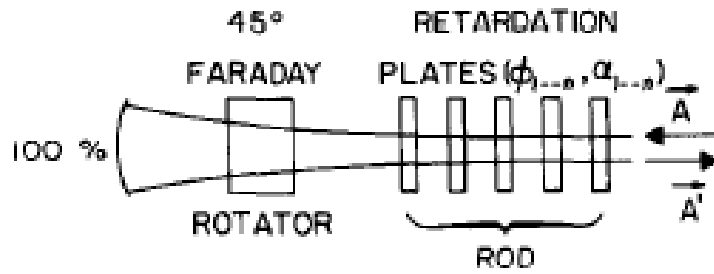


Figure 8.5: Laser cavity with 45° Faraday rotator with laser rod broken into retardation plates. This is the polarisation flip cavity analysed by Giuliani and Ristori [8.12].

Clarkson, Felgate and Hanna [8.13] describe how thermal stress birefringence can be largely compensated in a linearly polarised laser cavity simply by placing a quarter wave plate between the laser rod and high reflectivity mirror, figure 8.6. This double pass of a quarter plate introduces a π phase shift for light polarised at 45° to the optical axis. This is equivalent to the 45° rotator in figure 8.5 for those components and consequently these will be perfectly compensated.

Polarisation states aligned with the quarter waveplate fast and slow axis will experience no rotation and will not be compensated. Other polarisation states will be rotated by varying amounts given by 2ϕ , where ϕ is the angle between the polarisation direction and the slow axis of the quarter wave plate. These will experience some compensation of depolarisation.

Fortunately, the principal axes of stress birefringence in a cylindrically symmetric system are along the radial and tangential directions. This results in more depolarisation in the 45° components and so compensation of these is much more important and this scheme can be very effective at reducing depolarisation loss. If the cavity is unfolded then it is equivalent to two laser rods separated by a half-wave plate

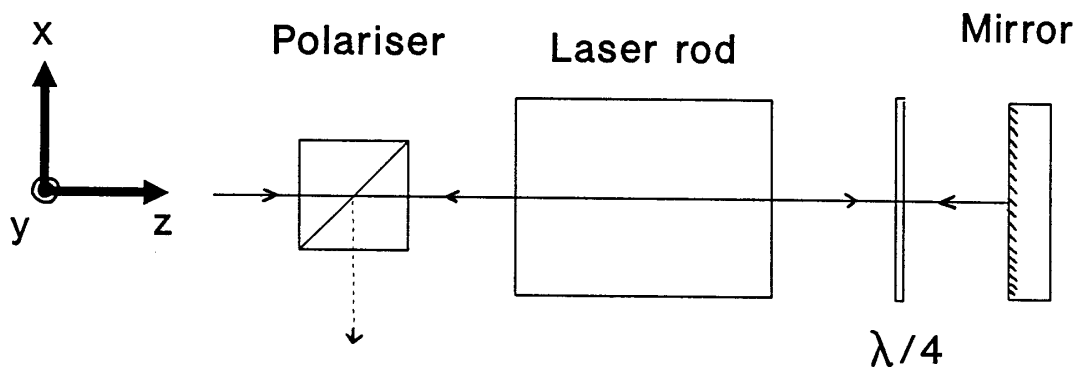


Figure 8.6: Thermal Birefringence compensation using a quarter-wave plate [8.13].

b) Thermal Stress Induced Birefringence Compensation in Faraday Isolators

The above analysis of birefringence compensation in laser cavities is also relevant for compensation of thermally induced stress in Faraday isolators. The same principals can be applied to a Faraday design if the 45° rotating element is split into two or more pieces with a polarisation rotating element between. This has been analysed in detail by Khazanov et. al. for the configurations in figure 8.7 [8.14-8.17].

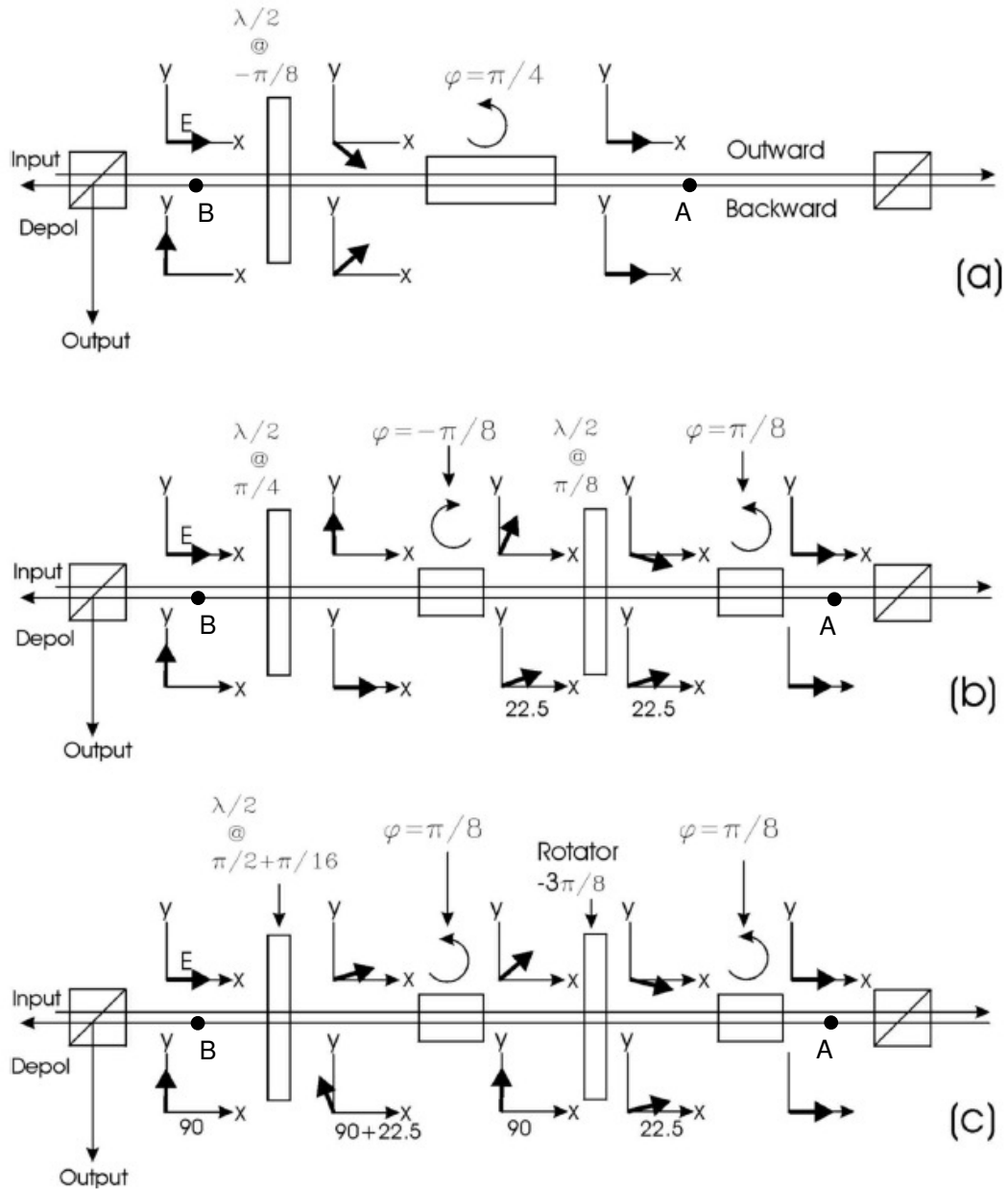


Figure 8.7: Design of a) traditional Faraday isolator b) isolator with counter-rotating 22.5° Faraday rotators and a half wave ($\lambda/2$) plate and c) isolator with two 22.5° rotators separated by a quartz rotator [8.27].

In these designs the addition of a half wave plate leaves the polarisation state unaffected in the forward direction. So that in the absence of thermal birefringence the light travelling in the forward direction leaves with the same polarisation state as it started. In the reverse direction the polarisation is rotated 90° and the light is reflected off the first polariser. Following the explanation (and notation) of Khazanov if we consider the point A in the backward travelling light after the polariser where the complex field amplitude is

$$\vec{E}_A = E_0 \vec{x}_0 \quad (8.13)$$

where x_0 is a unit vector along the x axis. Then at point B (where the light should be rotated into the y-axis) the depolarisation Γ is defined by

$$\Gamma = \frac{|\vec{E}_B \cdot \vec{x}_0|^2}{|E_0|^2} \quad (8.14)$$

Where E_B is the complex amplitude at point B of the return pass (figure 8.7) and can be found using Jones Matrices. The Jones Matrix for a quartz rotator with a rotation of β_R and a half-wave plate with an angle of β_L between its optical axis and the x-axis are given by

$$R(\beta_R) = \begin{bmatrix} \cos \beta_R & -\sin \beta_R \\ \sin \beta_R & \cos \beta_R \end{bmatrix} \quad (8.15)$$

$$L(\beta_L) = \begin{bmatrix} \cos 2\beta_L & \sin 2\beta_L \\ \sin 2\beta_L & -\cos 2\beta_L \end{bmatrix}$$

Following the work of Chen and Trabor [8.20] the Jones Matrix of a Faraday rotator with both wanted circular birefringence and parasitic linear birefringence is

$$F = \sin\left(\frac{\delta}{2}\right) \begin{bmatrix} \cot\left(\frac{\delta}{2}\right) - i \sin\left(\frac{\delta_{lin}}{2}\right) \cos(2\Psi) & -\frac{\delta_c}{\delta} - i \frac{\delta_{lin}}{\delta} \sin(2\Psi) \\ \frac{\delta_c}{\delta} - i \frac{\delta_{lin}}{\delta} \sin(2\Psi) & \cot\left(\frac{\delta}{2}\right) + i \sin\left(\frac{\delta_{lin}}{2}\right) \cos(2\Psi) \end{bmatrix} \quad (8.16)$$

Where δ_{in} and δ_c are the phase shifts due to linear and circular birefringence, ψ is the angle between the intrinsic linear birefringence and the x-axis and

$$\delta^2 = \delta_{lin}^2 + \delta_c^2 \quad (8.17)$$

Using these matrices the complex field amplitude E_B at point B can be found for each of the three designs in figure 8.7 (using subscript A,B,C for the three designs)

$$\begin{aligned} E_{BA} &= L\left(\frac{-\pi}{8}\right)F\left(\Phi = \frac{\pi}{4}, \delta_{lin}\right)E_A \\ E_{BB} &= L\left(\frac{\pi}{4}\right)F\left(\Phi = \frac{-\pi}{8}, \frac{\delta_{lin}}{2}\right)L\left(\frac{\pi}{8}\right)F\left(\Phi = \frac{\pi}{8}, \frac{\delta_{lin}}{2}\right)E_A \\ E_{BC} &= L\left(\frac{3\pi}{8}\right)F\left(\Phi = \frac{\pi}{8}, \frac{\delta_{lin}}{2}\right)R\left(\frac{-3\pi}{8}\right)F\left(\Phi = \frac{\pi}{8}, \frac{\delta_{lin}}{2}\right)E_A \end{aligned} \quad (8.18)$$

Note that the quartz rotator in figure 8.7c is set to give a rotation of 67.5° (not 90°) for optimum compensation. This is different to the laser rod equivalent examined earlier and accounts for the fact that the Faraday rotators are rotating in the same direction and the beam has already been rotated by 22.5° by the first Faraday rotator. Plugging equations 8.18 into equation 8.14 allows us to calculate the depolarisation, assuming that the entire beam sees the same birefringence.

If the birefringence varies across the beam cross section, as occurs in TGG, then over the entire beam cross section the depolarisation is given by

$$\gamma = \frac{\int_0^{2\pi} d\varphi \int_0^\infty \Gamma e^{\left(\frac{r^2}{r_0^2}\right)} r dr}{\int_0^{2\pi} d\varphi \int_0^\infty e^{\left(\frac{r^2}{r_0^2}\right)} r dr} \quad (8.19)$$

The profile of linear phase retardation and ψ through a Faraday rotator of length L in the presence of thermal stress and a temperature gradient dT/dr are given by

$$\begin{aligned} \delta_{lin}(r, \varphi) &= 4\pi \frac{L}{\lambda} Q \left[\frac{1 + \xi_a^2 \tan^2(2\Psi - 2\theta)}{1 + \tan^2(2\Psi - 2\theta)} \right]^{1/2} \frac{1}{r} \int_0^r r^2 \frac{dT}{dr} dr \\ \tan(2\Psi - 2\theta) &= \xi_a \tan(2\varphi - 2\theta) \end{aligned} \quad (8.20)$$

Where r and φ are the polar coordinates which define the geometry of the system, θ is the angle between the crystal axis and the x-axis, ξ is a factor which takes account of the difference in photoelastic constants along optical axis in an anisotropic material and Q is a stress-optic coefficient.

The temperature gradient in a cylindrical piece of TGG (assuming that the beam has a Gaussian profile) is given by (section 9.1)

$$\frac{dT}{dr} = -\frac{\alpha P_0}{2\pi\kappa r} \left(1 - \exp\left(\frac{-r^2}{r_0^2}\right) \right) \quad (8.21)$$

Where α is the absorption coefficient of the material, P_0 is the power of the laser beam, r_0 is the 1/e beam radius and κ is the thermal conductivity.

Using the above equations the depolarisation γ can be calculated for each of the three designs as (assuming that $\delta_1 \ll 1$)

$$\begin{aligned} \gamma_A &= p^2 \frac{A_1}{\pi^2} \left[1 + (\xi^2 - 1) \cos^2\left(2\theta - \frac{\pi}{4}\right) \right] \\ \gamma_B &= p^4 \frac{A_2}{\pi^4} \left[6a^2 \left(1 + \frac{2}{3}\xi^2 + \xi^4 \right) + 8b^2 \xi^2 + 6b^2 (1 - \xi^2) \sin^2\left(4\theta - \frac{\pi}{4}\right) - 12ab(\xi^4 - 1) \sin\left(4\theta - \frac{\pi}{4}\right) \right] \\ \gamma_C &= p^4 \frac{6a^2 A_2}{\pi^4} \left(1 + \frac{2}{3}\xi^2 + \xi^4 \right) \end{aligned} \quad (8.22)$$

Where

$$\begin{aligned} A_1 &= \int_0^\infty \left[\frac{1}{y} - \frac{\exp(-y)}{y} - 1 \right]^2 \frac{dy}{\exp(y)} \approx 0.137 \\ A_2 &= \int_0^\infty \left[\frac{1}{y} - \frac{\exp(-y)}{y} - 1 \right]^4 \frac{dy}{\exp(y)} \approx 0.042 \\ p &= \frac{L\alpha Q}{\lambda\kappa} P_0 \end{aligned} \quad (8.23)$$

The isolation is given by

$$I = -10 \log\left(\frac{1}{\gamma}\right) \quad (8.24)$$

This analysis shows that depolarisation in the traditional “single” 45° rotator design isolator increases with the square of the input power, absorption and crystal length. In both the compensated designs the depolarisation γ_b and γ_c increase with the fourth power of these quantities. Fortunately, the starting value of the depolarisation in the compensated dual rotator designs is much smaller than in the traditional design. This is illustrated in figure 8.8 which shows the predicted isolation with power of the three design variations. The parameters used in these calculations are appropriate for TGG and are given in table 8.1. Note: These were plotted using the best case crystal orientation θ .

The calculated isolation for the compensated schemes figures 8.7b and 8.7c are clearly much better than the traditional. Design c with a 90° quartz rotator and additive 22.5° Faraday rotators performs slightly better than design b with a half wave plate and opposing 22.5° rotators. The reason for this is the same as the cavity design of Hanna described earlier (figure 8.6). With a half wave plate the polarisation components on axis are not “swapped” and so they are not compensated. This is still significantly better than the uncompensated isolator.

A benefit of the half wave plate design is that it can be made with opposing magnets. This increases the field strength through the magnet bores and reduces the length of Faraday material needed to achieve the correct rotation. This decreases the amount of depolarisation and reduces the length of the device. The relationship between isolation and Faraday rotator length is shown in figure 8.9.

| | |
|---|------------------------|
| Thermal Conductivity ($\text{Wm}^{-1}\text{K}^{-1}$) | 7.4 |
| Optical Absorption (m^{-1}) | 0.1 to 0.4 |
| Thermo-Optic Coefficient Q (K^{-1}) | -2.1×10^{-6} |
| Anisotropy Factor ξ | 2.25 |
| dn/dT (K^{-1}) | 16×10^{-6} |
| $(1/V)dV/dT$ | -3.47×10^{-3} |
| Refractive Index @1064nm | 1.954 |

Table 8.1: TGG parameters used in depolarisation model.

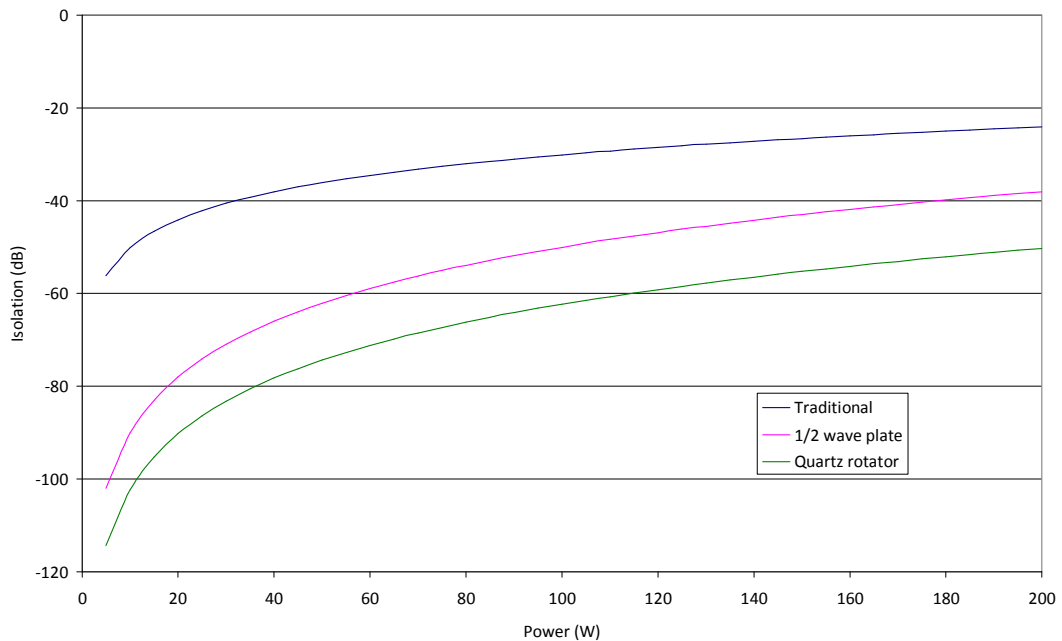


Figure 8.8: Dependence of isolation on input power for the three isolator designs. TGG length of 40mm and best orientation angle.

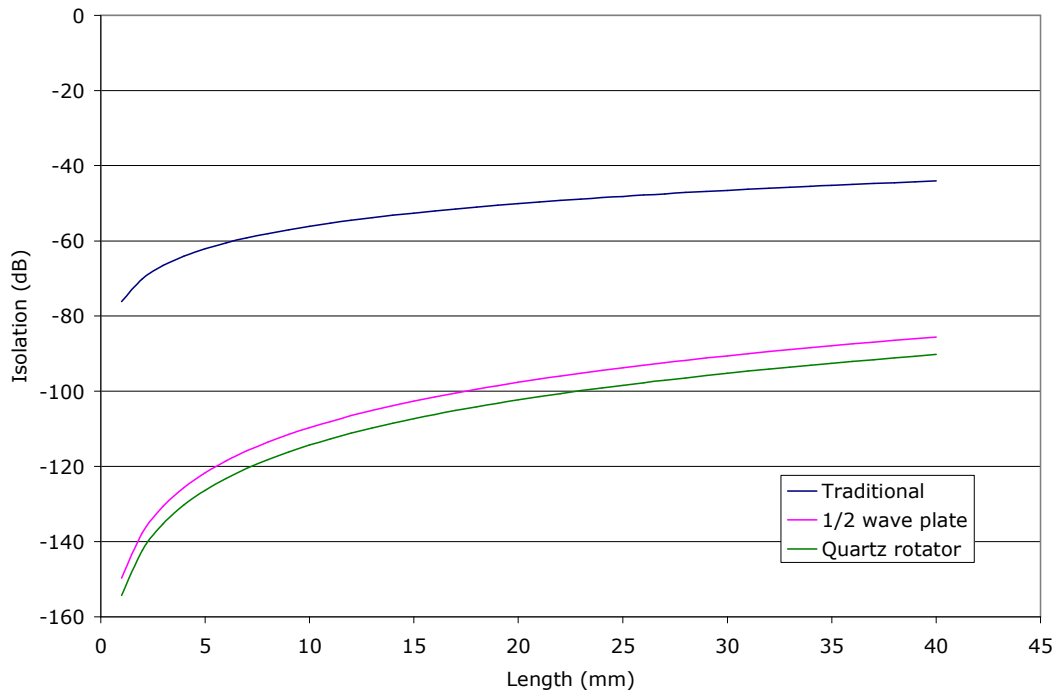


Figure 8.9: Dependence of isolation on length of TGG crystal for the three isolator designs. Best orientation angle.

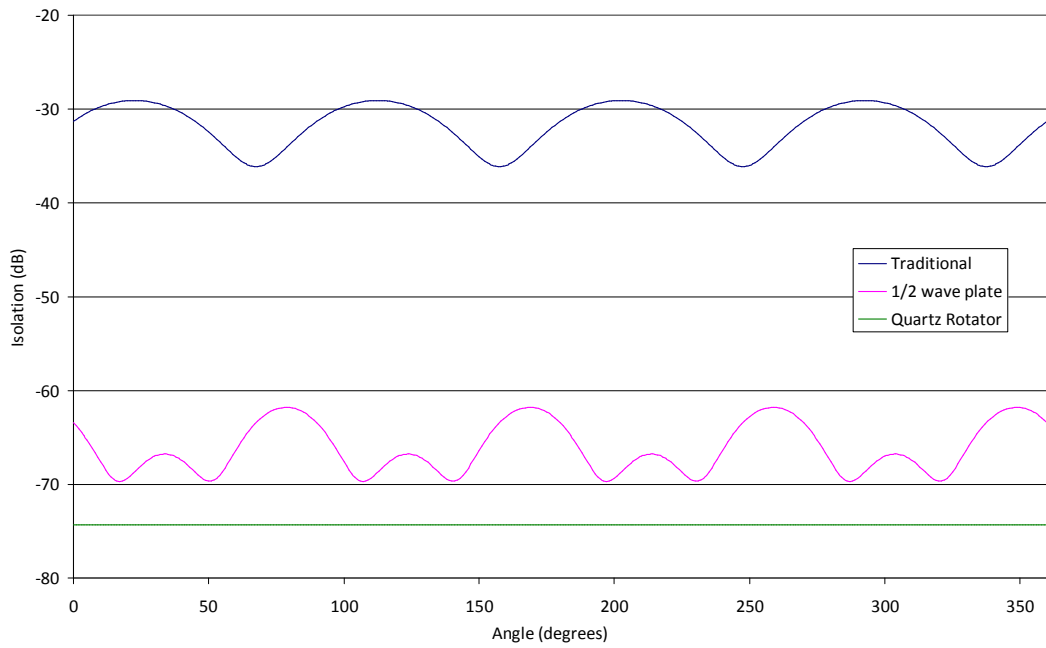


Figure 8.10: Dependence of isolation on $\langle 001 \rangle$ TGG axis orientation for the three isolator designs.

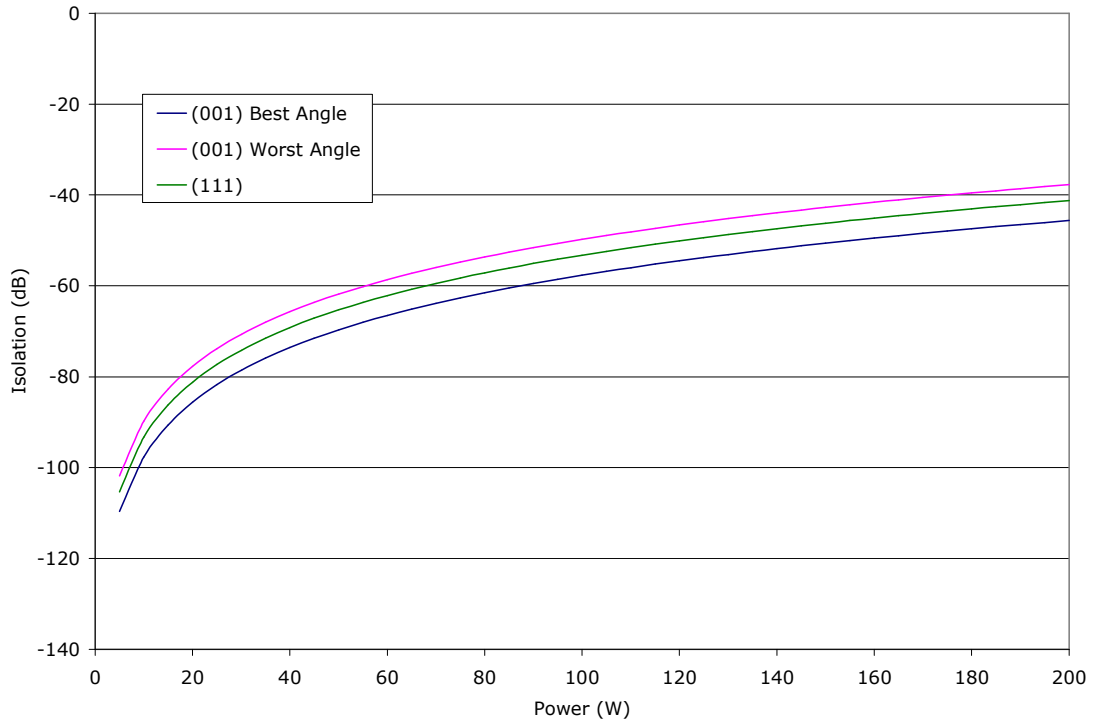


Figure 8.11: Isolation of half wave plate compensated isolator using <001> TGG in the best and worst orientation and using <111> TGG.

The depolarisation of the traditional isolator γ_a depends on where the <100> crystal axis is with respect to the input polarisation. If <001> material is used then the TGG has to be rotated into the correct orientation for optimum performance. The variation of isolation with angle is shown in figure 8.10. From equation 8.22 and figure 8.10 it is easy to see that the optimum angles for the traditional design occur at

$$\theta_{\min} = (4n - 1) \frac{\pi}{8} \quad n = -2, -1, 0, 1, 2, \dots \quad (8.25)$$

So for a single rotation of the TGG crystal there are 4 orientations which will give the best isolation. These correspond to rotations through the regions with the lowest depolarisations as seen in figure 8.3. The good thing for our polarisation independent isolator is that these optimum positions are spaced by 90° so that we can achieve optimum isolation for both orthogonal polarisations at the same time in the crystal.

Using TGG with the <111> orientation eliminates this sensitivity on orientation. The downside is that the depolarisation is worse in this orientation to begin with. The isolation versus power calculated for the <111> orientation is plotted in figure 8.11 alongside the “best” and “worst” case isolations for the

<001> orientation. Expressions for the <111> orientation can be obtained from the <001> expressions above by substituting [8.14]

$$\xi \rightarrow 1 \quad Q \rightarrow Q(1 + 2\xi)/3 \quad (8.26)$$

Isolator design b, like the traditional design, also has a dependence on the angle between the <001> crystal axis and the input linear polarisation. This can be seen in the equation for γ_b and is plotted alongside the angle variation of the traditional design in figure 8.10. This dependence is more complicated than the traditional design and there are 8 minima per rotation of the TGG rods – this is expected because it is where the input polarisation lines up with the areas of least depolarisation in each rod. From equation 8.22 the minima can be found at

$$\theta_{\min} = \left(n + \frac{3}{8} \right) \frac{\pi}{2} + \frac{1}{4} \left(\frac{\pi}{2} - \arcsin \left(\frac{a}{b} \frac{\xi^4 - 1}{(1 - \xi^2)^2} \right) \right) \quad n = -2, -1, 0, 1, 2, \dots \quad (8.27)$$

Again, fortunately for a polarisation independent isolator the minima are spaced by 90° so you can simultaneously achieve optimum isolation for both orthogonal polarisations.

Design c has no dependence on θ . It is therefore not necessary to optimise the orientation of the Faraday rotators. For this design the depolarisation for the <111> TGG and the <001> TGG is identical. So for this design it is beneficial to use the <111> cut material because this requires no mutual alignment of the two Faraday rotators.

The quartz rotator isolator works regardless of TGG rotation and is perfect for all input polarisations. This is equivalent to the use of a quartz rotator between two rods in a laser cavity described earlier. The use of a half wave plate reduces birefringence but is not perfect because the polarisation components along the fast and slow axis of the half wave plate are not swapped. The angle that the crystal stress fields makes with the input polarisation then becomes important. If the polarisation is aligned with the regions of low birefringence in the crystal, along the nodes of the cross in figure 8.3, then the compensation will be most effective. This is equivalent to the work of Hannah described earlier where a half wave plate was inserted into a laser cavity.

One of the surprising results from this analysis is that the depolarisation, in any of the designs, does not depend on the radius of the input beam.

In a polarisation independent isolator it is usual to have both orthogonal polarisations travel through the same Faraday rotator. This complicates the temperature distribution in the material and affects the

symmetry of stress fields. This is very difficult to analyse analytically and will reduce the isolation slightly from the ideal case of Gaussian pumped, infinite cylinders analysed above.

8.4.2 Thermal Lens

The second thermal effect to become an issue as power increases is thermal lensing. Thermal lensing describes a number of processes due to absorption heating, which result in the formation of a power-dependent focal shift. The thermo-optic effect, the elasto-optic (photoelastic) effect and the shape change of the sample through thermal expansion, especially “bulging” of the crystals end faces, have been identified as the most important thermal lens contributing processes.

In a Gaussian pumped material the thermo-optic effect makes the greatest contribution to thermal lensing [8.21]. The thermo-optic effect simply describes the change of a materials refractive index with temperature and is characterised by the thermal dispersion of the material dn/dT .

If the material has a thermal gradient then through the thermo-optic effect it will also have a refractive index gradient. In most cases the temperature profiles created by laser absorption are symmetric around the beam centre and approximate well to a parabola. This creates a parabolic refractive index profile similar to the type formed intentionally in a gradient index lens, with a magnitude proportional to the amount of absorbed power. If the material has a positive dn/dT then it will form a converging (positive) thermal lens. A material with a negative dn/dT will form a divergent (negative) thermal lens.

The thermo optic effect is particularly bad for Gaussian beams because the intensity on axis is at its “fundamental” highest for a given diameter. This produces a large radial temperature gradient and strong thermal lensing. Top-hat beams, for obvious reasons would produce smaller temperature gradients across the beam and show smaller lensing. Ambient increases in temperature increase the optical path length through a sample, but do not create temperature gradients and therefore do not contribute to thermal lensing.

If the thermal gradient is not symmetric around the beam centre then the thermo-optic effect will lead to aberrations and beam steering. Also, in a crystal it is usual to have different dn/dT coefficients along different axes. This causes the thermal lens focal length to vary along different directions of the beam and can lead to astigmatism in the output beam. Fortunately, this can also be corrected by using a two rod design and a rotator, so that both parts of the beam travel through the same optical path length.

The change in refractive index at radial position r with a temperature $T(r)$ is given by

$$\Delta n_T(r) = \frac{dn}{dT} T(r) \quad (8.28)$$

The elasto-optic effect makes a smaller contribution to the thermal lens, estimated by Mansell et. al to be about 1/5 the contribution of the thermo-optic effect in a Gaussian pumped rod of TGG [8.21]. The elasto-optic effect describes how the refractive index of a material reacts to stress (which may be caused by heating and expansion or contraction). It is closely related to the problem of thermal stress induced depolarisation discussed in section 8.4.1 and is caught in equation 8.20 through the stress optic constant Q and the anisotropy factor ξ . The change in refractive index due to stress in a material is calculated by multiplying the strain tensor ϵ by the photoelastic tensor p [8.19]

$$\Delta \left(\frac{1}{n^2} \right)_i = p_{ij} \epsilon_j \quad (8.29)$$

In a cubic isotropic material, for light polarised along the i axis this becomes

$$n_i - n_0 = -\frac{1}{2} n_0^3 p_{ij} \epsilon_j \quad (8.30)$$

This approximation is justified for terbium gallium garnet because it is only weakly anisotropic (the difference between the photoelastic tensor coefficients ($p_{11}-p_{12}-2p_{44}$) is very small. The change in refractive index with temperature is then simply related to the change in stress induced by thermal expansion. The stress tensor components can then be approximated by [8.18]

$$\Delta n_{e-o}(r) = -\frac{1}{2} n_0^3 p_{12} \alpha \Delta T(r) \quad (8.31)$$

A final effect which can be important, especially if there is high absorption in a small volume near the surface of the material (like in a contaminated AR coating), can be shape changes or “bulging” at the boundaries of the crystal. This effect, in the majority of cases, is also very small compared to the thermal refractive index change of the thermo-optic effect. Mansell et. al. [2.18] argue that the expansion is confined to a depth given by the Gaussian spot size, so that the change in optical path length for a crystal is given by

$$\Delta OPL_{\text{expansion}}(r) = 2\alpha n \omega \Delta T(r) \quad (8.32)$$

The overall optical path length change due to thermal effects in a crystal are obtained through

$$\Delta OPL(r) = \Delta n_T(r)L + \Delta n_{e-o}(r)L + \Delta OPL_{\text{expansion}}(r) \quad (8.33)$$

At moderate power levels thermal lensing is not a problem for the operation of the isolator, it does not significantly affect isolation or insertion loss. It is more of a problem for end users of the isolator who may want to operate the laser at several different power levels during a process. If the system they are using has a strong thermal lens then the position of the work piece will have to be repositioned for each power level for optimum performance. This reduces the flexibility of use for which fibre lasers are well known. A major advantage of fibre lasers for processing is that they are intrinsically “free” of thermal lensing because the beam parameters are determined by the fibre properties and not the cavity.

The possibility for compensation of thermal lensing within the isolator is interesting as it has never been implemented on a commercial device. The basic idea of compensation is quite simple – you have to induce a power dependent shift of the focal position in the opposite direction to the intrinsic thermal lens. This can be achieved in several ways both actively and passively. In this context “active” means introducing an adaptive element which has to be changed as power is increased to provide compensation. This could include using a moveable lens, a writable phase plate or a deformable mirror. Active compensation will be discussed in more detail in chapter 9.

Passive compensation requires no moveable or changing parts and can be achieved by introducing an extra material into the isolator with a negative thermal dispersion dn/dT . This would create a thermal lens with an equal magnitude, but opposite direction to the intrinsic thermal lens. That to a first approximation will balance the focal shifts, assuming that the focal lengths of the thermal lenses are much greater than the distance separating them. This idea seems to have been first implemented in an Nd:YAG laser cavity using a polymer gel as the compensating material [8.22]. Since then it has been demonstrated in high power, bulk optic, Faraday isolator designs using FK51 glass and deuterated KDP [8.23, 8.24].

The passive methods clearly have an advantage of simplicity over active methods which rely on moving optics, deformable mirrors and adaptive phase plates. The downside is that it can not compensate for aberrations produced by thermal lensing. However, at these power levels aberrations are expected to be small.

8.4.3 Thermal dependence of Verdet Constant and Magnetic Field Strength and Compensation

The final thermal issue facing the Faraday isolator is the reduction in rotation (and hence isolation) of the Faraday rotator as temperature increases. There are two effects which cause this:

1. The change in Verdet constant with temperature, dV/dT .
2. The change in magnetic field strength with temperature, dB/dT .

Ignoring the change in length with temperature the change of rotation in a Faraday material with temperature is given by

$$\frac{1}{\theta} \frac{d\theta}{dT} = \frac{1}{B} \frac{dB}{dT} + \frac{1}{V} \frac{dV}{dT} \quad (8.34)$$

where we have applied the chain rule to equation 8.1 following the example of Barnes and Petway [8.20]. If we ignore temperature gradients then the polarisation rotation will change with temperature uniformly across the beam, this will affect the isolation and insertion loss of the isolator. This effect is quite significant in the isolator with a reduction in isolation of around 15dB in 20°C from the optimised temperature.

To counter this effect the isolators can be optimised to produce maximum isolation at a slightly elevated temperature, around which the isolator is expected to work during normal operation. This provides a good compromise as most industrial lasers and isolators are used in well controlled environments. Another solution is to insert a half wave plate between the polarisers that can be rotated to make up for the change in rotation caused by the temperature effect. This trades off isolation in the reverse against insertion loss in the forward direction. The downside of inserting a moveable wave plate is that it requires manual optimisation and could result in “poor” or even no isolation if poorly aligned. Rotating the wave plate automatically requires either an active temperature sensor and motor or possibly a complex thermo-mechanical setup. These have the disadvantage of being complicated to implement and design.

In the EGO gravitational wave interferometer isolation compensation for ambient increases in temperature are made using a remotely tuneable half wave plate [8.21]. At 240W rotation of the half wave plate recovers 7dB of isolation for an increase in insertion loss of just 2%.

Another compensation method involves moving the Faraday rotators further into the magnet core as temperature increases. This increases the magnetic field strength and maintains the polarisation

rotation of light as temperature increases. In theory this should provide good isolation-temperature performance without affecting the insertion loss. The problem is that it requires a complex setup and having moveable Faraday crystals may prevent effective heat sinking which would exacerbate other thermal problems. Nevertheless, the possibility of passive compensation using this method and bimetallic strips has been proposed [8.26].

Looking at equation 8.32 increasing the field strength with temperature effectively produces a positive dB/dT which will compensate for a negative dV/dT . Compensating for a negative dV/dT will require reducing the field strength with temperature. The aim of this compensation method is to balance the right hand components of equation 8.32 by manipulating B and dB/dT so that

$$\frac{1}{B} \frac{dB}{dT} = - \frac{1}{V} \frac{dV}{dT} \quad (8.35)$$

It could also be possible to achieve the same effect with a complicated magnet design. One possible implementation of this could be to surround the magnets with a material (magnetic conductor) with temperature dependant permeability. This would screen the magnetic flux at lower temperatures and direct more flux through the central bore of the magnet as temperature increases. The advantage of this scheme is that it requires no moving parts. The disadvantage is that we are limited on available materials to make this work and it also increase the size of the isolator magnet ensemble.

The temperature dependence of the Verdet constant and magnetic field could also be compensated by introducing an optically active component which is optically active with a temperature coefficient for rotation opposite to $d\theta/dT$ for the Faraday rotator. This would maintain the overall rotation within the isolator in the reverse direction. However, because this rotation would be reciprocal it would also introduce a small temperature dependent insertion loss in the forward direction, which may or may not be acceptable. In terms of operation this method is equivalent to the first method of introducing a half wave plate. However, it has the advantage of being entirely passive.

When we introduce temperature gradients into our explanation things get very complicated as we do not have a homogenous change in rotation across the beam. Across the beam this results in localised position dependent depolarisation at the polarisers. This reduces the effectiveness of many of the compensation schemes envisaged above. Except the last scheme – if the absorption, thermal conductivity, boundary conditions and temperature coefficients are matched in the Faraday rotator and optically active material then they will have the same temperature distribution and rotate the local depolarisation across the beam by the desired amount at each position.

However, for perfect compensation this relies on a complex (and fortuitous) coincidence in materials. It also relies on the Verdet constant temperature dependence in the Faraday rotator and optically

active material to be homogenous along crystal axis and not depend on the orientation of the material to the input polarisation.

Compensating elements would also have to be taken into account for thermal stress depolarisation compensation and thermal lens compensation.

8.5 State of the Art

The state of the art high power Faraday isolators are being constructed for the large gravitational wave observatories – LIGO in USA, VIRGO in Europe and ACIGA in Australia. These observatories consist of interferometers with arms several kilometres long and aim to detect theoretically predicted gravitational waves through a minute change in path length. They use Faraday isolators to reduce noise at various points in the interferometer.

To increase the sensitivity of these instruments they are moving to higher laser powers of between 50W and 200W. This increases the thermal problems seen in all components of the interferometer, especially the Faraday Isolator which uses terbium gallium garnet (TGG) and has a moderate intrinsic absorption at 1064nm. These problems like thermal lensing and thermal stress induced depolarisation reduce the efficiency of coupling light into the interferometer cavities and increase noise.

These Faraday isolators are described in [8.14, 8.15, 8.23] and have been designed to maintain the beam quality of the laser passing through them by compensating for thermal stress induced depolarisation and thermal lensing. These isolators are not fibre coupled devices but except for the collimator design are essentially the same as the type of isolator proposed in this project. They use the isolator design shown in figure 8.7c with two 22.5° Faraday rotators with the same sense of rotation separated by a 67.5° quartz rotator. Their operating wavelength is around 1064nm and they use TGG as the Faraday material.

As mentioned in section 8.4.1 the advantage of the two rod design with the quartz rotator is that the depolarisation does not depend on the angle the TGG rod axis makes with the input polarisation. Using the [111] cut of TGG they also need not align the two TGG rods with respect to each other. The design we plan to use is the one shown in figure 8.7b which uses two 22.5° Faraday rotators with opposite sense of rotation separated by a half wave plate. The disadvantage of this design, as shown by Khazanov [8.16] and in section 8.4.1 is that the isolation depends on the angle of incidence between the input polarisation and the axis of the TGG crystal. It is also more efficient with the [001] cut of TGG and so requires mutual alignment of the two TGG rods optical axis. The advantage of the design in figure 8.7b is that the magnet arrangement can be made more powerful by having opposing magnets. This increases the field strength through the TGG which allows us to use a shorter length

and hence decrease depolarisation that way, since according to equation 8.22 the depolarisation of the two “compensated” designs is proportional to L^4 .

This more powerful magnet arrangement is important in our application because the size of the isolator is limited. Increased size is usually more expensive and less desirable. For the gravitational wave application the size constraints are much less limited and so larger magnet ensembles can be used to make up for the field strength. The lax requirement on length in their application probably allows them to use a triple opposing magnet type design, or a five magnet design. This could combine the advantages of using opposing magnets to increase the field strength and the quartz rotator design, but would result in a longer device.

Using a complex arrangement of magnets and magnetic conductors they have produced a single element Faraday isolator with a TGG crystal that is just 11mm long. The magnet design enhances the field at the location of the TGG to a huge 2.1T. The finished design is capable of isolation of greater than 30dB at 400W power in a 4.2mm diameter beam [8.25]. The disadvantage of this setup is the size (10.5kg) which for obvious reasons is too heavy and expensive for most commercial applications.

They have also implemented compensation for thermal lensing using both FK51 glass and DKDP crystal [8.23, 8.24]. They conclude that DKDP is more efficient for adaptive compensation because the photoelastic effect in glass distorts the beam shape. DKDP causes less distortion of the beam because of its natural birefringence which reduces the effect of thermally induced birefringence. Using a gel as the compensating element, as has been done in laser cavities [8.22] should completely remove the problem of stress induced birefringence.

All-fibre Faraday isolators which replace the bulk optic polarisers and the Faraday material with their fibre optic counterparts have long drawn attention [8.27-8.30]. They have potential to be much simpler to construct than bulk optic isolators and are intrinsically free of thermal lensing. The disadvantage is their small Verdet constant and strong linear birefringence which tends to overwhelm the Faraday rotation in the fibre and imposes a limit on the size of the device. In earlier designs using single mode fibre several meters of fibre were required to produce 45° rotation.

In an early demonstration of Faraday rotation in fibre optic Turner and Stolen [8.17] showed that Faraday rotation in optical fibres could be enhanced by alternating the magnetic field at intervals equal to the fibre beat length. By using a combination of 14 alternating magnets with a period equal to the beat frequency they were able to achieve 45° rotation in a 7m length of silica fibre. The Verdet constant of silica at 632nm is just 3.6rad/T.m

Day et. al. [8.28] showed that the same effect to alternating the magnetic field could be achieved by coiling the fibre inside a magnetic field with a coil radius given by the beat length of the fibre. They

achieved 56° rotation in a fibre coil of 36 turns with a radius of 7.65mm. The downside of this device was the bend loss induced in the fibre which introduced 6dB loss.

Recently Sun et. al. [8.29, 8.30] have demonstrated Faraday rotation in optical fibre with a high doping concentration of terbium. Their fibre is doped with 65-wt%-Tb and has a Verdet constant of -32.1rad/T.m which is 27 times larger than the Verdet constant of silica fibre (1.1rad/mT @1064nm) and only 15% lower than the Verdet constant of TGG. With a 4cm length of terbium fibre they achieved an isolation of over 19dB at 1054nm with an insertion loss of 6.1dB. The insertion loss was dominated by loss in the chiral scattering grating fibre polarisers and they expect to be able to reduce the loss to below 3dB soon.

The greatest advantage that all fibre Faraday isolators have over bulk optic isolators is that the light remains in a fibre. This allows it to be spliced to other fibre outputs or further amplifier stages directly. In-line bulk optic isolators require the light to exit the fibre and pass through a free space isolator before being coupled back into fibre. This introduces substantial loss and is difficult at high powers since lost light from misalignment goes into the cladding of the fibre and can easily cause damage. The main use of a high power all-fibre isolator would therefore seem to be between amplifier stages to prevent back reflected light and ASE.

References

- [8.1] Eugene Hecht, *Optics*, 3rd Ed., Addison-Wesley, 1998
- [8.2] Ian Kenyon, "The Light Fantastic: A Modern Introduction to Classical and Quantum Optics," ed. 2, Oxford University Press, 2011
- [8.3] F. L. Pedrotti; P. A. Bandettini, "Faraday rotation in the undergraduate advanced laboratory," *American Journal of Physics*, 1990, Volume 58, pp.542-545
- [8.4] S Winter, C Mok, A Kumarakrishnan "Tools for laser spectroscopy: The design and construction of a Faraday isolator," *Canadian Journal of Physics*, 2006, Vol. 84, pp. 845-855
- [8.5] Soe-Mie F. Nee, "Polarization Method," invited book chapter, Chapter 60, pp. 60.1-24, *The Measurement, Instrumentation and Sensors Handbook*, CRC Press and IEEE Press, 1999.
- [8.6] Rüdiger Paschotta, "Encyclopedia of laser physics and technology," Wiley-VCH, 2008
- [8.7] Yehuda Benzion Band, "Light and matter: electromagnetism, optics, spectroscopy and lasers," John Wiley and Sons, 2006
- [8.8] Northrup Grunman TGG data sheet, online:
http://www.as.northropgrunman.com/products/synoptics_tgg/assets/tgg_data_sheet.pdf Retrieved 07/08/2011
- [8.9] Optical Isolator, online:
http://en.wikipedia.org/wiki/Faraday_isolator#Polarization_dependent_isolator Retrieved: 07/08/2011

- [8.10] Efim Khazanov, Mikhail Grishin (Ed.), "Faraday Isolators for High Average Power Lasers", Chapter in "Advances in Solid State Lasers Development and Applications," InTech, 2010 Online: <http://www.intechopen.com/articles/show/title/faraday-isolators-for-high-average-power-lasers>
- [8.11] Walter Koechner, "Solid-State Laser Engineering," 6 ed., Berlin: Springer, 2006
- [8.12] Giampiero Giuliani and Paola Ristori, "Polarization Flip Cavities: A New Approach to Laser Resonators," *Optics Communications*, 1980, Vol. 35
- [8.13] Clarkson, W. A., Felgate, N. S. and Hanna, D. C. "Simple method for compensation of thermally-induced birefringence in high-power solid-state lasers," In Conference on Lasers and Electro-Optics, Glasgow, GB, 13 - 18 Sep 1998.
- [8.14] E A Khazanov, "Compensation of thermally induced polarisation distortions in Faraday isolators," *Quantum Electronics*, 1999, Vol. 29 (1), pp. 59-64
- [8.15] E A Khazanov, "Characteristic features of the operation of different designs of the Faraday solator for a high average laser-radiation power," *Quantum Electronics*, 2000, Vol. 30 (2), pp. 147-151
- [8.16] Efim Khazanov, Nicolay Andreev, Oleg Palashov, Anatoly Poteomkin, Alexander Sergeev, Oliver Mehl, and David H. Reitze, "Effect of terbium gallium garnet crystal orientation on the isolation ratio of a Faraday isolator at high average power," *Applied Optics*, 2002, Vol. 41, No. 3
- [8.17] W. J. Tabor and F. S. Chen, "Electromagnetic Propagation through Materials Possessing Both Faraday Rotation and Birefringence: Experiments with Ytterbium Orthoferrite," *J. Appl. Phys.*, 1969 Vol. 40, 2760
- [8.18] Justin D. Mansell, Joseph Hennawi, Eric K. Gustafson, Martin M. Fejer, Robert L. Byer, David Clubley, Sanichiro Yoshida, and David H. Reitze, "Evaluating the Effect of Transmissive Optic Thermal Lensing on Laser Beam Quality With a Shack-Hartmann Wave-Front Sensor," *Applied Optics*, 2001, Vol. 40, Issue 3, pp. 366-374
- [8.19] Lockwood, David J.; Pavesi, Lorenzo (Eds.) "Silicon Photonics II," 1st Edition., Springer, 2011
- [8.20] Norman P. Barnes and Larry B. Petway, "Variation of the Verdet constant with temperature of terbium gallium garnet," *JOSA B*, 1992, Vol. 9, Issue 10, pp. 1912-1915
- [8.21] Julien Marque, Presentation "High Power Input Optics for Advanced Virgo," online: <http://moriond.in2p3.fr/J11/transparentes/marque.ppt#266,6>, The Faraday Isolator: rotation angle Gravitational Waves and Experimental Gravity, Rencontres de Moriond and GPhyS Colloquium La Thuile, 20 - 27 March 2011
- [8.22] Eduard Wyss, Michelle Roth, Thomas Graf, and Heinz P. Weber, "Thermo-optical Compensation Methods for High-Power Lasers," *IEEE Journal of Quantum Electronics*, 2002, Vol. 38, No. 12, pp. 1620-1628
- [8.23] Victor Zelenogorsky, Oleg Palashov and Efim Khazanov, "Adaptive compensation of thermally induced phase aberrations in Faraday isolators by means of a DKDP crystal Optic Communications," *Optics Communications*, 2007, Volume 278, Issue 1, pp. 8-13
- [8.24] Victor V. Zelenogorsky, Andrey A. Shaykin, Eugene E. Kamenetsky, Oleg V. Palashov, and

- Efim A. Khazanov, "Using DKDP Crystals for Adaptive Compensation of Thermal Lens in Faraday Isolators," 2006, Lasers and Electro-Optics, 2006 and 2006 Quantum Electronics and Laser Science Conference
- [8.25] Ivan Mukhin, Alexandr Voitovich, Oleg Palashov, Efim Khazanov, "2.1 Tesla permanent-magnet Faraday isolator for subkilowatt average power lasers," Optics Communications, 2009, Vol. 282, Iss. 10, pp. 1969-1972
- [8.26] Chris Pannell. Internal Correspondence.
- [8.27] E. H. Turner and R. H. Stolen, "Fiber Faraday circulator or isolator," Optics Letters, 1981, Vol. 6, No. 7, pp. 322-323
- [8.28] Day, G.W., Payne, D.N., Barlow, A.J. and Ramskov Hansen, J.J, "Faraday rotation in coiled, monomode optical fibres: isolators, filters and magnetic sensors," Optics Letters, 1982, Vol. 7, (5), pp. 238-240
- [8.29] L. Sun, S. Jiang, J. D. Zuegel, and J. R. Marciante, "All-fiber optical isolator based on Faraday rotation in highly terbium-doped fiber," Optics Letters, 2010, Vol. 35, No. 5 , pp.706-708
- [8.30] L. Sun, S. Jiang, and J. R. Marciante, "Compact all-fiber optical Faraday components using 65-wt%-terbium-doped fiber with a record Verdet constant of $-32 \text{ rad}/(\text{Tm})$," Optics Express, 2010, Vol. 18, No. 12, pp.12191-12196

Appendix A8.1: Derivation of equation 8.4

An EM wave $E(z,t)$ propagating in the z direction can be decomposed into two orthogonal components E_x and E_y

$$\begin{aligned} E(z,t) &= \hat{x}E_x(z,t) + \hat{y}E_y(z,t) \\ E_x(z,t) &= E_{ox}e^{i(kz-\omega t)} \\ E_y(z,t) &= E_{oy}e^{i(kz-\omega t+\phi)} \end{aligned} \quad (\text{A1.1})$$

Linearly polarised light can be made from a combination of right E_{RH} and left E_{LH} circularly polarised light with the same magnitude. Using Euler's formula and equation A1.1 right and left circularly polarised waves with magnitude $A/2$ can be expressed as

$$E_{RH}(z,t) = \frac{A}{2}\cos(k_R z - \omega t)\underline{i} + \frac{A}{2}\cos(k_R z - \omega t + \frac{\pi}{2})\underline{j} \quad (\text{A1.2})$$

$$E_{LH}(z,t) = \frac{A}{2}\cos(k_L z - \omega t)\underline{i} + \frac{A}{2}\cos(k_L z - \omega t - \frac{\pi}{2})\underline{j} \quad (\text{A1.3})$$

Where k_R and k_L are the wavenumber of right and left circularly polarised light. From Equations A1.2 and A1.3

$$E_{RH}(z,t) = \frac{A}{2}\cos(k_R z - \omega t)\underline{i} - \frac{A}{2}\sin(k_R z - \omega t)\underline{j} \quad (\text{A1.4})$$

$$E_{LH}(z,t) = \frac{A}{2}\cos(k_L z - \omega t)\underline{i} + \frac{A}{2}\sin(k_L z - \omega t)\underline{j} \quad (\text{A1.5})$$

Adding these two waves and using the trigonometric functions for $\cos+\cos$ and $\sin+\sin$ yields

$$E_{RH}(z,t) = A\cos\left(\frac{(k_R + k_L)}{2}z - \omega t\right)\cos\left(\frac{(k_R - k_L)}{2}z\right)\underline{i} + A\cos\left(\frac{(k_R + k_L)}{2}z - \omega t\right)\sin\left(\frac{(k_R - k_L)}{2}z\right)\underline{j} \quad (\text{A1.6})$$

This is a plane wave (since there is no phase difference between the x and y components). The angle that this wave makes to the y axis is given by

$$\theta = \tan^{-1}\left[\frac{E_y}{E_x}\right] = \frac{(k_R - k_L)}{2}z = (n_R - n_L)\frac{\pi z}{\lambda} \quad (\text{A1.7})$$

In a material with circular birefringence the refractive index for right circularly polarised light n_R is not equal to the refractive index for left circularly polarised light n_L . Therefore the angle of linear polarisation rotates as the wave travels along the z direction.

Chapter 9 - Thermal Lens Effect in Faraday Isolator

This Chapter describes the limitations imposed upon Faraday isolators by thermal effects as optical power is increased. The chapter focuses mostly on thermal lensing; How to model thermal lensing? How to measure thermal lensing? And how to compensate for thermal lensing?

This chapter is structured as follows:

- **Section 9.1 – Thermal Gradients in Optical Materials** - Introduces the theory of thermal self-heating and the use of the thermal diffusion equation to calculate temperature rises and gradients.
- **Section 9.2 - Calculating Thermal Lens Focal Length** - Describes how temperature gradients create power dependent thermal lenses and how they can be used to predict thermal lensing.
- **Section 9.3 - Measuring Thermal Lens Power (Geometrical)** - Describes the geometrical method used to measure thermal lensing.
- **Section 9.4 - Focal Shift in Terms of Rayleigh Length** – Describes connection between the two most common thermal lens measurands, dioptres per kW and Rayleigh length per kW.
- **Section 9.5 - Our Thermal Lens Measurement Setup** – Describes the equipment and procedure used to measure thermal lensing
- **Section 9.6 - Other Thermal Lens Measurement Techniques** – Literature review of other methods used to measure thermal lensing.
- **Section 9.7 - Thermal Lens Compensation** – Describes use of negative dn/dT material to compensate for thermal lensing.
- **Section 9.8 - Temperature variation of the Verdet Constant and magnetic field strength**

9.1 Thermal Gradients in Optical Materials

As light passes through a medium it is absorbed. The amount of absorption is characterised by the absorption coefficient α calculated from the Beer-Lambert Law

$$I = I_0 e^{-\alpha d} \quad (9.1)$$

which relates the transmission of light through a sample (I/I_0) to the thickness of the sample d .

The energy of the absorbed light, if not reradiated, is lost as heat. This creates temperature rises and thermal gradients within the material. The temperature distribution in the material can be calculated by solving the thermal diffusion equation [9.1]

$$\frac{\partial T}{\partial t} = k \nabla^2 T + Q \quad (9.2)$$

Where k is the thermal conductivity, T is the temperature and Q is the rate of heat generation per unit volume.

The thermal diffusion equation is solvable analytically only for a small number of systems with relatively simple geometries and boundary conditions. Complex heat transfer problems can be solved numerically using finite element modelling and lots of thermal modelling packages are available for this purpose [9.2, 9.3]. Fortunately, our problem is fairly simple and a semi-analytical solution is possible for the steady state temperature distribution. The problem closely resembles the heating associated with CW end pumping of a laser rod and is well understood [9.4-9.6].

In our isolator the TGG crystals are cylindrical rods with large(ish) length to diameter ratios and heat sinking on the annular surface. The light which is causing the self heating comes from a single mode optical fibre so its spatial distribution is closely described by a Gaussian. The light is collimated so does not change spatially over the length of the TGG and the absorption of the TGG is small, so that depletion is negligible. Under these conditions the heating term Q is given by

$$Q(r) = \frac{2\alpha P_0}{\pi\omega^2} \exp\left(-\frac{2r^2}{\omega^2}\right) \quad (9.3)$$

This is simply a Gaussian function with a beam width 2ω (at the $1/e^2$ intensity points), power P and absorption coefficient α . This is simply the radial distribution of absorption (energy deposited) in the TGG.

Putting (9.3) into (9.2) and expressing in cylindrical coordinates and steady state ($dT/dt=0$) yields

$$\frac{1}{r} \frac{d}{dr} \left(r \frac{dT}{dr} \right) = -\alpha \frac{P_0}{\pi\omega^2} \frac{1}{k} \exp\left(-\frac{2r^2}{\omega^2}\right) \quad (9.4)$$

Where α is the absorption (m^{-1}), P_0 is the power (W), r_0 is the spot radius (m), k is the thermal conductivity ($Wm^{-1}k^{-1}$) and $T(r)$ is the temperature rise at position r to be calculated.

A semi-analytical solution for this equation can be found for the case of an infinite cylinder with radius a , and Dirichlet boundary conditions at the surface so that $T_{\text{surface}} = T_{\text{amb}}$ [9.4, 9.5, 9.7]. Derived in appendix A9.1

$$T(r) = \frac{\alpha P_0}{4\pi k} \left[-2 \ln\left(\frac{r}{a}\right) + E_i\left(\frac{2r^2}{\omega^2}\right) - E_i\left(\frac{2a^2}{\omega^2}\right) \right] + T_{\text{amb}} \quad (9.5)$$

Where E_i is the exponential integral function

$$E_i(x) = \int_x^\infty \frac{e^{-t}}{t} dt \quad (9.6)$$

A plot of equation (9.5) can be seen in figure 9.1. With $P_0 = 1000\text{W}$, $\omega = 0.5\text{mm}$, $\alpha = 0.0015\text{cm}^{-1}$, $a = 6\text{mm}$ and $T_{\text{amb}} = 20^\circ\text{C}$ and crystal radius 6mm.

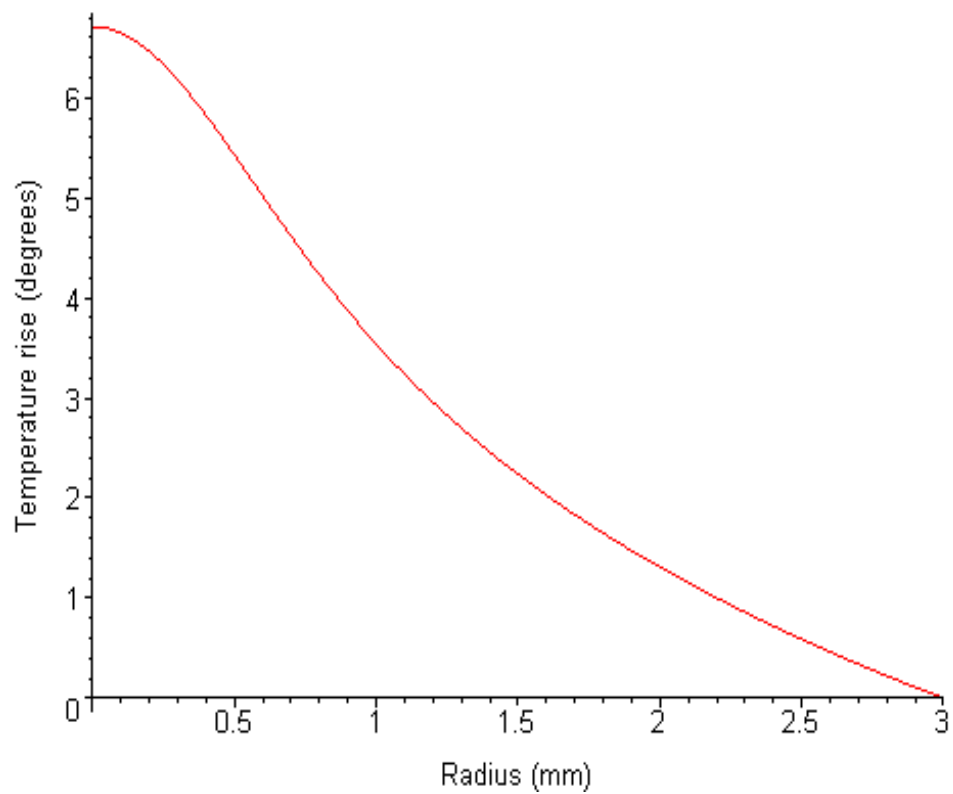


Figure 9.1: Temperature profile

9.2 Calculating Thermal Lens Focal Length

The radial temperature profile given by equation 9.5 gives rise to a radial refractive index profile in the medium. This can be calculated from the thermal dispersion coefficient of the material (dn/dT) and the intrinsic refractive index (n_0). [9.4-9.7]

$$n(r) = n_0 + \frac{dn}{dT}T(r) \quad (9.7)$$

Figure 9.2 shows the refractive index profile from the centre of the TGG rod out to 0.5mm which would be produced in TGG by the temperature profile in figure 9.1, for TGG $dn/dT = 19.1 \times 10^{-6}$ and $n_0 = 1.95$ at 1060nm. This is the section of the crystal through which the light travels. This has been fitted with a polynomial of the form.

$$n(r) = n_0 - \frac{1}{2}n_2r^2 \quad (9.8)$$

The use of the polynomial fit is necessary so that the thermal lens can be equated to a gradient index lens. Gradient index lenses are easy to understand and have parabolic refractive index profiles of the above type. Established theory can then be used to predict the focal length of the thermal lens and a simple ray matrix approach used to reconstruct the measurement setup and make a prediction of the expected position of the beam waist. The ray matrix for a gradient index lens is [9.8]

$$\mathbf{M}_{grin} = \begin{bmatrix} \cos(\gamma z) & (n_0 \gamma)^{-1} \sin(\gamma z) \\ -(n_0 \gamma) \sin(\gamma z) & \cos(\gamma z) \end{bmatrix} \quad (9.9)$$

Where

$$\gamma^2 = \frac{n_2}{n_0}$$

The effective focal length of a grin lens of is given by

$$f = \frac{1}{n_0 \gamma \sin(\gamma L)} \quad (9.10)$$

The focal length of the parabola in figure 9.2 is 0.53m. A more accurate approach would be to fit the curve with a more appropriate polynomial and use a beam propagation or ray-tracing program (like

Zemax) to model the resultant lens. This would have the added advantage of being able to model complex temperature gradients and analyse aberrations.

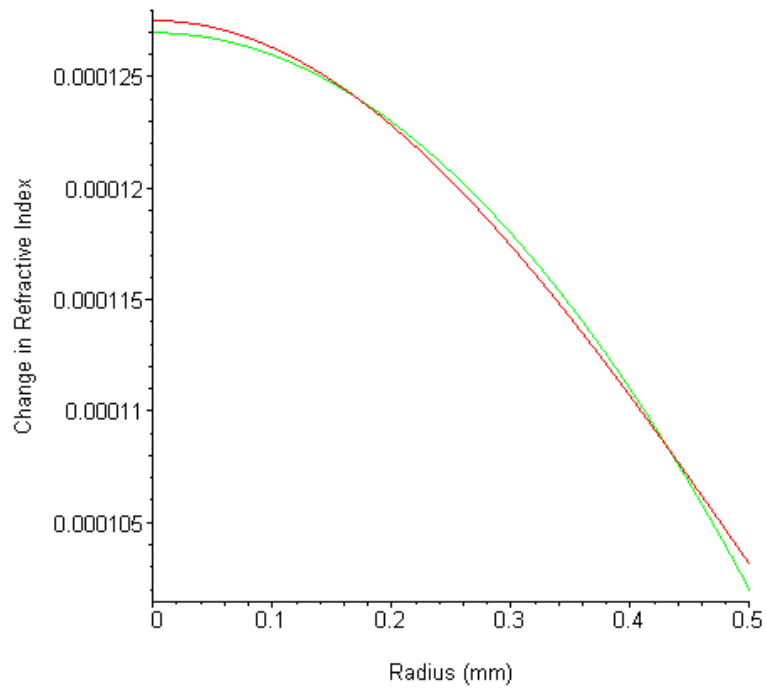


Figure 9.2: Refractive index in centre of a 6mm radius TGG crystal heated by a 1kW Gaussian beam with a spot size of 1mm. Red – modelled refractive index. Green – fitted parabola.

Figure 9.3 shows the change of the dioptric power ($1/f$) of the thermal lens in the TGG with power. The slope of this graph predicts about 8 Dioptres/kW.

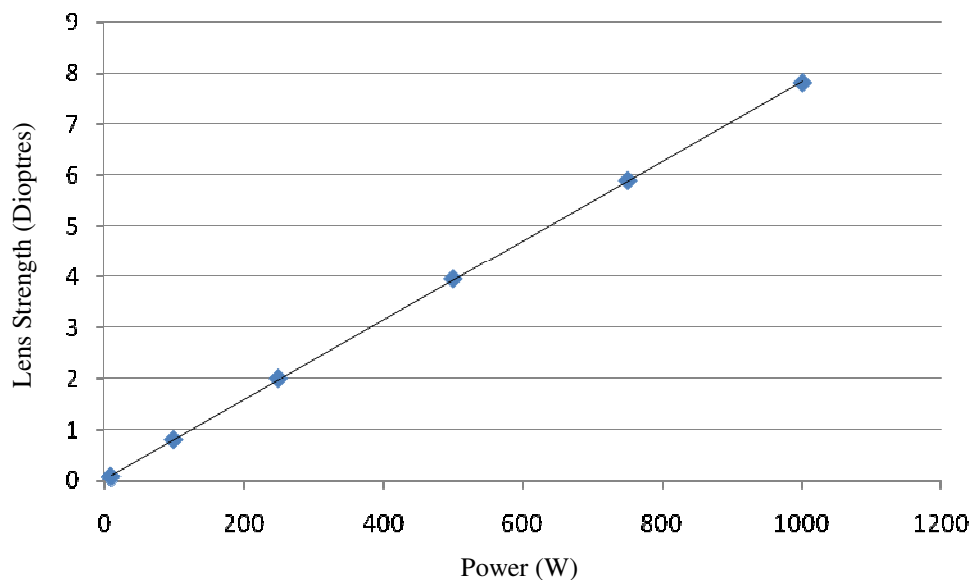


Figure 9.3: Dioptric power of thermal lens against power in 30mm piece of TGG.

The above discussion predicts the thermal lens focal length caused by the thermo-optic effect. It ignores the other contributions made to the thermal lens by the photoelastic effect and thermal expansion. However, Koechner [9.9] and Mansell [9.10] estimate that these effects will be small (<20%) in comparison.

9.3 Measuring Thermal Lens Power (Geometrical)

The measurement of the focal length (or dioptric power) of a thermal lens in a sample involves combining an accurate measurement of the position of the beam waist after the sample with knowledge of the experimental setup, especially the beam parameters before the sample. The focal length of the thermal lens can then be calculated by comparing the change in beam parameters before and after the sample with what would be expected of a thin lens. Making this measurement at different power levels gives the change in the focal length of the thermal lens as a function of the power, as calculated by the model in figure 9.3. This would give a good measurement of the strength of the thermal lens effect. However, this is a difficult measurement to make as it depends on good characterisation of the beam in all parts of the test setup. It also involves a calculation approximating the thermal lens with an aberration free thin lens.

A measurement of the shift in the focal position with power in mm/kW can be made more easily and used directly as a measurement of the thermal lens. However, this measurement only allows comparison of samples in the same setup, it is not universal. It does not allow comparison between different systems without additional knowledge, for example a small shift in a beam with a short Rayleigh length has a larger effect on the power density at the measurement plane than the same shift in a beam with a long Rayleigh length. In order to compare different systems with different beam parameters it is the quotient between the shift with power and the Rayleigh length of the output beam which is important. The result is a distance moved in Rayleigh lengths per unit of power (Rz/kW) which is invariant of the experimental setup (section 9.4).

The measurement of a shift in Rz/kW requires the simultaneous measurement of the beam waist position and Rayleigh length of the output beam at each power level. These are both available from measurements of the beam caustic (or M^2). This is a measurement of the beam size ω along the beam path and fits the well known equation for light propagation in the z direction [9.10].

$$\omega^2 = \omega_0^2 + \left(\frac{M^2 \lambda}{\pi \omega_0} \right)^2 (z - z_0)^2 \quad (9.11)$$

This is a quadratic in z with a minimum at z_0 , where M^2 is the beam propagation factor and ω_0 is the beam radius at the beam waist position. The M^2 of a laser beam tells us how well it can be focused compared to a Gaussian beam. A Gaussian beam has an $M^2 = 1$, all other beams have $M^2 > 1$.

According to ISO 11146 to calculate the M^2 of a laser beam the beam size should be measured at 10 points, 5 within ± 1 Rayleigh length of the waist and 5 greater than 1 Rayleigh length away from the waist. The measured points can then be fit to equation 9.11 and the M^2 calculated. ISO 11146 also stipulates that the beam size should be measured using the second moment definition. [9.11]

Expanding equation 9.11 produces

$$\omega^2 = \left(\frac{M^2 \lambda}{\pi \omega_0} \right)^2 z^2 + \left(-2z_0 \left(\frac{M^2 \lambda}{\pi \omega_0} \right)^2 \right) z + \left(\left(\frac{M^2 \lambda}{\pi \omega_0} \right)^2 z_0^2 + \omega_0^2 \right) \quad (9.12)$$

Comparing to a quadratic of the form

$$\omega^2 = az^2 + bz + c \quad (9.13)$$

It can easily be shown that

$$z_0 = \frac{-b}{2a} \quad \omega_0 = \sqrt{c - \frac{b^2}{4a}} \quad M^2 = \frac{\pi}{2\lambda} \sqrt{4ac - b^2} \quad z_R = \frac{1}{a} \sqrt{ac - \frac{b^2}{4}} \quad (9.14)$$

To calculate these quantities an Excel spreadsheet was used. This took input measurements of the beam size at different distances and returned the above quantities. Difference measurements of z_0 between power levels were used to produce graphs of power change versus shift in waist position. The waist position was normalised to the average of the Rayleigh lengths of the two measurements. The gradient of the final graph gives a measurement of the thermal lens in Rz/kW.

This thermal lens measurement appears in several papers and conference proceedings [9.12, 9.13]. Other sources use the more traditional thermal lens measurement of focal length/dioptres and focus position shift per kW. However, no sources were found to show the equality between the two. Section 9.4 will try to satisfy this with a geometrical argument.

9.4 Focal Shift in Terms of Rayleigh Length

At this point we have a model which can calculate the focal length of a thermal lens from the temperature profile and material properties of the TGG rod. From which we can extrapolate a prediction of the thermal lens shift in units of dioptres/kW. We also have a simple method to measure the thermal lens in units of Rayleigh length per kilowatt. What we now require is a transformation which will allow comparison between the two.

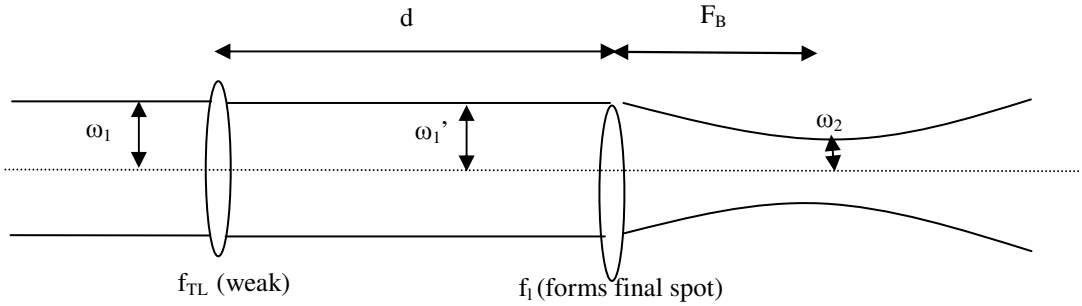


Figure 9.4: Two lens system used to derive argument to compare focal shift in Rz/kW to Dioptres/kW.

In appendix 9.2 a geometrical argument based on a two lens system with one fixed lens and one thermal lens, as shown in figure 9.4, is used to demonstrate that [9.14]

$$\frac{1}{z_{R2}} \frac{\partial f_B}{\partial P} = -z_{R1} \frac{\partial \left(\frac{1}{f} \right)}{\partial P} \quad (9.15)$$

Here f_B is the back focal length of the two lens system, f is the focal length of the thermal lens, P is the power of the beam and z_{R1} and z_{R2} are the Rayleigh Lengths of the input and output beam respectively.

The LHS of equation 9.15 is the power dependent shift in Rayleigh lengths of the back focal length of a two lens system with one power dependent thermal lens. The RHS is the change in focal power (dioptres) of the thermal lens with power.

This simple result shows that the shift in the thermal lens focal length in dioptres per kW multiplied by the Rayleigh length of the input beams gives the thermal lens shift of the output beam waist in units of Rayleigh length (of the final beam) per kW.

For an input beam with a diameter of 1mm and an $M^2 = 1$ the Rayleigh range $z_{R1} = 0.78\text{m}$. From figure 9.3 the predicted shift in focal power of the induced thermal lens for a 30mm piece of TGG with an absorption of 0.0015cm^{-1} is around 8 Dioptres/kW. Therefore the change in focal position is expected to be

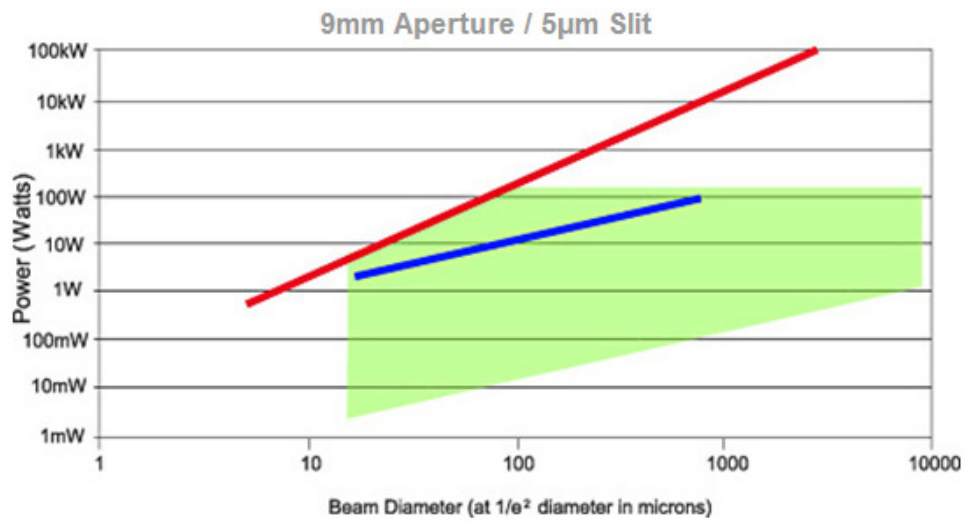
$$\frac{\partial f_B}{\partial P} \approx -0.78 \times 8D / kW \approx -6R_z / kW \quad (9.16)$$

The negative sign accounts for the fact that the thermal lens is positive and causes the focal plane to move closer to the TGG rod.

9.5 Our Thermal Lens Measurement Setup – Equipment and procedure

To measure the focal shift created by a thermal lens a pyroelectric knife edge profiler (Nanoscan, Photon Inc.) with a 9mm aperture and a $5\mu\text{m}$ slit width is used. This detector is ideal because it operates over a large dynamic range of powers. This allows measurements to be made at different locations along a focussed beam's propagation without adding attenuation to deal with the higher power densities at the focus. The operation space of the detector is shown in figure 9.5. If this was done with a silicon or germanium detector then the power would need to be attenuated to below 10mW. This is possible using reflections; however care must be taken so that the attenuators don't induce significant levels of thermal lens or beam distortion/steering.

NanoScan Operating Space Chart for Pyroelectric Detectors



Pulsed Operation: Upper limit of the operating space for pulsed laser measurements.

Slit Damage: Power density (watts/cm^2) where one can begin to cut the slits. Refer to Photon's Aperture Damage due to High Incident Power document.

Left Boundary: Smallest beam size limited to 4-5 times the slit width. Some models have another limit due to electrical bandwidth.

Right Boundary: Instrument entrance aperture. The largest beam width ($1/e^2$) will be the aperture divided by 1.2-1.4.

Figure 9.5: Operating Space chart for Nanoscan pyroelectric scanning-slit detector

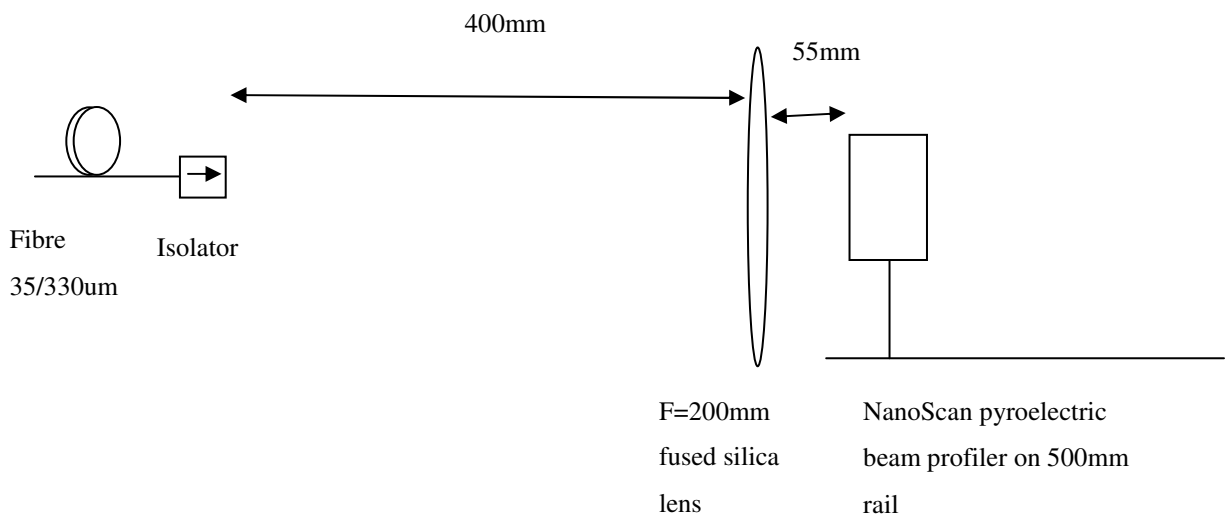


Figure 9.6: Setup for measurement of thermal lens from an isolator.

The profiler is positioned on an automated rail system that can be accurately aligned with the beam path. A plano-convex fused silica lens ($f=100\text{mm}$ to 250mm) is used to form a focus over the rail, as shown in figure 9.6. As the Nanoscan is moved along the rail, software records the beam diameter in two orthogonal planes (x and y) at each position. The x and y planes are randomly orientated with respect to the beam. These can be rotated to align with the “worst” axis in an astigmatic, non-circular beam.

The beam radius squared (ω^2) with distance along the rail for the x and y measurement planes for a typical scan are shown in figure 9.7. These show excellent correlation with the parabola given by equation 9.12. Using a least squares method the coefficients of the parabolas can easily be found and from these the M^2 , waist position z_0 , waist size w_0 , divergence θ and Rayleigh Length z_r for each plane can be extracted using equations 9.14. The circularity and astigmatism of the beam can also be measured by comparing the two planes.

The parameters of the beam measured in figure 9.7 are shown in table 9.1. These correspond to M^2 values of 3.84 and 3.88 for the x and y measurements respectively. Transformations using ray matrices (or otherwise) can be used to calculate the beam parameters at any other part of the setup from those measured.

These measurements and calculations are made at different power levels and the difference measurements used to create graphs of the focal position shift normalised to the Rayleigh length with power, like the one shown in figure 9.8. The gradient of the graph gives a measure of the thermal lens in R_e/kW which can be used to directly compare different setups.

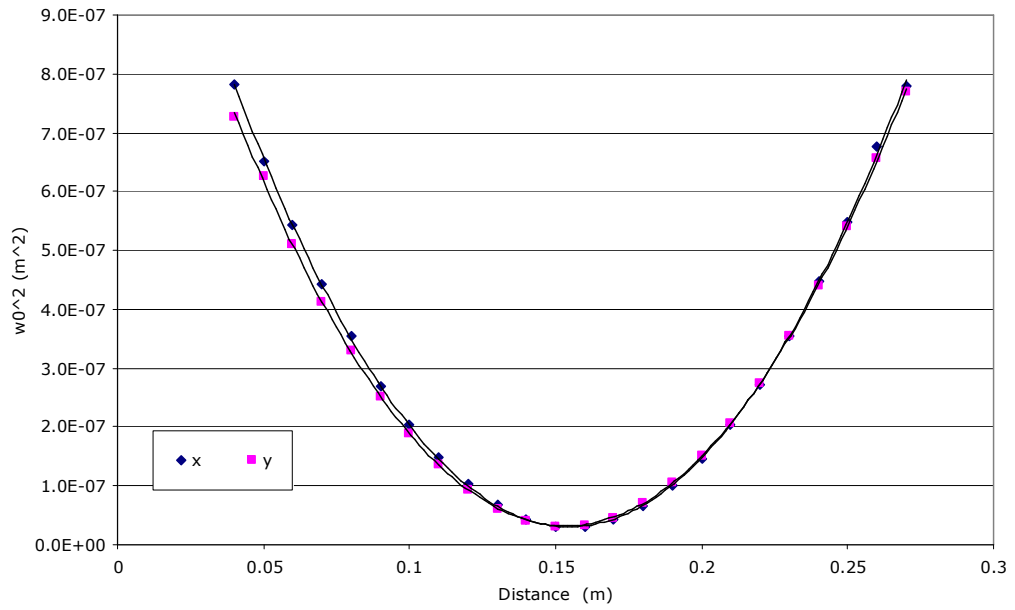


Figure 9.7: Measurement of beam radius with position made by Nanomodescan system.

| | a | b | c |
|---|----------|-----------|----------|
| x | 5.73E-05 | -1.77E-05 | 1.40E-06 |
| y | 5.46E-05 | -1.68E-05 | 1.32E-06 |

| | x | y |
|--------------------|---------|---------|
| M ² (y) | 3.88 | 3.84 |
| Z0 (mm) | 153.49 | 154.83 |
| W0 (um) | 178.75 | 172.71 |
| Theta (rads) | 0.00739 | 0.00757 |
| Zr (mm) | 24.19 | 22.81 |

Table 9.1: Coefficients of parabola fit for curves in figure 9.7 and calculated beam parameters.

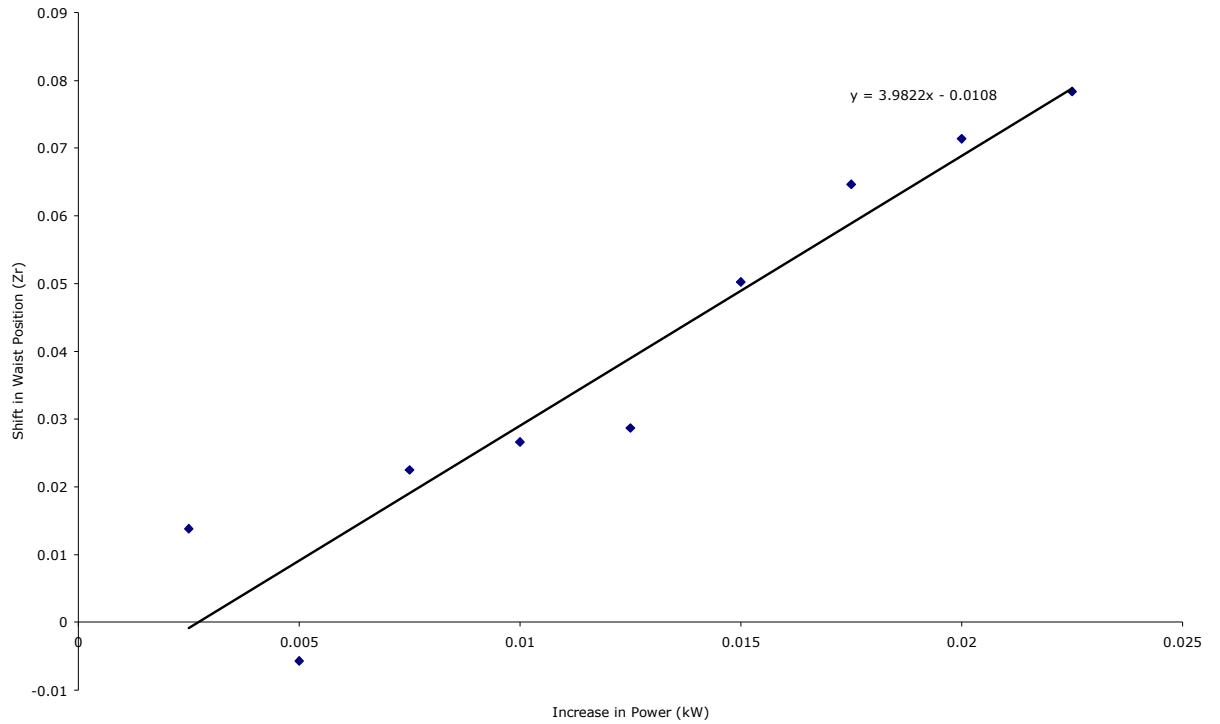


Figure 9.8: Example thermal lens measurement.

The isolators can be tested using either a 200W 1060nm CW ytterbium fibre laser or a 30W 1060nm pulsed fibre laser. The pulsed fibre laser has a fibre output which can be directly spliced to a collimator or isolator for testing. The fibre has a 35 μ m core and a 330 μ m cladding and supports multiple propagation modes. The M^2 of the light leaving the fibre is around 3.

The CW laser has a fibre with a 10 μ m core and 330 μ m cladding which is single mode. However, it is spliced permanently to beam delivery optics. The output is a collimated 5mm diameter beam that can be reduced as necessary by a selection of lenses. The light can also be coupled into another 10/330 μ m fibre using a 40mm achromatic lens with about 75% efficiency. Using active water/air cooling and stable stages we have managed to couple over 100W into a single mode fibre in this way. Coupling 20W can be achieved with a long term stability of <5% over several hundred hours. Figure 9.9 shows the fibre coupling jig with water and forced air cooling.

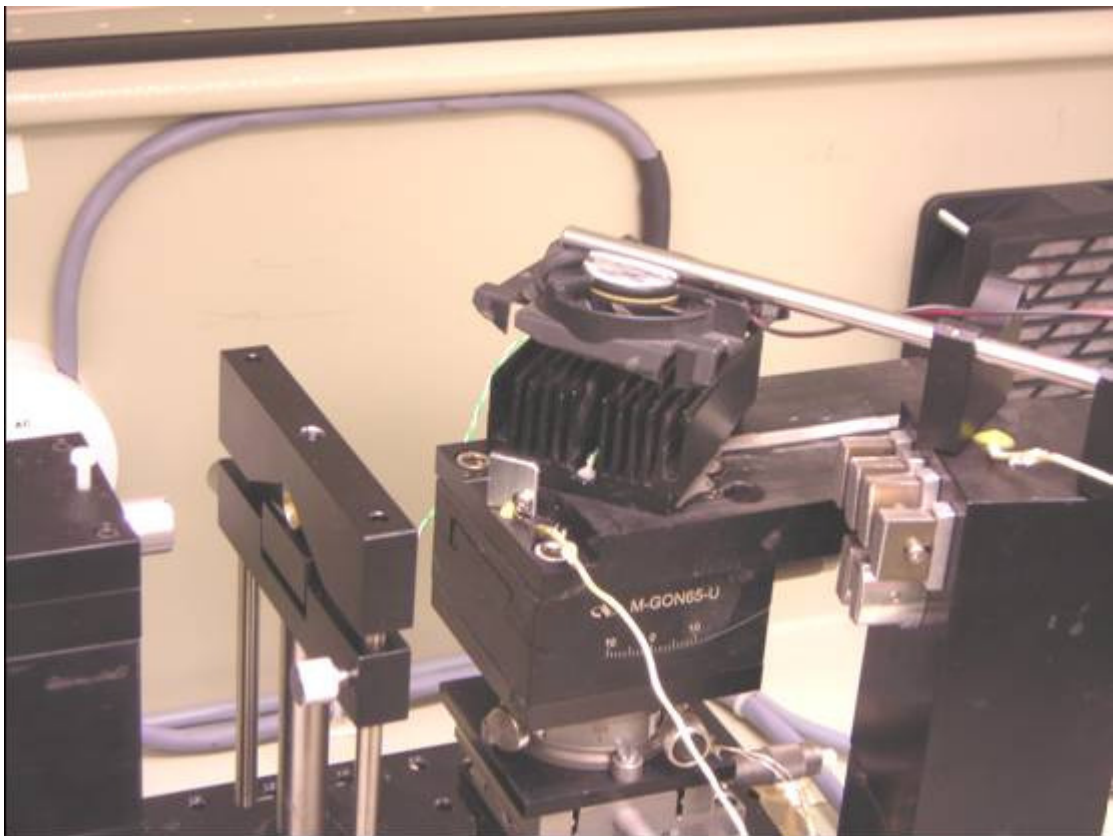
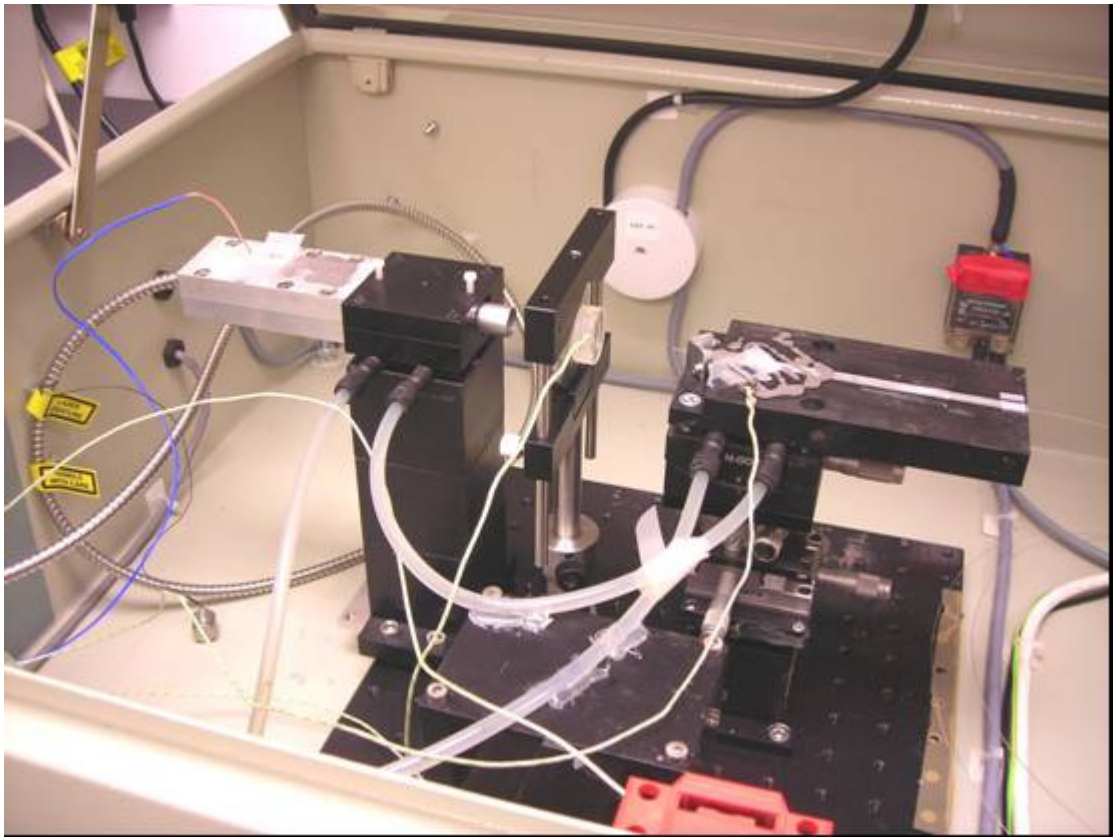


Figure 9.9: Fibre coupling jig with water (top) and forced air (bottom) cooling.

9.6 Other Thermal Lens Measurement Techniques

A large number of other techniques have been used to measure the thermal lens effect. The simplest and most common techniques use geometrical optics and measure the change in propagation of a laser beam as it passes through a material with a thermal gradient.

D.C. Burnham [9.15] describes a simple method for measuring thermal lensing in a flash lamp pumped laser rod. They measure the amount of light transmitted through an aperture at different distances around the laser waist before and after a flash lamp pulse. Using this information they can accurately determine the waist position of the laser transmitted through the rod with and without the thermal lens. The focal length of the thermal lens can be calculated from the waist position with and without a thermal lens created by the lamp pulse. This method has an additional benefit for pulsed operation as it allows the transient effects of the thermal lens upon cooling to be evaluated.

Hu and Whinnery [9.16] describe a similar method where they measure the temporal response of light passing through an aperture in the far field and calculate the change in divergence of the beam. They use this to calculate the absorption of the sample. This method forms the basis of thermal lens spectroscopy which is now commonly used to measure small absorption of highly transparent materials. Using thermal lens techniques absorption coefficients down to 10^{-7} can be measured. Good reviews of thermal lens spectroscopy and other photothermal techniques can be found in the literature [9.18, 9.19]

Dual beam pump-probe setups are often used for their increased flexibility when measuring transient properties. Pump-probe methods allow continuous monitoring of a low power probe beam with a pulsed pump and so allow the measurement of transient thermal lenses during a pulse and relaxation after the pulse. They also allow different pump probe geometries to be tested. This may be important for studies of laser rods in cavities as the pump and signals are often optimised to have different diameters. These are explained in [9.18, 9.19]. As a further example Nunes et. al. [9.20] use a mode mismatched pump-probe technique to measure the thermal properties of Nd:YAG.

Blomster et. al. [9.12] make the equivalent measurement to ours. However, instead of measuring the pump beam directly using a high power detector they measure the propagation of a low power probe beam using a CCD camera. The pump and probe occupy the same focal region in the sample but travel with a slight angle between them. This allows them to be easily spatially separated for detection. The disadvantage of this technique is the lower resolution of the camera compared to the knife edge detector. Muzzamil et. al. [9.21] use the same method to measure the thermal lens focal shift produced in a glass block with radial heating.

The deflection of a probe beam as it propagates through a region with a temperature gradient can also be used to measure the strength of a thermal lens. This is demonstrated in figure 9.10. Paugstadt and Bass [9.22] demonstrate the method using a position sensitive detector. The advantage of their technique is that by scanning the probe laser over the crystal a map of the refractive index profile can be made with high spatial and temporal resolution. This also has the power to resolve aberrations caused by the thermal lens.

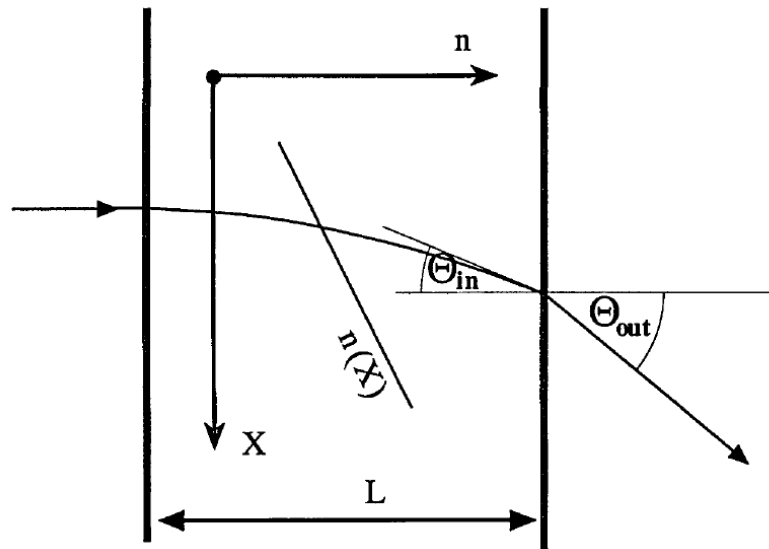


Figure 9.10: Probe deflection thermal lens measurement [9.22].

The focal length of an intracavity thermal lens can also be determined from measurements of the beam outside of the cavity by applying paraxial transformations or by varying the cavity to determine the stability zones. Beat Neuenschwander et. al. [9.24] showed that the focal length of a stable spherical cavity could be measured from the far field beam waist diameter. They also show that the M^2 of the beam can be calculated if the near field waist diameter is also known. The error in the measurement of the focal length could be as high as $\pm 60\%$ when the beam deviates from single mode.

Another approach is to measure the power at which a resonator loses stability. This approach is used by Liu et. al. [9.25]. They show that a simple asymmetric plane-plane cavity with the gain medium close to one output mirror becomes unstable when the focal length of the thermal lens equals the distance between the other mirror and the laser medium.

More accurate measurements can be made using interferometry to measure the path length (phase) difference across the sample directly. Khizinyak et. al. [9.26] use a phase shifting Mach-Zender interferometer to measure the wavefront of a probe beam as it passes through an active laser rod. Blows et. al. [9.27] use holographic lateral shear interferometry to measure the thermal focal length of Nd:YVO₄ under lasing and non lasing conditions.

The wavefront of a beam can also be measured directly with a Shack-Hartmann wavefront sensor. In a Shack-Hartmann wavefront sensor an array of lenses form an array of focussed spots on a CCD sensor the position of these change in accordance with the local tilt of the wavefront. The sensitivity of this device can be very high ($>\lambda/100$).

S. Chenais et. al. [9.28] describe using a Shack-Hartmann sensor to measure the thermal lens focal length in various laser rods under lasing and non-lasing conditions. Their minimum detectable dioptric power is below 1m^{-1} . Mansell et. al. [9.29] use a similar setup to measure the thermal lens of transmissive optics used in the LIGO long baseline interferometer setup. They calculated that the minimum detectable optical path length change measurable with the Shack-Hartmann sensor used to be below 10nm.

In an interesting adaption of the technique Zelenogorsky et. al. [9.30] use a scanning Shack-Hartmann system to measure the wavefront distortions of a thermal lens in TGG. Instead of using a microlens array and a CCD sensor for the Shack Hartmann measurement their system uses a single lens and scans a probe laser through the TGG building up a Shack Hartmann diffraction pattern point-by-point. In a traditional Shack-Hartmann device edge diffraction from each lens in the array limits the ultimate sensitivity of the measurement. The scanning method effectively circumvents the use of a lens array and increases the sensitivity of the measurement. The downside is the increased time to make a measurement which limits this technique to examining steady state thermal lens only.

Shack-Hartmann and interferometer measurements allow aberrations of the thermal lens to be seen directly. This is particularly advantageous for some applications. The geometric and cavity based techniques need to be coupled with other measurements to do this. Our measurement method gives an indirect measurement of aberrations through the M^2 measurement of the beam. The focal length of beams with a higher M^2 will shift less with power than low M^2 beams because the power in the beams is spread more evenly over the beam diameter. This causes smaller thermal gradients for the same absorbed power and hence less thermal lens shift.

9.7 Thermal Lens Compensation

So far Chapter 9 has discussed the origin of the thermal lens effect and methods of modelling and measuring the thermal lens effect. This section will now look at methods which have been used to compensate for thermal lensing.

In solid state laser cavities designed for high power operation the thermal lens effect can be reduced by including a pair of telescopic lenses. Hannah et. al. [9.31] showed that a combination of lenses

within a cavity could be used to expand the beam size through the laser rod, thus reducing thermal lensing and extending the power stability of the laser resonator.

These two papers and patent [9.32-9.34] report on thermal lens compensation by using an output mirror which could be translated along the optical axis. This allows for adaptive compensation which is very useful for applications which require a good beam quality over a wide range of output powers. The disadvantage with this approach is the requirement to actively and precisely translate the output mirror which requires additional system complexity. It also does not compensate for aberrations induced by the non ideal form of the thermal lens.

The use of adaptive optics to compensate for the thermal lens effects has also been demonstrated. These methods use adaptive elements to maintain a specified wavefront at some point in the system through sensing and electronic feedback control. These can effectively compensate for the thermal lens induced focus shift and also simple aberrations. However they are complex and expensive to implement.

Schwarz et. al. [9.35] use a mechanically deformable mirror to compensate the thermal lensing in a Nd:YAG laser. Their system uses a manual adjustment of the mirror, but it's easy to see how electronic control could be integrated.

In another approach Degallaix et. al. [9.36] proposes compensating for a thermal focal shift by inducing the inverse temperature gradient in a silica plate to form a defocusing lens. They achieved this by heating the circumference of the plate so that the plate was coolest at its centre. The approach has recently been demonstrated [9.37] using annular ring heaters bonded to the circumference of a cylindrical piece of SF57. They showed that the focal length could be varied widely, and also that by using non uniform heating they could compensate for thermal astigmatism.

Muzamil et. al. [9.38] use a CO₂ laser to induce a thermal pattern into a silica plate to produce a tunable thermal lens. They propose that both positive and negative lenses can be created by the choice of heating pattern (beam shape) or by changing between materials with either positive or negative dn/dT. This has recently been demonstrated in the LIGO interferometer with feedback control to maintain coupling.

The problem with active methods of compensation is that you have to monitor the wavefront of the beam passing through the system to provide a feedback signal that can be used to optimise the compensation. This requires a complex detection system and also complex control of the compensating system. This cannot be practically applied to our Faraday isolator which is supposed to be a passive component.

Graf et. al. [9.39] showed that the thermal lens of an Nd:YAG laser could be effectively compensated passively by introducing an optical element with a negative dn/dT into the cavity. They used several different liquids and gels for this including OCF-446 and Sylgard 184. They found that a resonator which became unstable at a pump power of around 370W could be pumped at over 600W (pump limited) without becoming unstable. The thermal lens power with compensation was reduced to just 1.6 diopters/kW from around 17 diopters/kW uncompensated. Yoshida et. al [9.40] demonstrated the same effect using a rod of poly-methyl methacrylate (PMMA).

Zelenegorsky et. al. [9.41] showed that the thermal lens created in TGG in a Faraday isolator could be successfully compensated for using deuterated potassium phosphate (DKDP or KD*P). They showed that the loss of power from the Gaussian mode could be reduced from 25% to below 0.5% at 45W laser power. Khazanov and Zelenegorsky [9.42] demonstrated a similar approach using FK51 glass. In chapter 10 we will look at the practicality of applying thermal lens compensation to our isolator design. We will also look at the results of thermal lens focal shift measurements made on the isolator with and without a compensating element.

9.8 Compensation of thermal lens with DKDP

Table 9.2 shows the properties of DKDP alongside TGG. These can be used in the model above, sections 9.1 and 9.2, to predict the length of KDP required to compensate for the thermal lens produced in the TGG. If we assume that the thermal lens focal shift (strength of the thermal lens) is directly proportional to the length of the crystal. Then compensation should be easy to calculate by simply keeping the ratio of TGG to DKDP fixed.

| | TGG | DKDP |
|--|---------------------|----------------------------|
| Thermal Conductivity ($Wm^{-1}K^{-1}$) | 7.4 | ~2 |
| Optical Absorption (m^{-1}) | 0.4 | 0.5 |
| dn/dT @ 1064nm (K^{-1}) | 16×10^{-6} | -44×10^{-6} |
| Refractive Index @1064nm | 1.954 | no = 1.4931 ne = 1.4582 |

Table 9.2: TGG and DKDP parameters used in model.

Figure 9.11 shows the refractive index profile of a DKDP rod with a 1kW 1.1mm beam. With a 20W beam through a 4mm piece of TGG the model calculates that this would produce a divergent 2m focal length lens. This would compensate for a converging thermal lens of 2m in the TGG if the distance between the lenses is small compared to the focal length of the lenses. The equation for the effective focal length of a two lens system is given by

$$\frac{1}{f} = \frac{1}{f_1} + \frac{1}{f_2} - \frac{d}{f_1 f_2} \quad (9.17)$$

Where d is the distance between the two lenses and f_1 and f_2 are the effective focal lengths.

This can be looked at in another way. Following the reasoning of Amin [9.44], if the change in refractive index at a position r through a crystal is

$$\Delta n(r) = \frac{dn(r)}{dT} \quad (9.18)$$

Then the optical path difference at that point is

$$\Delta OPL(r) = L \frac{dn}{dT} T(r) = L \frac{dn}{dT} \frac{\alpha P_0}{4\pi k} \left[-2 \ln\left(\frac{r}{a}\right) + E_i\left(\frac{2r^2}{\omega^2}\right) - E_i\left(\frac{2a^2}{\omega^2}\right) \right] + T_{amb} \quad (9.19)$$

If the TGG and DKDP crystals have the same diameter a and the absorption is small so that P_0 is constant then for zero optical path difference at point r through the two crystals is

$$\Delta OPL_{TGG}(r) = \Delta OPL_{DKDP}(r) \quad (9.20)$$

$$\left(L \frac{dn}{dT} \frac{\alpha}{k} \right)_{TGG} = \left(L \frac{dn}{dT} \frac{\alpha}{k} \right)_{DKDP}$$

Since dn/dT , the absorption coefficient and the thermal conductivity are material specific properties then it is only the length of TGG and DKDP that we have left to change to achieve thermal lens compensation. From 9.20 the ratio of TGG length to DKDP length is given by

$$\frac{L_{TGG}}{L_{DKDP}} = \frac{\left(\frac{dn}{dT} \frac{\alpha}{k} \right)_{TGG}}{\left(\frac{dn}{dT} \frac{\alpha}{k} \right)_{DKDP}} \quad (9.21)$$

Using the properties of TGG and DKDP in table 9.2 the ratio of TGG to DKDP calculates to around 11:1. So, for a 40mm piece of TGG the DKDP compensator should be around 4mm in length.

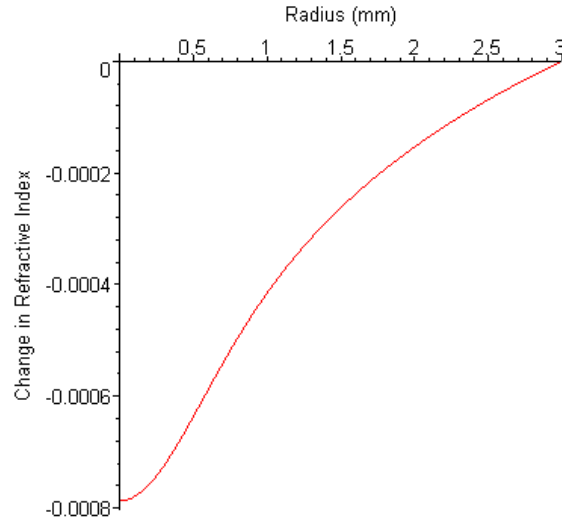


Figure 9.11: Refractive index profile in 3mm radius DKDP pumped with a 1kW Gaussian laser with a radius of 0.5mm.

9.9 Temperature variation of the Verdet Constant and magnetic field strength

Following the work of Barnes and Petway [9.43]. The rotation angle θ of a Faraday rotator varies with temperature according to

$$\frac{1}{\theta} \frac{d\theta}{dT} = \frac{1}{B} \frac{dB}{dT} + \frac{1}{V} \frac{dV}{dT} \quad (9.17)$$

Where B is the magnetic field strength and V is the Verdet constant. They measured the variation in Verdet constant near room temperature to be

$$\frac{1}{V} \frac{dV}{dT} = -3.47 \times 10^{-3} K^{-1} \quad (9.18)$$

The variation of the magnetic field strength is easily measurable and is usually given by the magnet manufacturers, typically

$$\frac{1}{B} \frac{\partial B}{\partial T} = -0.001 K^{-1} \quad (9.19)$$

If maximum isolation occurs for a rotation angle of $\pi/4$ (45°) then it is easy to show that the isolation (in dBs) will vary with temperature according to

$$dB = 10 \log_{10} \left\{ 10^{-5} + \sin^2 \left[\frac{\partial \theta}{\partial T} (T - T_0) \right] \right\} \quad (9.20)$$

Where T_0 is the design temperature of the isolator (the temperature at which the rotation angle is exactly $\pi/4$) and the factor of 10^{-5} is added to account for the fact that a real isolator would probably have a maximum isolation of ~ 50 dB and not infinite as this simple theory would predict. Figure 9.12 is a plot of equation 9.20 with the appropriate values.

From this it can be seen that the temperature has to be maintained to a fairly narrow range ± 10 K if the isolation is to remain above ~ 30 dB. To extend this we would need some kind of compensation for the change in rotation with temperature.

This simple analysis shows the effect of uniform increases in temperature. If we consider temperature gradients in the TGG then these will affect the homogeneity of rotation across the beam. This will further decrease the isolation.

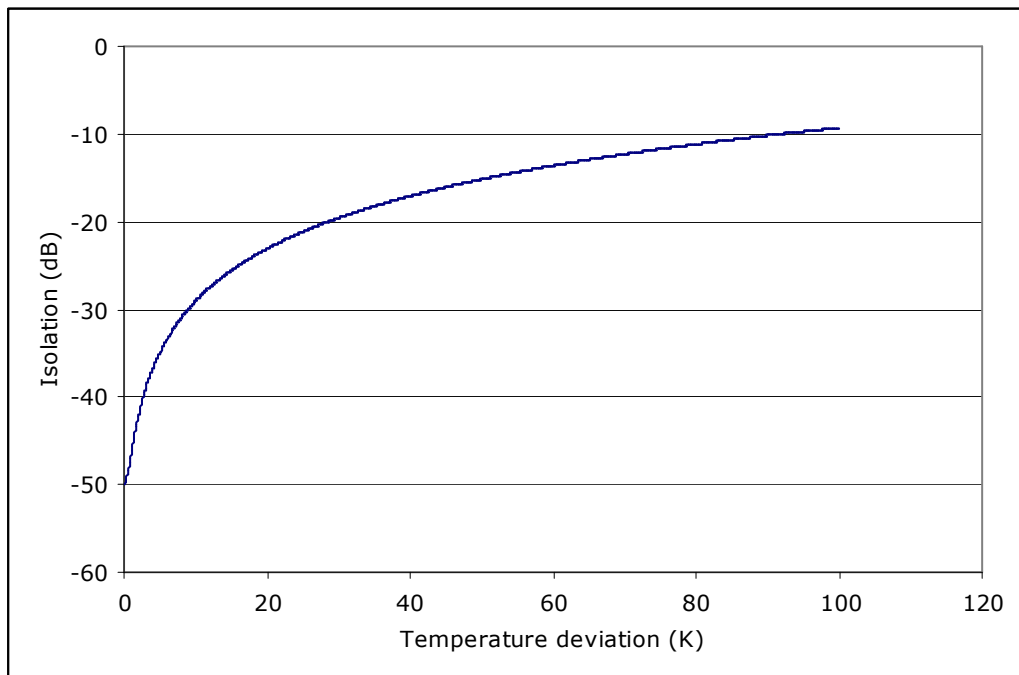


Figure 9. 12: Variation of isolation with Temperature caused just by temperature variation of the magnetic field strength and Verdet constant.

References

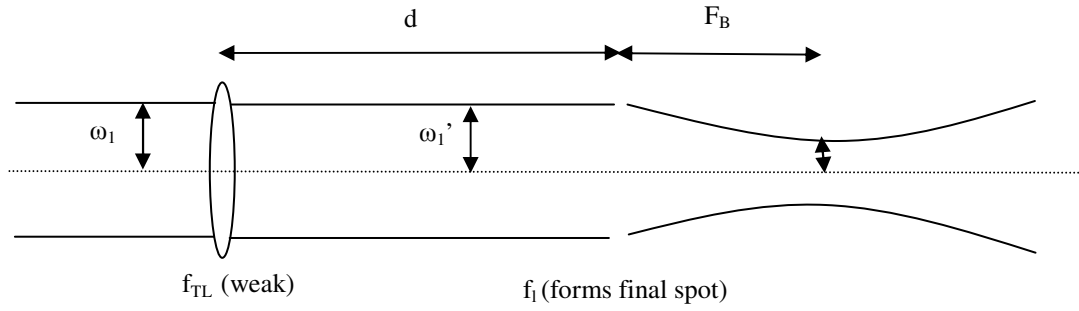
- [9.1] John H. Lienhard IV, Professor, University of Houston
John H. Lienhard V, Professor, Massachusetts Institute of Technology “A Heat Transfer Textbook”,
4th edition <http://web.mit.edu/lienhard/www/ahtt.html>
- [9.2] Ansys Multiphysics
<http://www.ansys.com/Products/Simulation+Technology/Multiphysics#/0/15>
- [9.3] Solidworks simulation premium
http://www.solidworks.com/sw/products/10172_ENU_HTML.htm
- [9.4] M. E. Innocenzi, H. T. Yura, C. L. Fincher, and R. A. Fields, “Thermal modeling of continuous wave endpumped solid state lasers” *Appl. Phys. Lett.*, 1990, Vol. 56, No. 19, pp. 1831-1833
- [9.5] Shuzhen Fan, Xingyu Zhang, Qingpu Wang, Shutao Li, Shuanghong Ding, Fufang Su, “More precise determination of thermal lens focal length for end-pumped solid-state lasers” *Optics Communications*, 2006, Vol. 266, pp. 620–626
- [9.6] Patrice Hello and Jean-Yves Vinet, “Analytical models of thermal aberrations in massive mirrors heated by high power laser beams”, *J. Phys. France*, 1990, Vol. 51, pp. 1267-1282
- [9.7] J. R. P’hinneru, D. T. Miller, F. Dabby, “Thermal Convection and Spherical Aberration Distortion of Laser Beams in Low-Loss Liquids”, *IEEE Journal of Quantum Electronics*, 1967, vol. 3, Iss. 9, pp. 382-283
- [9.8] Walter Koechner, “Solid-state laser engineering”, 6th ed., Springer, 2006
- [9.9] W. Koechner “Thermal Lensing in a Nd:YAG Laser Rod”, *Applied Optics*, 1970, Vol. 9, No. 11, pp. 2548-2553
- [9.10] A. E. Siegman, “Defining, measuring, and optimizing laser beam quality”, *Proc. SPIE*, 1993 Vol. 1868, 2
- [9.11] ISO 11146-1:2005(E), "Lasers and laser-related equipment — Test methods for laser beam widths, divergence angles and beam propagation ratios — Part 1: Stigmatic and simple astigmatic beams."
- [9.12] Ola Blomster, Magnus Pålsson, Sven-Olov Roos, Mats Blomqvist, Felix Abt, Friedrich Dausinger, Christoph Deininger, Martin Huonker, “Optics Performance at High-Power Levels” *Proc. SPIE*, 2008, Vol. 6871
- [9.13] Felix Abt, Axel Heß and Friedrich Dausinger, “Focusing High-Power, Single-Mode Laser Beams”, *Photonics Spectra*, May 2008, Online: <http://photonics.com/Article.aspx?AID=33535>
- [9.14] Chris Pannell. Internal Correspondence 11/2010
- [9.15] D. Burnham : “simple measurement of thermal lensing effects in laser rods”, *Appl. Opt.*, 1970 vol. 9, no. 7, pp.1727-1728
- [9.16] C. Hu, J.R. Whinnery, “New thermo-optical measurement method and a comparison with other methods”, *Appl. Opt.*, 1973, Vol. 12, No. 1, pp. 72-79 .
- [9.17] S. J. Sheldon, L. V. Knight, and J. M. Thorne, “Laser-induced thermal lens effect: a new theoretical model”, *Applied Optics*, 1982, Vol. 21, No. 9, pp. 1663-1669

- [9.18] Stephen Bialkowski, "Photothermal spectroscopy methods for chemical analysis", Wiley-Interscience, 1996
- [9.19] C. Jacinto, D.N. Messias, A.A. Andrade, S.M. Lima, M.L. Baesso, T. Catunda, "Thermal lens and Z-scan measurements: Thermal and optical properties of laser glasses – A review", *Journal of Non-Crystalline Solids*, 2006, Vol. 352, pp. 3582–3597
- [9.20] A. R. Nunes, J. H. Rohling, A. N. Medina, J. R. D. Pereira, A. C. Bento, and M. L. Baesso, "Time-resolved thermal lens determination of the thermo-optical coefficients in Nd-doped yttrium aluminum garnet as a function of temperature", *Appl. Phys. Lett.*, 2004, Vol. 84, No. 25
- [9.21] Muzammil A. Arain, William Z. Korth, Luke F. Williams, Rodica M. Martin, Guido Mueller, D. B. Tanner, and David H. Reitze, "Adaptive control of modal properties of optical beams using photothermal effects", *Optics Express*, 2010, Vol. 18, No. 3, pp. 2767-2781
- [9.22] R. Paugstadt and M. Bass, "Method for temporally and spatially resolved thermal-lensing measurements", *Applied Optics*, Vol. 33, No. 6, pp. 954-959
- [9.23] Raj M. Misra and Partha P. Banerjee, "Theoretical and experimental studies of pump-induced probe deflection in a thermal medium" *Applied Optics*, 1995, Vol. 34, No. 18, pp. 3358-3366
- [9.24] Beat Neuenschwander, Rudolf Weber, and Heinz P. Weber, "Determination of the Thermal Lens in Solid-state Lasers with Stable Cavities", *IEEE journal of Quantum Electronics*, 1995, Vol. 31, No. 6, pp. 1082-1087
- [9.25] Liu, Jun-hai, Lu, Jian-ren, Lu, Hun-hua, Shao, Zong-shu, Jiang, Min-hua, "Thermal Lens Determination of End-Pumped Solid State Lasers by a Simple Direct Approach", *Chinese Physical Letters*, 1999, Vol 16
- [9.26] A. Khizhnyak, G. Galich, M. Lopiitchouk, "Characteristics of thermal lens induced in active rod of cw Nd:YAG laser", *Semiconductor Physics, Quantum Electronics & Optoelectronics*. 1999. V. 2, No. 1, pp. 147-152
- [9.27] Justin L. Blows, Takashige Omatsu, Judith Dawes, Helen Pask, and Mitsuhiro Tateda, "Heat Generation In Nd:YVO With and Without Laser Action", *IEEE Photonics Technology Letters*, 1998, Vol. 10, No. 12, pp. 1727-1729
- [9.28] S. Chenais, F. Balembois, F. Druon, G. Lucas-leclin, P. Georges, "Thermal lensing in diode-pumped Ytterbium Lasers – Part I : Theoretical analysis and wavefront measurements", *IEEE J. Quant. Elec.*, 2004, Vol. 40, No. 9, pp. 1217-1234
- [9.29] Justin D. Mansell, Joseph Hennawi, Eric K. Gustafson, Martin M. Fejer, Robert L. Byer, David Clubley, Sanichiro Yoshida, and David H. Reitze, "Evaluating the effect of transmissive optic thermal lensing on laser beam quality with a Shack–Hartmann wave-front sensor", *Applied Optics*, 2001, Vol. 40, No. 3, pp. 366-374
- [9.30] Victor V. Zelenogorsky, Alexander A. Solovyov, Ilya E. Kozhevnikov, Eugene E. Kamenetsky, Eugene A. Rudenchik, Oleg V. Palashov, Dmitry E. Silin, and Efim A. Khazanov, "High-precision methods and devices for in situ measurements of thermally induced aberrations in optical elements", *Applied Optics*, 2006, Vol. 45, Issue 17, pp. 4092-4101

- [9.31] D. C. Hanna, C. G. Sawyers and M. A. Yuratich, "Telescopic resonators for large-volume TEM₀₀-mode operation", Vol. 13, No. 6, pp. 493-507
- [9.32] H. Chen, Q. Liu, X. Yan and M. Gong, "High Power Q-Switched TEM₀₀ Nd:YVO₄ Laser with Self Adaptive Compensation of Thermal Lensing Effect", *Laser Physics*, 2010, Vol. 20 No. 7, pp. 1594-1597
- [9.33] Charles X. Wang, Gary Y. Wang, Aclé V. Hicks, David R. Dudley, Henry Y. Pang, Norman Hodgson, "High Power Q-switched TEM₀₀ Mode Diode-Pumped Solid State Lasers with > 30W Output Power at 355nm" *Proc. of SPIE*, Vol. 6100
- [9.34] A. Caprara, "Solid-state laser having resonator configured for compensating for thermal lensing", US. Patent No. 6115402, 2002
- [9.35] J. Schwarz, M. Ramsey D. Headley, P. Rambo, I. Smith, J. Porter, "Thermal lens compensation by convex deformation of a flat mirror with variable annular force", *Appl. Phys. B*, 2006, Vol. 82, pp. 275–281
- [9.36] J. Degallaix, C. Zhao L. Ju, D. Blair, "Simulation of bulk-absorption thermal lensing in transmissive optics of gravitational waves detectors", *Appl. Phys. B*, 2003, Vol. 77, pp. 409–414
- [9.37] Muzammil A. Arain, William Z. Korth, Luke F. Williams, Rodica M. Martin, Guido Mueller, D. B. Tanner, and David H. Reitze, "Adaptive control of modal properties of optical beams using photothermal effects", *Optics Express*, 2010, Vol. 18, No. 3, pp 2767-2781
- [9.38] Muzammil A. Arain, Volker Quetschke, Joseph Gleason, Luke F. Williams, Malik Rakhmanov, Jinho Lee, Rachel J. Cruz, Guido Mueller, D. B. Tanner, and David. H. Reitze, "Adaptive beam shaping by controlled thermal lensing in Optical Elements", *Applied Optics*, 2007, Vol. 46, Issue 12, pp. 2153-2165
- [9.39] Eduard Wyss, Michelle Roth, Thomas Graf, and Heinz P. Weber, "Thermo-optical Compensation Methods for High-Power Lasers", *IEEE Journal of Quantum Electronics*, Vol. 38, No. 12, pp. 1620-1628
- [9.40] Hidetsugu Yoshida, Masahiro Nakatsuka, Norihiro Takeuchi, Hajime Okada and Hisanori Fujita, "Thermal lens correction of Nd:YAG rod laser used with thermo-optical compensation element of solid material", *Conference on Lasers and Electro-Optics Europe*, 2005
- [9.41] E. A. Khazanov, N. F. Andreev, A. N. Mal'shakov, O. V. Palashov, A. K. Poteomkin, A. M. Sergeev, A. A. Shaykin, V. V. Zelenogorsky, I. Ivanov, R. S. Amin, G. Mueller, D. B. Tanner, and D. H. Reitze, "Compensation of thermally induced modal distortions in Faraday isolators," *IEEE Journal of Quantum Electronics*, 2004, Vol. 40, pp. 1500-1510
- [9.42] Victor Zelenogorsky, Oleg Palashova and Efim Khazanov, "Adaptive compensation of thermally induced phase aberrations in Faraday isolators by means of a DKDP crystal", *Optic Communications*, 2007, Vol. 278, Iss. 1, pp. 8-13
- [9.43] Norman P. Barnes Larry B. Petway, "Variation of the Verdet constant with temperature of terbium gallium garnet", *J. Opt. Soc. Am. B*, 1992, Vol. 9, No. 10, pp. 1912-1915

[9.44] Rupal Amin, “A Technique for Passively Compensating Thermally Induced Modal Distortions in Faraday Isolators for Gravitational Wave Detector input optics”, Masters Thesis, 2002, University Of Florida

Appendix 9.1 – Thermal Lens Shift in Terms of Rayleigh Length (from internal correspondence – Chris Pannell G&H)



In geometrical optics the back focal length of a two lens system, like the one shown above is given by

$$f_B = \left(1 - \frac{d}{f}\right)F \quad (1)$$

Where

$$\frac{1}{F} = \frac{1}{f} + \frac{1}{f_1} - \frac{d}{f_1 f} \quad (2)$$

The change in the back focal length with power is

$$\frac{\partial f_b}{\partial P} = \frac{\partial F}{\partial P} - d \frac{\partial}{\partial P} \left(\frac{F}{f} \right) \quad (3)$$

Where (by parts)

$$\frac{\partial}{\partial P} \left(\frac{F}{f} \right) = \frac{1}{f} \frac{\partial F}{\partial P} - \frac{F}{f^2} \frac{\partial f}{\partial P} = \frac{1}{f} \left(\frac{\partial F}{\partial P} - \frac{F}{f} \frac{\partial f}{\partial P} \right) \quad (4)$$

Combining equations 3 and 4 (noting that $F/f \ll 1$)

$$\frac{\partial f_B}{\partial P} = \frac{\partial F}{\partial P} - \frac{d}{f} \frac{\partial F}{\partial P} + \frac{dF}{f^2} \frac{\partial f}{\partial P} \quad (5)$$

To find the change in F with power

$$\frac{\partial}{\partial P} \left(\frac{1}{F} \right) = -F^{-2} \frac{\partial F}{\partial P} \left(\frac{\partial}{\partial P} \right) \quad (6)$$

Rearranging

$$\begin{aligned}
\frac{\partial F}{\partial P} &= -F^2 \frac{\partial}{\partial P} \left(\frac{1}{f} \right) \\
&= -F^2 \left\{ \frac{\partial}{\partial P} \left(\frac{1}{f} \right) - \frac{d}{f_l} \frac{\partial}{\partial P} \left(\frac{1}{f} \right) \right\} \\
&= -F^2 \left(1 - \frac{d}{f_l} \right) \frac{\partial}{\partial P} \left(\frac{1}{f} \right) \\
&= -F^2 \left(1 - \frac{d}{f_l} \right) \left(-f^{-2} \frac{\partial f}{\partial P} \right) \\
\frac{\partial F}{\partial P} &= \left(\frac{F}{f} \right)^2 \left(1 - \frac{d}{f_l} \right) \frac{\partial f}{\partial P}
\end{aligned} \tag{7}$$

Combining equations 5 and 7 and factorising gives

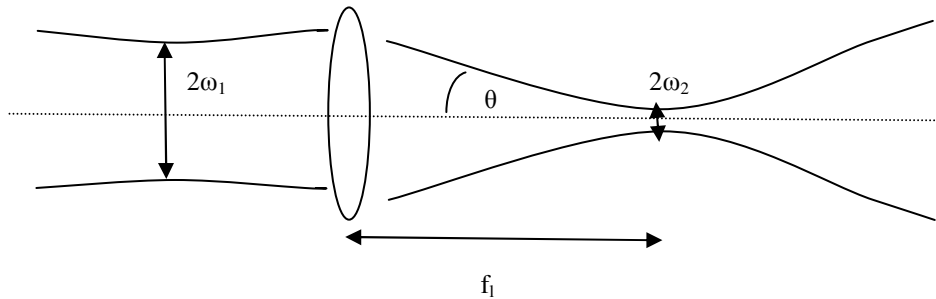
$$\begin{aligned}
\frac{\partial f_B}{\partial P} &= \left(\frac{F}{f} \right)^2 \left(1 - \frac{d}{f_l} \right) \frac{\partial f}{\partial P} - \frac{d}{f} \left(\frac{F}{f} \right)^2 \left(1 - \frac{d}{f_l} \right) \frac{\partial f}{\partial P} + \frac{dF}{f^2} \frac{\partial f}{\partial P} \\
&= \frac{1}{f^2} \left[F^2 \left(1 - \frac{d}{f_l} \right) \left(1 - \frac{d}{f_l} \right) + dF \right] \frac{\partial f}{\partial P}
\end{aligned} \tag{8}$$

But $F \sim f_l$ and $f \gg d$, so

$$\frac{\partial f_B}{\partial P} = \left(\frac{F}{f} \right)^2 \frac{\partial f}{\partial P} \tag{9}$$

Can obtain directly from equations 7 and 1 by applying same assumptions sooner $f \gg 1$ $f_l \sim f_B$

Assuming a weak thermal lens $f \gg 1$ then $f_l \sim f_B$



From standard Gaussian Optics the divergence angle θ and the Rayleigh of the output beam are given by

$$\theta = \frac{\lambda}{\pi\omega_2} \quad (10)$$

$$z_{R2} = \frac{\pi\omega_2^2}{\lambda}$$

The half beam width at the lens is

$$\omega_1 = f_l \tan\left(\frac{\lambda}{\pi\omega_2}\right) \quad (11)$$

Assuming small θ the final spot size is given by

$$\omega_2 = \frac{f_l \lambda}{\pi\omega_1} \quad (12)$$

Substituting 12 into 10 gives the Rayleigh length of the output beam in terms of the beam radius of the input beam and the focal length of the lens

$$z_{R2} = \frac{f_l^2 \lambda}{\pi\omega_1^2} = \frac{f_l^2}{z_{R1}} \quad (13)$$

Dividing equation 9 through by equation 13 yields

$$\left(\frac{1}{z_{R2}} \frac{\partial f_B}{\partial P}\right) = \frac{F^2}{f^2} \frac{z_{R1}}{f_l^2} \frac{\partial f}{\partial P} \quad (14)$$

However, from chain rule

$$\frac{\partial\left(\frac{1}{f}\right)}{\partial P} = -f^{-2} \frac{\partial f}{\partial P} \quad (15)$$

Combining equations 14 and 15 and noting that $F \sim f_l$ if $f \gg 1$ we obtain the final result

$$\frac{1}{z_{R2}} \frac{\partial f_B}{\partial P} = -z_{R1} \frac{\partial\left(\frac{1}{f}\right)}{\partial P} \quad (16)$$

Appendix 9.2: Derivation of temperature gradient

The steady state heat diffusion equation is

$$\nabla^2 T = -\frac{Q}{\kappa} \quad (1)$$

Where Q is the rate of heat generation. If the heating is by a Gaussian beam travelling in the z direction with small absorption α then

$$Q(r, z) = I_0 \alpha e^{-\frac{2r^2}{r_0^2}} e^{-\alpha z} \quad (2)$$

The total power in the laser beam is given by

$$P = \int_0^\infty \int_0^{2\pi} \int_0^\infty Q(r, z) r dr d\theta dz \quad (3)$$

Integrating gives

$$P = \frac{\pi I_0 \omega^2}{2} \quad (4)$$

Therefore Q in terms of laser power

$$Q(r, z) = \frac{2P\alpha}{\pi\omega^2} e^{-\frac{2r^2}{r_0^2}} e^{-\alpha z} \approx \frac{2P\alpha}{\pi\omega^2} e^{-\frac{2r^2}{r_0^2}} \quad (5)$$

Assuming small absorption ($\alpha z \ll 1$). Putting this into equation 1 and rewriting in spherical coordinates with no θ dependence

$$\frac{1}{r} \frac{d}{dr} \left(r \frac{dT}{dr} \right) = -\alpha \frac{P_0}{\pi\omega^2} \frac{1}{k} \exp\left(-\frac{2r^2}{\omega^2}\right) \quad (6)$$

$$\frac{d}{dr} \left(r \frac{dT}{dr} \right) = -\alpha \frac{P_0}{\pi\omega^2} \frac{1}{k} \int_0^r r \exp\left(-\frac{2r^2}{\omega^2}\right) dr \quad (7)$$

$$r \frac{dT}{dr} = \alpha \frac{P_o}{2\pi\kappa} \exp\left(-\frac{2r^2}{\omega^2}\right) + C \quad (8)$$

Apply boundary condition $dT/dr=0$ at $r=0$

$$C = -\frac{\alpha P_o}{2\pi\kappa} \quad (9)$$

$$\frac{dT}{dr} = -\alpha \frac{P_o}{2\pi\kappa} \left[1 - \exp\left(-\frac{2r^2}{\omega^2}\right) \right] \quad (10)$$

Therefore the change in temperature between r and a (the outer circumference of the crystal) is given by

$$\int_r^a dT = -\alpha \frac{P_o}{2\pi\kappa} \left[\int_r^a \frac{1}{r} dr - \int_r^a \frac{1}{r} \exp\left(-\frac{2r^2}{\omega^2}\right) dr \right] \quad (11)$$

$$T(a) - T(r) = -\alpha \frac{P_o}{2\pi\kappa} \left[-\ln\left(\frac{a}{r}\right) - \int_r^a \frac{1}{r} \exp\left(-\frac{2r^2}{\omega^2}\right) dr \right] \quad (12)$$

Substituting

$$u = \frac{2r^2}{\omega^2}$$

$$\int_r^a \frac{1}{r} \exp\left(-\frac{2r^2}{\omega^2}\right) dr = \int_{\frac{2r^2}{\omega^2}}^{\frac{2a^2}{\omega^2}} \frac{2r}{\omega^2} \exp(-u) \frac{\omega^2}{4r} du = \frac{1}{2} \int_{\frac{2r^2}{\omega^2}}^{\frac{2a^2}{\omega^2}} \frac{1}{u} \exp(-u) du \quad (13)$$

$$\frac{1}{2} \int_{\frac{2r^2}{\omega^2}}^{\frac{2a^2}{\omega^2}} \frac{1}{u} \exp(-u) du = \frac{1}{2} \left[\int_{\frac{2r^2}{\omega^2}}^{\infty} \frac{1}{u} \exp(-u) du - \int_{\frac{2a^2}{\omega^2}}^{\infty} \frac{1}{u} \exp(-u) du \right] = \frac{1}{2} \left[E_i\left(\frac{2r^2}{\omega^2}\right) - E_i\left(\frac{2a^2}{\omega^2}\right) \right]$$

Where E_i is the exponential integral function

$$E_i(x) = \int_x^{\infty} \frac{e^{-t}}{t} dt \quad (14)$$

If $T(a)=T_{amb}$ then the temperature function is given by substituting equation 13 into equation 12 as given in the text

$$T(r) = \frac{\alpha P_o}{4\pi\kappa} \left[-2\ln\left(\frac{r}{a}\right) + E_i\left(\frac{2r^2}{\omega^2}\right) - E_i\left(\frac{2a^2}{\omega^2}\right) \right] + T_{amb} \quad (15)$$

Chapter 10 - Faraday Isolator Design, Construction and Characterisation

This chapter describes the design and construction of our Faraday isolator, explaining the chosen design options with reference to the theory already presented. It also includes the experimental results made to characterise the device.

This chapter is structured as follows:

- **Section 10.1 - Design of Fibre-in Beam-out Faraday Isolator**
- **Section 10.2 - Optical Design and Polarisation Changes**
- **Section 10.3 – Magnet Design**
- **Section 10.4 – TGG**
- **Section 10.5 - Other Magneto-Optic Materials**
- **Section 10.6 - Thermal Lens measurement of Isolator**
- **Section 10.7 - Thermal Lens Compensation using DKDP**
- **Section 10.8 - Thermal Lens Compensation using Polymer**
- **Section 10.9 - Low Power Isolator Measurements**
- **Section 10.10 - High Power Isolator Measurements**
- **Section 10.11 - Summary**

10.1 Design of Fibre-in Beam-out Faraday Isolator

The design of our fibre-in beam-out isolator is complex and incorporates many of the elements explained in the previous chapters, such as dual TGG rods for thermal stress depolarisation compensation; half-wave plates for rotation compensation; and DKDP for thermal lens compensation.

A schematic of the isolator is shown in figure 10.1. The fibre from the amplifier is fed through the housing on the left and terminated with a short coreless piece of fibre (an end-cap) before being collimated by an aspheric lens. The purpose of the end cap (as explained in chapter 8) is to allow the light to expand from the core of the fibre and reduce the power density at the silica-air interface. This reduces the likelihood of laser induced damage to the fibre end. The laser induced damage threshold (LIDT) is often lower at a surface of a material (compared to the bulk) because of the presence of polishing defects and contamination. Andreas Kuhn et. al. found that the LIDT of a fibre end could be increased by laser annealing the surface to remove defects [10.1].

The product of fibre end-cap and aspheric lens is collectively referred to as a collimator. This is assembled separately to the rest of the isolator and aligned and fixed to the isolator during the final

stage of construction. The output is a low divergence “collimated” beam with a waist around 1.1mm. The beam passes through the isolator with a 1° angle to the optical surfaces.

The next component in the optical path is a birefringent walk-off plate made of Yttrium Orthovanadate (YVO_4). This is a positive uniaxial crystal cut so that its crystal axis is non parallel with the end of the material. This causes the two orthogonal polarisation states of the randomly polarised beam from the fibre to “walk-off” (or spatially separate) from each other so that they can be acted on independently to make a polarisation independent isolator. This is illustrated in figure 10.2.

The two beams from the walk-off plate then pass through two crystals of terbium gallium garnet (TGG) and two half wave plates. These rotate the plane of polarisation of the laser beams for the isolator to operate. TGG is the Faraday material of choice at the moment, because it is readily available and has a high Verdet constant and low absorption at 1060nm. This coincides with the gain wavelength of ytterbium doped fibre amplifiers. The use of two pieces of TGG and half wave plates allows for the compensation of thermally induced depolarisation as described in chapter 8.

The permanent magnets (neodymium-iron-boron “NdFeB”) around each piece of TGG are held in an opposing configuration. This increases the magnetic field strength inside the magnets bore and reduces the total amount of TGG required to give the necessary rotation. It also causes the sense of rotation to change through each TGG rod, which is one of the prerequisites for our thermal depolarisation compensation scheme.

A second YVO_4 walk off plate, identical to the first, is used to recombine the beams before they exit the device. To aid the insertion loss (IL) and optical return loss (ORL) of the isolator, all surfaces are anti reflection (AR) coated, and the beam passes through the optical components at an angle of $\sim 1^\circ$. This angle is corrected by a silica wedge at the output end of the device. An extra space has also been left to accept an undefined length of material with potential to compensate, at least partially, for any thermal lens produced within the device.

The mechanical structure in front of the collimator consists of a mirrored aperture angled at 45° and another 45 degree mirror to reflect the isolated light into beam dumps at the rear of the isolator. One of the major advantages of our design is that the forward transmitted light and reverse isolated light are spatially separated by a large distance. This means that we can easily separate the two beams with an aperture and move the unwanted light to a beam dump at a point where temperature rises can be easily controlled.

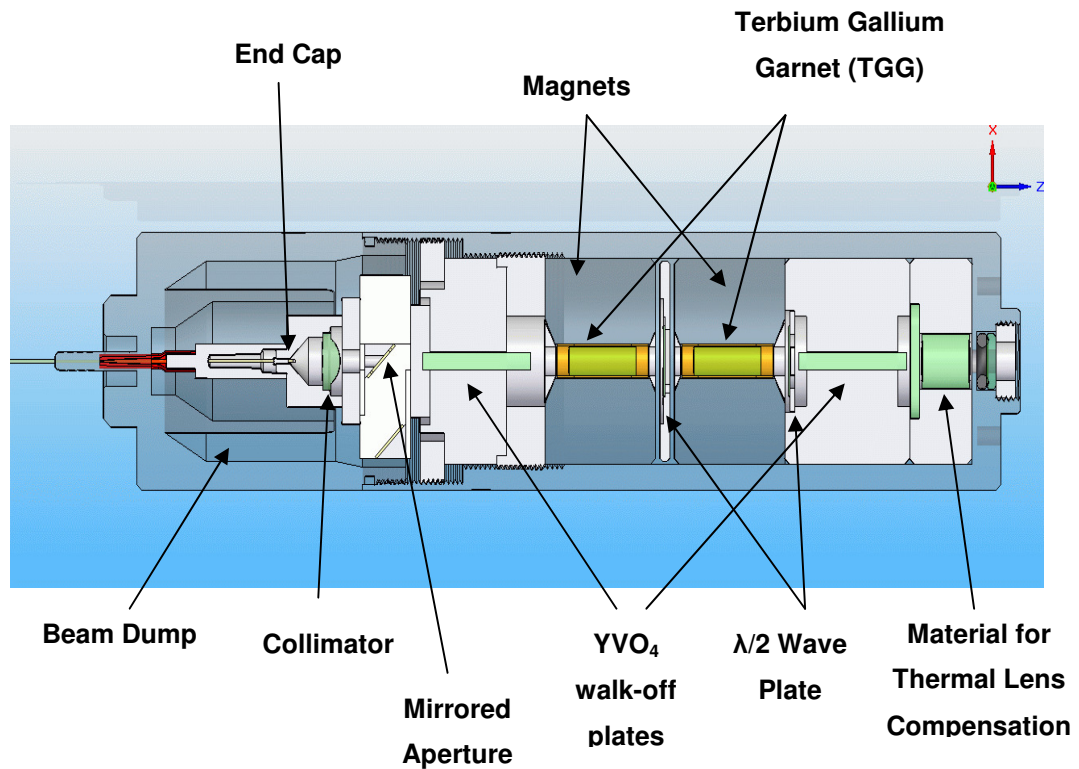


Figure 10.1: Mechanical (Top down) schematic of the Faraday isolator.

10.2 Optical Design and Polarisation Changes

A diagram of the optical paths that light takes through the isolator in the forward and reverse direction and the polarisation changes induced are shown in figure 10.2.

In the forward direction the randomly polarised beam from the collimator, shown in red, is spatially separated into two orthogonal, linearly polarised beams by the first YVO₄ walk-off plate. These are rotated 22.5° anti-clockwise by the first TGG crystal and a further 90° by a half wave plate. The second crystal of TGG then rotates the polarisation in the other sense (clockwise) 22.5° before the beams are returned to their original polarisation states by another half wave plate. The beams are then brought back together by the final YVO₄ walk-off plate.

Light propagating in the reverse direction (shown in blue) after rotation by the two pieces of TGG and the half wave plates, is left in a polarisation state orthogonal to the one in which it began. This causes the two beams to diverge in the walk-off plate so that they are spatially separated from the forward propagating light. They are then directed by the mirrored aperture to a beam dump at the rear of the isolator (away from the delicate fibre end).

Using Jones' calculus this design can be reconciled with the traditional Faraday isolator; a 45° rotator separated by two polarisers. In the simplest case, the action of two counter-rotators with rotation angle of θ , separated by a half wave plate with a fast axis horizontal, are equivalent to a single rotator with rotation angle 2θ [10.4]

$$\begin{bmatrix} \cos \theta & \sin \theta \\ -\sin \theta & \cos \theta \end{bmatrix} \begin{bmatrix} 1 & 0 \\ 0 & -1 \end{bmatrix} \begin{bmatrix} \cos \theta & -\sin \theta \\ \sin \theta & \cos \theta \end{bmatrix} = \begin{bmatrix} \cos 2\theta & -\sin 2\theta \\ -\sin 2\theta & -\cos 2\theta \end{bmatrix} \quad (10.1)$$

In the reverse direction

$$\begin{bmatrix} \cos \theta & -\sin \theta \\ \sin \theta & \cos \theta \end{bmatrix} \begin{bmatrix} 1 & 0 \\ 0 & -1 \end{bmatrix} \begin{bmatrix} \cos \theta & \sin \theta \\ -\sin \theta & \cos \theta \end{bmatrix} = \begin{bmatrix} -\cos 2\theta & \sin 2\theta \\ \sin 2\theta & \cos 2\theta \end{bmatrix} \quad (10.2)$$

These are two orthogonal matrices: one with rotation in the clockwise direction and one anticlockwise. This illustrates how two counter rotators providing essentially zero “net” rotation can be coupled with a half wave plate to provide an effective non reciprocal rotation. If the rotators are chosen to have $\theta=22.5^\circ$ then the forward light experiences $+45^\circ$ rotation and the reverse -45° rotation. This gives the 90° separation between the forward and reverse travelling light required to work as an effective isolator.

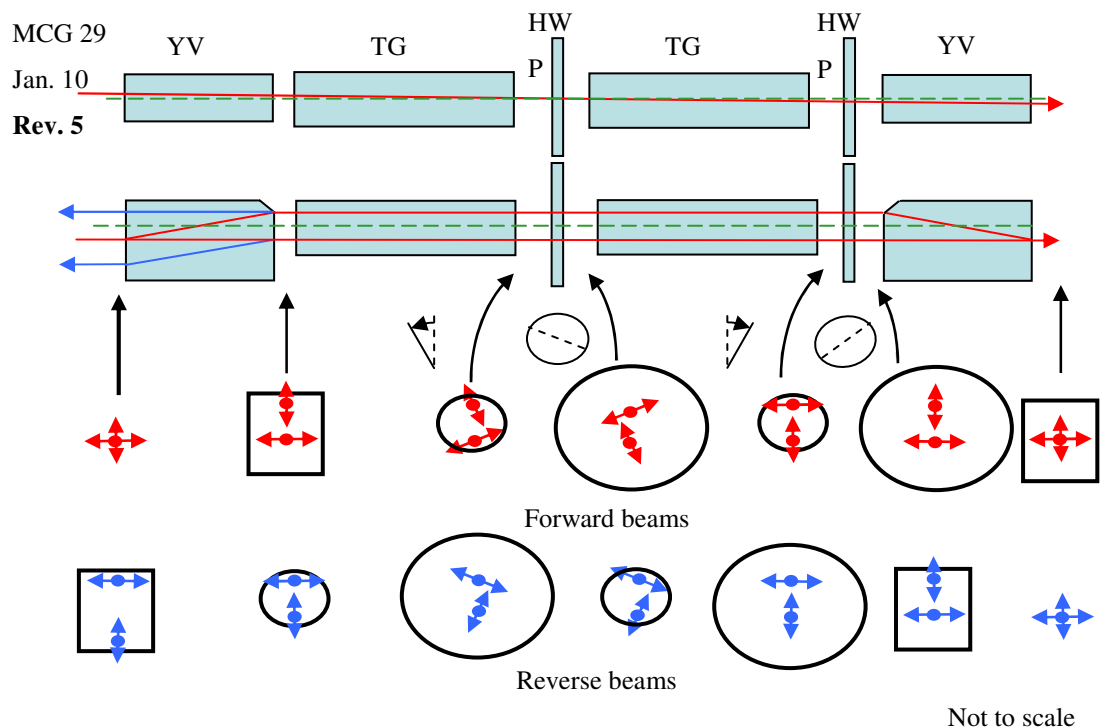


Figure 10.2: Beam paths through the isolator and polarisation changes for light travelling in the forward and reverse direction. [Mark Gardner].

The length of the walk off plates were chosen to provide the correct separation of the two orthogonally polarised beams. In a birefringent uniaxial crystal the refractive index perpendicular to the optical axis (ordinary refractive index (n_o)) is different to the refractive index parallel to the optical axis (extraordinary refractive index (n_e)). For a uniaxial crystal the effective refractive index of the extraordinary ray with respect to the optical axis is given by [10.3]

$$\frac{1}{n^2(\theta)} = \frac{\cos^2 \theta}{n_o^2} + \frac{\sin^2 \theta}{n_e^2} \quad (10.3)$$

Where θ is the angle between the optical axis and the direction of propagation of the extraordinary polarisation and the optical axis (where $n_e=n_o$ and the two waves travel together).

If a beam enters a birefringent material at an angle inclined to the optical axis, then it is easy to show from equation(8.1) that the o- and e-polarised beams will walk apart by the angle ρ , given by

$$\tan \rho = \frac{n^2(\theta)}{2} \left(\frac{1}{n_o^2} - \frac{1}{n_e^2} \right) \sin(2\theta) \quad (10.4)$$

Where

$$\theta = \tan^{-1} \left(\frac{n_e}{n_o} \right) \quad (10.5)$$

In YVO_4 a beam entering at 45° to the optic axis $n_e = 2.2$; $n_o = 2$ the walk off angle between the ordinary and extraordinary polarised beams is $\rho = 5.5^\circ$. This gives a centre-to-centre separation of around 2mm over our crystal length of 26mm.

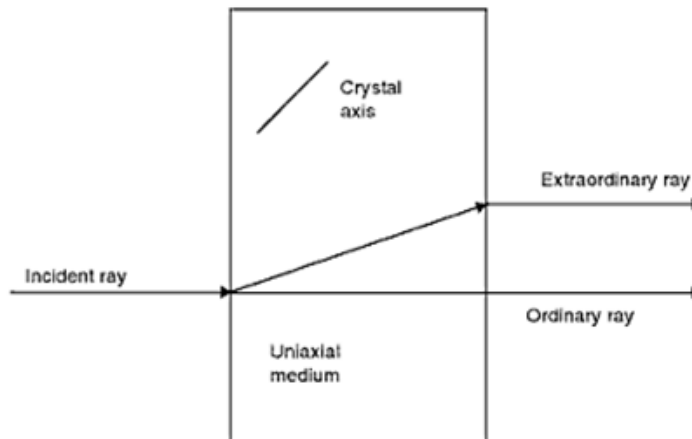


Figure 10.3: Birefringent walk-off plate.

10.3 Magnet design

In figure 10.4 the position of the magnets around the TGG can be seen. The magnet design was developed to produce a strong and uniform field through the TGG rods. The final design uses two 23mm long cylindrical sintered NdFeB magnets with 36mm outer diameters and 7mm inner diameters. The outside edge of the North end of each magnet is chamfered 1x1mm so that it is easily identifiable. The inner diameter of the North end of the magnet is chamfered 1x2mm and the South pole is chamfered 2x4mm. These chamfered regions are fitted with magnetic steel washers which improve the uniformity of the magnetic field in the bore of the magnet.

Peter MacKay modelled the magnetic field strength of this ensemble using “MagNet” software [10.4]. The result can be seen in figure 10.4. Figure 10.5 shows the magnetic field strength through the centre of the TGG rods. This is used to calculate the amount of rotation that the TGG would produce by averaging the magnetic field at the position of the TGG and applying the Faraday Equation (8.1).

The magnetic field and hence the rotation of the TGG can be adjusted slightly by changing the separation of the magnets, this results in an almost linear change in the rotation of $0.6^\circ/\text{mm}$ between 1 and 8mm as shown in figure 10.6. This allows us to compensate for lot-to-lot variations in the Verdet constant of TGG and the strength of the magnets.

The model also allows us to examine the uniformity of the magnetic field across the TGG rods. Figure 10.5 shows the magnetic field strength off-axis from 0mm to 2.5mm. The variation in rotation caused by the inhomogeneity of the magnetic field was calculated to be less than 0.04° across this region. This is very important and affects the depolarisation of the beam and the maximum isolation.

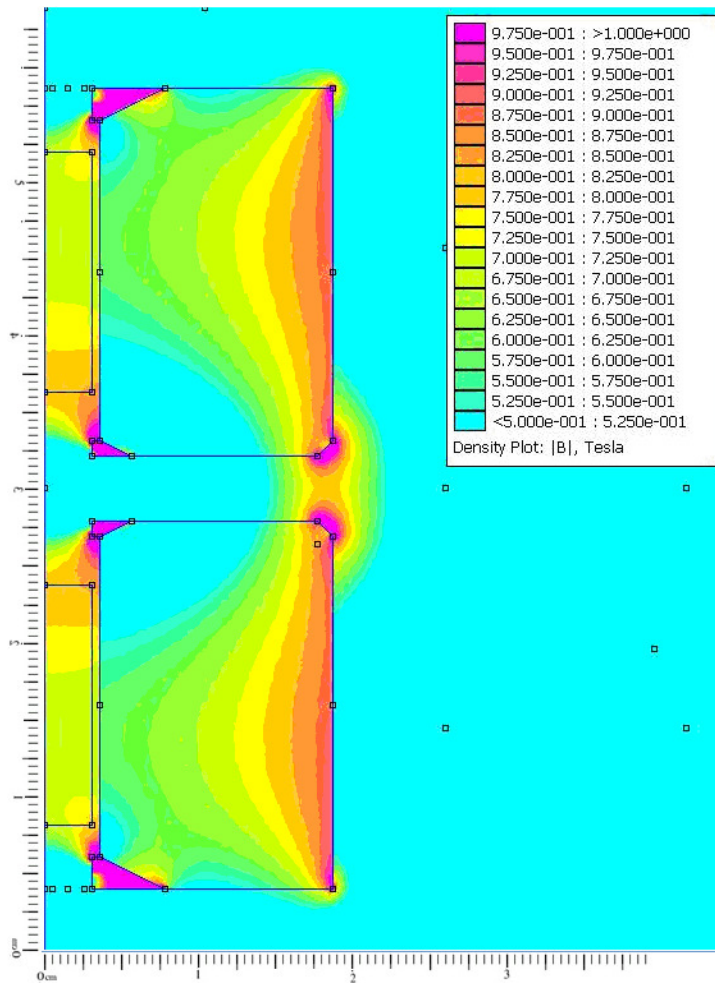


Figure 10.4: Diagram of magnetic field produced by the isolator magnet assembly.

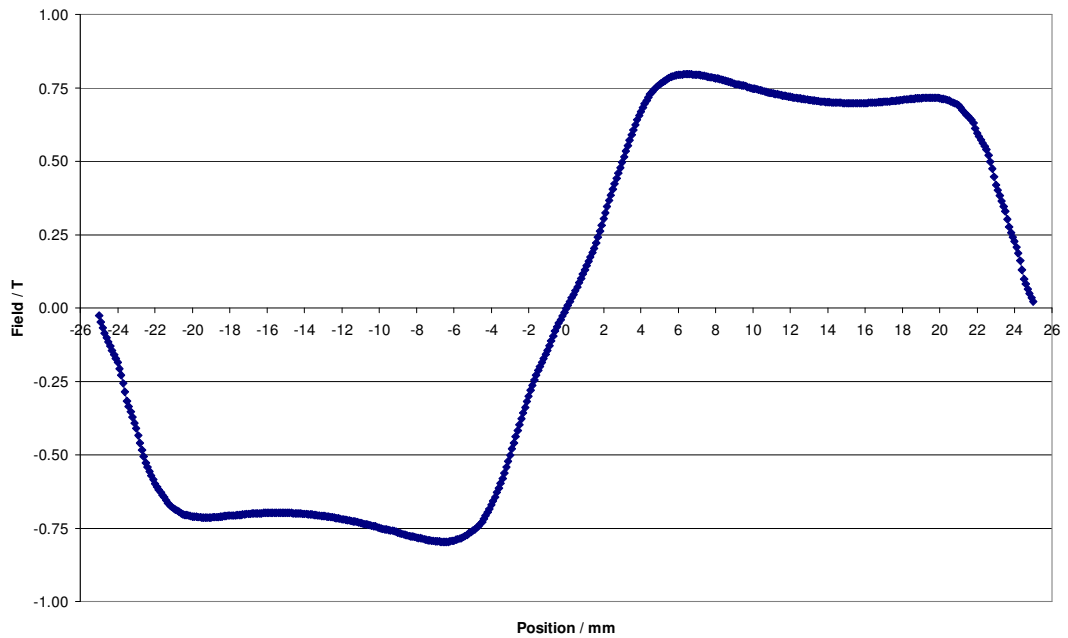


Figure 10.5: Magnetic field strength through centre of the TGG rods.

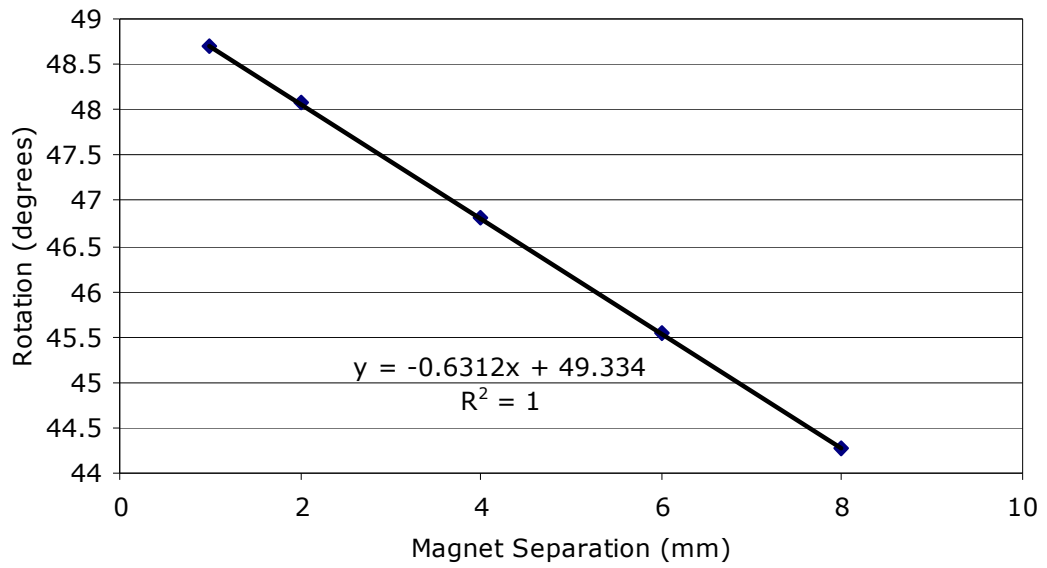


Figure 10.6: Polarisation rotation variation with the separation between magnets at 20°C.

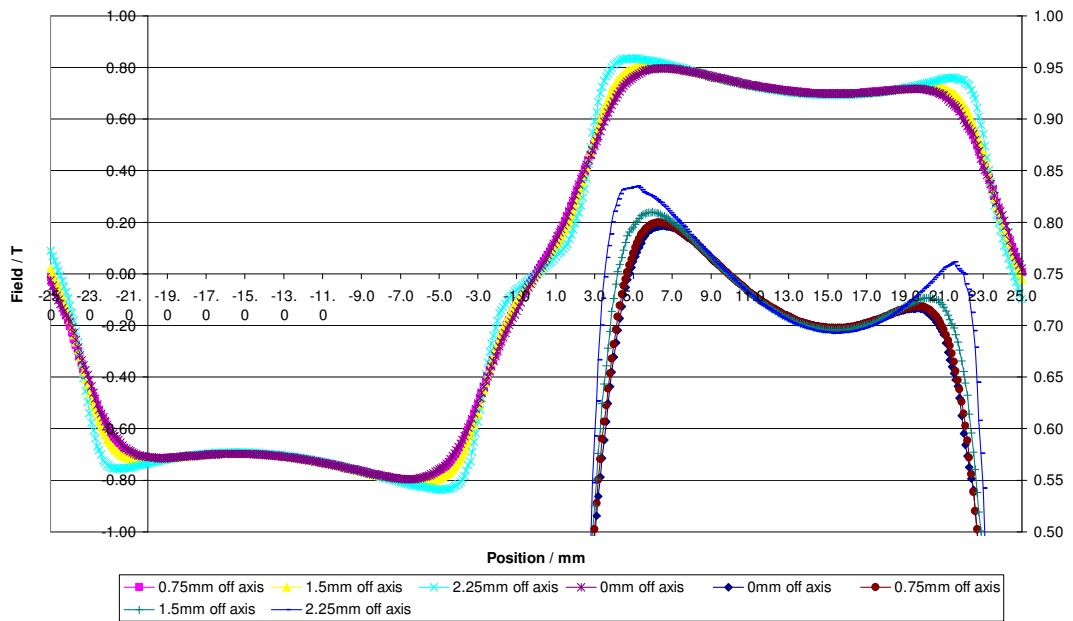


Figure 10.7: Variation of the magnetic field strength radially through the TGG rods.

The maximum field strength produced by two magnets with alternating polarities is much higher than the field strength produced by a single magnet. This allows us to get “more” out of the magnets and reduce the length of TGG required to give a total of 45° rotation [10.2]. It is also a requirement for the thermal depolarisation compensation scheme using a half wave plate described in section 8.4.

This design was found to be the optimum simple design which would fit within the footprint of our isolator. Adding magnets to either end of the two magnets can be used to boost the field slightly more but add complexity and are more expensive to manufacture and difficult to assemble [10.5]. In this paper [10.6] Mukhin et. al. describe a complex composite magnet which uses both axially and radially magnetised rings and magnetic conductors, like our steel washers, to create a permanent magnet assembly with a field strength of over 2T at the position of the rotator. However, this design is very complex and very large.

Another composite magnet design with an extremely strong field strength is explained in this paper [10.7]. This would fit within the footprint of our isolator and Magnetic modelling has shown that the field strength of this design would be almost twice as strong as our current magnets. However, the magnetic system is extremely complex and would be complicated to build requiring many different pieces.

10.4 TGG

The TGG used in our isolator was cut with a (111) crystal orientation. This is the most common orientation of TGG available. However, Khazanov et. al. [10.6] examined the depolarisation of various orientations of TGG and found that the (001) orientation causes less thermal stress depolarisation. In an uncompensated design with a 45° rotator the (001) orientation causes 3.2 times less depolarisation than the (111). In a compensated design the difference is more modest, with a 90° quartz rotator between two TGG rods they found that the depolarisation varied by just 1% between the two crystal orientations. In this case the (111) orientation would probably be preferable because the two rods would not have to be aligned with each other in the horizontal axis.

The TGG was ordered from Synoptics the datasheet quantities are shown in table 10.1.

| | |
|---------------------------------|---|
| Verdet Constant @ 1064nm | -40 RadT ⁻¹ m ⁻¹ |
| Verdet Constant @ 632nm | -134 RadT ⁻¹ m ⁻¹ |
| Absorption Coefficient | 0.0015 cm ⁻¹ |
| Thermal Conductivity | 7.4 Wm ⁻¹ K ⁻¹ |
| Refractive Index | 1.95 |
| Nonlinear Index | 8x10 ⁻¹³ |
| Figure of Merit (V/a) | 27 |
| Figure of Merit (V/n2) | 5 |

Table 10.1: TGG datasheet [10.8].

The length of TGG crystal needed to provide a 22.5° rotation when placed in the field of our magnets is calculated by averaging the magnetic field strength at the location of the TGG and multiplying by the length of TGG and Verdet constant. Using the magnetic field strengths in the model above the length of TGG was estimated to be 14mm to provide 22.5° rotation when placed in the centre of one magnet. Therefore, for the complete isolator we require two 14mm pieces of TGG. The diameter of the TGG was chosen to be 6mm to allow for clearance of the two 1.1mm beams and for mounting/heat sinking inside the magnet.

The surfaces of the TGG, and every other surface in the isolator, are antireflection (AR) coated for good transmission at both 1060nm and 630nm. The reflectivity of a coating on the surface of TGG is shown in figure 10.8. The design of this coating allows good transmission of both the signal light and a red target beam which is used in many applications. An image of a red target beam exiting the isolator can be seen in figure 10.9.

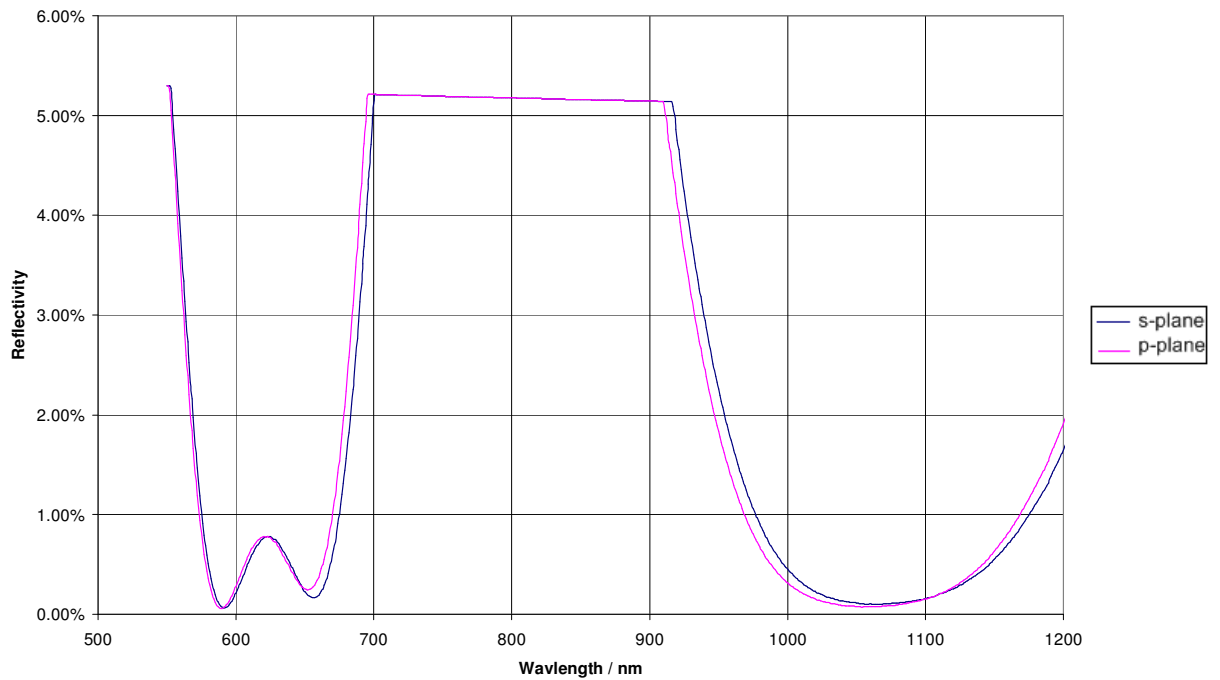


Figure 10.8: Reflectivity of AR coating on piece of TGG.

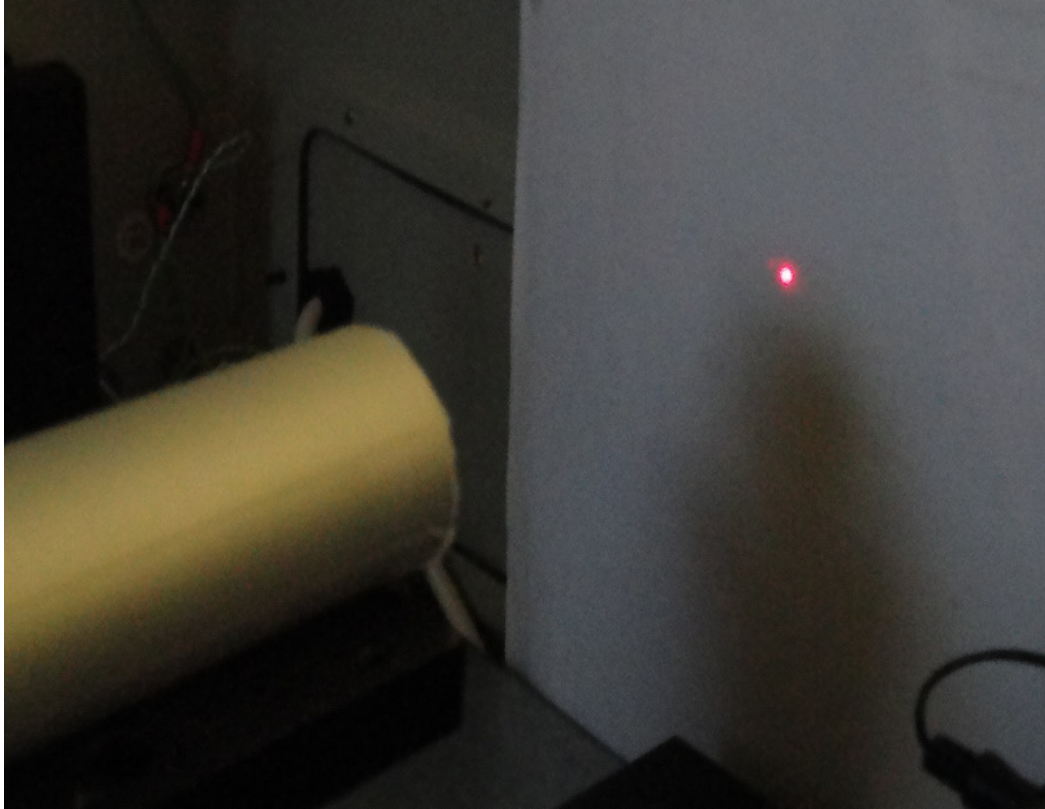


Figure 10.9: Image of red alignment laser transmission through isolator,

10.5 Other Magneto-Optic Materials

The magneto-optic material that we have used in our isolator, as discussed above, is TGG. TGG is the most commonly used Faraday rotator in the $1\mu\text{m}$ region and at room temperature it has a high figure of merit. It is easily available and can be grown widely as rods with cross sections up to around 3cm. However, it is not the only material available which exhibits strong Faraday rotation at 1060nm.

Other materials which can be used at 1060nm include glasses Kigre M18, MOS-4 and Mos-10 and other paramagnetic crystals like gadolinium gallium garnet, terbium aluminium garnet, terbium scandium aluminium garnet, sodium terbium tungstate $\text{NaTb}(\text{WO}_4)_2$ and lithium terbium molybdate $\text{LiTb}(\text{MoO}_4)_2$. The semiconductor cadmium manganese telluride (CdMnTe) is also a possibility, and recently the use of a TGG based ceramic has attracted attention [10.9].

A good overview of these materials was conducted by Starobor et. al [10.10] who were looking at materials for a cryogenic Faraday isolator at 1070nm. From the literature they have identified that terbium aluminium garnet (TAG), terbium scandium aluminium garnet (TSAG), $\text{NaTb}(\text{MoO}_4)_2$ and $\text{LiTb}(\text{MoO}_4)_2$ have Verdet constants at least 30% higher than TGG.

The magneto-optic properties of $\text{NaTb}(\text{WO}_4)_2$ were measured by Liu et. al. [10.11] and compared to a sample of TGG. They found that the Verdet constant of $\text{NaTb}(\text{WO}_4)_2$ was $-52\text{radT}^{-1}\text{m}^{-1}$ at 1064nm compared to $-40\text{radT}^{-1}\text{m}^{-1}$ for TGG. They also found that the absorption of their sample of $\text{NaTb}(\text{WO}_4)_2$ had a lower absorption coefficient than their sample of TGG, 0.44cm^{-1} compared to 0.50cm^{-1} . This means that at 1064nm their sample of $\text{NaTb}(\text{WO}_4)_2$ has a higher figure of merit than their TGG, 18.3 compared to 12.4. Although it should be noted that their measured absorption coefficients are very high as reported in their specification data – our TGG samples from Synoptics had absorptions from 0.0012 to 0.002cm^{-1} . I believe they may be a factor of 100 out which could be accounted for by a switch in units from m^{-1} to cm^{-1} .

Guo et. al. [10.12] measured the properties of lithium terbium molybdate $\text{LiTb}(\text{MoO}_4)_2$ and compared it to a sample of commercial TGG from Fuzhou TCT Co.. Their $\text{LiTb}(\text{MoO}_4)_2$ sample has a similar absorption coefficient to TGG in the 800nm-1500nm region. They also show that $\text{LiTb}(\text{MoO}_4)_2$ has a larger Verdet constant than TGG between 400nm and 1500nm. They determine that $\text{LiTb}(\text{MoO}_4)_2$ has a higher magneto-optic figure of merit than TGG between around 600nm and 1500nm. The Verdet constant at 1064nm was measured to be $-76\text{radT}^{-1}\text{m}^{-1}$.

Looking at the numbers both $\text{NaTb}(\text{WO}_4)_2$ and $\text{LiTb}(\text{MoO}_4)_2$ seem like promising alternative materials for use in a 1064nm Faraday isolator. However, they are not widely available and the difficulty of growth and crystal quality is unknown. The size of rod aperture that can be grown is also unknown. It is also impossible to give a full picture of their effectiveness as a Faraday rotator for high powers without knowing the thermal conductivity, LIDT and dn/dT of the crystals which will affect thermal lensing.

Another promising material is terbium aluminium garnet (TAG) which has a Verdet constant approximately 30% higher than TGG [10.10, 10.13]. It also has excellent transmission between 400nm and 1300nm [10.13]. The problem with TAG is that crystals are very difficult to grow larger than around 4mm in diameter. This limits the usefulness of TAG for high power applications. To address this problem attempts have been made to make terbium scandium aluminium garnet which has similar properties but is easier to grow to large sizes [10.13]. However, Starobor [10.13] reports that the quality of samples obtained to date has not been very good.

The semiconductor cadmium manganese telluride (CdMnTe) has a massive Verdet constant at 1060nm of between around $170\text{radT}^{-1}\text{m}^{-1}$ and $260\text{radT}^{-1}\text{m}^{-1}$ depending on the concentration of Cadmium to Manganese [10.14]. This is over 4 times larger than the Verdet constant of TGG. This high Verdet constant allows very short isolators to be constructed. The disadvantage of CdMnTe is that the absorption is high - between 0.2 and 0.7cm^{-1} [10.10]. This limits the power handling of the crystal because it exacerbates thermal effects. It is therefore unsuitable for a high power device at

1060nm. CdMnTe may well be the Faraday material of choice at longer wavelengths >2um as the absorption is significantly smaller.

The magneto-optical glasses Kigre M18, MOS-4 and Mos-10 are doped with elements like terbium to increase their Verdet constant which tend to be about half the value of TGG. They can also be produced with high purity and good absorption – which can be modified slightly by adjusting dopants. The really big advantage of magneto-optic glasses, for high power use, is that they can be made with very large, essentially unlimited, apertures. However, for our application this does not help much because large apertures require large magnets and a device size which would be impractical for our application. Over a very large aperture magnetic field uniformity also becomes an issue. The thermal conductivity of glass is also much lower than the thermal conductivity of crystals and exacerbates thermal problems for high power operation.

When comparing magneto-optic materials lots of people still use cgs units of min/(Oe-cm). To convert to SI units of $\text{radT}^{-1}\text{m}^{-1}$

$$V(\text{radT}^{-1}\text{m}^{-1}) = 290.9V(\text{min Oe}^{-1}\text{cm}^{-1}) \quad (10.6)$$

10.6 Thermal Lens measurement of Isolator

The thermal lens of a complete isolator was measured using the method outlined in section 9.4 and the setup shown in figure 10.10. The isolator input fibre has a 20 μm core and 330 μm cladding. This fibre allows propagation of several low order modes. The M^2 of light leaving the fibre is around 1.4. Measurements of the focal position and Rayleigh range were made at 2W intervals from 4W to 20W and as you can see in figure 10.11 the focal shift is very linear over this range. The negative sign indicates that the focus position shifts towards the lens in the setup, indicating that the thermal lens is positive (converging). The x-axis in this graph represents the change in power.

The result was a focal shift of -9 Rayleigh lengths per kW. This compares favourably with the value of -7 Rayleigh lengths per kW predicted by the model presented in chapter 9. The slight discrepancy between the measured value and the model is probably down to the assumption that only the TGG contributes to the focal shift of the isolator. It is also likely that the actual value of the absorption coefficient for our TGG is different to the values used in the model.

The absorption coefficients of ten pieces of TGG were measured using a laser calorimeter at Gooch and Housego (Cleveland). The results can be seen in table 10.2. As you can see there is a fairly large

variance in the absorption between samples. The average absorption coefficient is 0.00184cm^{-1} the lowest measured was 0.0015cm^{-1} and the highest was 0.0022cm^{-1} . The lower values match up well with the manufacturers quoted value given in table 10.1.

The M^2 of the light leaving the fibre was measured at each power level to check that it remained constant. If the M^2 degraded with power because of depolarisation then we would expect the focal shift with power to be nonlinear and decrease with increasing power. This was shown in reference [10.16]. In reference [10.16] they do not give a reason for this dependence of focal shift on M^2 . We believe it is because the temperature gradients decrease with M^2 because the peak of the transverse Gaussian intensity profile decreases.

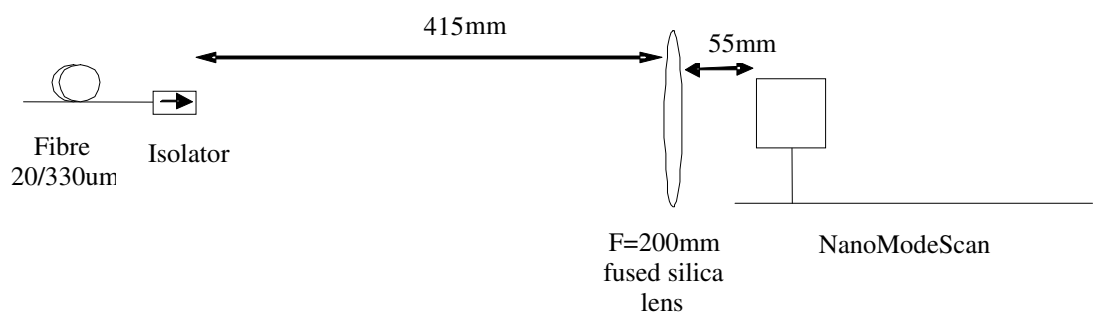


Figure 10.10: Setup used to measure the thermal lens of a complete isolator.

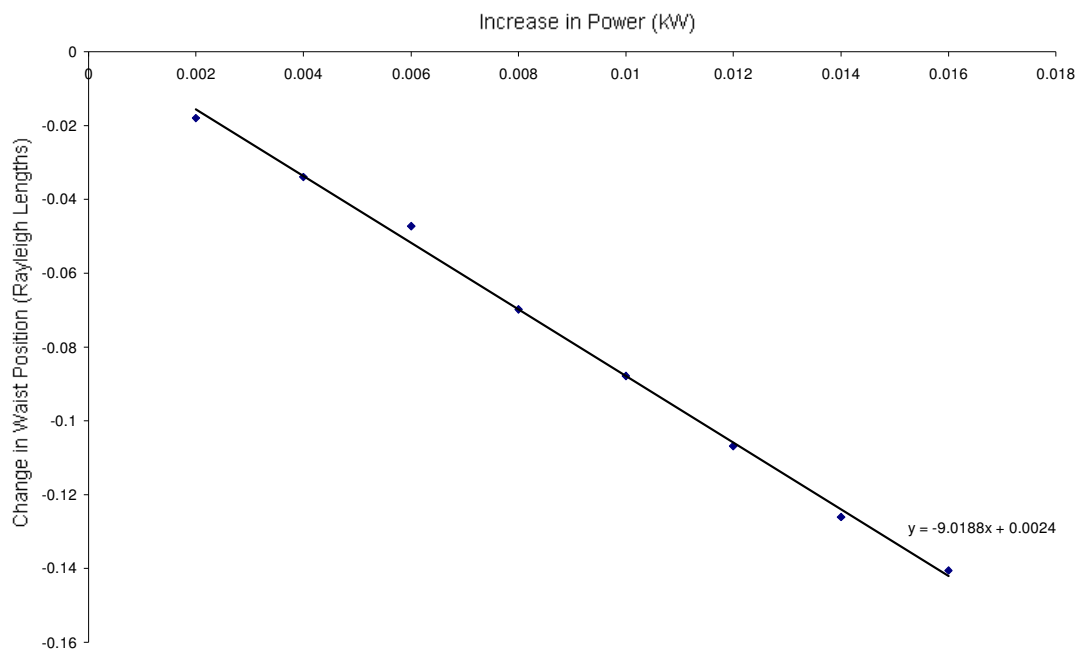


Figure 10.11: Focus position shift with power of complete isolator.

| Serial Number | Absorption Coefficient (cm ⁻¹) |
|---------------|--|
| T21645 | 0.0021 |
| T24004 | 0.0015 |
| T29857 | 0.0016 |
| T35861 | 0.0019 |
| T36209 | 0.0021 |
| T36213 | 0.0020 |
| T36217 | 0.0015 |
| T36221 | 0.0016 |
| T36225 | 0.0019 |
| T36229 | 0.0022 |

Table 10.2: Measured Absorption of TGG samples (calorimeter, Cleveland)

10.7 Thermal Lens Compensation using DKDP

A 15mm piece of DKDP from Gooch and Housego (Cleveland) was introduced into the setup 15mm in front of the isolator. The thermal focal shift of the isolator and piece of DKDP together was measured to be 4.4 Rayleigh lengths per kW, figure 10.12. This indicates that a 15mm rod of DKDP produces a negative (diverging) thermal lens with a power dependent shift of around 13 Rayleigh lengths per kW. This is close to the prediction of 15Rz/kW of the model. This was our first experimental proof that the power dependent focal shift could be compensated for with a passive element of DKDP. It also confirmed what was expected from the model, that a 15mm piece of TGG overcompensates for the thermal lens in the isolator.

The DKDP in the beam path did not degrade the beam quality, the M^2 of the measured beam in all cases is <1.4 . The repeatability of focal shift measurements made using this setup is very good back to back measurements vary by $< 1.5Rz/kW$.

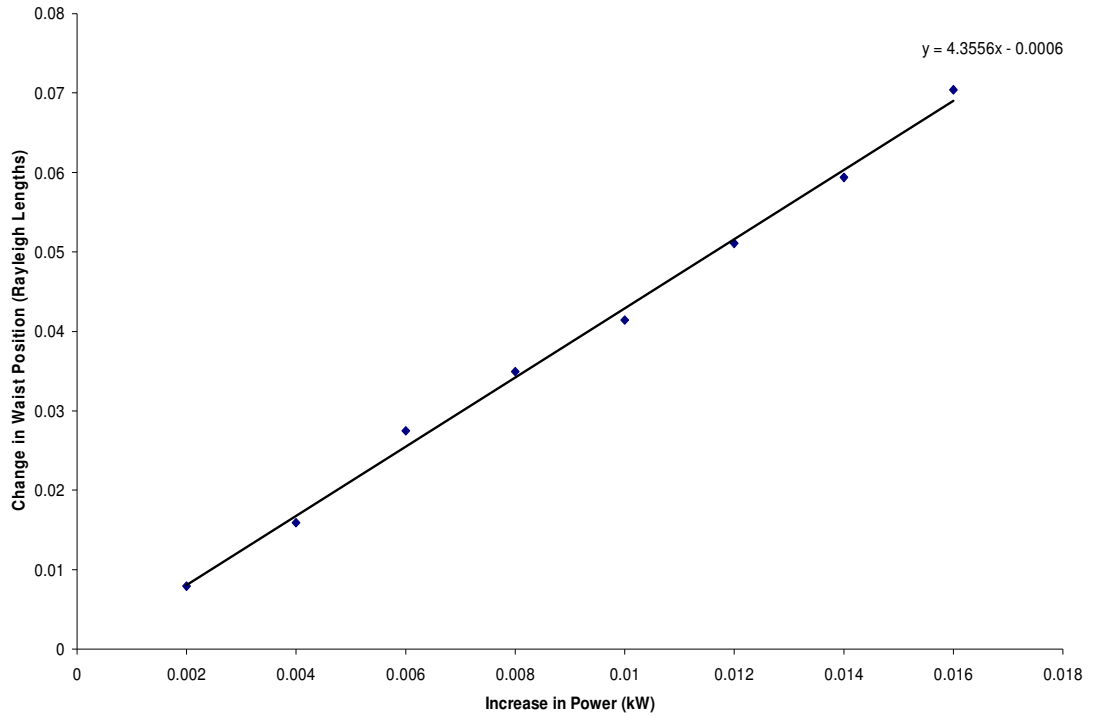


Figure 10.12: Focal shift of isolator and 15mm DKDP.

These measurements were used to calculate the length of DKDP compensating element that we should use to compensate for the thermal lensing of the isolator. Assuming that the focal length of the thermal lens is long compared to the distance between the isolator and DKDP; and that the focussing power of the DKDP is proportional to its length; then the length of DKDP required for compensation of the thermal focal shift is given by

$$\frac{\text{ThermalLensDKDP}}{\text{ThermalLensIsolator}} \times \text{LengthofDKDP} = \frac{13R_z / kW}{9R_z / kW} \times 15\text{mm} \approx 10\text{mm} \quad (10.7)$$

Therefore, 10mm of DKDP is required to compensate for the thermal lens in 28mm of TGG. This ratio of TGG to DKDP is 2.8:1 is a long way from the predicted value of 11:1 calculated in section 9.8. It is likely that the parameters used in the model were not consistent with the actual piece of DKDP used. Notably the absorption at 1060nm varies considerably with the amount of deuteration.

A compensation unit with this length and the correct dimensions to fit into an isolator was constructed for testing. Figure 10.14 shows this DKDP compensation piece. The DKDP is held securely without over-compression in a metal holder which fits neatly into the space provided in the isolator body, figure 10.1.

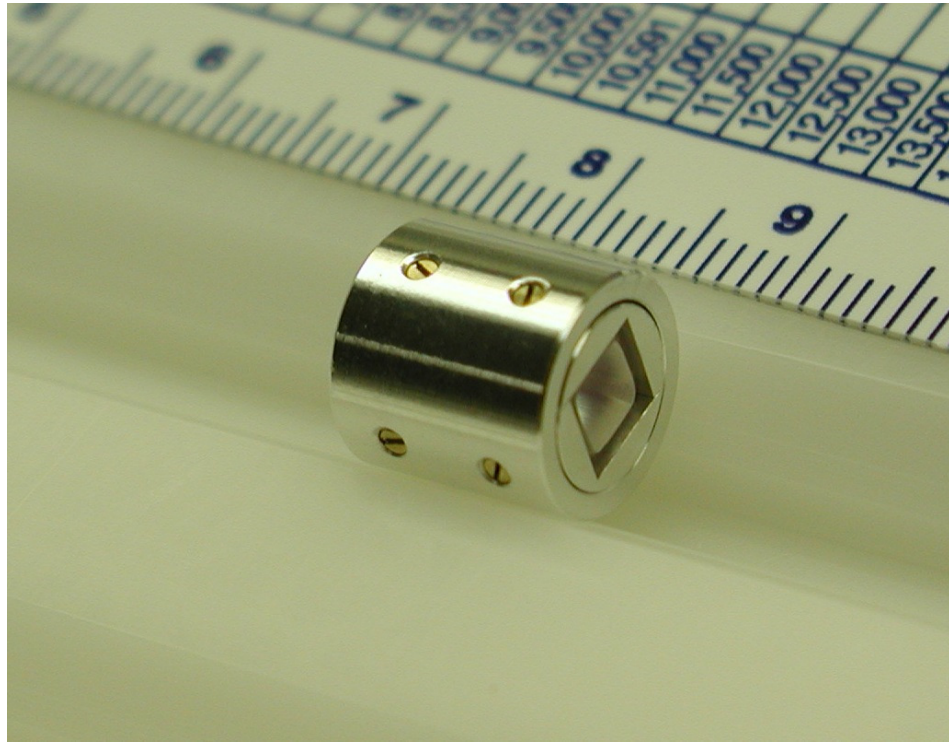


Figure 10.13: 99% DKDP sample constructed as isolating component for testing with isolator.

The thermal lens of a different isolator was measured with and without the DKDP compensator using the setup shown in figure 10.14. This isolator was not fibre coupled, so the beam direct from the delivery optics of the fibre laser was used. The diameter of this beam was reduced from 5mm to 1mm using a Kepler telescope arrangement using two plano-convex lenses, $f=100\text{mm}$ and $f=20\text{mm}$.

The power dependent focal shift of the isolator, DKDP and both together was then measured. The results can be seen in figure 10.15. This isolator had a focal shift of -9.8 Rayleigh lengths per kW, which is comparable to measurements made on other isolators. The 10mm length of DKDP had a focal shift of 16 Rayleigh lengths per kW. This is larger than was expected from the measurements above and we believe there could be several reasons for this

- 1) The 10mm DKDP crystal used in the compensation device was AR coated. The 15mm piece of DKDP measured earlier was not. In both cases the power was measured after the DKDP. Therefore to measure the same power at the detector the uncoated crystal would have to “see” more power to account for Fresnel reflection. This was not taken into account in the scaling used to estimate the length of DKDP earlier.
- 2) The DKDP samples were from different batches and so could have different levels of deuteration and quality which could affect absorption and change the thermal lensing.
- 3) DKDP is also hygroscopic and so different storage conditions could have affected the amount of water impurities in the sample and increased the absorption.

- 4) It is also common to find in the literature [10.16, 10.17] that small absorption in the thin layer of the dielectric AR coating can add a significant amount of thermal lensing through deformation (bulging) of the surface.

The combination of isolator and DKDP produced a focal shift of around 3.9 Rz/kW. The combination of the two measurements separately is around 6Rz/kW (DKDP + TGG = 16 – 10 = 6Rz/kW). The difference was attributed to the thermal lens of the isolator changing the spot size through the DKDP. Nonetheless these results clearly show the principle of thermal lens compensation using DKDP.

After these measurements were made, the DKDP compensation module was built into a complete isolator (s/n 01460264). This had a fibre with a 3523µm core and 330µm cladding. This fibre could be spliced directly to the 35W pulsed fibre laser that we have and has an M^2 of around 3.5.

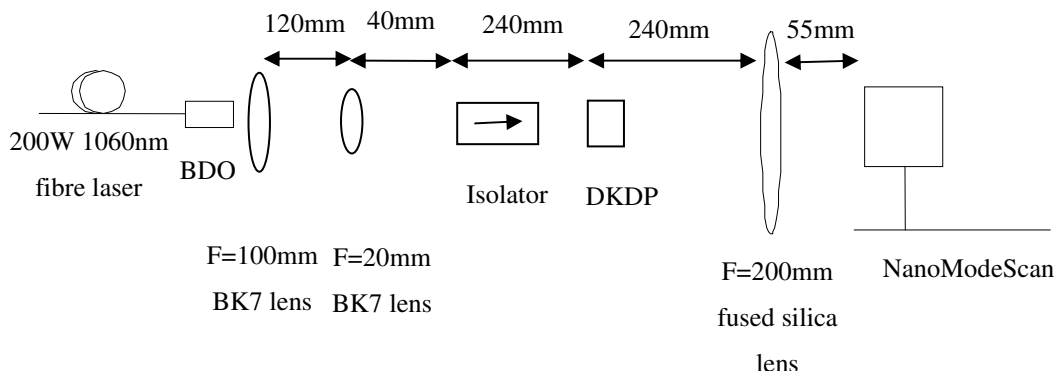


Figure 10.14: Setup used to measure the thermal lens of an isolator and DKDP.

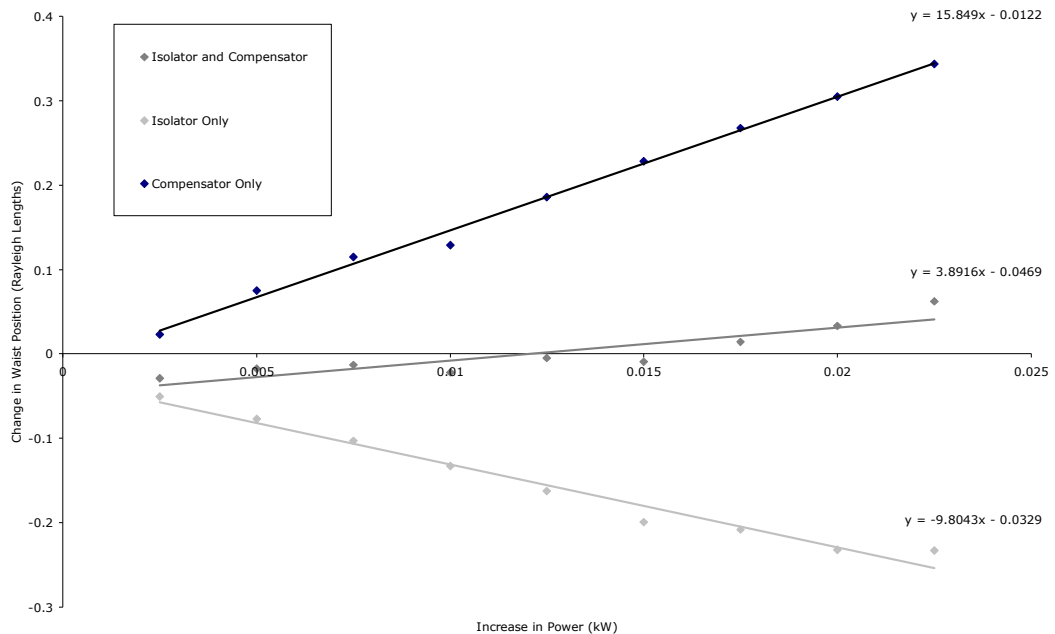


Figure 10.15: Power dependent focal shift of isolator (s/n 01460261) with and without DKDP compensator.

Figure 10.16 shows the setup used to measure isolator (s/n 01460264) with integrated DKDP compensation module. Two measurements of this isolator can be seen in figure 10.17 and show that the overall isolator has a thermal lens of $\sim 2Rz/kW$. The beam waist exiting the isolator was calculated using the parameters measured and is shown in figure 10.18 alongside some direct measurements. The beam is clearly not very well collimated. Through the isolator (in the region marked by the box on the graph) the beam goes through a waist of diameter around $600\mu m$ this doubles to $1200\mu m$ in about 200mm. This would have affected the measurements slightly. However, compensation is still impressive as long as the beam size is fairly constant through the TGG and DKDP

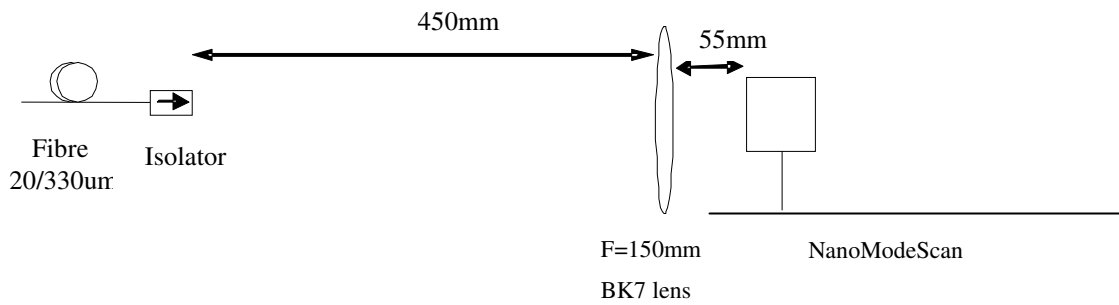


Figure 10.16: Setup used to measure the thermal lens of isolator with DKDP compensation model.

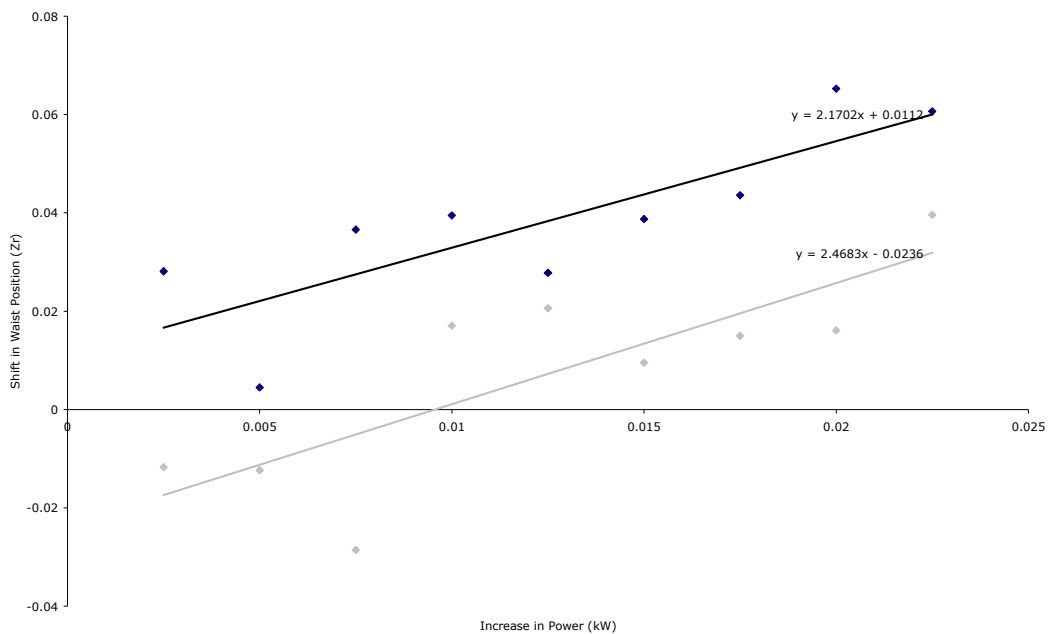


Figure 10.17: Thermal lens measurement of isolator (s/n 01460264) with DKDP module.

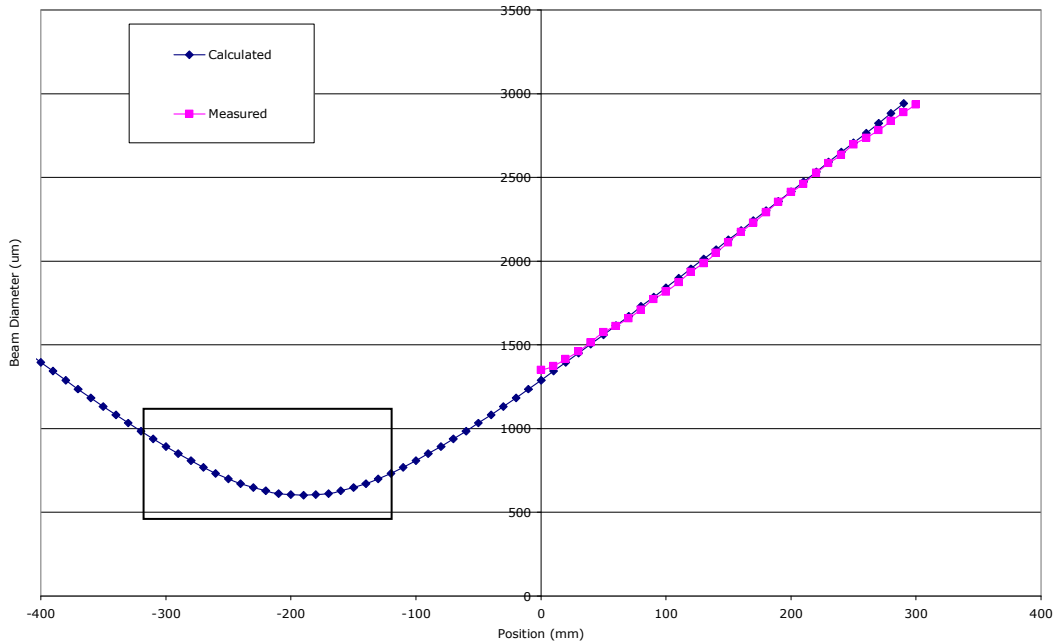


Figure 10.18: Propagation of light after exiting the isolator, and inside isolator (ignoring refraction of the crystals).

10.8 Thermal Lens Compensation using Polymer

The use of a polymer to compensate for thermal lensing is also being explored. The advantage of using a polymer is that they often have very high thermal coefficients of refractive index dn/dT . They are also relatively cheap, as they require little energy to produce compared to growing a crystal, and require less processing. If a polymer with a suitable refractive index is chosen then the required thickness can be pressed between two sheets of glass (or silica) without the need for internal AR coatings.

The use of polymers for thermal lens compensation was first demonstrated inside an Nd:YAG laser cavity by Graf et. al [10.18]. They placed the polymer in a gap between two laser rods so that the temperature profile in the pumped laser rods was conducted, with a similar form, into the polymer. They used several different polymers including OCF-446 (Nye) and Sylgard-184 (Dow Corning) and found that the laser cavity was stable at over double the output power of the uncompensated cavity. The M^2 of the cavity was also improved at moderate powers by the insertion of the compensating element.

Sylgard 184 manufactured by Dow Corning has a refractive index around 1.46; a dn/dT of around $-4.5 \times 10^{-4} \text{ K}^{-1}$; and absorption of 0.25%/mm at 1064nm. The type of element we would consider using is a

thin layer of Sylgard 184 sandwiched between two sheets of silica. The refractive index of Sylgard 184 is closely matched to silica so no AR coating should be required on the inside of the silica sheets. AR coatings in contact with the Sylgard 184 could ruin the thermal lensing of the compensating element as even small absorption in the coating could lead to a large change in the temperature gradients and thermal lens produced in a thin sample.

The modelling of temperature gradients in a thin film of material is more difficult than in a long rod. This is because the assumptions made in section 9.1 for a cylindrical rod are no longer valid and the boundary conditions are different. So far, for these reasons, no attempt has been made at modelling thermal gradients in Gaussian pumped thin sheets. An estimate of the thickness of Sylgard 184 required to compensate for the isolator thermal lens was made simply on the basis of the thermal dispersion of the refractive index and the absorption. Several samples with thicknesses ranging from 1mm to 3mm were produced with the intention of conducting thermal lens measurements. However, it was found that the thermal lens produced by these was too strong and immeasurable. Thinner samples are currently being made and should hopefully be available soon for measuring.

In the meantime the samples already available were used to evaluate the power handling of Sylgard 184. A 3mm thick sample between 2 silica plates was irradiated by an 0.8mm diameter beam at 1064nm $M^2=1$ for >4hrs at just under 60W without damage. The power was then turned up to 75W for an hour without damage. The sample was damaged when we tried to increase the power to 90W. This is 40W higher than the target power of the isolator. Figure 10.19 shows the results of this test. Five different locations on the sample were then irradiated separately and found to damage at between 80 to 100W.

Long term reliability testing of the Sylgard 184 component would obviously be necessary if this was to become part of the isolator design. Though it could be envisaged that this forms a “bolt-on” accessory for the isolator if the mean time between failures is found to be short, ~100's of hours, because the production cost could be substantially cheaper than including a DKDP crystal inside the isolator. It would then probably be considered a consumable which needs periodic replacement.

The important thing to discover then is how the performance of Sylgard 184 degrades during operation, does the absorption increase with time, if so then the thermal lens compensation performance will degrade, or does it cause beam aberrations as it fails.

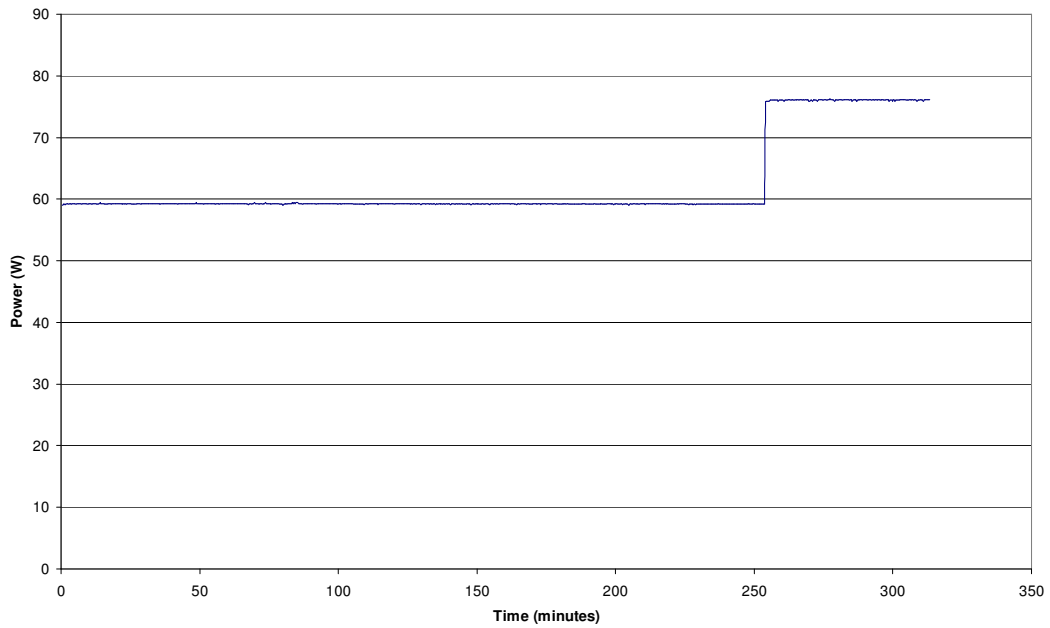


Figure 10.19: High power testing of Sylgard 184.

10.9 Low Power Isolator Measurements

This section describes measurements of the isolation, insertion loss and return loss of an isolator. These measurements are made at low power and used to characterise the device. The assumptions and errors in these measurements are discussed where appropriate.

- Section 10.9.1 discusses isolation measurements
- Section 10.9.2 discusses Insertion loss measurements, and
- Section 10.9.3 discusses return loss measurements.

10.9.1 Isolation Measurements

To measure the isolation at low powers a 10mW 1064nm DPSS laser with a 0.8mm diameter beam is shone through the isolator in the reverse direction, without the beam dumps in place. A CCD camera is then used to find the two high power “isolated” beams which exit the isolator, as shown in figure 10.20a. The “residual” beam which contains the non-isolated light is situated between these two beams. A pinhole is then positioned to block the two isolated beams and pass the central residual beam. The residual beam should be visible on the CCD when the CCD is not being saturated by the other beams, figure 10.20b. The pinhole is then positioned to ensure that there is no clipping. The

power in the residual beam P_{res} is then measured and compared to the input power P_{in} . The isolation in dB can then be calculated using

$$Isolation(dB) = -10\log\left(\frac{P_{res}}{P_{in}}\right) \quad (10.8)$$

This isolation is the intrinsic isolation of the isolator and does not include the coupling loss which will be present with a collimator in place. It can therefore be thought of as the worst case isolation and assumes 100% coupling between the input beam and the collimator.

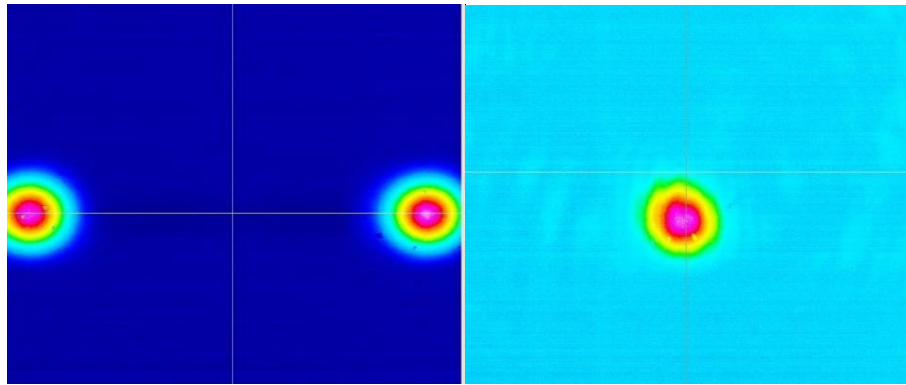


Figure 10.20: Isolation measurement beams on a CCD a) isolated beams and b) residual/not isolated beams.

When an isolator is constructed it is setup in an assembly jig so that this measurement can be made in real time. The wave plate and TGG orientations are then adjusted to optimise the isolation. Using this approach we can often achieve an isolation of >35dB. This is a rather ideal situation as it uses a narrow linewidth laser and would not be the isolation that you would get when used with a typical high power fibre laser, which will almost certainly have a much larger linewidth.

For example, when an isolator with an isolation of 32-33dB optimised with the DPSS laser is measured using our 200W SPI fibre laser the isolation is reduced to about 23dB. This is to do with the wavelength dependence of the Verdet constant and the linewidth of the laser. The linewidth of the DPSS laser is very narrow <0.1nm compared to the SPI fibre laser which is greater than 10nm. There is also a slight difference in the central wavelength between the SPI laser and the DPSS laser.

Optimisation of the isolator wave plates with the SPI laser can increase the isolation to around 26dB. Ideally, it would be good to optimise the isolation using the source with which it is intended to finally operate.

10.9.2 Insertion Loss Measurement

The insertion loss of an isolator is measured by shining the 0.8mm DPSS laser through the device in the forward direction and recording the transmitted power with and without the isolator in place. The insertion loss in dB is then calculated from

$$IL(dB) = 10 \log \left(\frac{P_{incident}}{P_{transmitted}} \right) \quad (10.9)$$

Where $P_{incident}$ is the power without the isolator in place and $P_{transmitted}$ is the power after the isolator. A typical insertion loss for an isolator is between 0.3 and 0.5dB.

The insertion loss can also be measured after the collimator is attached, by performing a fibre cut-back measurement. The isolator fibre is spliced to a 1064nm source and the power in the exiting beam $P_{transmitted}$ is measured. The fibre is then cleaved on the isolator side of the splice and the power $P_{incident}$ measured. The difference in these powers then gives the insertion loss the same as before.

For measurement simplicity we prefer to measure the insertion loss using the first method because a lot of the fibres used with isolators are few-moded. When using these fibres the insertion loss and other measured quantities tend to vary depending on the modal distribution in the fibre, which is often unstable.

10.9.3 Return loss measurement

The return loss of the isolator is measured using the setup shown in figure 10.21. A 1064nm source is spliced onto port 1 of a 3dB splitter. The isolator (or other component under test) is spliced onto port 2. The reflected power P_r from the isolator, or other component, is then measured on port 4. Port 3 is terminated with an angle cleave and immersed in index matching gel to prevent back reflections from this redundant arm.

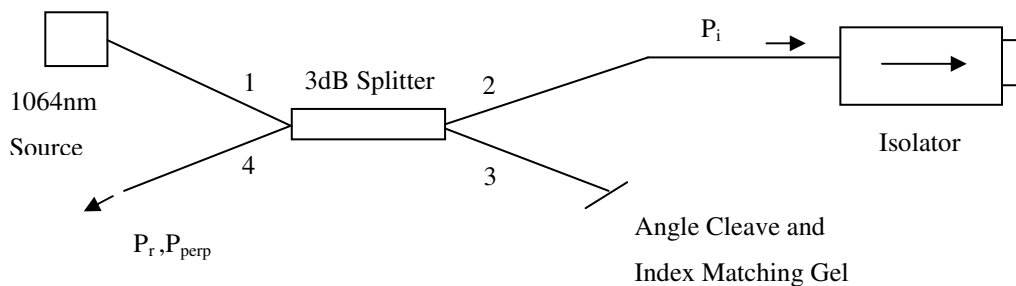


Figure 10.21: Setup for measuring the return loss of an isolator.

The optical return loss is then calculated from

$$ORL(dB) = 10 \log \left(\frac{P_i}{P_r} \right) - 3 \quad (10.10)$$

This requires that the incident power P_i is well known; that the 3dB splitter is exact and that any reflections from splices and the 3dB tap are negligible.

A method of normalisation which removes these errors is to reference the optical return loss to a known value, like the 14.7dB (4%) reflection from a perpendicularly cleaved fibre. This can also be used for measuring ORL from multimode components where the splice loss between the 3dB splitter and the component is directionally dependent. Using this method the return loss is given by

$$ORL(dB) = 10 \log \left(\frac{P_{perp} 10^{1.47}}{P_r} \right) \quad (10.11)$$

where P_{perp} is the back reflected power measured out of port 4 with a perpendicularly cleaved fibre on port 2 and P_r is the power measured out of port 4 with the isolator spliced onto port 2.

An optical return loss measurement made by Dr Norman Fisher is shown in figure 10.22. The upper graph in figure 10.21 is of the back reflected power from the isolator P_r . The bottom graph is of the reflected power from a perpendicular cleave P_{perp} . These are recorded over several minutes to provide a good average for the mean value. This is important because the reflected powers from the isolator are very low. During the recordings the fibre is manipulated slightly to give an idea of the polarisation and modal dependence of the return loss.

These measurements are made with a data acquisition card which records the 0-1V power proportional output voltage from a Newport power meter. The scale is linear with power, but the units are arbitrary. Fortunately this is unimportant as it is the ratio of the mean values of each of these readings which are important to make an optical return loss measurement.

This particular isolator has an optical return loss of 51 ± 5 dB. Typical return loss measurements for the latest design of isolator are >50 dB.

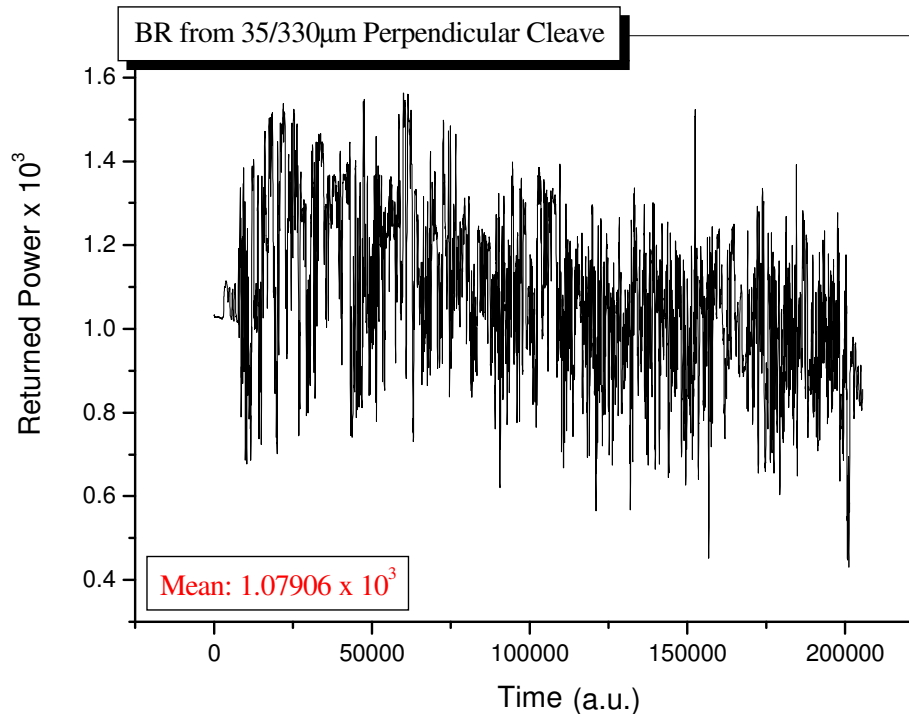
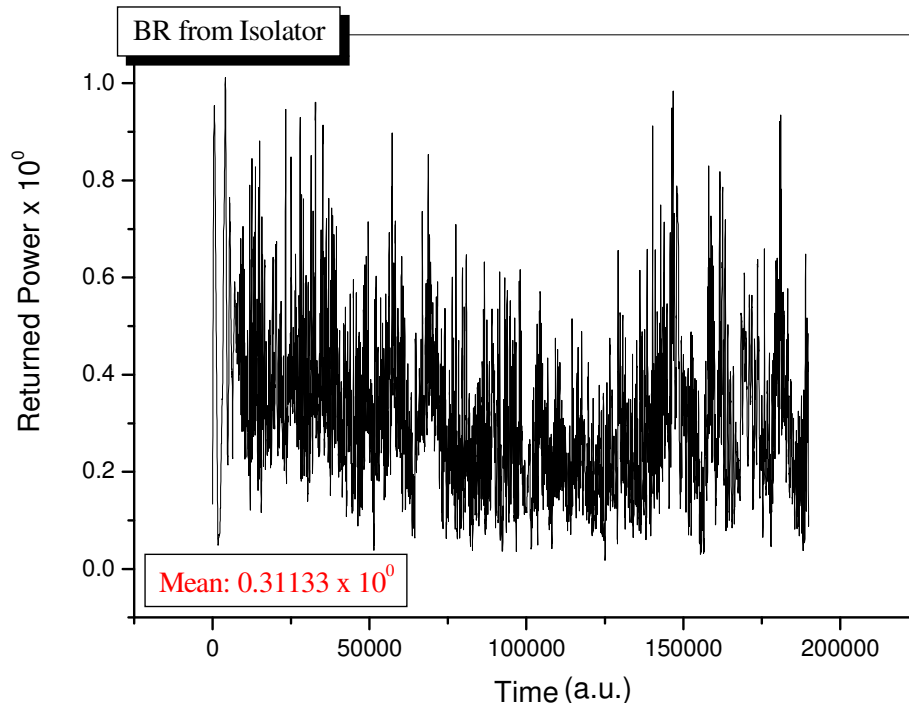


Figure 10.22: Measurement of Return Loss of isolator.

10.10 High Power Isolator Measurements

This section describes measurements of the isolator at high power. Including measurements of the isolation with power and the isolation verse temperature changes caused by absorbing a high power beam in the beam dumps.

- Section 10.10.1 discusses isolation measurements at high powers
- Section 10.10.2 discusses isolation measurements with the beam dumps in place, and
- Section 10.10.3 discusses a 200hr burn in test on an isolator.

10.10.1 Isolation-Power Measurements

To demonstrate that our isolation does not change significantly with power we conducted the following experiment. We used an isolator with no collimator or beam dumps on the back and aligned it in reverse with a 1mm beam from the 200W SPI fibre laser with a central wavelength around 1060nm and a linewidth of ~10nm. With no beam dumps or collimator we get three beams exiting the isolator, as shown earlier in figure 10.18. The central beam is the residual beam which has not been effectively isolated; the other two beams are the isolated beams which have not been recombined onto the optical axis. Ideally all the power should be in the outer beams and we would have no central beam.

To make isolation measurements the two outside beams are separated from the residual beam using a mirrored aperture and the power in the central beam recorded on a power meter, as shown in figure 10.23. The isolation of the isolator is then calculated from the ratio of the power in the residual beam P_{res} to the input power P_{in} (in dB) as follows

$$Isolation(dB) = -10\log\left(\frac{P_{res}}{P_{in}}\right) \quad (10.12)$$

Conducting this measurement without the collimator on the isolator removes the problem of coupling light into the fibre to measure isolation. This is very difficult and even in the best case will probably introduce an extra 1dB loss. The isolation measured using this setup will therefore be worse than the isolation of the complete isolator.

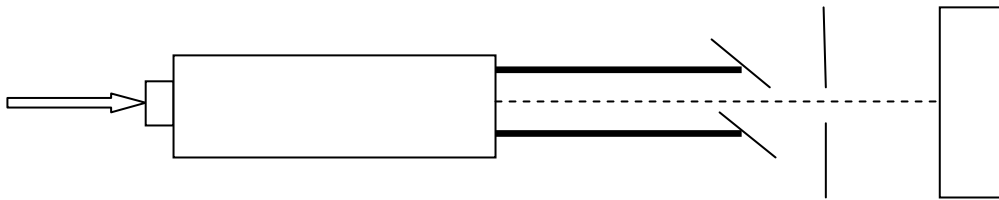


Figure 10.23: Setup for measuring isolation at high powers.

This isolator when built was optimised with a 1064nm DPSS laser with about 10mW output power. This has a narrow linewidth <1nm and the isolation of this source is around 33dB. When we transfer this to the high power fibre laser with a linewidth of around 10nm the isolation decreases to around 23dB. Optimising for this laser source gives a best case isolation of around 26dB.

Using this setup the isolation of this isolator was measured at a range of output powers from 5W to 60W. The isolator was allowed to dwell at each power setting for 5 minutes before a measurement was made. This was to ensure that we were reaching a thermal equilibrium and taking measurements under realistic conditions. As shown in figure 10.24 the isolation does not change significantly with power.

This is an important result which supports that the thermal stress induced depolarisation compensation works.

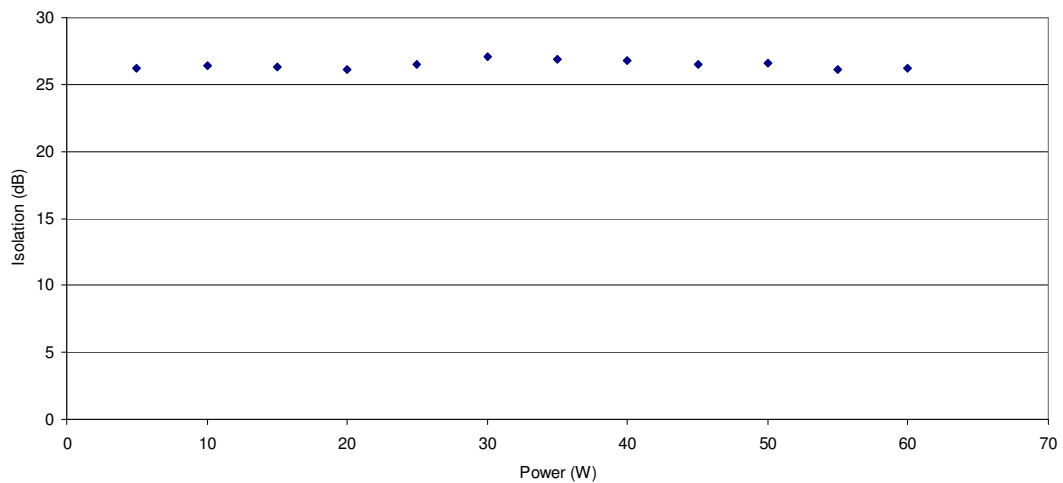


Figure 10.24: Isolation against input power.

10.10.2 Isolation with Beam Dumps and Temperature Measurements

In another test the isolation of the isolator was monitored with the beam dumps in place. The aim was to see how the dumped energy heated the isolator and see how the raised ambient temperature affects

isolation. From section 9.8 we know that increasing the ambient temperature affects the isolation by changing both the magnetic field strength of the magnets and the Verdet constant of the TGG.

This is a longer term effect than stress induced depolarisation as the Faraday isolator and magnets form a large thermal mass and take a while to reach equilibrium temperature. The heating of the whole isolator from room temperature to a stable raised temperature for a given input power takes several hours. On the other hand the heating of crystals inside the isolator and the setting up of temperature gradients, which cause thermal stress depolarisation and thermal lensing, will probably only take the order of 10's seconds because of their small size and high thermal conductivity.

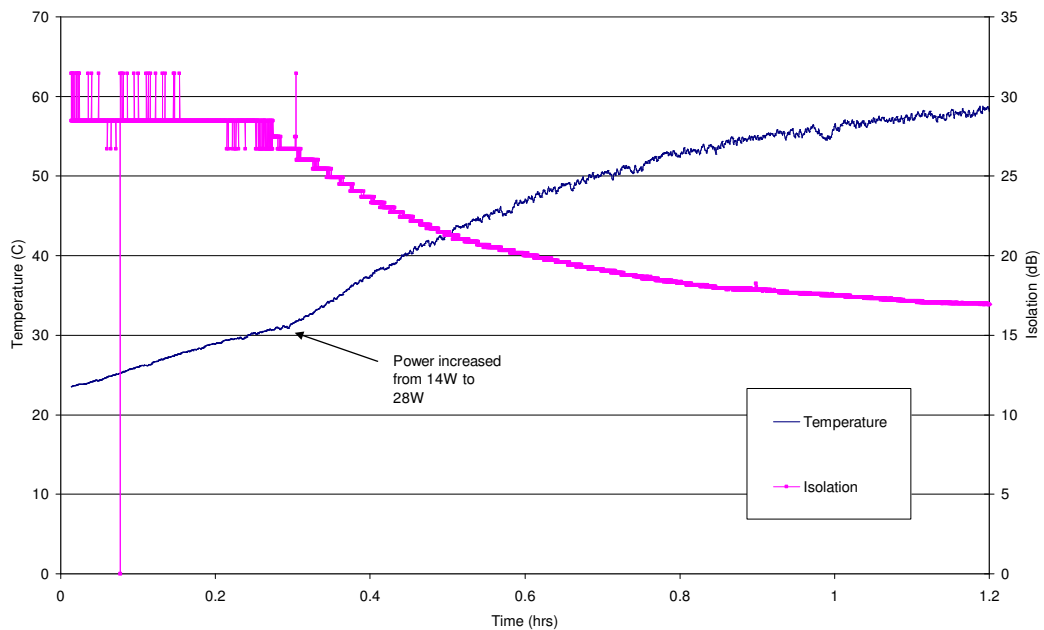


Figure 10.25: Temperature rise of isolator outer casing and isolation with 28W reverse input power.

When the beam dumps are on the isolator, the energy in the isolated beams is absorbed in the device. This causes the isolator to heat up. As shown in figure 10.25 with 28W into the isolator in the reverse direction the isolator temperature, measured on the outside of the isolator case, rises from room temperature $\sim 23^{\circ}\text{C}$ to around 60°C . This is approaching the upper operating temperature of the isolator and represents what we would consider an “extremely” unlikely condition during operation, prolonged exposure to greater than half of the rated output power of the isolator.

The isolator was not adequately heat sunk for these tests, because we were interested in creating a temperature rise to see the effect on isolation. If these conditions were typical during normal operation then we could alleviate the temperature rise significantly by heat sinking the beam dumps to increase passive cooling, or by surrounding the heat dumps with a water jacket for active cooling.

The good news from the perspective of the isolator is that even under these challenging conditions the isolation remains above 15dB. Falling slowly from a starting value of around 28-29dB. The high isolation measurements in figure 10.21 are limited by the sensitivity and resolution of the pyroelectric detector which was used to make measurements of the isolated beam power.

10.10.3 200hrs 60W Power Handling Test

To test the durability of the isolator a short lifetime test of 200hrs was conducted. For this test a 1mm free space beam was passed through the isolator in the forward direction. The throughput power and the temperature of the isolator at several points on the outside of the case were then monitored. The results of this test are shown in figure 10.26.

The power through the isolator was maintained at above 50W for the 200 hour. The insertion loss and isolation were measured before and after the test and were found to be unchanged. The highest rise in temperature was $<2^{\circ}\text{C}$ above ambient beside the front collimator. This is near to the position where residual light (light which has been depolarised) in the forward direction hits the inner casing. At around 140hrs the test was stopped and restarted. At this point the interlocked box, in which the test was being conducted, was opened and the temperature dropped. At this time the fibre coupling of the laser was realigned with better coupling. Hence, the ambient (in the box) temperature and isolator temperatures are all lower after 140 hours.

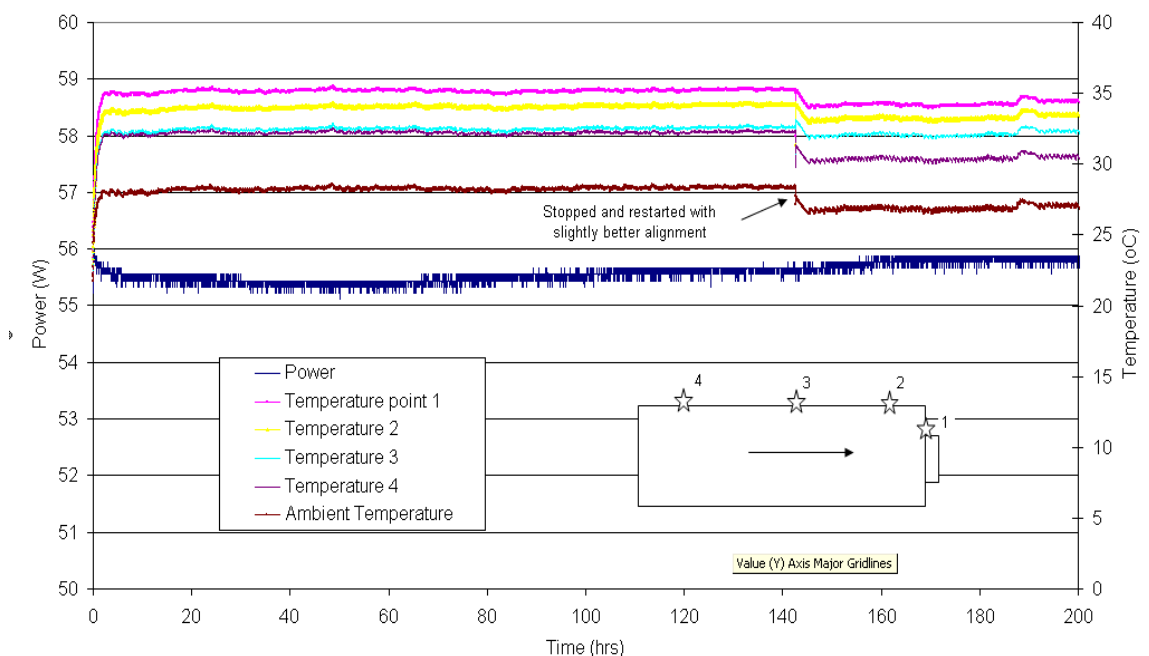


Figure 10.26: 200hr test of isolator with greater than 60W input.

References

- [10.1] Andreas Kuhn, Paul French, Duncan P. Hand, Ian J. Blewett, Mark Richmond, and Julian D. C. Jones. "Preparation of fiber optics for the delivery of high-energy high-beam-quality Nd:YAG laser pulses", *Applied Optics*, 2000, Vol. 39, No. 33, pp. 6136-6143
- [10.2] K. Shiraishi, F. Tajima, and S. Kawakami "Compact Faraday rotator for an optical isolator using magnets arranged with alternating polarities", *Optics Letters*, 1986, Vol. 11, No. 2, pp. 82-84
- [10.3] Alexander Knitsch, Axel Luft, Tobias Groß, Detlev Ristau, Peter Loosen, Reinhart Poprawe, "Diode laser modules of highest brilliance for materials processing", *Proceedings of SPIE*, 2002, Vol. 4651
- [10.4] MagNet Software Online: <http://www.infolytica.com/en/products/magnet/>
- [10.5] Daniel J. Gauthier, Paul Narum, and Robert W. Boyd, "Simple, compact, high-performance permanent-magnet Faraday isolator", *Optics Letters*, 1986, Vol. 11, No. 10, pp. 623-625
- [10.6] Ivan Mukhin, Alexandr Voitovich, Oleg Palashov, Efim Khazanov, "2.1 Tesla permanent-magnet Faraday isolator for subkilowatt average power lasers" *Optics Communications*, 2009, Vol. 282, Iss. 10, pp. 1969-1972
- [10.7] Gérard Tréneç, William Volondat, Orphée Cugat, and Jacques Vigué, "Permanent magnets for Faraday rotators inspired by the design of the magic sphere", *Applied Optics*, 2011 Vol. 50, No. 24
- [10.8] Northrup Grunman, "TGG datasheet", Online:
http://www.as.northropgrunman.com/products/synoptics_tgg/index.html
- [10.9] Mikhail A. Kagan and Efim A. Khazanov, "Thermally induced birefringence in Faraday devices made from terbium gallium garnet–polycrystalline ceramics", *Applied Optics*, 2004, Vol. 43, No. 32, pp. 6030-6039
- [10.10] Aleksey V. Starobor,* Dmitry S. Zheleznov, Oleg V. Palashov, and Efim A. Khazanov "Magnetoactive media for cryogenic Faraday isolators", *J. Opt. Soc. Am. B*, 2011, Vol. 28, No. 6, pp. 1409-1415
- [10.11] Jingjing Liu, Feiyun Guo, Bin Zhao, Naifeng Zhuang, Yanping Chen, Zhaoping Gao, Jianzhong Chen, "Growth and magneto-optical properties of NaTb(WO₄)₂", *Journal of Crystal Growth*, 2008, Vol. 310, pp. 2613–2616
- [10.12] F. Guo, J. Ru, H. Li, N. Zhuang, B. Zhao, J. Chen, "Growth and magneto-optical properties of LiTb(MoO₄)₂ crystal", *Appl Phys B*, 2009, Vol. 94, pp. 437–441
- [10.13] Mikio Geho, Takenori Sekijima, Takashi Fujii "Growth of terbium aluminum garnet (Tb₃Al₅O₁₂; TAG) single crystals by the hybrid laser floatingzone machine", *Journal of Crystal Growth*, 2004, Vol. 267, pp. 188–193
- [10.14] International Crystals, "CdMnTe datasheet", Online:
http://www.internationalcrystal.net/optics_05.htm
- [10.15] Marvin J. Weber, "Handbook of optical materials", CRC Press, 2003
- [10.16] Felix Abt, Axel Heß and Friedrich Dausinger Focusing High-Power, "Single-Mode Laser Beams", *Photonics spectra*, May 2008 online: <http://photonics.com/Article.aspx?AID=33535>

- [10.17] Christian Mühlig, Siegfried Kufert, Simon Bublitz, and Uwe Speck, “Laser induced deflection technique for absolute thin film absorption measurement: optimized concepts and experimental results”, *Applied Optics*, 2011, Vol. 50, No. 9, pp. C449-C456
- [10.18] Eduard Wyss, Michelle Roth, Thomas Graf, and Heinz P. Weber, “Thermo-optical Compensation Methods for High-Power Lasers”, *IEEE Journal of Quantum Electronics*, Vol. 38, No 12, pp. 1620-1628

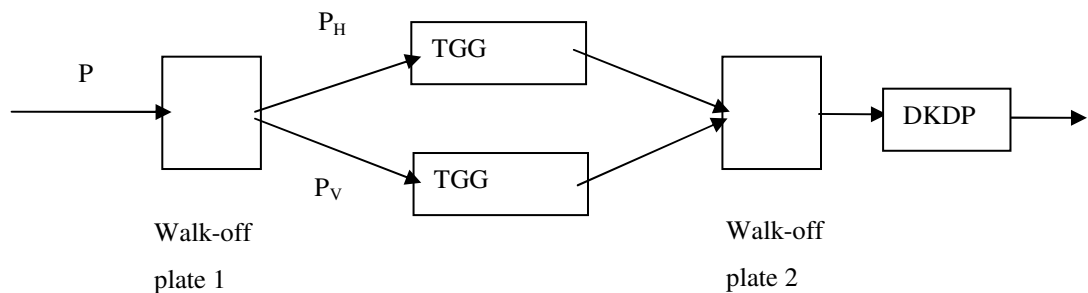
Appendix A10.1: Limits on Thermal Lens Compensation in Isolator if “bolt-on” DKDP compensator is used at output. (Chris Pannell - Internal correspondence)

In our isolator design we decided to place the thermal lens compensator after the second walk-off plate. The question was raised as to what effect this has on the efficiency of compensation? Is it better to place the compensator at this position or in between the two walk-off plates? The answer to these questions are complicated and depend on what is felt to be most important, compensation of thermal induced stress birefringence or compensation of thermal lensing.

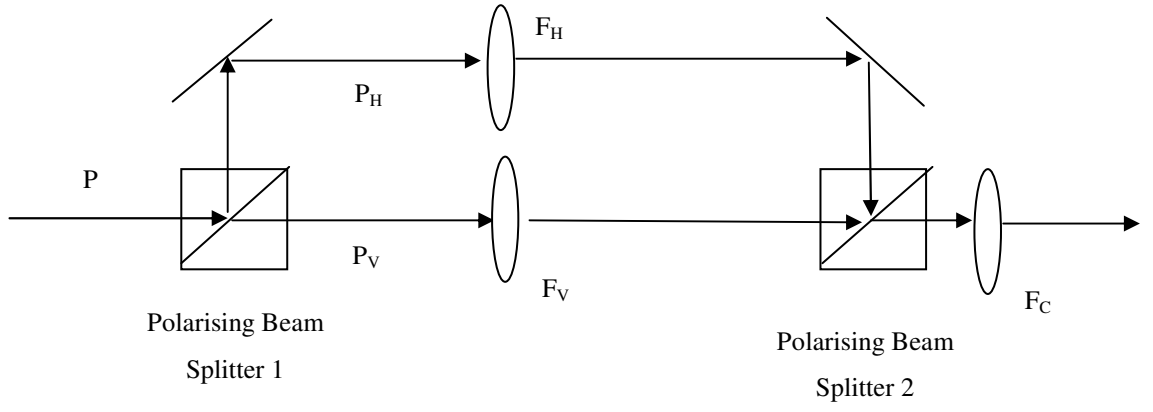
If the thermal lens compensator is placed between the two walk-off plates then it is possible to get perfect thermal lens compensation for all polarisation inputs into the isolator and not cause astigmatism in the output beam. However, then you run the possibility of the compensating element introducing birefringence and spoiling the isolation/insertion loss of the isolator.

If the thermal lens compensator is placed after the second walk-off plate then birefringence or depolarisation in the compensator does not effect the operation of the isolator. However, in this case perfect thermal lens compensation is not possible, but we can get fairly close.

The instantaneous input polarisation state into the isolator is unknown and varies randomly with time. The total power P in the beam is constant. The input polarisation is split into two orthogonal components by the walk-off plate. These travel separately through the TGG crystal before being recombined at the second walk-off plate. The DKDP then acts upon the beam after recombination. Schematically this can be shown as



Since the TGG is the main contributor to thermal lensing this is equivalent to something like this



Polarisation beam splitter 1 sends the H-component through a thermal lens whose focussing power ($1/f_H$) depends on the optical power P_H in the H-component. Likewise, the V-component travels through a lens with focussing power ($1/f_V$). The total power $P = P_H + P_V$.

To a good approximation the focussing power of f_H and f_V can be expressed as

$$\frac{1}{f_{H,V}} = a + bP_{H,V} + cP_{H,V}^2 + dP_{H,V}^3 \quad (\text{A10.1})$$

Where a, b, c and d are constants. The compensating lens from the DKDP now has to compensate for ($1/f_H$) and ($1/f_V$) using only one power-dependent focal length, f_C . Where

$$-\frac{1}{f_C} = a + bP + cP^2 + dP^3 \quad (\text{A10.2})$$

For a linear input polarisation state the power in the H-component and V-component transmitted by the polarisation beam splitter is given by

$$\begin{aligned} P_H &= P \cos^2 \theta \\ P_V &= P \sin^2 \theta \end{aligned} \quad (\text{A10.3})$$

where θ is the angle between the polariser axis and the polarisation direction of the input beam. If $\theta=0^\circ$ pure H-polarisation; $\theta=90^\circ$ pure V-polarisation. So for the H-component

$$\frac{1}{f_H} = a + b(P \cos^2 \theta) + c(P \cos^2 \theta)^2 + d(P \cos^2 \theta)^3 \quad (\text{A10.4})$$

$$\frac{1}{f_V} = a + b(P \sin^2 \theta) + c(P \sin^2 \theta)^2 + d(P \sin^2 \theta)^3$$

If we now choose a compensating element with

$$-\frac{1}{f_C} = a + b(\lambda P) + c(\lambda P)^2 + d(\lambda P)^3 \quad (\text{A10.5})$$

Where λ is an optimisation parameter ($0 < \lambda < 1$) which has to be chosen. If the distance between F_H and F_C is much smaller than their respective focal lengths, then to a good approximation the focal powers are additive, so

$$\frac{1}{f_H} + \frac{1}{f_C} = a + b(\cos^2 \theta - \lambda)P + c(\cos^4 \theta - \lambda^2)P^2 + d(\cos^6 \theta - \lambda^3)P^3 \quad (\text{A10.6})$$

Likewise for the V-component

$$\frac{1}{f_V} + \frac{1}{f_C} = a + b(\sin^2 \theta - \lambda)P + c(\sin^4 \theta - \lambda^2)P^2 + d(\sin^6 \theta - \lambda^3)P^3 \quad (\text{A10.7})$$

If $\theta=45^\circ$ $P_H=P_V$ and the H and V thermal lenses are equal strength ($1/f_H) = (1/f_V)$. In this case with $\lambda=1/2$

$$\frac{1}{f_H} + \frac{1}{f_C} = \frac{1}{f_V} + \frac{1}{f_C} \quad (\text{A10.8})$$

In this case we can achieve perfect compensation. For all other θ ($1/f_H) \neq (1/f_V)$ and so perfect compensation is not possible for both the H and V-components simultaneously.

The optimum value of λ , which gives the lowest possible total lens power in both the H and V-components varies with θ as

$$\lambda_{opt} = \cos^2 \theta \quad (\text{A10.9})$$

This has an average value of

$$\langle \lambda_{opt} \rangle = \langle \cos^2 \theta \rangle = \frac{1}{2} \quad (\text{A10.10})$$

Therefore for a randomly polarised beam the best we can do is compensate for $\theta=45^\circ$ with $\lambda=1/2$. In the worst case ($\theta=0^\circ$ or 90°) then we have

$$\frac{1}{f_H} + \frac{1}{f_C} = b \left(\frac{1}{2} \right) P + c \left(\frac{3}{4} \right) P^2 + d \left(\frac{7}{8} \right) P^3 \quad (\text{A10.11})$$

Compare this to the uncompensated case in equation (A10.1) and you can see that to a first approximation (linear in P) we have halved the power of the thermal lens.

In the best case ($\theta=45^\circ$) we have eliminated the thermal lens. In practice we will have compensation varying between perfect and half for all input polarisation state. The average value is given by working out the RMS of equations (A10.6) and (A10.7)

The above analysis assumes a random time-varying linear input polarisation from the fibre. If the input state is a scrambled mixture of modes each with a random polarisation orientation then on average $P_H \approx P_V$ and compensation will be more effective.

Note that if the DKDP was placed between the walk off plates so that both polarisations travel through the DKDP separately then we can achieve compensation for both polarisations independently. Then “perfect” compensation is possible for any given input polarisation.

The advantage of having the DKDP outside of the walk-off plates is that any depolarisation caused by the DKDP does not affect the isolation of the isolator. This is of more fundamental importance than the reduction of the power induced focal shift caused by the isolator.

Chapter 11 - Conclusion

This chapter summarises the results and conclusions from the Faraday isolator development. It also includes suggestions for improvements to the isolator and further development work that could be done to advance the isolator. This chapter also contains a short section on a triple pass fibre-in beam-out isolator which was designed and constructed early on in the project but was abandoned after disappointing early results. The chapter finishes with a section describing a 20W fibre-in fibre-out isolator that we are currently developing.

This chapter is structured as follows:

- **Section 11.1 - Summary of Isolator Development**
- **Section 11.2 - Next Steps**
- **Section 11.3 – 20W Fibre-in Fibre-out Isolator**

11.1 Summary of Isolator Development

A fibre-in beam-out isolator with excellent optical performance and compensation for thermal stress induced birefringence and thermal lensing has been developed. The possibility of compensating for isolation loss from temperature rises and wavelength changes has also been investigated, although not implemented.

The isolator has been tested at greater than 60W powers and found to not suffer from loss of isolation or increase in insertion loss. The loss of isolation that would occur due to stress induced birefringence in TGG has been understood and modelled following the work of Khazanov et. al. [11.1, 11.2]. A dual rod design with two contra rotating 22.5° Faraday rotators separated by a half wave plate was chosen to compensate for thermal stress induced birefringence which otherwise would have affected the isolation at high powers.

Thermal lensing has been treated both theoretically and experimentally. The thermal lens focal shift intrinsic to the isolator, caused by absorption in the terbium gallium garnet Faraday rotators has been measured as 9 Rayleigh lengths per kW. We also demonstrated that this could be compensated for by including a suitably chosen extra component which produces the opposite shift in the focal length, for this purpose deuterated KDP has been investigated.

The magnetic design of the isolator has been explained and calculations made of the magnetic fields produced by the NdFeB permanent magnets, simulated using the finite element package FEMM [11.3].

The mechanical design of the isolator has also been considered and the construction method. To simplify manufacture the isolator is built as an “in-tube” construction which allows very strong magnets to be compressed safely in an opposing configuration. The input collimator to be spliced onto a fibre laser is constructed separately from the isolator and only aligned and secured in the final stages of construction. This allows us to optimise parameters like pointing and offset with respect to the isolator body.

11.2 Next steps

The obvious next step in the isolator development would be to alter the mechanical design slightly to allow the TGG rods to be independently rotated. This would allow us to rotate each TGG rod into its best orientation for optimum PER performance. Also if we get a good supply of isotropic TGG with little initial stress then it would allow us to optimise the orientation of the TGG rods for thermal stress birefringence compensation. As shown in section 8.5 thermal stress birefringence is minimised when the TGG <100> axis makes an angle of θ_{\min} with the input polarisation. Where

$$\theta_{\min} = \left(n + \frac{3}{8} \right) \frac{\pi}{2} + \frac{1}{4} \left(\frac{\pi}{2} - \arcsin \left(\frac{a}{b} \frac{\xi^4 - 1}{(1 - \xi^2)^2} \right) \right) \quad n = -2, -1, 0, 1, 2, \dots \quad (11.1)$$

This requirement specifies that the axis of the two TGG rods also have to be mutually aligned. This should increase the isolation and decrease the insertion loss of the isolator and allow performance up to higher powers without degradation. Figure 8.10 shows that at 50W the difference between the best and worst case orientations could be as much as 8dB.

It would also be good to characterise some other parameters of the isolator like the pointing accuracy and pointing accuracy stability and drift with temperature. The pointing accuracy and stability in a laser marking or cutting system is obviously extremely important and we know from customer feedback that our collimator components fare extremely well in pointing accuracy and pointing drift with temperature. We attribute this to the simple single lens design; precise fibre positioning and the symmetric design using low stress, low thermal expansion adhesives. In the near future we plan to develop in-house testing methods for measuring these quantities more accurately.

Currently, we have begun development of a 20W fibre-in fibre-out (FIFO) isolator. This will be described in section 11.3. The biggest challenge with a FIFO isolator is not in the design of the isolator but in the coupling over long distance of two single mode fibres. Fortunately, at Gooch and Housego (Torquay) we have experience in this area from the development of the “Fibre-Q” an inline fibre AOM.

We were also considering increasing the performance of the isolator by increasing the size of the magnets and reducing the length of TGG in the isolator. As mentioned in chapter 8 reducing the length of TGG decreases the problems associated with parasitic thermal effects. It could also possibly reduce the cost of the isolator because the TGG crystal is by far the most expensive part. The downside is a larger and heavier device. Some modelling of magnet designs has already been done into this and we found that increasing the magnets outer diameter from 36mm to 54mm would reduce the TGG length from 28mm to around 20mm.

It would also be interesting to look at the other Faraday rotating materials like terbium aluminium garnet, Cadmium Manganese Telluride and Ceramic TGG highlighted in section 10.8. However, this would require a lot of work in the development of these materials as most have only been grown in laboratories. The production of high quality and consistent materials would be necessary to make them economical.

Finally, of longer term interest we would like to examine and investigate materials which produce Faraday rotation at $2\mu\text{m}$. This would allow us to produce Isolators targeting the emerging Thulium fibre laser market, which is currently underserved by component suppliers. A project aimed at increasing our capabilities in this important wavelength region has recently started. The largest unknown in this project is material availability, as very few materials have been measured for Faraday rotation at these wavelengths. Initial literature searches have highlighted AlGaAs, BaF₂ and ZnSe [11.4] however the Verdet constant of these materials at $2\mu\text{m}$ is still only a maximum of half the size of TGG at 1060nm.

11.3 Fibre-in Fibre-out Isolator

The most recent advancement of the isolator project has been to design a fibre-in fibre-out isolator for powers up to 20W. This is a logical step for the isolator project as it combines a number of capabilities within the company, including the design and construction of high quality collimators and the use of paired collimators to create fibre-coupled devices like the “Fibre-Q”, our fibre coupled AOM. The key to creating a high power and stable fibre out device is to optimise the coupling between collimators and control the removal of light from the cladding of the fibre so that it can be absorbed over a relatively long area. This prevents hotspots and failures in the output fibre. With our current solution and a 0.5dB coupling loss we believe that we can reliably couple around 30W before failure.

A future development project will involve looking at alternative methods to couple light out of the glass cladding of the fibre to allow the isolator to operate at higher powers. The use of graded index epoxies along the fibre length to progressively strip out larger quantities of light or the bonding of glass capillaries to the fibre may be a logical next step. At high powers it may be necessary to implement compensation for thermal lensing in the package. Thermal lensing will be seen as a power dependent insertion loss as it changes the beam parameters and will affect coupling between fibres.

This FIFO isolator will be of a single pass, single rotator design. This keeps the isolator simple to construct for the first iteration and avoids the problems we experienced with the FIBO triple pass isolator. Subsequent designs may revert to using a triple pass if it is found to work out more cost effective, or if the length of the isolator is decided to be too large.

The elements of the isolator and the polarisation rotations that we expect to see through the isolator are shown in figure 11.1. The design is similar to the triple pass design except the triple pass TGG rod has been replaced with a single pass 45° TGG rotator and the quartz rotators have been combined into one piece.

In the forward direction the unpolarised light is split by the YVO_4 walk-off plate into its two polarisations. These are then rotated clockwise 45° by a TGG rotator then 45° anticlockwise by the quartz rotator before being recombined by the second YVO_4 walk-off plate. In the reverse direction the beam is rotated 45° clockwise by the quartz rotator then a further 45° by the TGG so that it is left in a polarisation state orthogonal to the one in which it began and so separated by the walk-off plate.

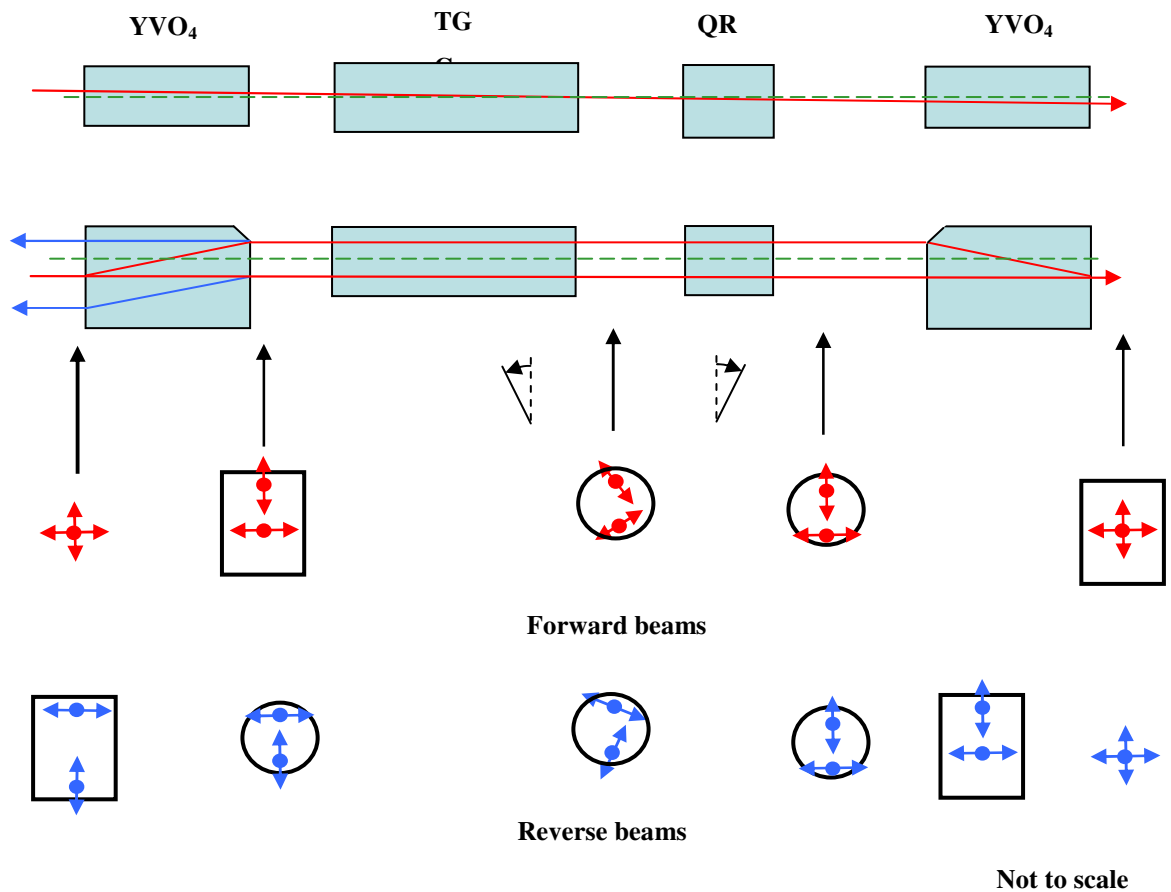


Figure 11.1: Path of beams through optical components of single-pass FIFO isolator, side view and top view, and polarisation changes in forward (red) and reverse (blue) propagation. [11.5]

A simple magnet assembly using three opposing magnets has been designed, figure 11.2. The TGG will sit in the bore of the centre magnet where the average field has been determined to be 0.93T. With this field strength the TGG should produce a rotation of 46.9°. The rotation has been chosen to be slightly higher than 45° because it will drop as temperature increases and it is expected that the isolator will operate at a temperature a little above ambient under real conditions. The variation in the rotation radially across the TGG from the centre of the crystal to a radius of 0.5mm is predicted to be better than 0.15°.

The magnetic field can be tuned by inserting non magnetic steel spacers between the magnets, figure 11.3. With 2mm spacers between the magnets the rotation in a 22mm piece of TGG is reduced from 47.1° to 45.8°. Counter intuitively increasing the space between the magnets improves the uniformity of the magnetic field, so that the difference in rotation between the centre of the beam and the outside of the beam falls from 0.15° to 0.07°.

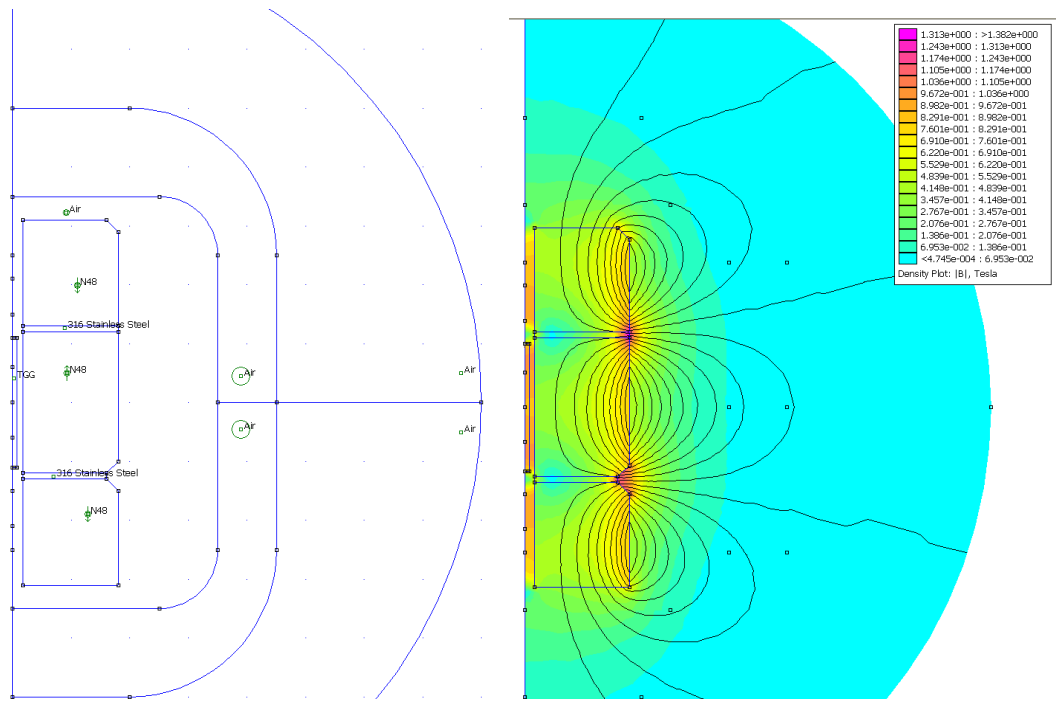


Figure 11.2: Magnetic field around triple magnet design calculated using finite element software FEMM [11.3].

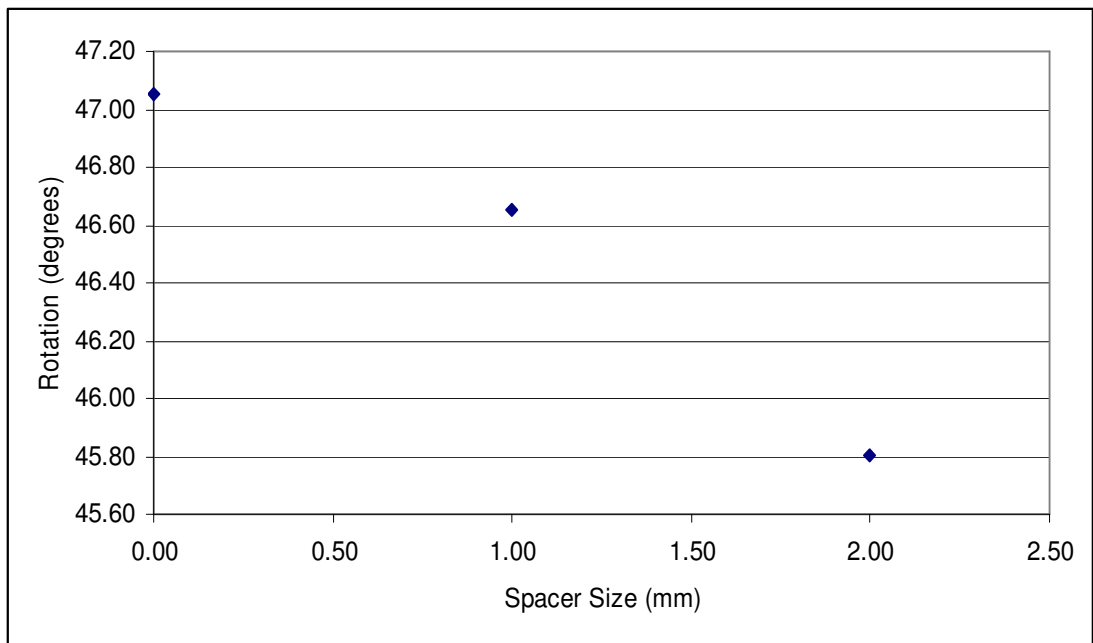


Figure 11.3: Rotation of TGG in triple magnet design, figure 11.6, with spacers between the magnets.

References

- [11.1] E A Khazanov, "Compensation of thermally induced polarisation distortions in Faraday isolators", *Quantum Electronics*, 1999, Vol. 29 (1) pp. 59-64
- [11.2] E A Khazanov, "Characteristic features of the operation of different designs of the Faraday isolator for a high average laser-radiation power", *Quantum Electronics*, 2000, Vol. 30, pp. 147-151
- [11.3] D. C. Meeker, *Finite Element Method Magnetics*, Version 4.0.1, Online:
<http://www.femm.info>
- [11.4] M.-H. Kim, V. Kurz, G. Acbas, C. T. Ellis, and J. Cerne, "Measurement of the infrared complex Faraday angle in semiconductors and insulators," *J. Opt. Soc. Am. B*, 2011, Vol. 28, pp. 199-207
- [11.5] Mark Gardner. Internal Presentation.